A relative moment tensor inversion technique applied to seismicity induced by mining

Lindsay Marguerite Andersen

A thesis submitted to the Faculty of Science, University of the Witwatersrand, Johannesburg, in fulfilment of the requirements for the degree of Doctor of Philosophy.

Johannesburg, 2001

DECLARATION

I declare that this thesis is entirely my own work aided only by the supervision and guidance I received from Dr. A. Cichowicz in the form of discussions during the course of the study. The thesis is being submitted for the degree of Doctor of Philosophy at the University of the Witwatersrand, Johannesburg. It has not been submitted before for any degree or examination at any other university.

Signed on this 18th day of July 2001

L Andersen

Lindsay Marguerite Andersen

PREFACE

This thesis began its life as a M.Sc. dissertation. The main objective of the work was to apply the relative moment tensor inversion method described in a 1995 paper by Dr T. Dahm in the *International Journal of Geophysics* entitled 'Relative moment tensor inversion based on ray theory: theory and synthetic tests' to data recorded in the underground environment. The pivotal aspect of Dahm's method is that a single reference event with a known radiation pattern is not a prerequisite when applied to seismic source clusters with different radiation patterns. In contrast to the standard inversion methods, this method does not require the complete calculation of synthetic Green's functions. Simplistically, the Green's tensor may be thought of as comprising a 'geometrical component' and a 'path effect.' The former depends on the geometric relationship between the source and receiver, while the latter depends on the properties of the medium through which the seismic waves propagate. This method is known as the relative moment tensor inversion method without a reference mechanism.

The primary objective of the M.Sc. study was to apply the relative moment tensor inversion method without a reference mechanism to microseismic data recorded underground in a deep level gold mine. An important aspect of the M.Sc. study at the time was that the inversion method had not previously been applied to mining-induced tremors in order to obtain seismic event source mechanisms. An ancillary objective was a performance assessment of the algorithm. To achieve this, a number of stability tests were carried out using recorded seismic data to determine the limitations of the relative inversion and possible sources of error or deficiency. These were not 'tests' in the rigorous sense, and may be better described as observations of the behaviour of the relative inversion (and resultant moment tensor components) in particular circumstances.

To achieve the objectives outlined above, the author prepared a computer program that performed the relative inversion without a reference mechanism to compute moment tensor solutions for clusters of microseismic events induced by mining. The relative inversion method of Dahm (1996) was developed in the time-domain for seismic sources belonging to a small source region, and assumed that the impulsive point source approximation was valid. Input data consisted of the peak amplitudes of the P, SH and SV-phases, measured from the time-integrated displacement traces to which a low-pass filter had been applied. Both P and S-phases were used simultaneously to assist in constraining the moment tensor components by adding different types of governing equations to the linear inversion problem. To facilitate interpretation, the program calculated not only radiation patterns for selected moment tensor components from the output moment tensor solutions, but also a number of source parameters of the events.

At this stage, it is important to emphasise that Dahm's relative method, when applied to events in a source cluster having different radiation patterns, solves for a separate moment tensor for each event, i.e. for different source mechanisms. This is mentioned to avoid confusion with the composite inversion methods where a single moment tensor solution is obtained from the joint processing of amplitude data from a number of seismic sources occurring within a given area. The composite method is subject to a number of spatial and temporal constraints because the events in the source cluster are assumed to have the same focal mechanism.

The inversion procedure was applied to waveform data recorded by the Portable Seismic System (PSS) developed by the erstwhile Chamber of Mines Research Organisation, now the CSIR Division of Mining Technology. The data were recorded at the Blyvooruitzicht Gold Mine experimental preconditioning site, where a strike-stabilising pillar was in the process of being extracted. The site was extensively monitored and geologically mapped to gauge the effectiveness of preconditioning, and hence provided an ideal setting in which to assess the capabilities and limitations of the relative inversion technique. The focal mechanisms determined from the moment tensor solutions could, at least in theory, be correlated with the fault slip inferred from the fracture mapping. Thus, a method of assessing the fidelity of the computed moment tensors by means of directly observable phenomena was available.

The relative method was applied to three families of microseismic events recorded at a depth in excess of 1900m at the Blyvooruitzicht Gold Mine experimental site. A total of 58 events with high signal-to-noise ratios were used in the inversion, with magnitudes in the range –1.4 to 0. The fault-plane solutions were found to correlate well with the fracture mapping of the site. The dominant source mechanism for most events was of the shear type (double-couple source model). However, the source parameters of one of the larger event families showed some deviation from the double-couple mechanism. The additional component contributing to the overall mechanism was thought to be due to the opening of the shear fracture. All of the events displayed a small positive isotropic component between 7 and 16 per cent, representing volumetric expansion.

The resolution of the moment tensor components is dependent on the accurate and adequate sampling of the radiation pattern, which is a function of the azimuthal coverage provided by the seismic network. A technique was developed where the moment tensor components computed from synthetic data are compared with those derived from observed amplitude data to give a qualitative indication of the error. It was found that the planar configuration of the seismic network used in this study leads to a variation in the moment tensor components oriented normal to the plane of the network, which coincides with that of the reef. In addition, source clusters located within the plane of the seismic network showed less variation than those located below the reef.

The work was submitted in January 1999, examined the same year, and passed with distinction. This happy result triggered a chain of events, the first of which was for the author's supervisor, Dr Cichowicz, to suggest the project be converted to Ph.D. level and resubmitted once more work had been done. Dr Cichowicz applied for a conversion of registration from M.Sc. to Ph.D. under Rule S81(a), on the grounds that

the research presented in the author's dissertation was beyond the requirements laid out for M.Sc. work. The proposed extension to the project included reformulating the relative inversion problem in the frequency-domain and applying this method in another case study situation.

While developing the method in the frequency-domain and exploring the relative methods further, the technique was applied extensively to a number of different data sets. It was found that the output of the relative inversion without a reference event was strongly dependent on the events in the cluster having significantly different mechanisms. This criterion becomes especially important when the input data are noisy. This is not a surprising observation since a cluster of events having very similar mechanisms leads to a near-singular least-squares matrix. When the noise level is of the same order as the differences in the mechanisms, the system of equations becomes near-singular, thereby significantly blurring the distinction between the mechanisms, and producing unreliable results. This is a disadvantage in the mining environment since clusters of events recorded in the underground environment are very likely to have similar mechanisms.

The relative moment tensor inversion method without a reference mechanism must, therefore, be applied with caution. The reason the technique was so successful in resolving the mechanisms of the Blyvooruitzicht event clusters is that the input data files were painstakingly created by hand after careful inspection of each individual waveform. These data files were surprisingly noise-free, thereby allowing the resolution of very similar mechanisms within each source cluster. This method of creating a data file in the mining environment would be prohibitively time-consuming - hence the need for the development of a more robust method for routine application to mining-induced tremors. This led to the development of the hybrid methods that form the main focus of this thesis.

ABSTRACT

Three hybrid moment tensor inversion methods were developed for seismic sources originating from a small source region. These techniques attempt to compensate for various types of systematic error (or noise) that influence seismograms recorded in the underground environment in order to achieve an accurate and robust measure of the seismic moment tensor. The term 'hybrid' was used to distinguish between the relative method proposed by Dahm (1995) and the methods developed in this thesis. The hybrid methods were essentially weighting schemes designed to enhance the accuracy of the computed moment tensors by decreasing the influence of any low quality observations, to damp (or amplify) any signals that have been overestimated (or underestimated) due to local site effects, and to correct for raypath focussing or defocussing that results from inhomogeneities in the rockmass.

The weighting or correction applied to a particular observation was derived from the residuals determined when observed data were compared with corresponding theoretical data (for a particular geophone site, sensor orientation and wave phase) and were calculated using a cluster of events rather than a single event. The first and second weighting schemes were indirectly related to the mean and the median of the residuals where the residuals were defined as the ratio of the theoretical to observed data. In the third scheme, the residuals were defined as the difference between the observed and theoretical data and the weights were based on the distance of a data point (measured in standard deviations) from the mean residual. In each of the weighting schemes, the correction was applied iteratively until the standard error of the least-squares solution (normalised to the scalar seismic moment) was a minimum. The schemes were non-linear because new weights were calculated for each iteration.

A number of stability tests using synthetic data were carried out to quantify the source resolving capabilities of the hybrid methods under various extreme conditions. The synthetic events were pure double-couple sources having identical fault-plane orientations, and differing only in rake. This similarity in the mechanisms was chosen because the waveforms of tightly grouped events recorded underground often show high degrees of similarity. For each test, the results computed using the three hybrid methods were compared with one another and with those computed using the single event, absolute method and two relative methods (with and without a reference mechanism). In the noise-free situation, it was found that the relative method without reference mechanism showed the highest resolution of mechanisms, provided that the coverage of the focal sphere was not too sparse (> 3 stations). The hybrid method using a median correction was found to be the most robust of all the methods tested in the most extreme case of poor coverage (2 stations) of the focal sphere.

When increasing levels of pseudo-random noise were applied to the data, the absolute moment tensor inversion method, the hybrid method using a median correction, and the hybrid method using a weighted mean correction all showed similar robustness and stability in extreme configurations concerning network coverage of the focal

sphere and noise level. When increasing levels of systematic noise were added to the data, the hybrid methods using a median correction and weighted mean correction were found to exhibit similar robustness and stability in extreme configurations concerning network coverage of the focal sphere and systematic noise. In all situations investigated, these two hybrid methods outperformed the relative and absolute methods.

The hybrid moment tensor inversion methods using a median and weighted mean correction were applied to a cluster of 14 events, having remarkably similar waveforms, recorded at Oryx Gold Mine. For comparative purposes, the absolute method was also applied. The inputs to the inversion methods consisted of the spectral plateaus of both P- and S-waves at frequencies below the corner frequency of the time-integrated displacement traces. The polarities of dominant motion were used as an additional constraint and were determined from cross-correlation of observed with synthetic P- or S-waves. The solutions computed using the hybrid moment tensor inversion using a median correction displayed a distinct improvement after the iterative residual correction procedure was applied. The radiation patterns and fault-plane solutions showed a high degree of similarity, and are probably more accurate reflections of reality than those computed using the absolute moment tensor inversion methods. These observations are very encouraging and point towards the method's potential for use as a standard processing tool for mine seismicity.

The implications of this work are a better understanding of the focal mechanisms of seismic events induced by mining activities, ultimately leading to improved safety underground.

ACKNOWLEDGEMENTS

The work presented in this thesis constitutes part-time studies carried out during the course of my employment at the Council for Scientific and Industrial Research (CSIR), Division of Mining Technology. Gratitude is extended to Güner Gürtunca, the Director of Miningtek, and to my various managers for their support and understanding over the years. Most importantly, I am grateful for the study leave to complete this thesis. Gary York and Archie – thanks.

Thanks are also due to Steve Spottiswoode for his encouragement, insights and all the fruitful discussions, the number of which is too large to remember, and for patiently waiting for me to understand his ideas!

I would also like to thank my supervisor Artur Cichowicz for helping me see the wood when I was baffled by trees and for his invaluable insights into the mathematical language of seismology. Not only was he enthusiastic and encouraging, but he also has the rare talent of keeping me focussed and on track, rather than allowing me to follow the figments of my imagination.

Thanks also to Ray Durrheim for drawing my attention to the fascinating paper on which the M.Sc. work is based. A vital part of any research is being intrigued by the subject. His continued interest in the Ph.D. is much appreciated.

Special gratitude is extended to John Napier for listening to my ramblings and including me in the interesting discussions he organised with some world-class scientists. The probing questions certainly kept me on the mathematical straight and narrow.

I am very grateful to the Management of Oryx Gold Mine who gave me their blessing to use their data. Special thanks are extended to Johan Scheepers who nurtures the seismic network – much of the success of the case study in this thesis is due to his wonderfully clean waveforms.

Many colleagues at Miningtek have been generous in sharing their programming and computational experience, insights into geology and rock engineering, proof reading, printing, and commenting on any science fiction I may have written, or in giving general encouragement. I particularly wish to thank Steve Spottiswoode, Van Zyl Brink, Steve Donovan, Nic Lightfoot, Tony Jager, Arno Daehnke, Francois Malan and Melanie Van Zyl.

Finally, my thanks to the friends, family and soon to be family, who took the time and energy to read the manuscript in the various stages of its development. These include Patrick Linzer, Barbara English, Kathy Sole and Jeanne Trickett. And thanks to my parents, for putting up with a daughter who, in their words, is a perpetual student.

DEDICATION

To Patrick.

A thousand thank yous for your love and support. The creation of this thesis must be owed to you.

TABLE OF CONTENTS

Chapter 1

INTRODUCTION

The waveforms of seismic body waves provide important information on the details of the source rupture process. Many methods have been developed to study focal mechanisms with varying degrees of success, one of which is moment tensor inversion. Since no systematic differences have been found between mine tremors and natural earthquakes, most of what has been discovered regarding the mechanism of earthquakes can be applied to mine tremors.

Moment tensor inversions have been routinely performed for several years for larger earthquakes recorded at teleseismic distances. However, the application of a moment tensor inversion technique to microseismic events induced by mining is a relatively recent innovation. Only a few works related to the use of moment tensor inversion in source mechanism studies of mining-induced seismic events have been published (e.g. Spottiswoode, 1984; Brawn, 1989), the reason being that the inversion methods are notoriously tedious and prone to errors.

The focus of this thesis is the development and application of a robust moment tensor inversion technique for the purpose of routine application to data recorded in the underground environment.

1.1 PROBLEM DESCRIPTION

The seismic source may be described by a model of equivalent forces that correspond to linear wave equations. These sources can be analysed in a unified and consistent way by using the concept of the seismic moment tensor, which encapsulates the equivalent forces model of a generalised point source. The full set of force couples that comprise the moment tensor may be summed in a variety of different combinations to produce a wide range of seismic source models. This aspect illustrates the great utility of the moment tensor.

1.1.1 Importance of source mechanism studies

Source mechanism studies of mine tremors play an important role in understanding the various modes of failure observed in the underground environment. Mapping these planes of failure using conventional techniques (such as geological fracture mapping) is often problematical due to limited access to the site, poor exposures, not to mention that fracture mapping is time consuming and requires trained personnel. An added difficulty is that planes of failure often do not follow faults of geological origin, but often are related to the geometry of the advancing stope face. For example, the development of face-parallel shear zones ahead of deep-level stope faces. In such

cases, the stresses induced by mining dominate over the geological structure in the critical region close to the stope. Seismic methods therefore have the potential of being the only practical method of studying the development of seismic shear zones underground.

1.1.2 Factors influencing the accuracy of moment tensor calculations

Through a mathematical process known as inversion, it is possible to compute the moment tensor from observed values of the ground displacement. Moment tensor inversion is one of the best approaches to study the mode of failure of a seismic source, provided that two major assumptions hold. Firstly, it is assumed that the point source approximation is valid (i.e. that the fault plane dimensions are shorter than the wavelength of the seismic waves used in the inversion), and secondly, that the effect of the earth's structure on the seismic waves is modelled correctly. If either of these assumptions does not hold, the resultant moment tensor may contain a large non-double-couple component, even if the source mechanism is a double-couple (Streliz, 1978; Barker & Langston, 1982).

A further factor contributing to the presence of 'false' components in the moment tensor is the quality of the available data. The quality of the moment tensor inversion and reliability of the results depends to a large extent on the number and quality of data points and on the azimuthal coverage of stations around the source. The GIGO principle (Garbage In, Garbage Out) is of particular relevance because data having poor signal-to-noise ratios have an adverse effect on the moment tensor solutions. There are a number of types of systematic error (or noise), which influence seismograms recorded underground. These are: raypath focussing and defocussing as a result of inhomogeneities in the rockmass; the degradation of the velocity model due to mining-induced fractures; low signal-to-noise ratios; poor P- and S-wave picks; and various other factors that adversely affect the fidelity of the seismograms.

This last factor forms the main thrust of this study – the development of robust moment tensor inversion methods to accurately estimate the moment tensor in the underground environment.

1.1.3 Classification of moment tensor inversion methods

Numbers of moment tensor inversion techniques have been proposed since the pioneering paper of Gilbert & Dziewonski (1975). The models of the seismic source and the methods applied differ greatly according to the available data and the purpose of the study. In this thesis, a distinction is made between the 'absolute' and 'relative' methods. These broad classes of inversion procedure are based on methods used to estimate the Green's functions: the displacement field due to a unidirectional unit pulse.

In the absolute methods, the wave propagation is evaluated theoretically or determined empirically from observations and a known source. Green's functions are

dependent on the assumed earth model, the location of the point source, and the receiver position. One of the difficulties in the absolute inversion (apart from noise) is the accurate estimation of the Green's functions for geologically complex media. In structurally complex environments, with possible lateral inhomogeneities, it is not always possible to calculate the Green's functions with adequate accuracy. The result is the introduction of systematic errors into the moment tensor elements. In the mining situation, it is possible to take measurements using geophones placed at depth, thereby removing the effect of surface weathering. This advantage is offset, or possibly exceeded, by the effect of mining voids on the seismic raypaths (pers. comm. Spottiswoode, 1998).

In contrast to the absolute methods, the relative inversion methods do not require the calculation of theoretical Green's functions for each event. The basis of relative methods is the concept of a common raypath between a cluster of seismic sources and a particular receiver. Generally, the radiation pattern of a reference event is used to estimate the wave propagation for events from the same source region. A difficulty in this approach is the dependence of the solution on the *a priori* knowledge of the reference event. Errors in the determination of the radiation pattern of the reference event may lead to biased moment tensor solutions for the other events in the source cluster. In the relative method without a reference mechanism, the path effects described by the Green's functions are eliminated analytically – thereby avoiding the explicit use of the Green's functions completely. This method, however, requires the events in the cluster to have different mechanisms.

Because of the reported advantages of the relative technique (without a reference mechanism), this formed the core of a preliminary investigation that aimed at determining whether or not the method was suitable to clusters of events recorded in the deep-level gold mining environment. However, this method was found to only give accurate results when the radiation patterns of the events in a cluster were significantly different. When the mechanisms are too similar the method is extremely sensitive to noise. This is a serious disadvantage in the underground environment where clusters of recorded events often have very similar mechanisms. This problem is accentuated when the method is applied to very small events having similar mechanisms, with signals just above the noise level.

1.1.4 Hybrid moment tensor inversion

To address the problems outlined above, a number of hybrid moment tensor inversion techniques are developed and described in this thesis. These revised techniques attempt to capitalise on the strengths of both the absolute and relative methods in order to achieve a robust measure of the seismic moment tensor. The relative aspect of the method is that a common raypath between each event in the source cluster and a particular receiver is assumed. For each source-receiver combination, each wavefront will experience similar wave propagation effects, however, some of the measurements at the receiver may be more accurate than others (Section 1.1.2).

Conceptually, each of the proposed methods involves computing the moment tensor components for each event in a cluster using absolute techniques (i.e. by evaluating the Green's function) and subsequently applying a weighting or correction, which is ascertained in a relative sense by considering all the events in the cluster. Essentially, the weight is determined using the distribution of computed residuals for a particular geophone site, channel and wave phase when measured data are compared with the theoretical data. The weight is defined in such a way that it downgrades the influences of noisy data on the system of equations. Once the corrections have been applied to the observations, a new set of moment tensor components is computed using the absolute technique, and these results are then subjected to a new relative correction as before. This process is applied iteratively until a predefined criterion, or set of criteria, is satisfied.

The proposed hybrid techniques attempt to compensate for various types of systematic error (or noise), which influence seismograms recorded underground. These methods can also be used to enhance signals recorded near a nodal plane in the radiation pattern, or to decrease the influence of a low quality observation.

An analogous approach has been applied to the seismic location problem, *viz.* the so-called 'JHD method' (joint hypocentral determination). The relative locations obtained through JHD are usually better than those determined by inversion of more complete and complex velocity models, and the resulting hypocentral locations often give a more focussed picture of the seismicity.

1.2 PRINCIPAL OBJECTIVES

The primary objective of this study is to develop a revised moment tensor inversion technique that exploits the strengths of both the absolute and relative methods in order to achieve a robust measure of the seismic moment tensor. These techniques are referred to as the hybrid methods because they share aspects of both absolute and relative methods. The hybrid methods are aimed at reducing the level of systematic error in the inversion, the source of these errors having been outlined above. If the hybrid methods prove to be successful and result in more 'focussed' moment tensor solutions, a useful tool will have been added to the currently applied seismic analysis methods. Improved moment tensor solutions will be highly useful in studies of seismic source mechanisms and will enhance the interpretations of the modes of failure in the underground environment, ultimately leading to improved safety.

An important aspect in the development of any new technique is extensive testing of the algorithm. This forms an intermediate objective of this study. The performance of the hybrid moment tensor inversion methods under various extreme situations is assessed using synthetic data.

The final objective is to determine whether the techniques developed can be successfully applied to real data.

1.3 METHODOLOGY

To achieve the objectives outlined above the author has developed three hybrid moment tensor inversion techniques and prepared a computer program to perform the hybrid inversions. For the purpose of comparison, the program also computes absolute and relative moment tensors in either the time- or frequency-domain. To facilitate interpretation, the program computes a number of source parameters and plots the radiation patterns and corresponding fault-plane solutions to the screen.

To meet the intermediate objective, the six moment tensor inversion methods (three hybrid methods, two relative methods and an absolute method) are applied to a cluster of synthetic events with known moment tensors and source parameters. A number of stability tests are carried out to quantify the source resolving capabilities of the methods for clustered events. This knowledge will enable the interpreter to distinguish artefacts introduced by processing from meaningful output. The first set of experiments explores the resolving power of the methods for various focal coverage situations in a noise-free situation. In the second set of experiments, the sensitivity of the hybrid inversion methods to random noise is explored. The input synthetic data are artificially contaminated with increasing levels of random noise, and the resultant focal mechanisms are compared. In addition, the number of recording stations is reduced from a situation of good focal sphere coverage to one of extremely poor coverage. Lastly, the sensitivity of the hybrid inversion methods to systematic noise is investigated. The input synthetic data are again contaminated with increasing levels of systematic noise, and the resultant focal mechanisms are compared. As before, the number of recording stations is reduced.

Lastly, the hybrid methods are applied to a cluster of 14 events recorded at Oryx Gold Mine. Absolute moment tensors are also computed for comparative purposes. The event cluster considered in the study is located ahead of an advancing development end at a depth of approximately 2500m. The cluster was selected for closer study due to the noticeably tight spatial grouping and markedly similar waveforms. In the absence of detailed fracture mapping, the similarity of the waveforms plays an important role in assessing the integrity of the hybrid moment tensor solutions in the sense of whether or not they are any better than those determined using absolute methods. Since the input waveforms of the cluster show such close similarity, it is reasonable to expect the output moment tensors and their corresponding radiation patterns to exhibit similar likenesses.

1.4 STRUCTURE OF THESIS

In Chapter 1, an overview of the objectives of this study, the general methodology of research and the thesis structure are outlined. Chapter 2 reviews the theoretical concepts involved in the description of seismic sources. Since mine seismicity is of particular interest in this study, a brief summary of the focal mechanisms identified underground is presented. Only the most relevant aspects are covered in this section –

details relevant to the subject, but not of direct importance to the thesis, are described in the appendices.

Chapter 3 provides an overview and summary of the various moment tensor inversion methods described in the literature. As before, concepts utilised in this thesis, but not immediately relevant are presented in the appendices. The moment tensor inversion methods are divided into absolute and relative methods, based on the manner in which the wave propagation between source and receiver (described by the Green's functions) is treated. These methods are mentioned to accentuate the differences between the absolute and relative methods, and subsequently highlight the significance of the hybrid methods.

The focus of Chapter 4 is the relative moment tensor inversion method without a reference mechanism. This technique is described in considerable detail because it forms the basis of the preliminary phase of this study. This chapter also covers the solution procedure and error analysis technique employed, and describes the implementation of the relative inversion by means of a computer program, RMTI, written by the author.

The results of a number of stability tests are described in Chapter 5. These are carried out to determine the limitations of the relative inversion technique described in Chapter 4, possible sources of error, and may be thought of as an optimisation exercise to determine which input situations give rise to stable results. In Sections 5.1 to 5.4, the tests are performed using recorded data, whereas the tests in Section 5.5 are applied to synthetic data. The results described in Section 5.5 have a pivotal role in defining the direction of the research outlined in the following chapters.

Chapter 6 through to Chapter 9 are the most important components of this thesis. In Chapter 6, the hybrid methods are developed and described. Since the hybrid methods are aimed at reducing the level of systematic error in the system of equations, the more common possible sources of noise are also discussed. In addition, the implementation of the inversion methods applied in this thesis, are discussed in Chapter 6. Six different methods are implemented – one absolute method, two relative methods and three hybrid methods. The 'moment tensor inversion toolbox' written by the author in Delphi is described.

The limitations of the algorithms and reliability of the results are addressed in Chapter 7. The hybrid inversion techniques are subsequently applied in Chapter 8 to a cluster of events recorded at Oryx Gold Mine at a depth of approximately 2500m. Chapter 9 provides a synopsis of the study.

Chapter 2

THEORETICAL CONCEPTS

One of the ultimate goals in seismology is the detailed understanding and quantification of the physical processes and geometry of the seismic source. This insight contributes to the improved assessment of seismic hazard, and in the mining environment, ultimately assists the mine planning process. This chapter outlines the various theoretical concepts and relevant equations relied upon in this thesis in an attempt to present the theory in a coherent way rather than refer to isolated equations when the need arises.

In this chapter, the various methods by which source models may be obtained from analyses of seismic waves are summarised. In one approach, source models are based purely on observational data. The wavefronts expand outwards from the seismic source, retaining the initial sense of deformation. The polarity of the wavefront can be related to near-source motions, which define the geometry of the source. Although this approach is not directly applied in the thesis, it has been included for completeness.

A more quantitative approach is taken, in the later parts of this chapter, to represent these complex physical phenomena mathematically. A dynamically equivalent, idealised system of forces is visualised to replace the actual rupture process. The equivalent force representation can then be placed into Newtonian equations of motion, from which a mathematical description of the seismic source (in the form of a moment tensor) is developed. The seismic waves predicted when using these theoretical source models can then compared with those observed in reality. The ultimate objective is to gain insight into the seismic source mechanism and to determine whether the theoretical models do, in fact, model reality.

2.1 SOURCE MODELS BASED ON OBSERVATIONS

The majority of seismic sources result from natural phenomena such as faulting or shearing motions on surfaces within the earth's crust. In addition, there are induced or triggered sources, caused by the activities of man. Induced sources occur over a vast range of energy scales, ranging from the small explosions used for mining and engineering purposes, to the larger sources such as underground nuclear tests. The seismic sources of interest in this study are those induced by deep-level mining (at depths in excess of 2000m). These events are recorded by sensitive mine-wide networks and range in local magnitude from –2 to 5.2 (the magnitude of the largest mining-induced event recorded in South Africa to date that occurred on 7th April 1977 in the Klerksdorp area).

2.1.1 Observed radiation patterns

Observations of P-wave first-motions generated by explosions show a spherically symmetric compression in the P-phase in all directions. An example of an explosional source is a 'solarquake' (Figure 2.1). Solar flares produce seismic waves in the Sun's interior that resemble those created by earthquakes. The solar seismic waves appear to be compression waves like the P-waves generated by an earthquake. The waves travel throughout the Sun's interior. The solarquake is illustrated schematically in Figure 2.2.

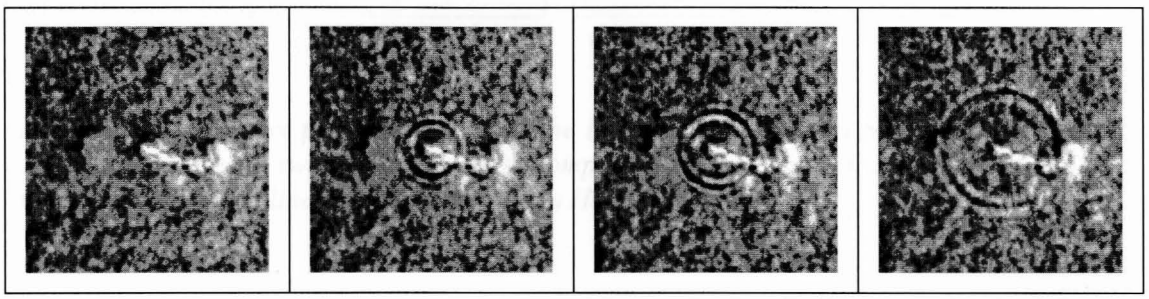

Figure 2.1: Waves on the surface of the sun (from Astronomy Now Online website: http://www.astronomynow.com/breaking/980527sunquake/sunquake.html)

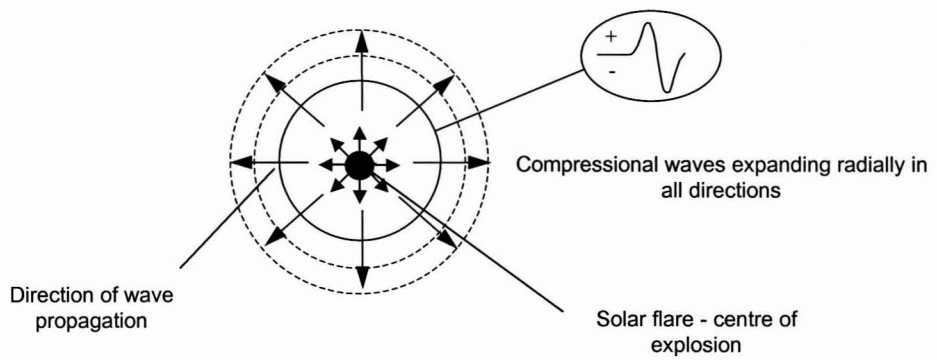

Figure 2.2: Spherically symmetric compressional wavefront generated by solar flare.

Unlike the explosive sources, most seismic sources lack spherical symmetry. For example, faulting involves shear dislocation (slip) on a planar surface. Recordings of the seismic waves (by means of seismometers) generated by slip on a planar surface show a characteristic 'clover-leaf' P-wave polarity pattern (Figures 2.3 and 2.4). The distribution of these polarities is systematic and a pair of mutually perpendicular lines may be drawn separating the compressional and dilatational groups. The solid dots indicate that the first motion of the P-wave is compressional, and the circles indicate dilatational P-wave first motion. These two lines, along which no P-wave motion occurs, are called nodal lines.

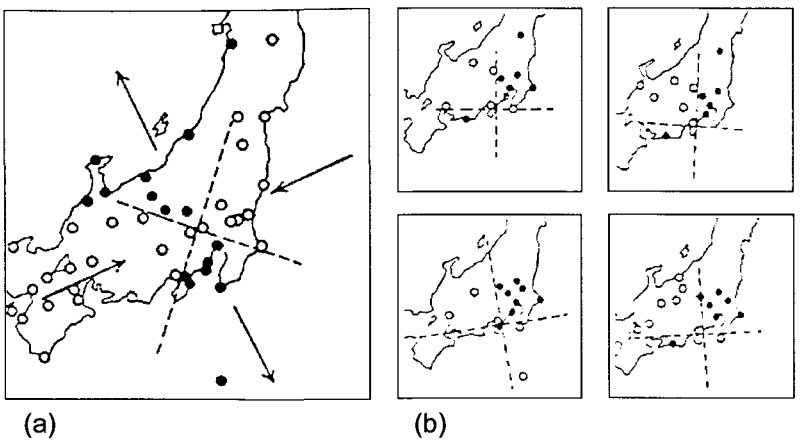

Figure 2.3: (a) P-wave polarity pattern for the 1931 Western Saitama earthquake and (b) the 1930 Ito earthquake swarm. Solid dots = compressional first motion; circles = dilatational first motion. Dashed lines = nodal lines (from Honda, 1954).

The geometry of the wavefront radiated by a shearing source is illustrated schematically in Figure 2.4. Alternating quadrants exist around the source where the initial motions of the P-arrival will be compressional or dilatational (Figures 2.3 and 2.4). The changes in initial P-wave polarity do not change abruptly from point to point in the medium, but form a smoothly varying three-dimensional radiation pattern around the source.

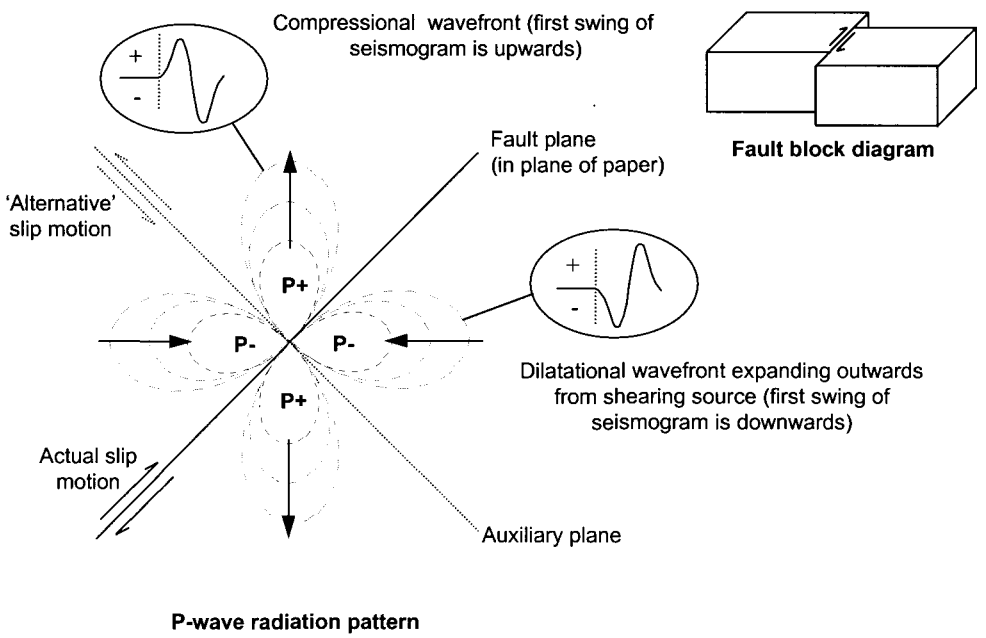

Figure 2.4: Schematic representation of the systematic four-lobed distribution of compressional and dilatational wavefronts generated by a faulting source.

Reversals in polarity occur where the wave amplitudes are zero, and the strongest P-wave motions are expected in the middle of the four quadrants, at 45° angles to the fault plane.

Such simple geometric patterns are characteristic of radiation from faults. However, due to the symmetry of the pattern of alternating compressional and dilatational quadrants, the fault plane cannot be determined uniquely using only P-wave first-motions. An orthogonal plane, known as the auxiliary plane, exists at right angles to the fault plane. This ambiguity is illustrated in Figure 2.4 where right-lateral motion on the fault plane produces a P-wave radiation pattern indistinguishable from that which results from left-lateral slip on the auxiliary plane.

2.1.2 Focal mechanism studies

The aim of focal mechanism studies is to determine the seismic fault model by finding the nodal planes of the observed polarity of P-waves radiated from a hypocentre. This is one of the oldest techniques used in observational seismology. Once the orientation of the nodal planes has been determined (Appendix A) the solution is referred to as the fault-plane solution.

This method assumes that the initial character of an elastic wave remains unchanged during its propagation, so that the evidence on the focal sphere represents the original polarity of wave radiation. In the case of mine-wide seismic networks, which record local events, this assumption is generally valid. However, in the case of teleseismic events (these earthquakes have epicentres over 1000km away) reversals in polarity may occur as the wave travels through complex structures in the Earth's crust. In addition to phase reversals, the seismic wave raypaths become curved, and ray-tracing techniques must be used.

The systematic distribution of the initial P-wave polarity in azimuth, as described by the radiation pattern, can be correlated with fault source parameters (such as fault plane orientation and direction of slip). The orientation of the nodal planes produces characteristic focal mechanism projections for different faulting types. Examples of focal mechanism projections for common fault types (Figure 2.5) are shown in Figure 2.6. The nomenclature used to describe fault plane orientation, slip direction, and to classify the various forms of faulting is described in Appendix B.

The fault-plane solution may be obtained using a variety of methods, of which only the most common approach, based on first-motion polarities of P-waves, has been described (Appendix A). P-wave amplitude data are often used together with the polarity data. S-waves are sometimes used to constrain the range of possible fault-plane solutions for a given set of data from P-waves. S-waves do not, however, remove the ambiguity posed by the auxiliary plane.

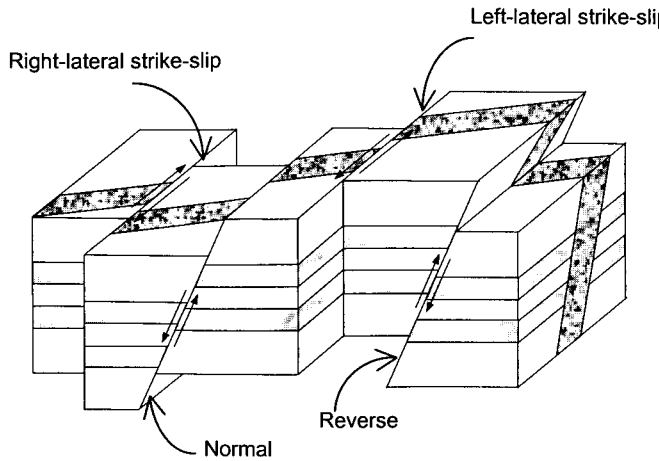

Figure 2.5: Block diagram showing examples of fault types (modified from Bolt, 1988).

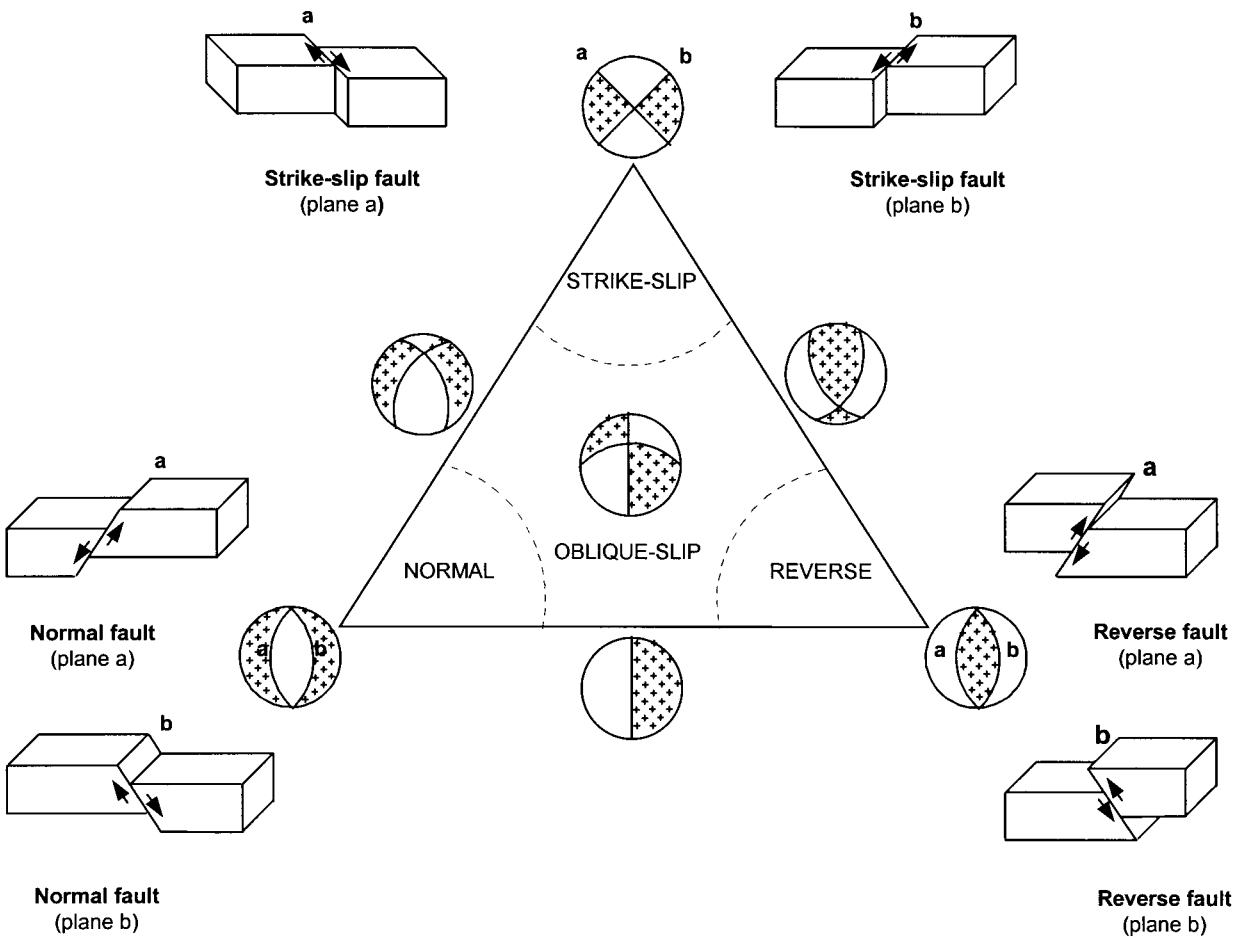

Figure 2.6: Triangle diagram for displaying the focal mechanism projections for common fault types. The three vertices correspond to pure strike-slip (top), reverse (right) and normal fault (left) mechanisms. Planes a and b represent either the fault plane or auxiliary plane. Shaded regions (++) indicate compressional P-wave motions.

Composite fault-plane solutions are obtained from joint processing of P-wave polarity data, or S-wave polarisation data from a number of seismic events occurring in a given area, within a limited time interval and having the same focal mechanism. This method is mentioned only because it shares some common features with the relative moment tensor inversion method applied later in this study. For example, both methods are applicable to clusters of events that are well constrained in time and space. However, the relative inversion method differs from the composite fault plane solution in that the focal mechanism is not constrained in the former, and different focal mechanisms may be obtained for events in the cluster.

Fault orientations may also be obtained analytically by using techniques such as fault parameter and moment tensor inversion. Inversion of the seismic moment tensor is the most general approach for determining a source mechanism. Since the technique of moment tensor inversion forms the focus of this study, it will be dealt with in some detail in Chapter 3. The seismic moment tensor describes a variety of source models, of which the double-couple source model (equivalent force system describing a fault dislocation) is an example.

2.2 EQUIVALENT FORCE MODEL

A seismic source may be described by a model of equivalent forces, corresponding to linear wave equations where non-linear effects in the near-source region are neglected (Aki & Richards, 1980). Equivalent forces are defined as those forces producing displacements at a given point that are identical to the displacements produced by the actual forces of the physical process and acting at the source. The concept of equivalent forces is a useful one, because these forces can be correlated with physical source models.

A number of theoretical models (Figure 2.7) consisting of various types of forces acting at a point source have been studied in attempts to explain the P-wave polarity observations. These models are mentioned because they form the framework around which a quantitative discussion of seismic sources is built later in this chapter.

The single force illustrated in Figure 2.7(a) is one of the simplest mathematical views of a source, but is not physically plausible because it implies the application of an external force. This is unlikely in a natural earthquake. The pair of forces of equal magnitude in (b) is, in principle, a more likely model because the opposite forces act simultaneously on two adjacent portions of the medium, so the resultant force is zero. The forces in the system illustrated by (c) balance one another, as in the previous case. The system, however, has a torque about the z-axis. This type of force system is referred to as a single-couple. The more complicated system of forces shown in (e) is an example of a double-couple. A double-couple consists of two single-couple systems having no resultant torques.

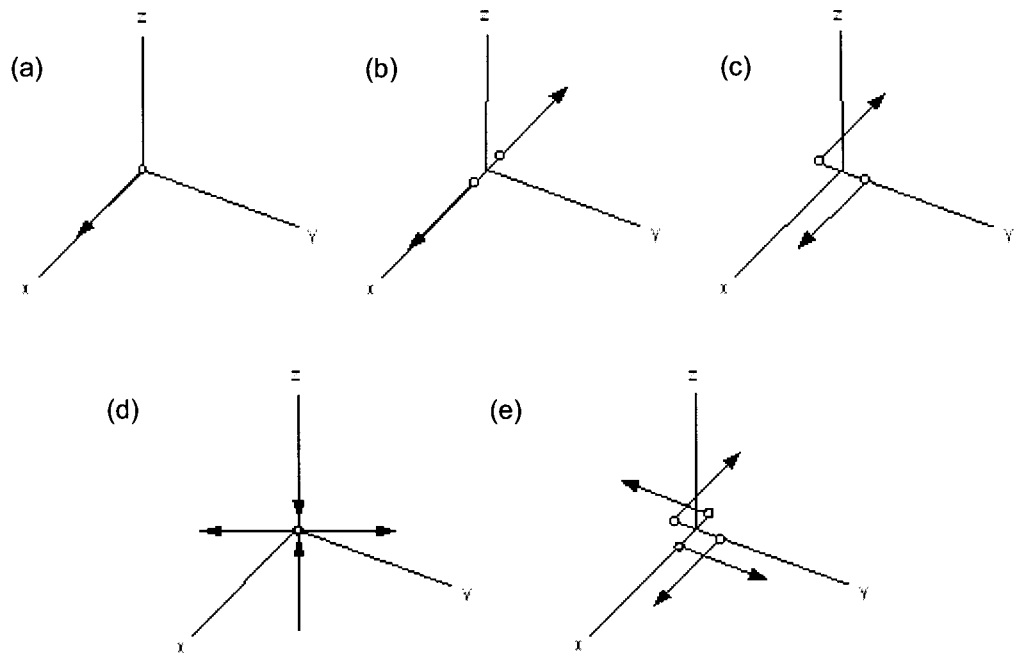

Figure 2.7: Various force types at a point source: (a) a single force; (b) a pair of equal and opposite forces in tension; (c) a pair of equal and opposite forces as a torque about the z-axis; (d) two pairs of forces, where tension and compression are of equal magnitude and are perpendicular to one another; (e) two pairs of forces with torques about the z-axis of equal magnitude and opposite in direction (redrawn from Kasahara, 1981).

Although the single-couple and double-couple models shown in (d) and (e) are equivalent with respect to their mechanical effect, the latter is the currently accepted model. The acceptance of this model is based on observational and theoretical evidence and a thorough understanding of the radiation pattern of P- and S-waves generated by the two types of sources (the double-couple source will be described in detail in this section). In addition, the force system shown in (e) is directly compatible with the tensor formulation for stress and strain used in rock mechanics (e.g. Jager & Cook, 1976; Aki & Richards, 1980).

2.2.1 Single force point source

Consider an explosive source. An explosion can be idealised as a sudden application of a pressure pulse within a small cavity of spherical symmetry. At the instant of the explosion, a P-wave is initiated in the surrounding medium, and a compressional wavefront spreads outwards from the source (Figure 2.8a). Immediately after the explosion, at some distance away from the source (the elastic radius), a spherical surface exists on which the elastic displacements and strains due to the effective pressure force can be predicted. The explosive point source may be represented by an equivalent force system (Figure 2.8b) consisting of three mutually perpendicular dipoles, which produces waves identical to those generated by the explosion.

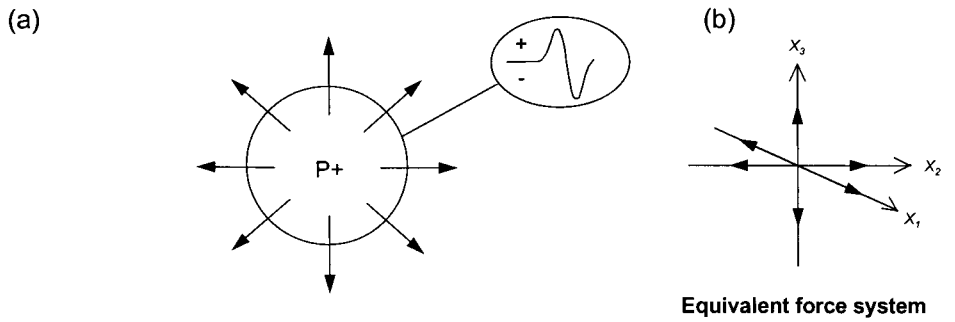

Figure 2.8: Equivalent forces for an explosion.

2.2.2 Double-couple source

The complex faulting geometry of a shear dislocation source in reality can be represented by a simple dislocation model (provided the wavelengths of the seismic waves are large relative to the dimensions of the fault and have wave periods longer than, or comparable to, the duration of rupture). In the simple dislocation model (Figure 2.9), the average properties of the rupture (e.g. total fracture area, average displacement over the fault D, average fracture velocity, and duration of rupture propagation) are considered.

The simplest form of the dislocation model is the point source model, in which a simple dislocation history approximates the process of seismic wave radiation during rupture. The point source approximation is only valid if the following conditions hold:

$$D >> \ell \qquad 2.1$$

and

$$\lambda >> \ell \qquad 2.2$$

where D is the distance of the observer from the source, and λ is the wavelength of the seismic waves under consideration and ℓ is the linear source dimension. In this case, the wavefield does not carry any information about the details of the source processes, but of the overall (integral) source process. As the ratio of seismic wavelength to fault length decreases, more complex models are necessary. For $\lambda << \ell$, the internal details of the rupture process can be determined. Such details would correspond to smaller and smaller elements of the rupture process (e.g. asperities and barriers).

The simplified average dislocation model (Figure 2.9) can then be replaced by a dynamically equivalent force system that would reproduce the seismic wave radiation. At first glance it appears that a time-varying force couple applied within the elastic medium would simulate the dislocation. However, the single-couple model of faulting introduces an unbalanced net moment into the medium where the dislocation

occurred. In order to balance the moment of the force system, a second force couple is needed so that no net moment is added to the medium. This currently preferred model of equivalent body forces for a dislocation source is known as the double-couple model.

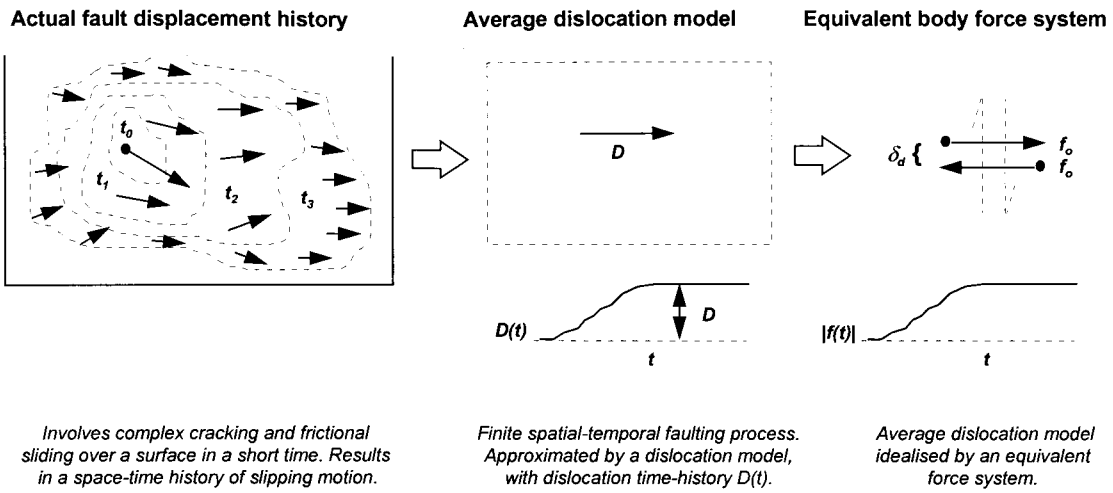

Figure 2.9: Equivalent body forces for a dislocation model (redrawn from Lay & Wallace, 1995).

The double-couple system can be transformed into an equivalent force system (Burridge & Knopoff, 1964) consisting of a pair of tensional and compressional dipoles at right angles with respect to one another and at 45° to the x and z axes (Figure 2.10). The axis parallel to the pair of tensile forces is referred to as the principal tension axis or T-axis, and that parallel to the compressive forces defines the principal compressional or P-axis.

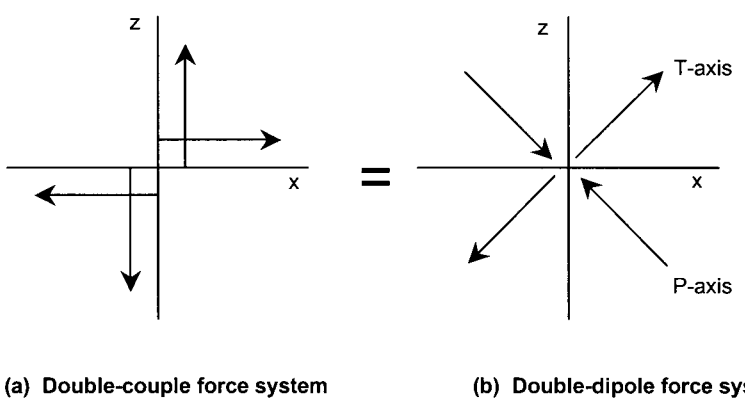

Figure 2.10 (a) A double-couple force system in the xz plane for a shear dislocation in the xy plane may be represented by (b) an equivalent set of point forces composed of two dipoles without shear (principal axes).

In the mining environment, since compression occurs in all directions at depth, the T-axis is not one of tension, but of minimum compression. A third axis known as the b-axis or null axis is defined orthogonal to the P- and T-axes since the radiation pattern of the P-waves is zero along this axis. These three axes are routinely determined in focal mechanism studies as an equivalent representation of double-couple sources.

The equivalence of the double-couple and the pair of tensional and compressional dipoles is important since it allows the following three vectors to be introduced:

$$\mathbf{t} = \tfrac{1}{\sqrt{2}}(1,\ 0,\ 1) \qquad 2.3$$

$$\mathbf{p} = \tfrac{1}{\sqrt{2}}(1,\ 0,\ -1) \qquad 2.4$$

$$\mathbf{b} = (0,\ 1,\ 0) \qquad 2.5$$

where vectors **t** and **p** are directed along the axes containing the dipoles, and **b** is oriented perpendicular to both **t** and **p** (Gibowicz & Kijko, 1994).

Two types of ambiguity are inherent in the interpretation of fault plane solutions. The first of these has been mentioned before, and relates to the fact that the fault plane cannot be distinguished from the auxiliary plane using only the fault plane solution. The local geology must be taken into account. The other uncertainty arises when the P- and T-axes are collinear with the greatest and least principal compressive stress directions. This would only be correct if the stress-drop tensor is equal to the stress tensor, which is hardly ever the case because the stress-drop tensor contains only shear stresses (Scholz, 1990). The P- and T-axes are at 45° to the fault plane, which is not the correct direction for Coulomb failure.

2.3 THE SEISMIC MOMENT TENSOR

2.3.1 General relations

There are a number of parameters which describe the size and strength of seismic sources (e.g. seismic intensity, magnitude, energy). One of these parameters is of particular relevance to this study - the scalar static seismic moment, given by:

$$M_o = \mu A \overline{D} \qquad 2.6$$

where μ is the rigidity (described by the Young or shear modulus of the medium), A is the surface area of the rupture, and $\overline{D}$ is the average final static displacement after the rupture. M_o is a measure of the irreversible inelastic deformation in the area of the rupture.

A parameter that gives more information about the deformation occurring in the vicinity of the seismic source is the seismic moment tensor. Determination of the moment tensor performed fairly routinely in the analysis of strong earthquakes. For example, the centroid moment tensor solutions published by the Harvard University

group (e.g. Dziewonski & Woodhouse, 1983) and by the U.S. Geological Survey. The seismic moment tensor is a useful concept because it provides a complete description of equivalent forces (Section 2.2) of a general seismic point source. A source can be considered a point source if conditions mentioned in Section 2.2.2 hold.

The theory of point sources plays a fundamental role in seismic studies due to the well-known double-couple representation of the seismic source. However, a detailed description of this theory is beyond the scope of this work. There are a number of excellent references that cover this material, in particular: Aki & Richards (1980), Jost & Herrmann (1989), Pujol & Herrmann (1990), Gibowicz & Kijko (1994) and Lay & Wallace (1995).

The moment tensor elements corresponding to a double-couple of equivalent forces in an isotropic medium are given by:

$$M_{ij} = \mu A \left(s_i n_j + s_j n_i\right) \qquad 2.7$$

where μ and A are as defined in Equation 2.6, and $s = (s_1, s_2, s_3)$ is the slip vector on the fault surface and $n = (n_1, n_2, n_3)$ is the vector normal to the fault-plane (Aki & Richards, 1980). The Einstein summation convention over repeated suffixes is used i.e., the repeated indices i where $i = 1, 2, 3$ imply summation over s_1, s_2, s_3 and equivalently for index j. The tensor describing the double-couple is given by the term in brackets. It is evident from the formulation that the slip vector and vector normal are interchangeable i.e. the slip vector could be the fault normal and vice versa. This ambiguity has been mentioned previously in Section 2.2.2.

2.3.2 Moment tensor sources

Although the single force (Figure 2.7a) is one of the simplest models of a seismic source, it is not physically plausible, since the external application of a force is unlikely to occur in natural earthquakes. A self-balancing force type is more probable, for example, a pair of opposite forces acting simultaneously on adjacent parts of the medium such that the resultant force is zero. Consider a pair of forces equal in magnitude, separated by a small distance ε in the x_2 direction, acting along the positive and negative x_3 directions, i.e. two forces $(0, 0, F_3)$ and $(0, 0, -F_3)$ acting at points $\left(\xi + \frac{1}{2}\varepsilon e_2\right)$ and $\left(\xi - \frac{1}{2}\varepsilon e_2\right)$, respectively, where e_2 is a unit vector in the x_2 direction. The total displacement u_i caused by the two forces is equal to the sum of the displacements caused by each force, so that:

$$u_i = \varepsilon F_3 * \left[G_{i3}\left(\xi + \tfrac{1}{2}\varepsilon e_2\right) - G_{i3}\left(\xi - \tfrac{1}{2}\varepsilon e_2\right)\right] / \varepsilon \qquad 2.8$$

(Pujol & Herrmann, 1990). Taking the limit of u_i as $F_3 \to \infty$, and $\varepsilon \to 0$, in such a way that the product εF_3 remains finite, yields:

$$u_i = M_{32} * \frac{\partial G_{i3}}{\partial \xi_2} \quad \text{where} \quad M_{32} = \varepsilon F_3 \qquad 2.9$$

(Pujol & Herrmann, 1990). This pair of forces is known in classical mechanics as a couple, and the quantity M_{32} as the moment of the couple, which has the dimension of *force* × *length*, and may be a function of time.

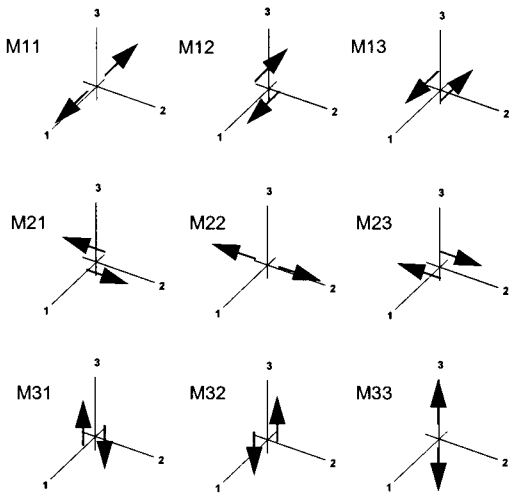

Figure 2.11: Representation of the nine possible couples M_{ij}. The directions of the force and arm of the couple are denoted by the indices i and j respectively (from Aki & Richards, 1980).

There are nine possible combinations of force and arm directions, represented by the moment M_{ij} of couple with forces in the x_i direction, and arm in the x_j direction (Figure 2.11). When x_i and x_j are the same, the couple is known as a vector dipole, or a couple without moment. All the other couples have a non-zero moment equivalent to the torque[1] they exert about the axis perpendicular to their plane of action.

The collection of nine terms M_{ij} is known as the seismic moment tensor of the source (Ben-Menahem & Singh, 1981). The moment tensor is a broad concept, which completely describes, as a first-order approximation, the equivalent forces of general point sources in the solid earth (Aki & Richards, 1980; Jost & Herrmann, 1989). This quantity depends on source strength and the orientation of the plane of failure. The great utility of the moment tensor lies in the fact that it characterises all the information regarding the seismic source that can be deduced from observations of waves having wavelengths much greater than the linear dimensions of the fault plane. The full set of couples can clearly be summed in different combinations to produce a wide range of seismic source models.

[1] In this context, the word 'moment' is equivalent to 'torque', and does not refer to the quantity εF_i.

2.3.3 P-, SV- and SH-wave radiation patterns

The far-field displacement u_k at position $x=(x_1,x_2,x_3)$ in a homogeneous, unbounded, isotropic medium generated by a point source at $\xi=(\xi_1,\xi_2,\xi_3)$ described by the moment tensor M_{ij} is given by Pujol & Herrmann (1990) as follows:

$$u_k(x,t)=\frac{1}{4\pi\rho\alpha^3}\gamma_k\gamma_i\gamma_j\frac{1}{r}\cdot\dot{M}_{ij}(t-r/\alpha)-\frac{1}{4\pi\rho\beta^3}(\gamma_k\gamma_i-\delta_{ki})\gamma_j\frac{1}{r}\cdot\dot{M}_{ij}(t-r/\beta) \qquad 2.10$$

where the dot over M_{ij} indicates the derivative with respect to the argument. Aki & Richards (1980) give the full expression for u_k (i.e. the near, intermediate and far-field displacements). In this equation, ρ indicates density, α and β are the P- and S-wave velocities respectively, r is the source-receiver distance such that $r = | x - \xi |$, and $\gamma_i=(x_i-\xi_i)/r$ are the direction cosines of the vector $(x-\xi)$ and form the components of a unit vector $\Gamma=(\gamma_1,\gamma_2,\gamma_3)$ directed along the source-receiver direction. δ_{ij} is the Kronecker delta ($\delta_{ij} = 1$ for $i = j$, and $\delta_{ij} = 0$ for $i \neq j$).

Equation 2.10 relates the far-field displacement to the time derivative of the moment tensor and is of particular importance because it forms the basis of the hybrid inversion schemes described later in this thesis. In practice, it is generally assumed that all the components of the moment tensor have the same time dependence, and that its time derivative can be ignored in radiation pattern calculations (Gibowicz & Kijko, 1994). This assumption is made in the moment tensor inversion schemes applied in this work.

The far-field displacement in Equation 2.10 is composed of two terms. The first is the component in the direction of Γ, corresponding to the P-wave motion, and the second in the direction perpendicular to Γ, corresponding to the S-wave motion. Therefore, the total displacement vector **u** can be written as the summation of its P- and S-wave contributions:

$$\mathbf{u} = \mathbf{u}^P + \mathbf{u}^S \qquad 2.11$$

The vector $\mathbf{u}^S$ can be decomposed into two components, one in a vertical plane that contains the source and the receiver, and the other in a horizontal plane, named $\mathbf{u}^{SV}$ and $\mathbf{u}^{SH}$ respectively (Figure 2.12). This decomposition is achieved by introducing unit vectors **R**, Φ and Θ in spherical coordinates (Figure 2.13), so that the following relations hold:

$$\mathbf{R} = (\sin\theta\cos\phi, \sin\theta\sin\phi, \cos\theta) \qquad 2.12$$

$$\Theta = (\cos\theta\cos\phi, \cos\theta\sin\phi, -\sin\theta) \qquad 2.13$$

$$\Phi = (-\sin\phi, \cos\phi, 0) \qquad 2.14$$

(Pujol & Herrmann, 1990). Vector **R** is in the radial direction and **R** = Γ. Vector Θ is the tangent to the meridian line, while Φ is tangential to the parallel line and has no component in the x_3 direction. Each vector is normal to the other two, the magnitude of each is equal to 1, and the three vectors are the basis of a right-handed orthonormal system.

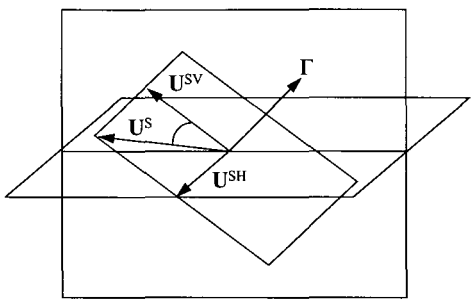

Figure 2.12: Decomposition of $\mathbf{u}^S$ *into* $\mathbf{u}^{SV}$ *and* $\mathbf{u}^{SH}$*. The vectors lie in a plane perpendicular to* Γ *(from Pujol & Herrmann, 1990).*

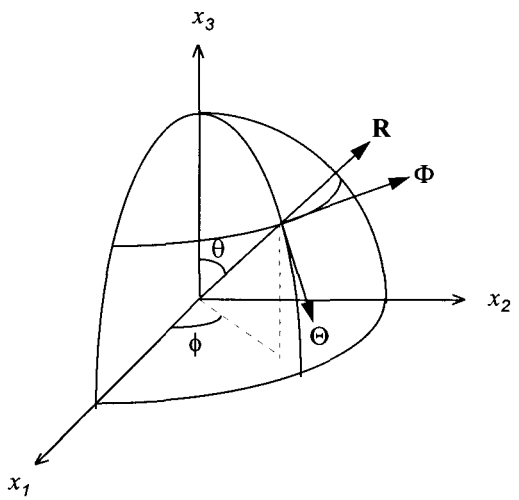

Figure 2.13: Spherical coordinates and unit vectors (from Pujol & Herrmann, 1990).

Using Equation 2.10, Pujol & Herrmann (1990) derive expressions for the displacement vectors $\mathbf{u}^P$, $\mathbf{u}^{SV}$ and $\mathbf{u}^{SH}$ in the far-field. These are:

$$\mathbf{u}^P = \frac{1}{4\pi\rho\alpha^3}\cdot\frac{1}{r}R^P\,\mathbf{R} \qquad 2.15$$

$$\mathbf{u}^{SV} = \frac{1}{4\pi\rho\beta^3}\cdot\frac{1}{r}R^{SV}\,\Theta \qquad 2.16$$

$$\mathbf{u}^{SH} = \frac{1}{4\pi\rho\beta^3}\cdot\frac{1}{r}R^{SH}\,\Phi \qquad 2.17$$

where R^P, R^{SH} and R^{SV} are the radiation patterns, which can be written in detail as:

$$R^P = \gamma_i \dot{M}_{ij} \gamma_j = \gamma_1 \upsilon_1 + \gamma_2 \upsilon_2 + \gamma_3 \upsilon_3 \qquad 2.18$$

$$R^{SV} = \theta_i \dot{M}_{ij} \gamma_j = \theta_1 \upsilon_1 + \theta_2 \upsilon_2 + \theta_3 \upsilon_3 \qquad 2.19$$

$$R^{SH} = \phi_i \dot{M}_{ij} \gamma_j = \phi_1 \upsilon_1 + \phi_2 \upsilon_2 + \phi_3 \upsilon_3 \qquad 2.20$$

where θ_i and ϕ_i are the components of Θ and Φ respectively, and:

$$\upsilon_i = \dot{M}_{i1}\gamma_1 + \dot{M}_{i2}\gamma_2 + \dot{M}_{i3}\gamma_3 \qquad 2.21$$

2.3.4 Properties of the seismic moment tensor

The second order seismic moment tensor **M** has nine components M_{ij} and can be written in the general form:

$$\mathbf{M} = M_{ij} e_i e_j \qquad 2.22$$

where e_i and e_j are the unit vectors along the x_i and x_j directions respectively. The moment tensor **M** contains information on both the magnitude and radiation pattern of the source.

The scalar moment M_o is a measure of the total energy release from the source and is calculated from the moment tensor elements by Equation 2.23:

$$M_o = \sqrt{\tfrac{1}{2} \sum_{i,j=1}^{3} M_{ij}^2} \qquad 2.23$$

The Euclidean normalised moment tensor $\mathbf{M}_E$ is described by:

$$\mathbf{M}_E = \frac{\mathbf{M}}{|M|} \qquad 2.24$$

where the Euclidean length, $|M|$, is given by:

$$|M| = \sqrt{\sum_{i,j=1}^{3} M_{ij}^2} \qquad 2.25$$

This allows the scalar seismic moment M_o to be separated from the moment tensor **M** and Equation 2.25 can be rewritten as:

$$\mathbf{M} = \sqrt{2} M_o \, \mathbf{M}_E \qquad 2.26$$

According to the Decomposition theorem of Ben-Menahem & Singh (1981), the moment tensor of Equation 2.22 can be expressed as follows:

$$
\begin{aligned}
M_{ij}e_ie_j = &\tfrac{1}{3}(M_{11}+M_{22}+M_{33})(e_1e_1+e_2e_2+e_3e_3)\\
&+\tfrac{1}{3}(2M_{11}-M_{22}-M_{33})e_1e_1+\tfrac{1}{3}(2M_{22}-M_{33}-M_{11})e_2e_2+\tfrac{1}{3}(2M_{33}-M_{11}-M_{22})e_3e_3\\
&+\tfrac{1}{2}(M_{32}+M_{23})(e_3e_2+e_2e_3)+\tfrac{1}{2}(M_{32}-M_{23})(e_3e_2-e_2e_3)\\
&+\tfrac{1}{2}(M_{13}+M_{31})(e_1e_3+e_3e_1)+\tfrac{1}{2}(M_{13}-M_{31})(e_1e_3-e_3e_1)\\
&+\tfrac{1}{2}(M_{21}+M_{12})(e_2e_1+e_1e_2)+\tfrac{1}{2}(M_{21}-M_{12})(e_2e_1-e_1e_2)
\end{aligned}
\qquad 2.27
$$

The first term on the right hand side of the equation describes a centre of compression, and is known as the isotropic part of the moment tensor. This corresponds to a volume change at the source. The remaining nine terms form the deviatoric part (constant volume) of the moment tensor. The successive terms describe three dipoles along the coordinate axes, three double-couples, and three torques about the coordinate axes, respectively.

The conservation of angular momentum for equivalent forces leads to the symmetry of the moment tensor (Gilbert, 1970). If the moment tensor is symmetric then $M_{ij} = M_{ji}$, and it can, therefore, be rotated into a principal-axis system so that the torques in Equation 2.27 vanish. The rotated moment tensor **M** may be expressed in matrix notation as:

$$
\mathbf{M} = \begin{bmatrix} M_{11} & M_{12} & M_{13} \\ M_{21} & M_{22} & M_{23} \\ M_{31} & M_{32} & M_{33} \end{bmatrix} \qquad 2.28
$$

When the moment tensor is expressed as a linear combination of differently oriented source dipoles without moment, as in Equation 2.28, the moment tensor components are dependent on the orientation of the coordinate system used during their determination, i.e. the geographical coordinates. The symmetric 3×3 tensor has six independent components, providing six degrees of freedom. In this form, a physical interpretation based on six parameters, whose orientations depend on a pre-defined coordinate system unrelated to the coordinate system of any particular source mechanism, is difficult.

Since the general seismic moment tensor is symmetric, it can be diagonalised. The diagonalised values are the eigenvalues m_i of the moment tensor **M**, with associated eigenvectors $\mathbf{a}_1$, $\mathbf{a}_2$ and $\mathbf{a}_3$. This is known as a principal axis transformation, and in reverse can be written in matrix notation as:

$$
\mathbf{M} = \mathbf{A}\,\mathbf{m}\,\mathbf{A}^{\mathrm{T}} = m_1\,\mathbf{a}_1\,\mathbf{a}_1 + m_2\,\mathbf{a}_2\,\mathbf{a}_2 + m_3\,\mathbf{a}_3\,\mathbf{a}_3 \qquad 2.29
$$

where **A** is a 3×3 matrix and whose three columns are the orthonormal eigenvectors of **M**, and **m** is the diagonalised matrix of **M** with elements m_i.

In this way, the moment tensor is described uniquely in terms of its corresponding eigenvectors and eigenvalues. The three eigenvectors represent the principal axes of

the source along which the principal forces act. The sizes of the eigenvalues denote the magnitude of these forces, and the sign indicates their direction (conventionally, a negative force would point towards the source).

In the case of the Euclidean normalised moment tensor the eigenvectors are also unitary (they have a length equal to 1) and are referred to as orthonormal. The following relation holds for the eigenvalues:

$$\sum_{i=1}^{3} m_i^2 = 1 \qquad 2.30$$

Using the decomposition theorem, the symmetric diagonalised moment tensor can be represented as the sum of an isotropic part (equivalent to the product of a scalar and the identity matrix), and a deviatoric part:

$$\mathbf{M} = \begin{bmatrix} m_1 & 0 & 0 \\ 0 & m_2 & 0 \\ 0 & 0 & m_3 \end{bmatrix} = \frac{1}{3}\begin{bmatrix} tr(M) & 0 & 0 \\ 0 & tr(M) & 0 \\ 0 & 0 & tr(M) \end{bmatrix} + \begin{bmatrix} m_1 - \frac{1}{3}tr(M) & 0 & 0 \\ 0 & m_2 - \frac{1}{3}tr(M) & 0 \\ 0 & 0 & m_3 - \frac{1}{3}tr(M) \end{bmatrix} \qquad 2.31$$

where $tr(M)$ represents the trace of the moment tensor, and is equal to the sum of the eigenvalues, i.e. $tr(M) = m_1 + m_2 + m_3$. The first term on the right hand side of Equation 2.31 describes the isotropic part of the moment tensor, which corresponds to volume changes in the medium. The second term consists of the purely deviatoric eigenvalues given by $m_i - \frac{1}{3}tr(M)$, and describes the deviatoric part of the moment tensor.

The eigenvalues of the moment tensor give insight into a number of source effects (Jost & Herrmann, 1989), summarised briefly as follows:

- The sum of the eigenvalues, $m_1 + m_2 + m_3$, describes a volume change at the source (isotropic component of the moment tensor).
- If $(m_1 + m_2 + m_3) > 0$, the isotropic component is due to an explosion.
- If $(m_1 + m_2 + m_3) < 0$, the isotropic component is due to an implosion.
- If $(m_1 + m_2 + m_3) = 0$, the isotropic component vanishes, and the moment tensor has only deviatoric components.
- If $(m_1 + m_2 + m_3) = 0$ and either m_1, m_2 or $m_3 = 0$, the deviatoric component represents a pure double-couple source.

- If $(m_1 + m_2 + m_3) = 0$ and $(m_1, m_2, m_3) \neq 0$, the deviatoric component can be decomposed into a major and a minor double-couple, or a double-couple and a compensated linear vector dipole (CLVD).

The diagonalised deviatoric moment tensor can be decomposed into a variety of eigenvalue combinations representing simple arrangements of equivalent forces. A multitude of decompositions is possible, but due their non-unique nature, only those most commonly used are outlined. These decompositions are used to characterise how well an equivalent body-force system of the moment tensor describes a particular seismic source.

Combination 1: Three vector dipoles

The deviatoric moment tensor, $\mathbf{M}_{DEV}$, can be decomposed into three vector dipoles where each of the dipoles acts in the directions of the eigenvectors of **M** (Ben-Menahem & Singh, 1981; Jost & Herrmann, 1989). From Equation 2.27, the deviatoric part can be written as:

$$\mathbf{M}_{DEV} = \tfrac{1}{3}(2m_1 - m_2 - m_3)\,\mathbf{a}_1\mathbf{a}_1 + \tfrac{1}{3}(2m_2 - m_3 - m_1)\,\mathbf{a}_2\mathbf{a}_2 + \tfrac{1}{3}(2m_3 - m_1 - m_2)\,\mathbf{a}_3\mathbf{a}_3 \qquad 2.32$$

Using matrix notation, and writing each vector in terms of $tr(M)$ yields:

$$\begin{aligned} \mathrm{M}_{DEV} &= \begin{bmatrix} m_1 - \frac{1}{3}tr(M) & 0 & 0 \\ 0 & m_2 - \frac{1}{3}tr(M) & 0 \\ 0 & 0 & m_3 - \frac{1}{3}tr(M) \end{bmatrix} \\ &= \begin{bmatrix} m_1 - \frac{1}{3}tr(M) & 0 & 0 \\ 0 & 0 & 0 \\ 0 & 0 & 0 \end{bmatrix} + \begin{bmatrix} 0 & 0 & 0 \\ 0 & m_2 - \frac{1}{3}tr(M) & 0 \\ 0 & 0 & 0 \end{bmatrix} + \begin{bmatrix} 0 & 0 & 0 \\ 0 & 0 & 0 \\ 0 & 0 & m_3 - \frac{1}{3}tr(M) \end{bmatrix} \\ &= 3\,\mathbf{M}_{DIPOLE} \end{aligned} \qquad 2.33$$

Combination 2: Three double-couples

The deviatoric part of the moment tensor can be decomposed into three double-couples where each deviatoric term is a double-couple (Ben-Menahem & Singh, 1981; Jost & Herrmann, 1989). Using Equation 2.27:

$$\begin{aligned} \mathbf{M}_{DEV} = {} & \tfrac{1}{3}(m_1 - m_2)(\mathbf{a}_1\mathbf{a}_1 - \mathbf{a}_2\mathbf{a}_2) + \tfrac{1}{3}(m_2 - m_3)(\mathbf{a}_2\mathbf{a}_2 - \mathbf{a}_3\mathbf{a}_3) \\ & + \tfrac{1}{3}(m_3 - m_1)(\mathbf{a}_3\mathbf{a}_3 - \mathbf{a}_1\mathbf{a}_1) \end{aligned} \qquad 2.34$$

Using matrix notation, Equation 2.34 can be written as follows:

$$\mathbf{M}_{DEV} = \frac{1}{3}\begin{bmatrix}(m_1-m_2) & 0 & 0\\ 0 & -(m_1-m_2) & 0\\ 0 & 0 & 0\end{bmatrix}+\frac{1}{3}\begin{bmatrix}0 & 0 & 0\\ 0 & (m_2-m_3) & 0\\ 0 & 0 & -(m_2-m_3)\end{bmatrix}$$
$$+\frac{1}{3}\begin{bmatrix}(m_1-m_3) & 0 & 0\\ 0 & 0 & 0\\ 0 & 0 & -(m_1-m_3)\end{bmatrix} \qquad 2.35$$

$$= 3\,\mathbf{M}_{DOUBLE\text{-}COUPLE}$$

Combination 3: Three CLVDs

Ben-Menahem & Singh (1981) and Jost & Herrmann (1989) show that another decomposition is possible:

$$\mathbf{M}_{DEV} = \tfrac{1}{3}m_1(2\mathbf{a}_1\mathbf{a}_1 - \mathbf{a}_2\mathbf{a}_2 - \mathbf{a}_3\mathbf{a}_3) + \tfrac{1}{3}m_2(2\mathbf{a}_2\mathbf{a}_2 - \mathbf{a}_3\mathbf{a}_3 - \mathbf{a}_1\mathbf{a}_1) + \tfrac{1}{3}m_3(2\mathbf{a}_3\mathbf{a}_3 - \mathbf{a}_1\mathbf{a}_1 - \mathbf{a}_2\mathbf{a}_2) \qquad 2.36$$

where $(2\mathbf{a}_1\mathbf{a}_1 - \mathbf{a}_2\mathbf{a}_2 - \mathbf{a}_3\mathbf{a}_3)$ represents a compressional dipole of strength 2 in the direction of eigenvector $\mathbf{a}_1$, and two dilatational dipoles, each of unit strength, along the $\mathbf{a}_2$ and $\mathbf{a}_3$ axes. This type of source is known as a compensated linear vector dipole (CLVD).

Expressing Equation 2.36 in matrix notation:

$$\mathrm{M}_{DEV} = \frac{1}{3}\begin{bmatrix}2m_1 & 0 & 0\\ 0 & -m_1 & 0\\ 0 & 0 & -m_1\end{bmatrix}+\frac{1}{3}\begin{bmatrix}-m_2 & 0 & 0\\ 0 & 2m_2 & 0\\ 0 & 0 & -m_2\end{bmatrix}+\frac{1}{3}\begin{bmatrix}-m_3 & 0 & 0\\ 0 & -m_3 & 0\\ 0 & 0 & 2m_3\end{bmatrix}$$

$$= \frac{1}{3}m_1\begin{bmatrix}2 & 0 & 0\\ 0 & -1 & 0\\ 0 & 0 & -1\end{bmatrix}+\frac{1}{3}m_2\begin{bmatrix}-1 & 0 & 0\\ 0 & 2 & 0\\ 0 & 0 & -1\end{bmatrix}+\frac{1}{3}m_3\begin{bmatrix}-1 & 0 & 0\\ 0 & -1 & 0\\ 0 & 0 & 2\end{bmatrix} \qquad 2.37$$

$$= 3\,\mathbf{M}_{CLVD}$$

Combination 4: A double-couple and a CLVD

Following Knopoff & Randall (1970) and Fitch *et al.* (1980), the deviatoric moment tensor can be decomposed into a double-couple and a CLVD. Assuming that $|m_3^*| \geq |m_2^*| \geq |m_1^*|$, and that the same principal stresses produce the double-couple radiation and the CLVD, the following decomposition is obtained:

$$\mathbf{M}_{DEV} = m_3^* F\,(2\mathbf{a}_3\mathbf{a}_3 - \mathbf{a}_2\mathbf{a}_2 - \mathbf{a}_1\mathbf{a}_1) + m_3^*(1-2F)(\mathbf{a}_3\mathbf{a}_3 - \mathbf{a}_2\mathbf{a}_2) \qquad 2.38$$

(Jost & Herrmann, 1989) where $F = -m_1^* / m_3^*$ and $m_i^* = m_i - \frac{1}{3}tr(M)$.

Expressed in matrix notation:

$$\mathrm{M}_{DEV} = m_3^*(1-2F)\begin{bmatrix} 0 & 0 & 0 \\ 0 & -1 & 0 \\ 0 & 0 & 1 \end{bmatrix} + m_3^* F \begin{bmatrix} -1 & 0 & 0 \\ 0 & -1 & 0 \\ 0 & 0 & 2 \end{bmatrix} \qquad 2.39$$

$$= \mathbf{M}_{DOUBLE\text{-}COUPLE} + \mathbf{M}_{CLVD}$$

Direct comparisons of the isotropic, deviatoric and CLVD components can be performed by equating them into the following percentage decompositions:

$$\%ISO = \frac{100\,tr(\mathbf{M}_E)}{|tr(\mathbf{M}_E)| + \sum_{i=1}^{3}|m_i^*|} \qquad 2.40$$

$$\%DC = \frac{m_3^*(1-2F)}{|m_3^*(1-2F)| + |2m_3^* F|}(100 - \%ISO) \qquad 2.41$$

$$\%CLVD = \frac{2m_3^* F}{|m_3^*(1-2F)| + |2m_3^* F|}(100 - \%ISO) \qquad 2.42$$

Despite being mathematically convenient, these decompositions do not, in general, correspond to any readily recognisable physical attributes of the source. To date, there is no physical source model that matches the CLVD. Such a model would require a Poisson's ratio of 0.5, whereas rock generally has a value of ~0.25. Decomposition into three vector dipoles or three double-couples is the most useful from an interpretation point of view.

The deviation ε of the seismic source from the model of pure double-couple is expressed as the ratio of the minimum to maximum deviatoric eigenvalue:

$$\varepsilon = \left|\frac{e_3}{e_1}\right| \qquad 2.43$$

where $|e_1| \geq |e_2| \geq |e_3|$, $\varepsilon = 0$ for a pure double-couple source, and $\varepsilon = 0.5$ for a pure CLVD (Dziewonski *et al.* 1981).

Silver & Jordan (1982) have developed a method for the estimation for the isotropic and deviatoric components of the moment tensor using isotropic, deviatoric and total scalar seismic moments. According to these researchers, the isotropic source component *ISO%,* expressed as a percentage is given by:

$$ISO\% = \frac{trace}{|trace|} \cdot \left(\frac{M_I}{M_T} \right)^2 \cdot 100 \ \ per\ cent \qquad 2.44$$

where

$$M_I = \frac{trace}{\sqrt{6}} \qquad 2.45$$

and

$$M_T = \sqrt{\sum_{p,q} M^o_{pq} M^o_{pq} / 2} \qquad 2.46$$

The six independent components of the Cartesian moment tensor for a shear dislocation (whose orientation and sense of slip are described by strike, dip, rake and moment) can be expressed in the geographical coordinate system (Figure 2.14) as follows:

$$\begin{aligned}
M_{11} &= -M_o \left(sin\delta cos\lambda sin2\phi_S + sin2\delta sin\lambda sin^2\phi_S \right) \\
M_{12} &= M_{21} = M_o \left(sin\delta cos\lambda cos2\phi_S + \tfrac{1}{2} sin2\delta sin\lambda sin\phi_S \right) \\
M_{13} &= M_{31} = -M_o \left(cos\delta cos\lambda cos\phi_S + cos2\delta sin\lambda sin\phi_S \right) \\
M_{22} &= M_o \left(sin\delta cos\lambda sin2\phi_S - sin2\delta sin\lambda cos^2\phi_S \right) \\
M_{23} &= M_{32} = M_o \left(cos\delta cos\lambda sin\phi_S - cos2\delta sin\lambda cos\phi_S \right) \\
M_{33} &= M_o \, sin2\delta sin\lambda
\end{aligned} \qquad 2.47$$

(Aki & Richards, 1980). Equations 2.47 and 2.15-2.21 can be combined to give the relations for the P, SV and SH radiation patterns in the far-field in terms of the fault and receiver parameters. These equations are given because they are used to generate synthetic seismograms later in this thesis. Alternatively, the far-field displacements can be computed directly from the fault geometry without calculating the moment tensor first. Although the following equations are not used in this thesis, they are provided for completion. In dimensionless form, the radiation patterns are given by Aki & Richards (1980) as:

$$\begin{aligned}
R^P = {} & cos\lambda sin\delta sin^2 i_\xi \, sin2(\phi - \phi_S) - cos\lambda cos\delta sin2i_\xi \, cos(\phi - \phi_S) \\
& + sin\lambda sin2\delta \left[cos^2 i_\xi - sin^2 i_\xi \, sin^2(\phi - \phi_S) \right] \\
& + sin\lambda cos2\delta sin2i_\xi \, sin(\phi - \phi_S)
\end{aligned} \qquad 2.48$$

$$\begin{aligned}
R^{SV} = {} & sin\lambda cos2\delta cos2i_\xi \, sin(\phi - \phi_S) - cos\lambda cos\delta cos2i_\xi \, cos(\phi - \phi_S) \\
& + \tfrac{1}{2} cos\lambda sin\delta sin2i_\xi \, sin2(\phi - \phi_S) \\
& - \tfrac{1}{2} sin\lambda sin2\delta sin2i_\xi \left[1 + sin^2(\phi - \phi_S) \right]
\end{aligned} \qquad 2.49$$

$$\begin{aligned}
R^{SH} = {} & cos\lambda cos\delta cosi_\xi \, sin(\phi - \phi_S) + cos\lambda sin\delta sini_\xi \, cos2(\phi - \phi_S) \\
& + sin\lambda cos2\delta cosi_\xi \, cos(\phi - \phi_S) \\
& - \tfrac{1}{2} sin\lambda sin2\delta sini_\xi \, sin2(\phi - \phi_S)
\end{aligned} \qquad 2.50$$

The associated far-field displacements are given by:

$$\mathbf{u}^P = \frac{\mu A}{4\pi\rho\alpha^3 r}\dot{u}\left(t-\frac{r}{\alpha}\right)R^P\ \mathbf{R} \qquad 2.51$$

$$\mathbf{u}^{SV} = \frac{\mu A}{4\pi\rho\beta^3 r}\dot{u}\left(t-\frac{r}{\beta}\right)R^{SV}\ \Theta \qquad 2.52$$

$$\mathbf{u}^{SH} = \frac{\mu A}{4\pi\rho\beta^3 r}\dot{u}\left(t-\frac{r}{\beta}\right)R^{SH}\ \Phi \qquad 2.53$$

where $\dot{u}$ is the particle velocity at the source, averaged over the fault area and evaluated at retarded time. α and β are the velocities of either the P- or S-wave, respectively, and r is the distance between source and receiver. **R**, Φ and Θ are unit vectors in spherical coordinates (Figure 2.13) given by Equations 2.12 – 2.14.

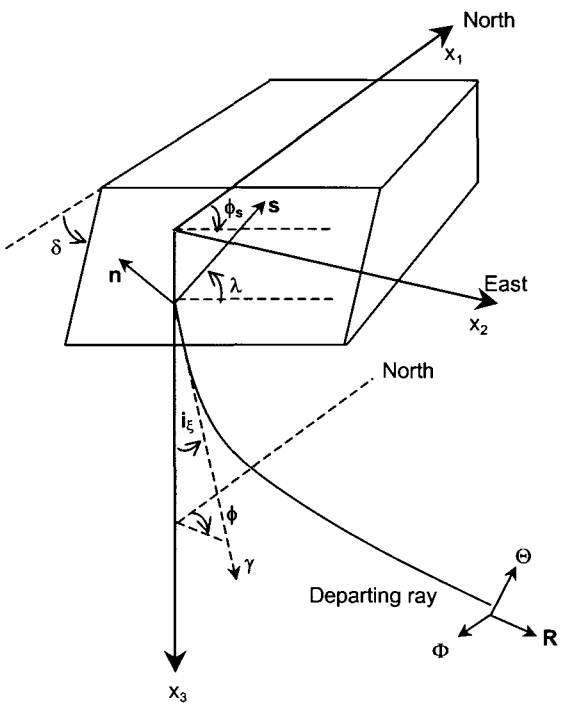

*Figure 2.14: Definition of Cartesian coordinates used to obtain the P, SV and SH radiation patterns from a fault whose orientation is defined by strike, dip and rake. The orientation of the fault is in geographical coordinates. The axis points to the North, to the East, and points downwards. **n** is the normal vector to the fault plane, and **s** is the slip vector. The take-off angle i_ξ is measured from the vertical axis to the raypath. Since **R** is the longitudinal direction along the raypath, **R** = γ for homogeneous media, where γ is the longitudinal direction from the source (from Aki & Richards, 1980).*

2.4 SOURCE MECHANISMS

The aim of focal mechanism studies is to determine the orientation of the geological fault along which a seismic event occurred, through analyses of recorded seismic waves. Since mine seismicity is of particular interest in this study, a brief summary of focal mechanisms identified underground is given.

2.4.1 Source models for mine-induced seismicity

Mine tremors can be broadly classified into two types: those directly related to mining activities, i.e. those associated with the formation of fractures at stope faces; and those associated with movement on pre-existing geological structures (Gibowicz, 1990). Hasegawa *et al.* (1989) have proposed six models of induced seismicity (Figure 2.15). The last three models (d, e and f) correspond to a double-couple focal mechanism, whereas the first three (a, b and c) are of different equivalent force types.

No systematic differences have been found between mining-induced tremors and natural earthquakes and, as a result, much of what has been discovered regarding the mechanism of earthquakes may be applied to those induced by mining activities. Studies of mine tremors have confirmed that large events are usually caused by shear failure on fault planes in the rock mass (e.g. Gay & Ortlepp, 1979). The small seismic events that occur at stope faces also tend to be shear failure events (Spottiswoode, 1984), but, as will be described in the following sections, other modes of failure sometimes contribute to the overall mechanism.

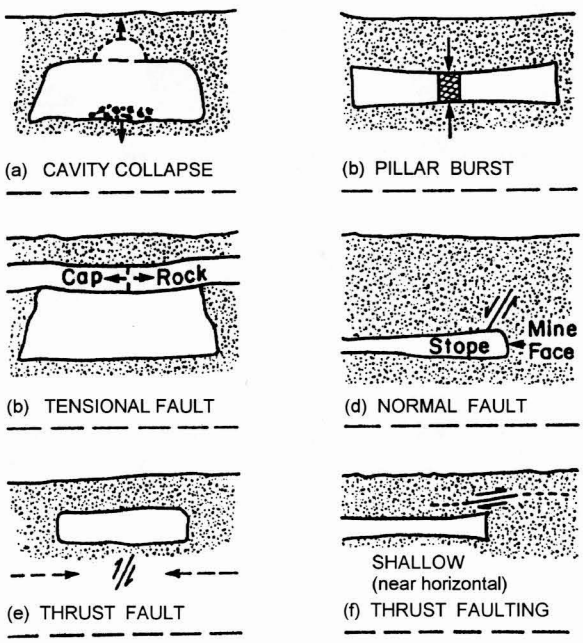

Figure 2.15: Schematic diagram of six possible models for mining-induced seismicity. Solid arrows indicate mining-induced force directions on host rock during induced events, and dashed arrows indicate ambient tectonic stress (from Hasegawa et al., 1989).

2.4.2 Non-double-couple seismic events

In an interesting study at the Rudna copper mine, the isotropic component was found to contribute as much as 25 per cent to the source mechanism Poland (Wiejacz, 1991 cited in Gibowicz & Kijko, 1994). Wiejacz (1991) studied the source mechanisms of 60 small seismic events (moment range 10^{11} to 10^{12} N.m).

The moment tensor inversion was applied in the time domain using first motion amplitudes and P-wave polarity, and the amplitude of SV-waves recorded by the mine underground network composed of over 20 vertical sensors. The time-independent solutions were obtained for a general six component moment tensor; constrained solutions corresponding to sources with no volumes changes, and constrained solutions corresponding to double-couple sources (Figure 2.16).

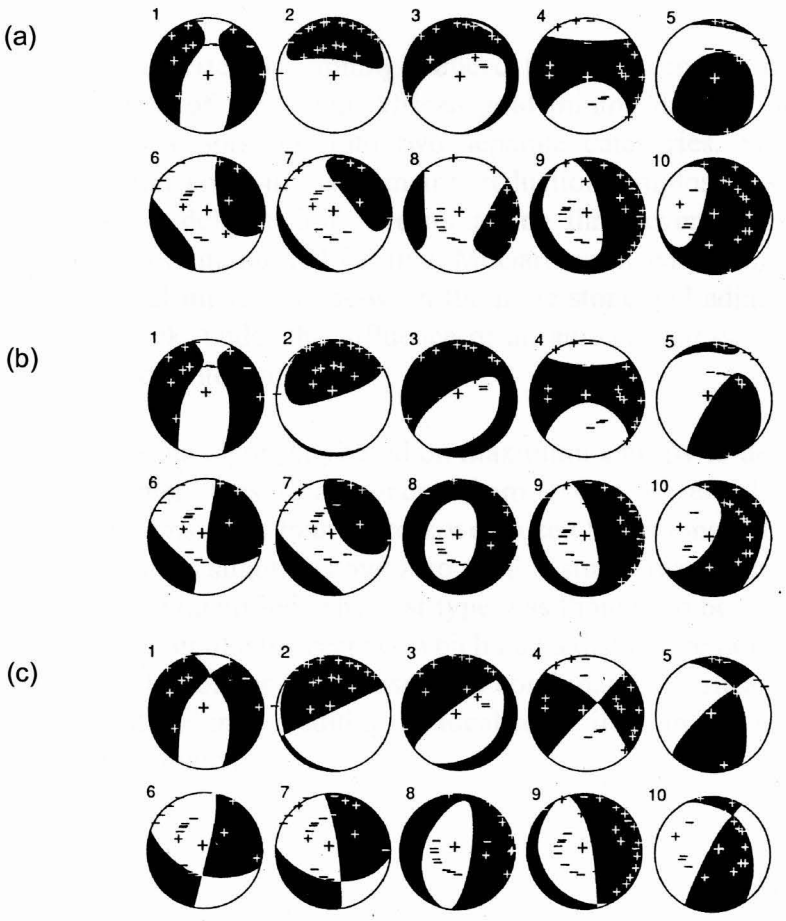

Figure 2.16: Nodal lines deduced from moment tensor inversion for 10 selected seismic events that occurred in 1991 at Rudna copper mine, Poland. A lower hemisphere equal-area projection is used where the shaded areas represent the regions of upward P-wave motion. Three solutions are shown for each event: (a) for a general six component moment tensor, (b) for a constrained moment tensor corresponding to sources with no volumes changes, and (c) constrained solutions corresponding to double-couple sources (from Wiejacz, 1991, cited in Gibowicz & Kijko, 1994).

Wiejacz concluded that the solutions that are well constrained by observations (i.e. good coverage over the focal sphere) have dominant shear components, although occasionally the isotropic component could be as large as 25 per cent of the mechanism. The CLVD component corresponds to uniaxial compression in all cases, and is usually larger than the isotropic component.

The nature of source mechanisms of mining-induced tremors has been a controversial topic (e.g. Wong & McGarr, 1990). However, a number of studies have revealed definitive demonstrations of isotropic components in the moment tensors of some of these events. For example, Feigner & Young (1992) inverted accelerometer recordings of microseismic events in the Underground Research Laboratory, Manitoba, to determine moment tensors and found events with both explosive and implosive components. Stickney & Sprenke (1992) used a comprehensive seismic network to demonstrate that the P-wave first motions for tremors recorded in the Coeur d'Alene mining district, Idaho, required a significant implosive component to the source mechanism.

McGarr (1992b) inverted 10 mining-induced tremors recorded on the surface and underground in two of the South African gold mining districts and found that the resulting moment tensors fell into two separate categories. Seven of the events involved substantial coseismic volumetric reduction (implosive source component) together with shear deformation. The remaining three events were largely double-couple sources involving normal faulting. McGarr surmised that the coseismic closure indicates substantial interaction between the mine stope and adjacent shear failure in the surrounding rock, under the influence of an ambient stress where the maximum principal stress is oriented vertically.

Brawn (1989) used an algorithm based on maximum entropy to determine the higher-order seismic moment tensor components from a set of observed seismograms. Four suites of seismograms from four sources were used to demonstrate the method, all of which had magnitudes slightly above zero. In this study, two types of mining-induced seismic events were identified. The first type was thought to be directly controlled by nearby excavations, unlike the second, which had a distinctive failure-slip mechanism. Brawn described the former mechanism as a combination of shear and tensile failure, or 'compressional failure', resulting in localised failure in the rock at the point at which the source initiated.

Chapter 3

MOMENT TENSOR INVERSION

Gilbert (1970) introduced the seismic moment tensor for calculating the displacement at the free surface, expressed as the sum of moment tensor elements multiplied by their corresponding Green's functions. The linearity between the moment tensor and the Green's function was first used by Gilbert (1973) to determine moment tensor elements from observations, a process now known as moment tensor inversion.

Mathematical inversion in itself is a diverse topic, not because the underlying concepts are difficult, but because of the wide range of techniques used to perform the inversion. Since inversion is used in this study as a tool to perform a particular task, the intricacies of the mathematics of inversion are not discussed in this chapter, and are considered to be beyond the scope of this work. For the details of geophysical inversion theory, consult Menke (1989) and Tarantolla (1987).

A plethora of moment tensor inversion techniques has been proposed since the pioneering paper of Gilbert & Dziewonski (1975) in which free oscillation data was inverted to retrieve the source moment tensor of large earthquakes. The models of the seismic source and the methods applied differ greatly according to the available data and the purpose of the study. This chapter attempts to summarise the essence of several moment tensor inversion techniques, focussing on the different techniques used to evaluate the Green's function and schemes applied to reduce the effect of noisy data on the inversion results.

In this thesis, a distinction is made between the 'absolute' and 'relative' methods. Two broad classes of inversion procedure are recognised, based on the methods used in the literature to evaluate the Green's functions. Absolute inversion methods require the wave propagation (i.e. the Green's function) between the source and receiver to be known, and are used to estimate the moment tensor of a single source. The Green's functions may be evaluated theoretically (e.g. Dziewonski & Gilbert, 1974; Stump & Johnson, 1977; Fitch *et al.*, 1980; de Natale *et al.*, 1987; Ebel & Bonjer 1990; Bowers 1997) or determined empirically from observations and a known source (e.g. Hutchings, 1994). Relative inversion methods are based on the concept of a common raypath between a cluster of seismic sources and a particular receiver, and assume that all the events in the cluster experience the same wave propagation effects to a given receiver. Generally, the radiation pattern of a reference event is used to estimate the Green's functions for events from the same source region (e.g. Patton, 1980; Strelitz, 1980; Oncescu, 1986). In the relative method proposed by Dahm (1996) the path effects described by the Green's functions are eliminated analytically – thereby avoiding the explicit use of the Green's functions completely. No reference event is

needed when the method is applied to a cluster of events with different radiation patterns.

3.1 Overview Of Inversion Methods

The goal of all inversion methods is to use observed values of ground displacement to infer properties of the source, as characterised by the moment tensor. This can be posed as a linear algebraic inverse problem in either the time or the frequency-domain and is described in some detail in Section 3.2.1.

In general, moment tensor inversions involve two major assumptions. Firstly, it is assumed that the point source approximation holds, i.e. that fault plane dimensions are shorter than the wavelength of the seismic waves used in the inversion and, secondly, that the effect of the earth structure on the seismic waves is modelled correctly. If either of these assumptions does not hold, the resultant moment tensor may contain a large non-double-couple component, even if the source mechanism is a double-couple (Strelitz, 1978; Barker & Langston, 1982). Increasing the complexity of the source structure models to improve the fit of the Green's functions to the observed seismograms, improving the data set's azimuthal coverage, and leaving the source-time function free to compensate partially for the deficiencies of the Green's functions are all techniques that can be used to decrease the size of the non-double-couple component (Johnston & Langston, 1984).

The quality of the moment tensor inversion depends to a large extent on the number and quality of data points available and on the azimuthal coverage of stations around the source. A systematic overview of the effects caused by the use of only P-waves, P- and SH-waves, P-, SH- and SV-waves and differences in azimuthal coverage is given in Dufumier (1996). When considering the quality of the input data, an important principle to keep in mind is the GIGO principle (Garbage In, Garbage Out) – data having poor signal-to-noise ratios have an adverse effect on the moment tensor solutions resulting in the presence of 'false' moment tensor components (this is demonstrated briefly in Chapter 6 and at length in Chapter 7). Other sources of error can be due to erroneous velocity models used in the Green's function calculations and/or wrong hypocentral coordinates. A methodical study of the effects of these factors can be found in Šílený *et al.* 1992; Šílený & Psencik (1995) and Šílený *et al.* (1996).

3.1.1 Inversion in the time- and frequency-domain

There are numerous methods of inversion for moment tensor elements. The inversion can be done in the time-domain (e.g. Stump & Johnson, 1977; Fitch *et al.*, 1980) using the formulation given by Equation 3.8. If the assumption of a synchronous source does not hold, or the source-time function is not known, the frequency-domain formulation given by Equation 3.9 is used (e.g. Dziewonski & Gilbert, 1974; Patton, 1980).

3.1.2 Variations in input data

Different data (e.g. body and surface waves, different seismogram components) can be used in the inversion, either separately or in combination. Bowers (1997) used body wave data recorded at teleseismic distances to determine the source depth and moment tensor from a seismic event (M = 4.7) in South Africa on 30 October, 1994. Fan & Wallace (1995) determined the source mechanism of the same event using broadband inversion of three component waveforms from two regional stations. Ebel & Bonjer (1990) used the direct P- and S-wave amplitudes for six earthquakes in the Southern Black Forest of West Germany in an inversion for the source moment tensor. Kikuchi & Kanamori (1991) inverted complex[1] body waves, using P, SV, SH and PP-phases simultaneously in the inversion. Fitch *et al.* (1980) inverted amplitude data from direct and near-source reflected phases to obtain point-source moment tensors.

3.1.3 Application of *a priori* constraints

In addition to variations in input data, different *a priori* constraints can be applied to stabilise the inversion. For example, the trace (sum of the eigenvalues, Chapter 2) can be constrained to zero, restricting the moment tensor to purely deviatoric components. If one of the eigenvalues is constrained to zero, the deviatoric moment tensor components represent a pure double-couple source.

For shallow earthquakes (depths < 30 km), the moment tensor elements M_{13} and M_{23} (which correspond to vertical dip-slip faulting) are not well constrained from long-period surface wave data (Fitch *et al.*, 1981; Dziewonski & Woodhouse, 1983). These moment tensor components may be constrained to zero, so that possible fault mechanisms are restricted to vertical strike-slip, or 45° dip-slip (Kanamori & Given, 1981).

Kikuchi & Kanamori (1986) represented the rupture pattern of earthquakes by a sequence of subevents[2] distributed on a fault plane. In the inversion, they assumed that all the subevents have the same mechanism, usually determined from the first-motions data. In later work, Kikuchi & Kanamori (1991) extended their method to a more general case where subevents are allowed to have different mechanisms. However, when subevent mechanisms are allowed to vary, the inversion often becomes unstable. By varying the constraints, they were able to explore the range of allowable solutions.

---

[1] When source-time functions become sufficiently complicated to suggest earthquake multiplicity, the event is known as a complex earthquake.

[2] When earthquakes reach a certain size, the faulting heterogeneity can be represented using the concept of subevents, i.e. for some large events, the seismic source process can be thought of as a series of moderate sized events.

3.2 ABSOLUTE MOMENT TENSOR INVERSION

The seismic displacement field radiated from a seismic source may be described as a convolution in the time-domain of the moment tensor and the spatial derivatives of the Green's functions. This statement describes the basis of the absolute inversion, in which observations of the ground displacement u_k and knowledge of the wave propagation between source and receiver, described by the Green's function, are used to determine the moment tensor M_{ij}.

The main difficulty in the absolute inversion is the accurate estimation of the Green's functions for geologically complex media. The Green's functions are dependent on the earth model, the location of the point source, and the receiver position. The effect of lateral inhomogeneities is problematic because calculation of the Green's functions is usually based on parallel layers of lateral homogeneity (Jost & Herrmann, 1989). Insufficient knowledge of the Green's functions can introduce systematic errors into the moment tensor elements. This is a fundamental problem because it is possible to separate the source effect from the observed seismogram to limited accuracy only (Jost & Herrmann, 1989).

In geologically and structurally complex environments (with possible lateral inhomogeneities) it is often not possible to calculate the Green's functions with adequate accuracy. In such cases an empirical approach is useful, and the Green's functions are determined from observations and a known source.

3.2.1 Formulation of the inverse problem

By using the representation theorem for seismic sources (Aki & Richards, 1980), the observed displacement u_k at an arbitrary position $x=(x_1,x_2,x_3)$ at time t due to a distribution of equivalent body force densities f_i within a source volume V is given by:

$$u_k(x,t)=\int_{-\infty}^{+\infty}\int_V G_{ki}(x,t;x',t')f_i(x',t')dV(x')dt' \qquad 3.1$$

where $G_{ki}(x,t;x',t')$ are the components of the Green's functions containing the propagation effects between the source (x',t') and receiver (x,t), and x' is a vector such that $x'=(x_1',x_2',x_3')$. For repeated indices the summation convention holds. The subscript k indicates the component of the displacement.

The origin of the coordinate system is placed at a reference point $\xi=(\xi_1,\xi_2,\xi_3)$ within V, and the Green's functions may be expanded into the following Taylor series:

$$G_{ki}(x,t;x',t')=\sum_{n=0}^{\infty}\frac{1}{n!}(x'_{j_1}-\xi_{j_1})\cdots(x'_{j_n}-\xi_{j_n})G_{ki,j_1\ldots j_n}(x,t;\xi,t') \qquad 3.2$$

The comma between the indices in Equation 3.2 describes partial derivatives with respect to the coordinates after the comma, i.e. $\frac{\partial G_{ki}}{\partial \xi_j}$.

The moment of the equivalent body forces may be defined in terms of the components of the time-dependent force moment tensor such that:

$$M_{ij_1\cdots j_n}(\xi,t') = \int_V (x'_{j_1} - \xi_{j_1})\cdots(x'_{j_n} - \xi_{j_n}) f_i(x',t') dV \qquad 3.3$$

If conservation of linear momentum applies (such as for a source in the interior of a body) then a term in M_i does not exist in Equation 3.3.

Using the Taylor expansion of Equation 3.2 and the definition of the time-dependent moment tensor of Equation 3.3, the displacement u_k described by Equation 3.1 may be written as:

$$u_k(x,t) = \sum_{n=0}^{\infty} \frac{1}{n!} G_{ki,j_1\cdots j_n}(x,t;\xi,t') * M_{ij_1\cdots j_n}(\xi,t') \qquad 3.4$$

(e.g. Aki & Richards, 1980; Jost & Herrmann, 1989) where * denotes the temporal convolution[3].

If the point source approximation holds (i.e. source dimensions are small in comparison to the observed wavelengths of seismic waves), only the first term of Equation 3.4 need be considered. Finally, if the equivalent body forces conserve angular momentum, M_{ij} is a symmetric second-rank tensor. The displacement u_k can then be written as (Gibowicz & Kijko, 1994):

$$u_k(x,t) = G_{ki,j}(x,t;0,0) * M_{ij}(0,t) \text{ for } \xi = 0 \qquad 3.5$$

3.2.2 Formulation in the time and frequency-domain

From this point the analysis can diverge into either of two approaches. In the time-domain approach, it is assumed that all the components of $M_{ij}(0,t)$ have the same time dependence, $s(t)$. This case is referred to as the synchronous source (Silver & Jordan, 1982) and may be represented by:

$$M_{ij}(0,t) = M_{ij}s(t) \qquad 3.6$$

where M_{ij} is the set of constant terms, and $s(t)$ is referred to as the source-time function.

[3] The convolution of $f(t)$ and $g(t)$ may be represented symbolically by $f(t)*g(t)$ and is expressed by $f(t)*g(t) = \int_0 f(t-t')g(t')dt'$

Equation 3.5 becomes:

$$u_k(x,t) = \left[G_{ki,j}(x,t;0,0) * s(t)\right] M_{ij} \qquad 3.7$$

If the source-time function is an impulse, i.e. $s(t) = \delta(t)$, the convolution of $G_{ki,j}$ with $\delta(t)$ will be itself, i.e. $G_{ki,j}$ (sifting property of the delta function). Equation 3.7 can then be written as follows:

$$u_k(x,t) = G_{ki,j}(x,t) M_{ij} \qquad 3.8$$

If the source is not assumed to be synchronous, the frequency-domain approach is necessary. Taking the Fourier transform of Equation 3.5 to obtain its frequency-domain equivalent gives the displacement u_k for each frequency f such that:

$$u_k(x,f) = G_{ki,j}(x,f) M_{ij}(f) \qquad 3.9$$

where the convolution operation in the time-domain becomes a multiplication operation in the frequency-domain.

Both the time- and frequency-domain formulations of the displacement (Equations 3.8 and 3.9) can be written in matrix form as:

$$\mathbf{u} = \mathbf{G}\,\mathbf{m} \qquad 3.10$$

In the time-domain, the vector **u** consists of n sampled values of the observed ground displacement recorded at various times, stations and sensor components and is a vector of dimension n. The matrix **G** is composed of the Green's functions in the coordinate system of the receivers and has dimensions $n \times 6$. **m** is a vector consisting of the six independent moment tensor components $M_{11}, M_{22}, M_{33}, M_{12}, M_{13}$ and M_{23}. Each component of each station is stacked into the **u** vector while the appropriate Green's function is put into the **G** matrix. In most cases $n >> 6$ and the system of equations is, in principle, overdetermined.

In the frequency-domain, Equation 3.10 is written separately for each frequency. Vector **u** consists of the real and imaginary parts of each displacement for a particular frequency and has dimension $2n$ for the case of n seismograms. The matrix **G** is composed of the real and imaginary parts of the Fourier transform of the Green's functions for the particular frequency and has dimension $2n \times 12$. Vector **m** (dimension 12) consists of the real and imaginary parts of the components of the moment tensor at the particular frequency. When $n < 6$, the problem is underdetermined, exact if $n = 6$ and overdetermined if $n > 6$. The underdetermined case may be improved by introducing constraints (e.g. setting the isotropic component to zero, so that $M_{11} + M_{22} + M_{33} = 0$).

Generally, calculation of the Green's functions for the corresponding moment tensor component constitutes one of the most important parts of the inversion scheme. A

variety of methods exist to compute synthetic seismograms (e.g. Dornboos, 1988). Some of the synthetic seismogram codes allow calculation for the moment tensor elements as input source parameters, while others allow input for double-couple and explosive point sources. The general moment tensor can be decomposed in various ways using moment tensor components of double-couple and explosive sources so that the synthetic seismogram codes employing these source parametisations can also be used in the inversion of Equation 3.10.

3.2.3 Solution of the inverse problem

In order to solve for the components of the moment tensor **m**, Equation 3.10 is written as an inverse problem such that:

$$\mathbf{m} = \mathbf{G}^{-1}\mathbf{u} \qquad 3.11$$

where $\mathbf{G}^{-1}$ is the generalised inverse of **G**. A branch of mathematics known as Inverse Theory has developed to study the solution of such systems. A number of algorithms are available to perform the inversion, for example, the singular value decomposition method (Lawson & Hanson, 1974) or the generalised linearised inverse technique (e.g. Barker & Langston, 1982).

3.2.4 Inversion of single station three-component data

Equation 3.11 applies to each time step in the observed seismogram, $u(x,t)$. In theory, the full moment tensor can be recovered from three-component data recorded at a single station. In practice, this technique is sensitive to noise, uncertainties in the Green's functions and source-time function, and the limited bandwidth of recording instruments. However, three-component single station inversion can be applied with success, (e.g. Kanamori *et al.*, 1990) to events recorded at local and near-regional distances (where the effects of structure can be easily accounted for) and to very broadband, high dynamic range instruments. An example is illustrated in Figure 3.1.

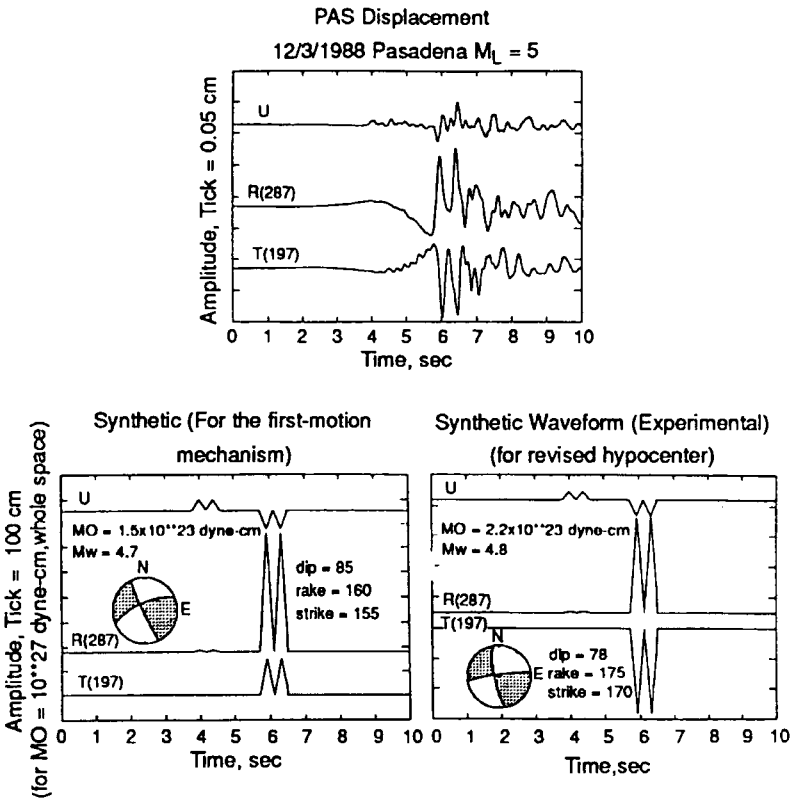

Figure 3.1: The determination of a focal mechanism by modelling the three-component data recorded at a single broadband station at Pasadena (PAS), California (modified from Kanamori et al., 1990)

3.2.5 Simultaneous inversion of multiple-station data

A more stable procedure is to simultaneously invert seismograms recorded at a number of stations. For a given time t with multiple stations, Equation 3.10 can be written in matrix-vector form as follows:

$$\begin{bmatrix} u_1 \\ u_2 \\ \vdots \\ u_n \end{bmatrix} = \begin{bmatrix} G_{11} & G_{12} & \cdots & G_{16} \\ G_{21} & G_{22} & \cdots & G_{26} \\ \vdots & \vdots & \ddots & \vdots \\ G_{n1} & G_{n2} & \cdots & G_{n6} \end{bmatrix} \begin{bmatrix} m_1 \\ m_2 \\ \vdots \\ m_6 \end{bmatrix} \qquad 3.12$$

where $m_1 = M_{11}$, $m_2 = M_{12}$, $m_3 = M_{13}$, $m_4 = M_{22}$, $m_5 = M_{23}$, $m_6 = M_{33}$ and n represents the number of seismograms of interest. When $n > 6$ the system is overdetermined and it should be possible to resolve **m**. In practice, the system must be significantly overdetermined (i.e. $n >> 6$) to resolve **m**, which is easily achieved using multiple time samples.

3.2.6 Weighted inversion using P-wave polarity and S-wave polarisation angle

In the discussion so far, the issue of data reliability has been sorely neglected. In every least-squares system concerning a combination of observations, it is desirable to apply a weighting scheme to the input data – an example would be to give a high weighting to reliable data and a lower weighting to the less reliable data. Although this idea was not the focal issue of their paper, one of the first weighting schemes was proposed by Udias & Baumann (1969). Their work predates that of Gilbert (1973) and as a result the linearity between the moment tensor and the Green's function is not exploited. In fact, the moment tensor inversion is not mentioned at all! Despite this, the relevant parts of their methodology are described because of the similarities shared with the hybrid moment tensor inversion technique developed in this thesis.

The inversion method of Udias & Baumann (1969) uses a small number of homogeneous long-period undisturbed observations of the sign of the P-wave, and the polarisation angle of the S-wave. These researchers define the error for the P-wave data as:

$$N_{pw} = \sum_{i=1}^{N} \left| sgn\, u_{Pi} - sgn\, u_{Pci} \right| \cdot D_i \qquad 3.13$$

where the term in brackets is the difference between the signs of the measured or recorded P-wave first-motion u_{Pi} and the computed theoretical values of the first-motion u_{Pci}. D_i is a factor which multiples the number of the stations with inconsistent P-wave data and expresses the weight given to the P-data.

The standard deviation of the residuals of the polarisation angles of the S-wave, S_ε, is then combined with the error for the P-wave data, N_{Pw}, into a total error E whose minimum is sought:

$$E = S_\varepsilon + N_{Pw} \qquad 3.14$$

The P-wave data can be weighted by use of the factor D_i. This can be done in different ways. If only very clear first motions are used, and the P-wave data are intended to be used as a constraint, D_i is given the value of 100. The weight D_i can also be defined as a function of the signal to noise ratio, or according to an arbitrary scale based on the quality of the P-wave reading.

The angles of polarisation of the S-wave are weighted according to the clearness and linearity of the particle motion diagrams. To do this, the measurements of the polarisation angles are given within an estimate, for example, $\gamma = 32^\circ \pm 5^\circ$, depending on how accurately the observer thinks the polarisation angle can be determined. According to Udias & Baumann (1969), although this introduces a decision on the part of the observer, it still is more realistic than giving all measurements the same degree of accuracy.

3.2.7 Iterative inversion with variable hypocentral depth and structural model

In most moment tensor inversions, either the hypocentre is fixed, or allowed to change using a given velocity model. Šílený *et al.* (1992) proposed a more general method in which both the depth of the source and the structural model representing the area in which the event occurred are permitted to vary within an *a priori* chosen range. The procedure allows the retrieval of the moment tensor of a point source as a function of time. The method consists of two steps: (1) linear waveform inversion of the source parameters for a fixed source depth and structural model, followed by (2) perturbation of the source depth and structural parameters. These two steps are iterated until the convergence between the observed and computed records is reached, within a pre-assigned threshold for the L_2 norm of their differences. This is done because the source depth strongly influences the waveforms and the precision with which this parameter is determined using standard procedures is generally not satisfactory. For similar reasons, these workers allow changes in the structural model. These researchers also apply a weighting scheme to enhance the stations with low recorded amplitudes (due to being close to a node in the radiation pattern) or to downgrade the weight of low quality signals.

Šílený *et al.* (1992) tested the method using synthetic data generated for instantaneous and finite duration sources. The synthetic data were computed for two structures: one belonging to the structural range within which the base functions were computed, and the other lying outside of this range. Random noise was superimposed on the input data. When the synthetic records computed for a structure lying within the specified range, the full six-component moment tensor was obtained satisfactorily, provided that the noise level did not exceed 10 per cent of the peak signal amplitude and that the variation in focal depth occurred in sufficiently small increments. Violation of some of these conditions gave rise to a spurious volumetric component which had to be removed. The remaining deviatoric part of the moment tensor contained the true source mechanism information.

In addition to the synthetic tests, the procedure was applied to vertical component seismograms recorded in the Friuli (NE Italy) area for the M_L = 2.9 event of 27 December 1987. The retrieved source mechanism was found to be in agreement with the distribution of the few first arrival polarities available, and the source-time function indicated a possible multiple rupture process (Figure 3.2).

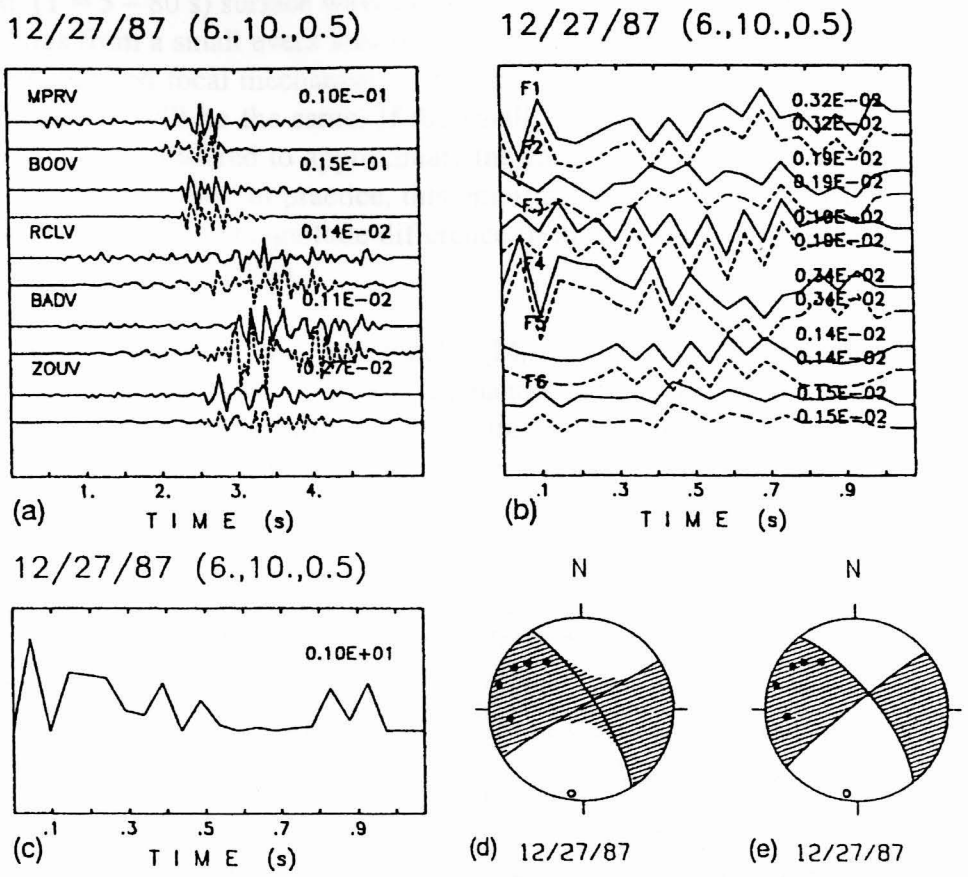

Figure 3.2: Inversion of waveforms of the Friuli event of 27 December 1987, recorded by five local stations (MPRV, BOOV, RCLV, BADV and ZOUV) at epicentral distances of 8.7, 13.8, 25.9, 26.3 and 28.2km, and azimuths of 144°, 83°, 232°, 10° and 8°, respectively. Origin time: 00:21:55 (a) Data (solid lines) and synthetic seismograms (dashed lines) obtained with the unconstrained inversion with base functions constructed in the 6-10km depth interval, with a spacing of 0.5km; data and synthetic seismograms are truncated with a D2 window with a duration of 5.4s. (b) $M_{ij}(t)$ *functions (solid lines) obtained with the unconstrained inversion and their reduced values* $m_{ij}(t)$ *(dashed lines). (c) Joint source-time function, constrained between 0 and 1. (d) 'Average' focal mechanism obtained from the six multipliers* λ_i *where* λ_i *are the amplitudes of the moment tensor (shaded area = compressions, white area = dilatations). (e) Focal mechanism obtained from the first significant peak of the* $m_{ij}(t)$ *function, shown in (b). (from Šílený et al., 1992).*

3.2.8 Empirical evaluation of the Green's functions

There are many instances where it is not possible to compute accurate theoretical Green's functions to allow source information to be retrieved from recorded signals: for example, in areas of geological complexity; broadband recordings of secondary body waves with complex paths in the earth (PP, SSS, etc.); as well as for short-

period (T = 5 – 80 s) surface waves (Lay & Wallace, 1995). In this approach, seismic recordings from a small event located near a large event are considered. Providing the source depth and focal mechanism of the two events are identical, the earth response at each station will be the same. If the small event has an impulse-like source-time function, it is considered to approximate the earth's Green's functions and is used to model the larger event. In practice, this empirical procedure is applicable if there are two or more orders of magnitude difference in the seismic moments of the large and small events (Kataka, 1998).

Hutchings (1994) used two aftershocks (M_L = 3.3 and 3.5) as empirical Green's functions to model the 1971 San Fernando earthquake (M_L = 6.4). His work demonstrates that simple kinematic rupture models, used together with empirical Green's functions, can be used to predict very realistic seismograms (Figure 3.3).

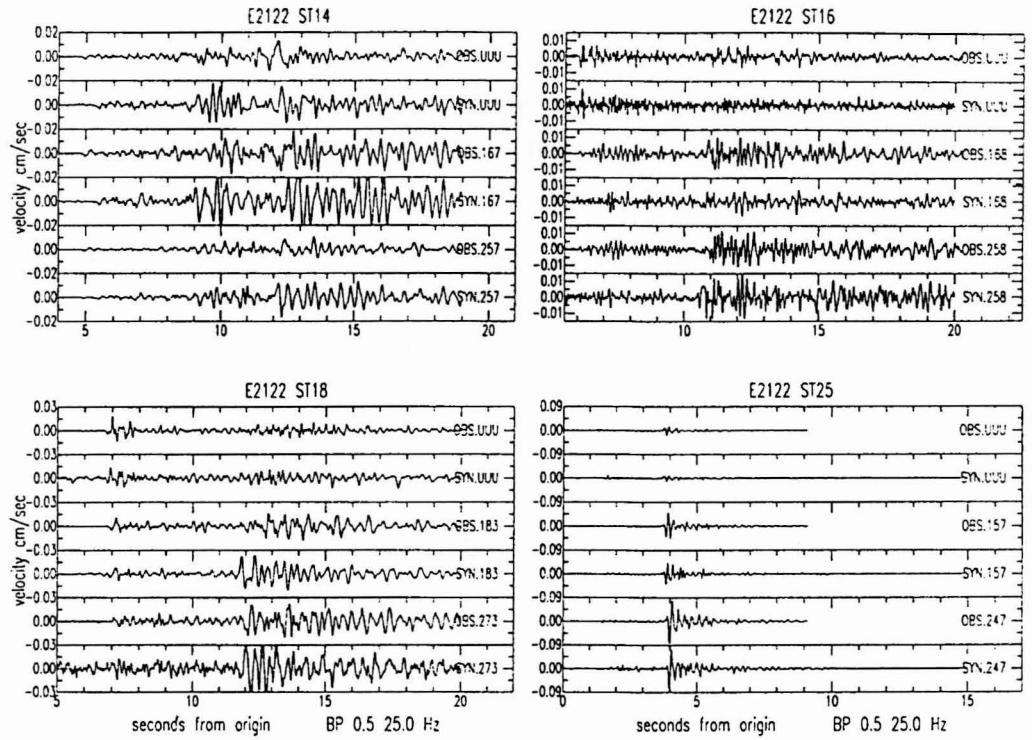

Figure 3.3: Seismograms recorded at stations ST14, ST16, ST18 and ST25 synthesised using aftershock E2122 as an empirical Green's function. Observed trace drawn from above synthetic trace (from Hutchings, 1994).

Chapter 4

RELATIVE MOMENT TENSOR INVERSION

In this chapter, the relative moment tensor inversion method without a reference mechanism as formulated by Dahm (1996) is described in considerable detail. The reason for the detail is that this method is applied in a preliminary investigation to clusters of events recorded in the mining environment to determine whether this method fits the requirements for routine processing on the mines, i.e. is sufficiently robust, resilient to noise and relatively quick and easy to implement by trained mine personnel. The method is of particular interest because the formulation does not require a reference event or reference mechanism when it is applied to events in a cluster with different mechanisms. Since the clusters of events recorded underground often have no dominant shock (i.e. no reference event) this method is potentially very useful.

Also included in this chapter is an overview of the solution procedure and error analysis. In addition, the implementation of the relative inversion by means of a computer program written by the author is described.

4.1 THEORETICAL FORMULATION

The far-field displacement in an elastic earth $u=(u_1,u_2,u_3)$ of a single body-wave phase[1] at an arbitrary position $x=(x_1,x_2,x_3)$ and time t from a point source at location ξ_0 and time τ is:

$$u^k(x,t)=\int_{-\infty}^{+\infty}\sum_{p,q=1}^{3}\dot{M}_{pq}(\tau)G_p^k(x,t-\tau;\xi_o)s_q\,d\tau \qquad k=1,2,3 \qquad 4.1$$

where $\dot{M}_{pq}$ is the moment tensor of the point source differentiated with respect to time (Dahm, 1996).

s_q represents the slowness vector, which geometrically defines the direction of the ray leaving the source. The slowness vector s_q is defined by the derivative of the travel time function $T(x,\xi_o)$ with respect to the source coordinate ξ_0 expressed as:

[1] The P-wave first arrival is referred to as the P-phase, and the horizontally and vertically polarised components of the S-wave arrival are referred to as the SH- and SV-phase, respectively.

$$s_q = \left. \frac{\partial T}{\partial \xi_q} \right|_{\xi_o} \qquad 4.2$$

The *kp*-component G_p^k of the Green's tensor is defined as the displacement response in the *k*-direction of the elastic earth at the receiver due to an impulse force in the *p*-direction at the source. At this stage in the theoretical development, a comment on the notation is necessary. Usually, the component of displacement in the direction *k* is written as a subscript (this convention has been followed in Chapter 2). However, to avoid an excessive number of subscripts, the direction *k* is represented by a superscript).

If the period of the waves to be considered is much longer than the duration of the source-time function, it is sufficient to take into account the first two terms of the Taylor series expansion of the Green's tensor around a centroid source time τ_0 (Dahm, 1996). Expanding Equation 4.1 about a source time τ_0 yields:

$$u^k(x,t) = \sum_{p,q=1}^{3} \left[M_{pq}^o G_p^k(x, t-\tau_o; \xi_o)\, s_q + \int_{-\infty}^{+\infty} \dot{M}_{pq}(\tau)(\tau - \tau_o) d\tau\, \dot{G}_p^k(x, t-\tau_o; \xi_o)\, s_q \right] \qquad 4.3$$

where

$$M_{pq}^o = \int_{-\infty}^{+\infty} \dot{M}_{pq}(\tau) d\tau \qquad 4.4$$

In general, it is not possible to select τ_0 such that the integral in Equation 4.3 vanishes for all values of *p* and *q*. One of two procedures may be used to overcome this problem. The moment tensor components may be assumed to have similar time functions, or all six integrals can be minimised in a least-squares sense (Backus, 1977). Dahm takes the former approach and assumes that the source has a non-zero static moment tensor M_{pq}^o at time $\tau \to \infty$. The centroid source time τ_0 is defined so that the integral in Equation 4.3 vanishes so that the equation reduces to:

$$u^k(x,t) = \sum_{p,q=1}^{3} \left[M_{pq}^o G_p^k(x, t-\tau_o; \xi_o)\, s_q \right] \qquad 4.5$$

Dahm (1996) considers the ray theoretical limit of the Green's tensor in Equation 4.5 and simplifies the tensor further. The nine independent components for direction *k* degenerate to one component for every ray, which is weighted with functions of the ray take-off angle θ and azimuth φ.

Aki & Richards (1980) derive the body-wave excitation for P-, SH- and SV-waves for homogeneous media. Their source representation can still be applied for inhomogeneous media when the P-, SH- and SV-amplitudes are reduced to the focal sphere (Dahm, 1996). Dahm (1996) then derives the source representation at the station using the set of coordinate rotations given later, where it is assumed that the medium in the vicinity of the source is isotropic and homogeneous. Three types of waves leave the source in the direction *s*, *viz.* a longitudinal P-wave with polarisation

vectors parallel to s, and two types of shear waves with polarisation vectors perpendicular to s in the horizontal (SH) direction and in a vertical plane (SV). The Green's tensor of Equation 4.5 may be written as the sum:

$$G={}^{P}G+{}^{SH}G+{}^{SV}G \qquad 4.6$$

It is further assumed that the observed phases in the far-field can be ray traced back to the source, so that the corresponding azimuths and take-off angles of the rays at the source can be calculated. For every ray, a local Cartesian coordinate system with x_o in the SV-direction, y_o in the SH-direction, and z_o in the P- or s-direction is chosen, so that the slowness vector at the source is $s = \left(0,0,s_{z_o}\right)$. Hence, P-waves at the source are excited by equivalent forces in the z_o-direction, SH-waves by forces in the y_o-direction, and SV-waves by forces in the x_o-direction.

For a given k-direction, the Green's tensors $G^k s$ of the displacement components in the local coordinate system are as follows:

$${}^{P}G^k s = \begin{bmatrix} 0 & 0 & 0 \\ 0 & 0 & 0 \\ 0 & 0 & {}^{P}G^k_{z_o} s_{z_o} \end{bmatrix}, {}^{SH}G^k s = \begin{bmatrix} 0 & 0 & 0 \\ 0 & 0 & {}^{SH}G^k_{y_o} s_{z_o} \\ 0 & 0 & 0 \end{bmatrix}, {}^{SV}G^k s = \begin{bmatrix} 0 & 0 & {}^{SV}G^k_{x_o} s_{z_o} \\ 0 & 0 & 0 \\ 0 & 0 & 0 \end{bmatrix} \qquad 4.7$$

In the local coordinate system, the Green's subtensor for every wave propagation mode has a single component. Two tensor rotations are necessary to transform the tensor to the north-east-down coordinate system used in Equation 4.5: the first rotation of an angle $-\theta$ around the y_o-axis, and a second with angle $-\varphi$ around the z_o axis. The rotation angles can be identified as the take-off angle θ and the azimuth φ from the source (Figure 4.1).

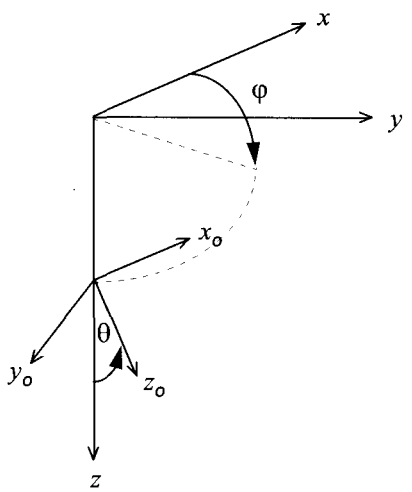

Figure 4.1: Geometry of the local coordinate system $\left(x_o, y_o, z_o\right)$. The azimuth φ is measured clockwise from North and the take-off angle θ is zero when z_o points downwards (from Dahm, 1996).

As a result of the rotation, two new indices i and j are introduced. The displacement component u_{ij}^k in the k direction for source i and phase observation j is given by:

$$u_{ij}^k = I_j^k \sum_{r=1}^{6} m_{ri} a_{jr} \qquad 4.8$$

with

P-Phase:

$$\begin{aligned} &a_{j1} = -\sin^2\theta\cos 2\varphi, \quad a_{j2} = \sin^2\theta\sin 2\theta, \quad a_{j3} = \sin 2\theta\cos\varphi, \\ &a_{j4} = \sin 2\theta\sin\varphi, \quad a_{j5} = \sin^2\theta - 2\cos^2\theta, \quad a_{j6} = 1, \quad I_j^k = {}^{P}G_{z_o}^k s_{z_o} \end{aligned} \qquad 4.9$$

SH-Phase:

$$\begin{aligned} &a_{j1} = \sin\theta\sin 2\varphi, \quad a_{j2} = \sin\theta\cos 2\varphi, \quad a_{j3} = -\cos\theta\sin\varphi, \\ &a_{j4} = \cos\theta\cos\varphi, \quad a_{j5} = 0, \quad a_{j6} = 0, \quad I_j^k = {}^{SH}G_{z_o}^k s_{z_o} \end{aligned} \qquad 4.10$$

SV-Phase:

$$\begin{aligned} &a_{j1} = -\tfrac{1}{2}\sin 2\theta\cos 2\varphi, \quad a_{j2} = \tfrac{1}{2}\sin 2\theta\cos 2\varphi, \quad a_{j3} = \cos 2\theta\cos\varphi, \\ &a_{j4} = \cos 2\theta\sin\varphi, \quad a_{j5} = \tfrac{3}{2}\sin 2\theta, \quad a_{j6} = 0, \quad I_j^k = {}^{SV}G_{z_o}^k s_{z_o} \end{aligned} \qquad 4.11$$

and

$$\begin{aligned} &m_{1i} = \tfrac{1}{2}(M_{22} - M_{11}), \quad m_{2i} = M_{12}, \quad m_{3i} = M_{13}, \\ &m_{4i} = M_{23}, \quad m_{5i} = \tfrac{1}{3}\left(\tfrac{1}{2}(M_{22} + M_{11}) - M_{33}\right) \\ &m_{6i} = \tfrac{1}{3}(M_{11} + M_{22} + M_{33}) \end{aligned} \qquad 4.12$$

where M represents the moment tensor of the i^{th} source, φ is the azimuth and θ the take-off angle of the j^{th} ray from the i^{th} source. The summation convention is not used. The index j also relates to a particular phase of the body-wave observation (i.e. P-, SH- or SV-phase). Observation u_{ij}^k represents the amplitude values (peak-to-peak or maximum amplitude) of a single observed phase j recorded at the station from at least two sources.

The term I_j^k represents the scalar components of the Green's subtensor (i.e. ${}^{P}G_{z_o}^k s_{z_o}$, ${}^{SH}G_{y_o}^k s_{z_o}$, and ${}^{SV}G_{x_o}^k s_{z_o}$ as defined in Equation 4.7) for a given wave propagation mode (i.e. P, SH or SV-phase) and displacement component. For simplicity, the scalar function I_j^k is referred to as the '*I*-term'.

The source parameters are defined in such a way that m_{1i} and m_{2i} represent the 2π-periodic (with azimuth) strike-slip radiation pattern of the source i; m_{3i} and m_{4i} represent the π-periodic dip-slip radiation pattern; m_{5i} represents the pattern of the vertical CLVD component, and m_{6i} represents the isotropic source component (Dahm, 1996). Solving Equation 4.12 simultaneously for the Cartesian moment tensor components (the M_{11}, M_{22} etc.) yields:

$$M_{11} = m_{i5} + m_{i6} - m_{i1}, \quad M_{22} = m_{i1} + m_{i5} + \mathrm{m}_{i6}, \quad M_{33} = m_{i6} - 2m_{i5}, \quad M_{12} = m_{i2}, \quad M_{13} = m_{i3}, \quad M_{23} = m_{i4} \qquad 4.13$$

To summarise the theoretical development thus far, the Green's functions of Equation 4.5 have been separated into the two components appearing in Equation 4.8: a scalar portion describing the linear wave propagation effects (given by the term I_j^k); and a part describing the geometry between source and receiver (given by the terms a_{jr}) consisting of functions of the ray take-off angle θ and azimuth φ.

4.1.1 Relative inversion with a reference mechanism

The next step in Dahm's formulation is to eliminate the linear wave propagation effects described by I_j^k. Specifically, a corresponding ray-amplitude observation originating from a second source located at the same source point as the first source is used to eliminate I_j^k. Consider two sources (i = 1 and i = 2) originating from the same source point. Applying Equation 4.8 (the summation convention is not used) yields:

Source 1 (i = 1)

$$u_{1j}^k = I_j^k \sum_{r=1}^{6} m_{r1} a_{jr} \qquad 4.14$$

Source 2 (i = 2)

$$u_{2j}^k = I_j^k \sum_{s=1}^{6} m_{s2} a_{js} \qquad 4.15$$

Equations 4.14 and 4.15 may be rearranged so that I_j^k is isolated on the right hand side (RHS) and the remaining terms in m, a and u are on the LHS. Setting the LHS of Equation 4.14 equal to that of Equation 4.15 after this rearrangement yields an expression free of I_j^k:

$$\frac{u_{1j}^k}{\sum_{r=1}^{6} m_{r1} a_{jr}} = I_j^k = \frac{u_{2j}^k}{\sum_{s=1}^{6} m_{s2} a_{js}} \qquad 4.16$$

Rearranging Equation 4.16 gives:

$$u_{1j}^k \sum_{s=1}^{6} m_{s2} a_{js} = u_{2j}^k \sum_{r=1}^{6} m_{r1} a_{jr} \qquad 4.17$$

Equation 4.17 applies to one particular phase observation j, and may be written as:

$$f_j = u_{1j}^k \sum_{s=1}^{6} m_{s2} a_{js} \qquad 4.18$$

where

$$f_j = u_{2j}^k \sum_{r=1}^{6} m_{r1} a_{jr} \qquad 4.19$$

Equation 4.18 may appear to be an unnecessary complication, but it is useful when the formulation is extended to a number of phase observations. The discussion thus far has dealt with only one phase observation j from each of two sources. The equations can be expanded to include m observations from two sources such that $j = (1,2,3...m)$ i.e. $2m$ phase observations from two sources. In this case, Equation 4.18 can be rewritten in matrix form as:

$$\begin{pmatrix} f_1 \\ f_2 \\ f_3 \\ \vdots \\ f_m \end{pmatrix} = \begin{pmatrix} u_{11}^k a_{11} & u_{11}^k a_{12} & u_{11}^k a_{13} & \cdots & u_{11}^k a_{16} \\ u_{12}^k a_{21} & u_{12}^k a_{22} & u_{12}^k a_{23} & \cdots & u_{12}^k a_{26} \\ u_{13}^k a_{31} & u_{13}^k a_{32} & u_{13}^k a_{33} & \cdots & u_{13}^k a_{36} \\ \vdots & \vdots & \vdots & \ddots & \vdots \\ u_{1m}^k a_{m1} & u_{1m}^k a_{m2} & u_{1m}^k a_{m3} & \cdots & u_{1m}^k a_{m6} \end{pmatrix} \begin{pmatrix} m_{12} \\ m_{22} \\ m_{32} \\ \vdots \\ m_{62} \end{pmatrix} \qquad 4.20$$

where

$$f_j = u_{2j}^k \sum_{r=1}^{6} m_{r1} a_{jr} \qquad j = (1,2,...m) \qquad 4.21$$

The moment tensor components of the second source (m_{s2}) are linearly dependent on those of the first source (m_{r1}). Therefore, when the m_{r1} of the first source are known *a priori*, the source parameters m_{s2} can be estimated in a least-squares sense. For this reason, the moment tensor of the first source is referred to as a reference mechanism.

Equation 4.20 may be applied to estimate the moment tensors of aftershocks when the moment tensor of the main shock has been accurately determined using another independent method (Dahm, 1996).

4.1.2 Relative inversion without a reference mechanism

In particular cases, it is not possible to determine a reference moment tensor accurately. Such cases occur when there is no dominant shock, as is often the case in the mining environment. Another example would be a weak earthquake swarm with no main shock. There is thus a need for a method where a reference mechanism is not a prerequisite. It is possible to estimate the moment tensor of the first source, with the exception of a constant factor, when the two sources have different radiation patterns (Dahm, 1996).

To avoid a homogeneous system of equations, Dahm introduces an additional linear condition to Equation 4.20:

$$\sum_{i=1}^{n}\sum_{r=1}^{6} m_{ri} = c = constant \neq 0 \qquad 4.22$$

where $n = 2$ is the number of sources, and the constant c is chosen arbitrarily. The magnitude of c determines the magnitude of the output moment tensor components.

The inversion procedure is no longer restricted to the simultaneous use of two sources, but can be expanded to incorporate m observations from n sources. Applying the linear condition (Equation 4.22) to the matrices of Equation 4.20 results in (Dahm, 1996):

$$\begin{pmatrix} 0 \\ 0 \\ 0 \\ \vdots \\ 0. \\ c \end{pmatrix} = \begin{pmatrix} -A^2 & A^1 & 0 & 0 & \cdots & 0 \\ -A^3 & 0 & A^1 & 0 & \cdots & 0 \\ -A^4 & 0 & 0 & A^1 & \cdots & 0 \\ \vdots & \vdots & \vdots & \vdots & \ddots & \vdots \\ -A^n & 0 & 0 & 0 & \cdots & A^1 \\ 1 & 1 & 1 & 1 & \cdots & 1 \end{pmatrix} \begin{pmatrix} S^1 \\ S^2 \\ S^3 \\ \vdots \\ S^{n-1} \\ S^n \end{pmatrix} \qquad 4.23$$

with

$$A^i = \begin{pmatrix} u_{i1}^k a_{11} & u_{i1}^k a_{12} & u_{i1}^k a_{13} & \cdots & u_{i1}^k a_{16} \\ u_{i2}^k a_{21} & u_{i2}^k a_{22} & u_{i2}^k a_{23} & \cdots & u_{i2}^k a_{26} \\ u_{i3}^k a_{31} & u_{i3}^k a_{32} & u_{i3}^k a_{33} & \cdots & u_{i3}^k a_{36} \\ \vdots & \vdots & \vdots & \ddots & \vdots \\ u_{im}^k a_{m1} & u_{im}^k a_{m2} & u_{im}^k a_{m3} & \cdots & u_{im}^k a_{m6} \end{pmatrix} \qquad 4.24$$

and

$$1 = (1,\ 1,\ 1,\ 1,\ 1,\ 1) \qquad 4.25$$

$$S^i = (m_{1i},\ m_{2i},\ m_{3i},\ \ldots,\ m_{6i})^T \qquad 4.26$$

The large matrix in Equation 4.23 consisting of known quantities (linear combinations of the observed displacement u_{ij}^k and the geometrical component of the Green's function a_{jr}) described by A^i is known as the coefficient matrix. Generalised matrix inversion may be used to solve Equation 4.23 using m observations from an arbitrary number n of sources having different radiation patterns. The sources must have different radiation patterns because for identical radiation patterns the large matrix described by Equation 4.23 is singular.

4.1.3 Unweighted relative inversion without reference mechanism

On closer inspection of the matrix in Equation 4.23 it is apparent that since A^1 occurs n times within the matrix (located along the diagonal), source 1 plays a dominant role.

The result is that the observed phase amplitudes from source 1 have more weight than those from the other sources and, therefore, the solution will become biased towards the first source. In this situation, source 1 is referred to as the 'reference event'.

When the observed amplitudes all lie within the same noise envelope and are of the same quality with comparable errors, there is no reason to place more weight on any particular source. To overcome this difficulty, Dahm (1996) uses each source as a reference event in turn, placing equal weight on all sources, giving the following final system of equations:

$$\begin{pmatrix} 0 \\ 0 \\ 0 \\ \vdots \\ 0 \\ 0 \\ \\ 0 \\ 0 \\ \vdots \\ 0 \\ 0 \\ \\ 0 \\ \vdots \\ 0 \\ 0 \\ \\ \vdots \\ \\ 0 \\ \\ c \end{pmatrix} = \begin{pmatrix} -A^2 & A^1 & 0 & 0 & \cdots & 0 & 0 \\ -A^3 & 0 & A^1 & 0 & \cdots & 0 & 0 \\ -A^4 & 0 & 0 & A^1 & \cdots & 0 & 0 \\ \vdots & \vdots & \vdots & \vdots & \ddots & \vdots & \vdots \\ -A^{n-1} & 0 & 0 & 0 & \cdots & A^1 & 0 \\ -A^n & 0 & 0 & 0 & \cdots & 0 & A^1 \\ \\ 0 & -A^3 & A^2 & 0 & \cdots & 0 & 0 \\ 0 & -A^4 & 0 & A^2 & \cdots & 0 & 0 \\ \vdots & \vdots & \vdots & \vdots & \ddots & \vdots & \vdots \\ 0 & -A^{n-1} & 0 & 0 & \cdots & A^2 & 0 \\ 0 & -A^n & 0 & 0 & \cdots & 0 & A^2 \\ \\ 0 & 0 & -A^4 & A^3 & \cdots & 0 & 0 \\ \vdots & \vdots & \vdots & \vdots & \ddots & \vdots & \vdots \\ 0 & 0 & -A^{n-1} & 0 & \cdots & A^3 & 0 \\ 0 & 0 & -A^n & 0 & \cdots & 0 & A^3 \\ \\ \vdots & \vdots & \vdots & \vdots & \vdots & \vdots & \vdots \\ \\ 0 & 0 & 0 & 0 & \cdots & -A^n & A^{n-1} \\ \\ 1 & 1 & 1 & 1 & \cdots & 1 & 1 \end{pmatrix} \begin{pmatrix} S^1 \\ S^2 \\ S^3 \\ S^4 \\ S^5 \\ \vdots \\ S^n \end{pmatrix} \qquad 4.27$$

with

$$A^i = \begin{pmatrix} u_{i1}^k a_{11} & u_{i1}^k a_{12} & u_{i1}^k a_{13} & \cdots & u_{i1}^k a_{16} \\ u_{i2}^k a_{21} & u_{i2}^k a_{22} & u_{i2}^k a_{23} & \cdots & u_{i2}^k a_{26} \\ u_{i3}^k a_{31} & u_{i3}^k a_{32} & u_{i3}^k a_{33} & \cdots & u_{i3}^k a_{36} \\ \vdots & \vdots & \vdots & \ddots & \vdots \\ u_{im}^k a_{m1} & u_{im}^k a_{m2} & u_{im}^k a_{m3} & \cdots & u_{im}^k a_{m6} \end{pmatrix} \qquad 4.28$$

and

$$1 = (1,\ 1,\ 1,\ 1,\ 1,\ 1) \qquad 4.29$$

$$S^i = (m_{1i},\ m_{2i},\ m_{3i},\ \ldots,\ m_{6i})^T \qquad 4.30$$

The advantage of Equation 4.27 over Equation 4.23 is that the influence of equally distributed noise on the inversion results is reduced (Dahm, 1996). In the rare case where noise is absent (not in reality, but when using synthetic data), Equation 4.23 and 4.27 will produce the same result.

4.2 SOLVING THE RELATIVE INVERSION PROBLEM

Generalised matrix inversion may be used to solve Equation 4.27 using m observations from n number of sources having different radiation patterns. Before describing the inversion procedures, a comment on the sizes of the coefficient matrix is necessary. The compact notation used in Equation 4.23 and 4.27 to describe the coefficient matrix is deceptive because each A^i quantity represents a smaller $m \times 6$ matrix, i.e. in reality it is a matrix of smaller matrices. The total number of rows and columns of the coefficient matrix will be given by:

$$\begin{aligned} &\text{Total number of rows} \quad = R = \tfrac{1}{2} m \cdot n(n-1) + 1 \\ &\text{Total number of columns} = C = 6n \end{aligned} \qquad 4.31$$

An idea of the size of the coefficient matrix may be obtained by considering an example. For instance, retrieving the moment tensors of ten sources recorded by a network consisting of five triaxial sites (i.e. fifteen observations) will require a coefficient matrix with 676 rows by 60 columns. A cluster of 50 events recorded by the same network will give a 18376 × 300 matrix.

The linear system described by Equation 4.27 is highly overdetermined, i.e. the number of linear equations to be solved simultaneously exceeds the number of unknowns. The degree to which the linear system is overdetermined may be estimated by taking the ratio of the number of equations (given by the number of rows) to the number of unknowns (number of columns). The overdetermination factor is given by:

$$\frac{R}{C} \approx \frac{1}{12} m \cdot (n-1) \qquad 4.32$$

For ten sources recorded by three triaxial sites, the system will be overdetermined by a factor of ~11. For 50 sources recorded by the same network, the system will be overdetermined by a factor of ~61.

In general, there is no exact solution to such an overdetermined system of equations. The least-squares criterion is used in situations such as this one, where there is much more data available than parameters to be solved for. Least-squares may be regarded as an averaging process that smoothes the data. For ease of reference, Equation 4.27 can be written in matrix notation as:

$$\mathbf{y} = \mathbf{B}\mathbf{x} \qquad 4.33$$

where $\mathbf{y}$ is a vector of dimension R (number of observations), $\mathbf{x}$ is a vector of dimension C (number of unknowns, i.e. the moment tensor components or the model parameters), and $\mathbf{B}$ is the $R \times C$ coefficient matrix. For an overdetermined system, $R > C$. Equation 4.31 can be used to compute the values of R and C.

Applying the method of least-squares, the moment tensor components contained in $\mathbf{x}$ can then be determined from:

$$\mathbf{x} = [\mathbf{B}^T\mathbf{B}]^{-1}\mathbf{B}^T\mathbf{y} \qquad 4.34$$

where $[\mathbf{B}^T\mathbf{B}]^{-1}\mathbf{B}^T = \mathbf{B}^G$ is the generalised inverse of $\mathbf{B}$ (strictly speaking, $\mathbf{B}^G$ is the least-squares inverse because $\mathbf{B}^T\mathbf{B}$ is symmetric and has real, positive eigenvalues). Since the method of least-squares is a standard procedure, the method is not outlined here, but in Appendix C.

Two different approaches are used in this study to solve Equation 4.34 for the moment tensor components in $\mathbf{x}$: singular value decomposition (Appendix D) and Gaussian elimination (Appendix E). Computer subroutines to perform singular value decomposition and Gaussian elimination (amongst many other numerical procedures) are available in most numerical libraries (e.g. Numerical Recipes by Press *et. al.*, 1990).

4.3 ERROR ESTIMATION

An important aspect of any inversion is evaluating the significance of the inverse. The computation and analysis of errors or residuals is a field on its own, and a detailed analysis is considered to be beyond the scope of this study. Even though two different solution procedures are used to solve the inverse problem, in this study, only one approach is taken in the error analysis. Since error estimates are readily obtained from the singular value decomposition technique, these techniques are briefly summarised.

4.3.1 SVD and estimates of error

The condition number $\mathcal{K}$ of a matrix provides an estimate of the relative error in the solution (Buland, 1976). The higher the number, the lower the probability that a solution of the system of equations will lead to satisfactory results. Generally, the condition number $\mathcal{K}(\mathbf{B})$ of a square matrix $\mathbf{B}$ is defined as:

$$\mathcal{K}(\mathbf{B}) = \frac{\lambda^2_{max}}{\lambda^2_{min}} \qquad 4.35$$

where λ_{max} and λ_{min} are the maximum and minimum eigenvalues, respectively.

However, a significant reduction in the condition number can be achieved by application of the SVD technique (Gibowicz & Kijko, 1994). In this case $\mathcal{K}(\mathbf{B})$ of matrix **B** is defined as:

$$\mathcal{K}(\mathbf{B}) = \frac{\lambda_{max}}{\lambda_{min}} \qquad 4.36$$

The model derived from Equation D.9 (Appendix D) can be written as:

$$\mathbf{x}_q = \mathbf{B}_q^{-G}\mathbf{y} \qquad 4.37$$

where the model space $\mathbf{x}_q$ is spanned by q nonzero eigenvectors. Two further matrices can be defined: the resolution matrix **R**, and the information density matrix **D**, where:

$$\mathbf{R} = \mathbf{V}_q\mathbf{V}_q^{T} \qquad 4.38$$

$$\mathbf{D} = \mathbf{U}_q\mathbf{U}_q^{T} \qquad 4.39$$

The columns of the resolution matrix indicate how much the true model is 'smeared' into the various parameters of the inversion model. Ideally, **R** would be a diagonal matrix, allowing the recovery of the full model. If all the model parameters are associated with nonzero eigenvalues, then **R** is an identity matrix, and there is perfect resolution. Calculation of the resolution matrix is essential in assessing the inversion result. The information density matrix **D** is used to determine how important each observation is in constraining the solution.

4.4 RMTI Program Overview

The author has written a computer program, RMTI, to perform the relative moment tensor inversion described in theory by Dahm (1996) and to compute radiation patterns from the moment tensors. The program has been written in Fortran (Microsoft Fortran Powerstation v4.0) and utilises several routines from Numerical Recipes (a program library which accompanies the Fortran installation disk).

4.4.1 Program structure

The structure of RMTI is modular, containing functions and subroutines, written using a top-down design technique. The program consists of three main steps, illustrated by the flowchart in Figure 4.2. The first step involves a number of preliminary calculations during which the input to the coefficient matrix of Equation 4.27 is computed. RMTI reads two data files containing the network information, and phase amplitudes (for the P, SH and SV-phases of waveforms recorded by all geophone sites in the network). More detail regarding the creation of the input data file containing the phase amplitudes will be given towards the end of this section. Examples of the input files are given in Appendix F.1.

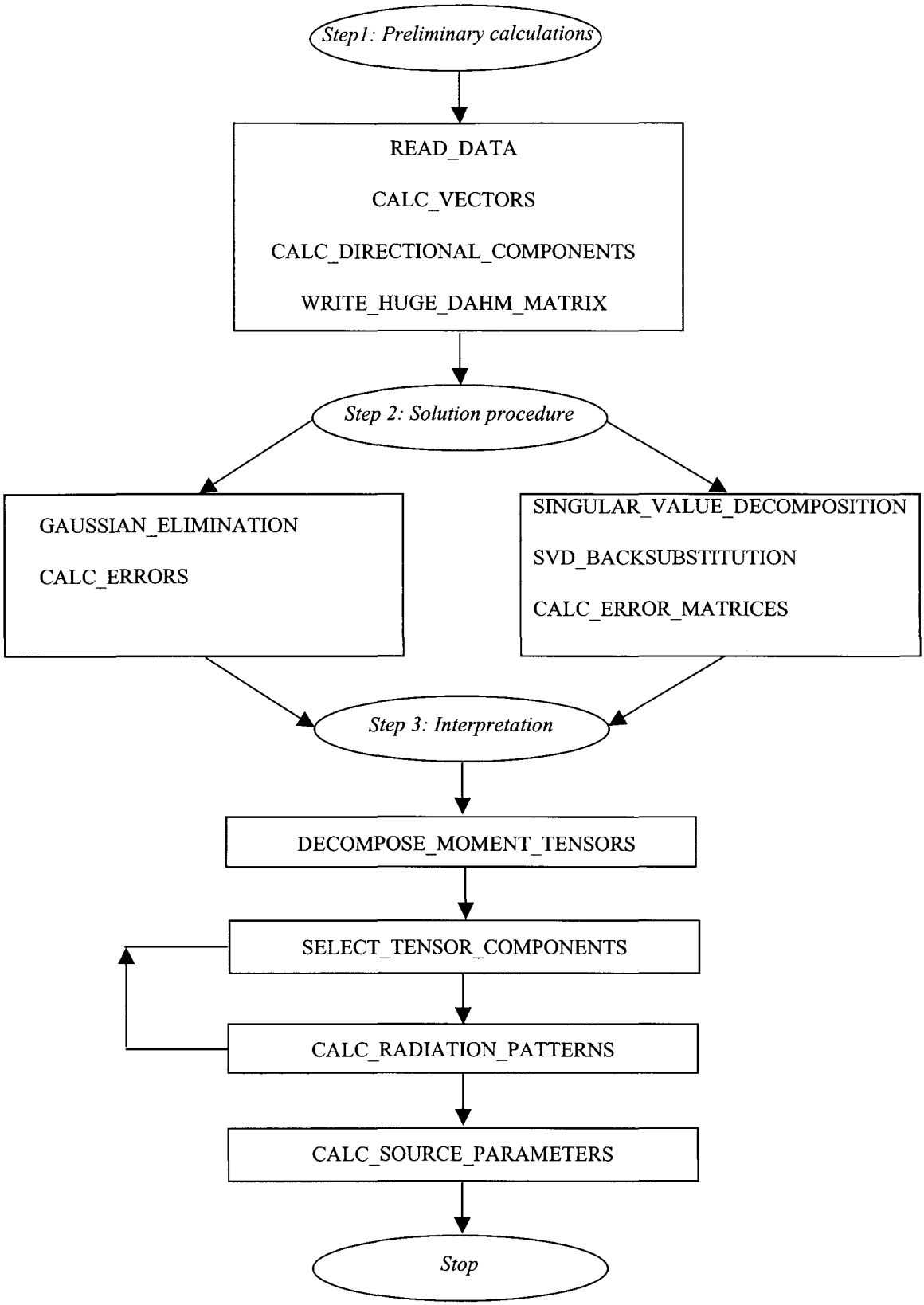

Figure 4.2: Flowchart illustrating the main computational steps (subroutines) in RMTI. Subroutines are written in capital letters. Conceptual steps are written using italics.

In the second step, Equation 4.27 is solved for the moment tensor matrix through a process of mathematical inversion, using either singular value decomposition (from Numerical Recipes, Press *et al.*, 1990) or Gaussian elimination techniques (solution procedure written in Pascal by Linzer (1998) and converted to Fortran by the author). Selection of solution procedure depends on the requirements of the user. The two solution procedures are compared with respect to memory requirements and speed of execution in Appendix H. The two solution procedures give rise to nearly identical results having relative errors of less than 1% (Table H.3). The differences lie in their computation speed and the subsequent error analysis. As illustrated in Table H.4, the Gaussian elimination solution process is far superior to the singular value decomposition with regard to solution time. In addition, this procedure can invert up to 60 events, whereas the singular value decomposition is not capable of processing beyond 30 events (this is for a relatively small network consisting of 3 triaxial geophones).

The third step is to facilitate interpretation of the quantities (the six components of the moment tensor) computed in the previous step. Two approaches are taken to facilitate interpretation. Firstly, a visual approach is taken, in which radiation patterns of various selected moment tensor components are plotted. The user has the option (during runtime) to select the moment tensor components from which radiation patterns for each event are to be calculated where:

Option 1: Deviatoric and isotropic components (i.e. full tensor)
2: Strike-slip components
3: Dip-slip components
4: Strike-slip and dip-slip components
5: CLVD
6: Deviatoric components
7: Isotropic

Separating the moment tensor into simple source parameters may enhance interpretation. For example, it is easier to fit a fault plane solution to the radiation pattern plotted from the deviatoric components, or strike-slip and dip-slip components, than to the full moment tensor. This facility also allows the user to visually observe the contribution of each component to the full moment tensor, and gives insight into the seismic source mechanism.

Using the selected moment tensor components, the P-wave polarities (for every 5°) are computed over the surface of a sphere enclosing the source event. The output files are written in the format (Appendix F.2) required by a commercial stereonet program, STEREO version 2.0 (part of RockWare Inc.). Once the files for a selected moment tensor component for all the events in the source cluster have been generated, the user has the option to select other components from which radiation patterns may be generated. An example of the radiation patterns produced by each of these components is given in Figure 4.3. Note that since RMTI only writes the take-off angle and azimuth of the P-wave compressional motion to a data file, fault-plane solutions must be determined manually. The procedure applied during this phase of the work is outlined in Appendix G.

The second approach in interpreting the output moment tensors is to determine various source parameters to quantify the contributions of each component (double-couple component, isotropic component etc.) to the moment tensor solution. The relevant equations are given in the following section.

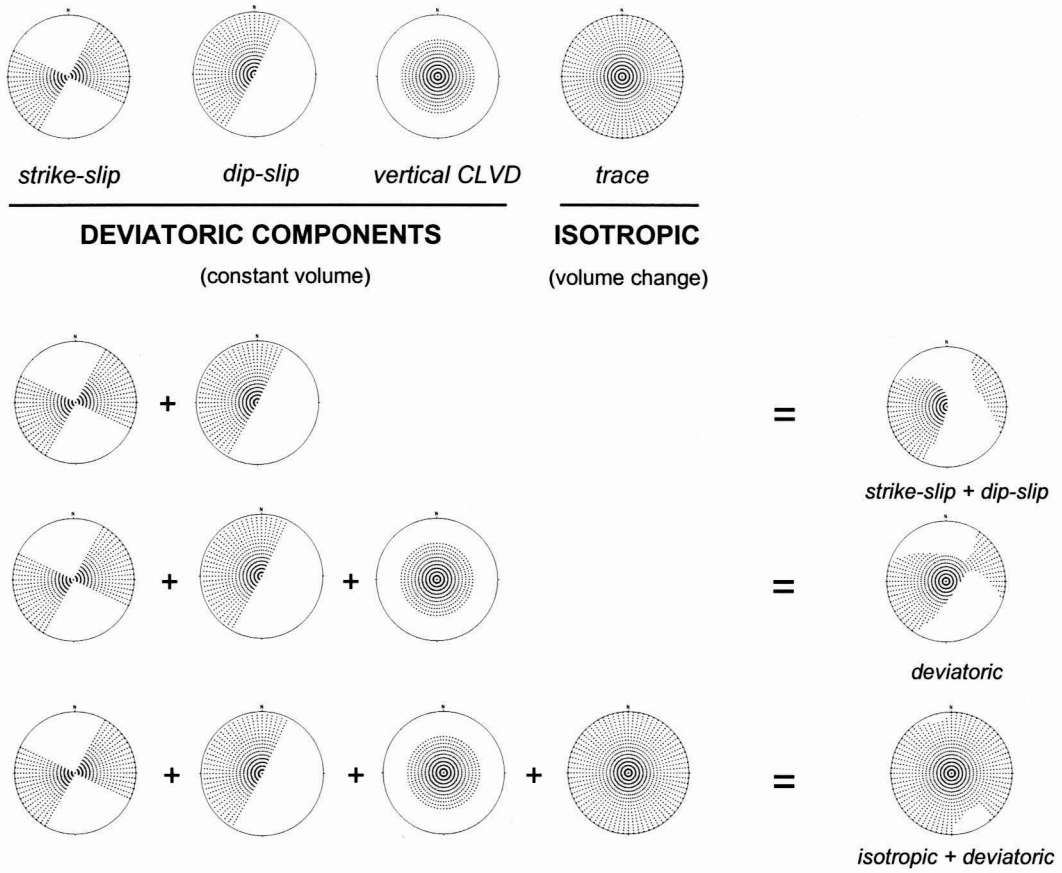

Figure 4.3: P-wave radiation patterns for source parameters defined by Dahm (1996). Shaded areas (++) denote compressional arrivals. Lower hemisphere equal-area projection.

4.4.2 Equations implemented in program

The relative inversion without a reference mechanism coded for this preliminary study follow the formulation given in Equation 4.27 with some modifications.

The azimuth and take-off angles for each event raypath (i.e. the vector which may be drawn from the seismic source hypocentre to the geophone observation site) are computed from the geophone positions and event locations. The azimuth is measured in a clockwise direction from North, and the take-off angle is defined as the angle between the vertical (z-axis) and the raypath (Figure 4.1). Straight raypaths from the source to receiver are assumed since the inversion program is applied to the data recorded by a microseismic network. The angles are computed using simple rules of

trigonometry. For larger networks, a velocity model (variation in velocity with depth) would be necessary to compute the azimuth and take-off angle that would result from a curved raypath.

Using the azimuth and take-off angle the directional components for each phase are computed using Equations 4.9 – 4.11, after which the elements of the A^i sub-matrices (Equation 4.28) are determined.

At this stage in the research, two modifications to the formulation of the relative inversion (Equation 4.27) are applied. The first modification involves the arbitrary constant, *c,* in Equation 4.22. Initially, this constant was set equal to unity. In the later stages of the development of RMTI, c was set equal to the number of events, i.e. $c = nev$. This allows the relative moment tensor output for one cluster with a particular number of events recorded on a particular number of channels to be compared with the moment tensors computed for another cluster, comprised of a different number of events and recorded using different numbers of channels. The second modification involves the magnitudes of the input phase amplitude data. If the events in the cluster are not of comparable magnitudes, there is a danger of the larger events dominating the solution. To prevent this, the phase amplitudes of each event are normalised to the maximum phase amplitude (in the absolute sense) for that event.

The output of RMTI gives the six moment tensor components as defined by Equation 4.12. The Cartesian moment tensor for each event is computed using Equation 4.13.

To compute the radiation pattern corresponding to a particular event, the moment tensor components and directional components are used in a forward calculation (Equation 4.8) to calculate the polarity of the displacement (of the P-, SH- or SV-phase) at a particular point on a sphere surrounding the source event. In this calculation, I_j^k is set equal to 1 since only the polarity is required to plot the corresponding radiation pattern.

To decompose the moment tensor into a number of source parameters, the moment tensor is diagonalised and its corresponding eigenvalues are determined. From the eigenvalues, the following source parameters are calculated, *viz.* relative strength (Equation 4.40), deviation of the moment tensor from a double couple source model (Equation 2.43), and the isotropic component (Equation 2.44).

The relative strength *MO%* between two sources (1) and (2) expressed by Dahm (1996) as a percentage is:

$$MO\% = \frac{M_T^{(2)}}{M_T^{(1)}} \cdot 100 \quad per\ cent \qquad 4.40$$

where

$$M_T = \sqrt{\sum_{p,q} M_{pq}^o M_{pq}^o / 2} \qquad 4.41$$

If singular value decomposition has been used to solve the system of equations, the following quantities are calculated. The condition number $\mathcal{K}$ of the system of

equations is computed using Equation 4.36. The resolution matrix **R**, and the information density matrix **D**, are computed using Equations 4.38 and 4.39, respectively.

In theory, the resolution matrix and information density matrix are easy to calculate since the **U** and **V** matrices are by-products of the singular value decomposition process. However, computation of these matrices, in particular the information density matrix **D**, is computationally expensive for overdetermined systems such as the one described by Dahm (1996). In addition, **D** is impractical to use. Conventionally, each entry in **D** is used to assess how important each observation is in constraining the solution. This approach is useful for small systems of equations, but ceases to be so for the highly overdetermined system described by Equation 4.27. This point is illustrated by the following example.

Consider applying the relative inversion technique to five events recorded by a network consisting of three triaxial sites. If three phases are used (P, SH and SV-phases) the coefficient matrix will consist of 91 rows by 30 columns. The resolution matrix **R** will have dimensions of 30 rows by 30 columns. The information density matrix **D** will also be square, having dimensions of 91 rows by 91 columns – a total of 8 281 elements.

$\mathbf{U}^T$ and **D** (generated from recorded data) are represented in a qualitative fashion in Figure 4.4. In this figure, the dark and light shades indicate high and low entries in the **D** matrix, receptively. The high values (dark shades) are important in constraining the solution, and *vice versa*. It is evident that analysis of each one of these elements by studying its magnitude and then comparing it with the relevant observation is neither convenient nor practical.

(a)

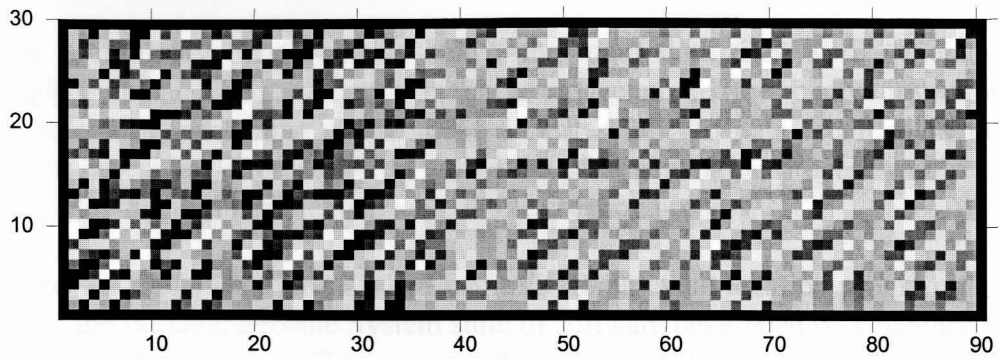

(b)

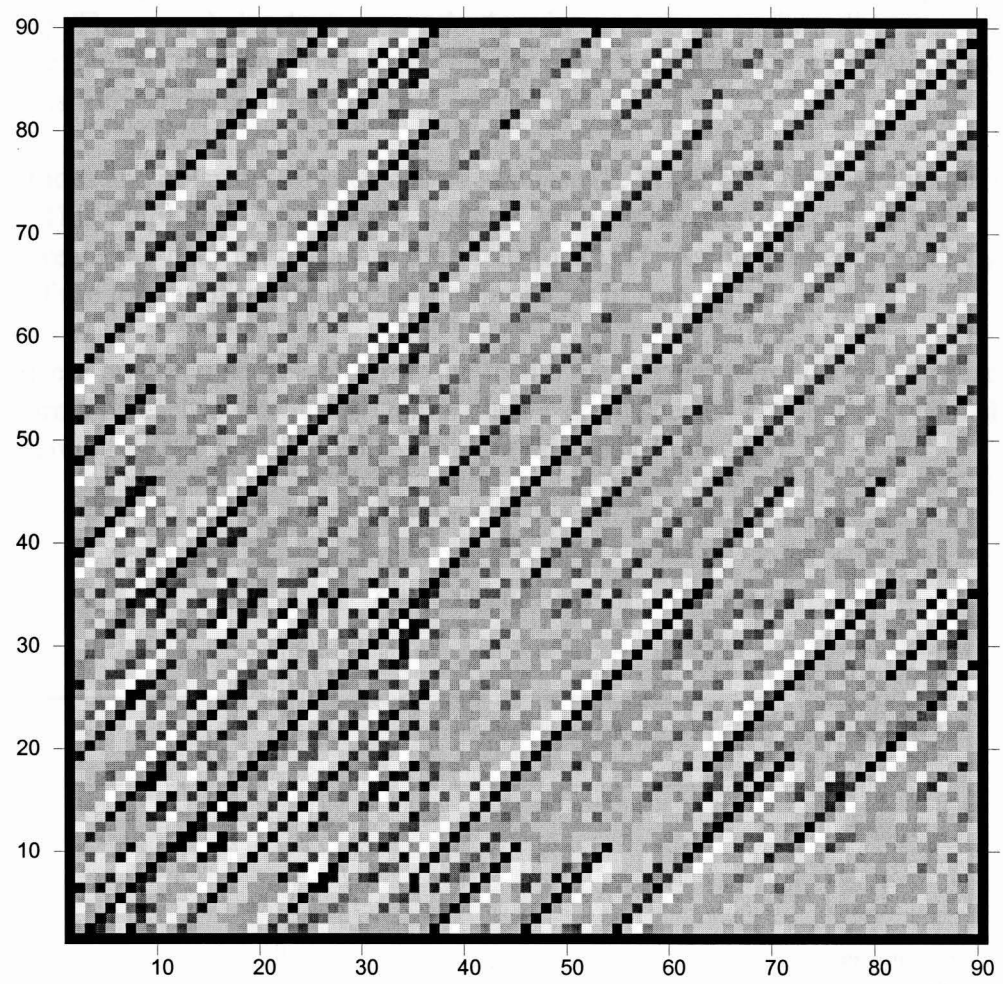

Figure 4.4: Qualitative representation of (a) matrix $\mathbf{U}^T$ *and (b) the information density matrix* **D** *computed using a cluster of five events recorded by three triaxial sites. Black = 0.997, and white = - 0.642 in this example.*

4.4.3 Input data file generation

During the preliminary phase of this study, the input data files were generated painstakingly by hand. The reasoning was that if the technique (the relative inversion without a reference mechanism) were applied successfully to data recorded in the mining environment, an effort to speed up the data file generation process would be made. The following outlines the manual data file creation process.

The recorded waveforms are first located using LOC, an event location program that forms part of the Portable Seismic System suite of software developed by Chamber of Mines Research Organisation. This requires the user to pick arrival times of the P and/or S-wave. The waveforms recorded at each triaxial geophone site are then rotated into a coordinate system, which allows the identification of the P, SH and SV-phases (Figure 4.5). The recorded velocity trace is then integrated to obtain a displacement trace. Figure 4.6 shows a time-integrated velocity trace. The integration operation acts as a low-pass filter and smoothes the data.

The amplitudes and polarities of each observed phase (P, SH or SV) for each event are measured. This amplitude information, together with the event locations, is used to manually create the data files that are the input to RMTI. As mentioned previously, examples of the format of the input data files is shown in Appendix F.1.

To minimise a potential source of error due to the inadvertent introduction of noise, the waveforms of each event in the source cluster are inspected channel by channel, and those having a poor signal-to-noise ratio are rejected (Figure 4.7).

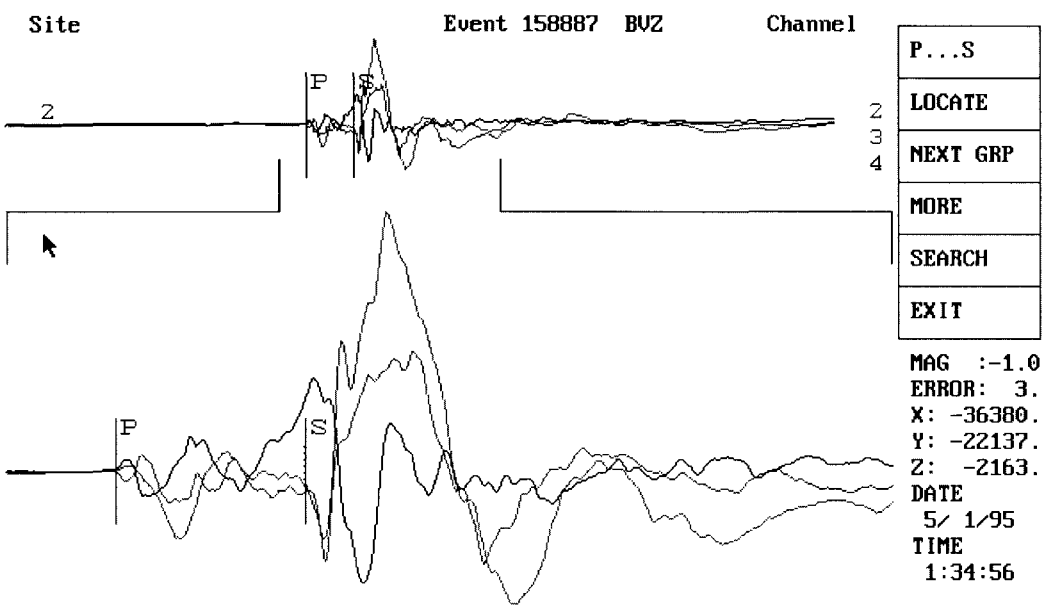

Figure 4.5: Screendump from LOC of a typical waveform recorded on three channels of a triaxial geophone site. Displacement trace (time-integrated velocity trace).

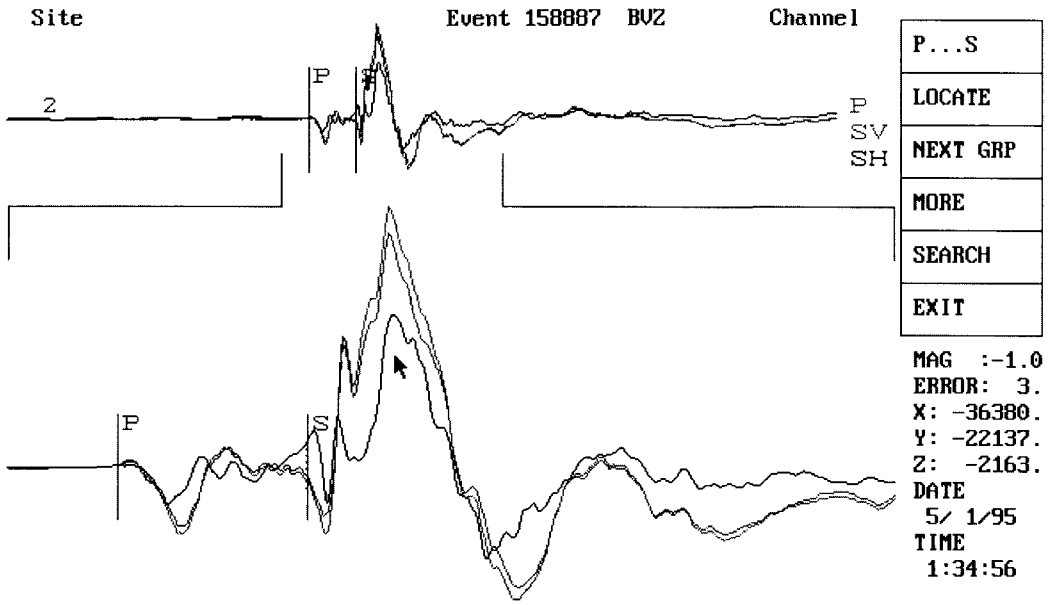

Figure 4.6: Screendump from LOC of the waveform rotated into P, SH and SV components. Displacement trace (time-integrated velocity trace).

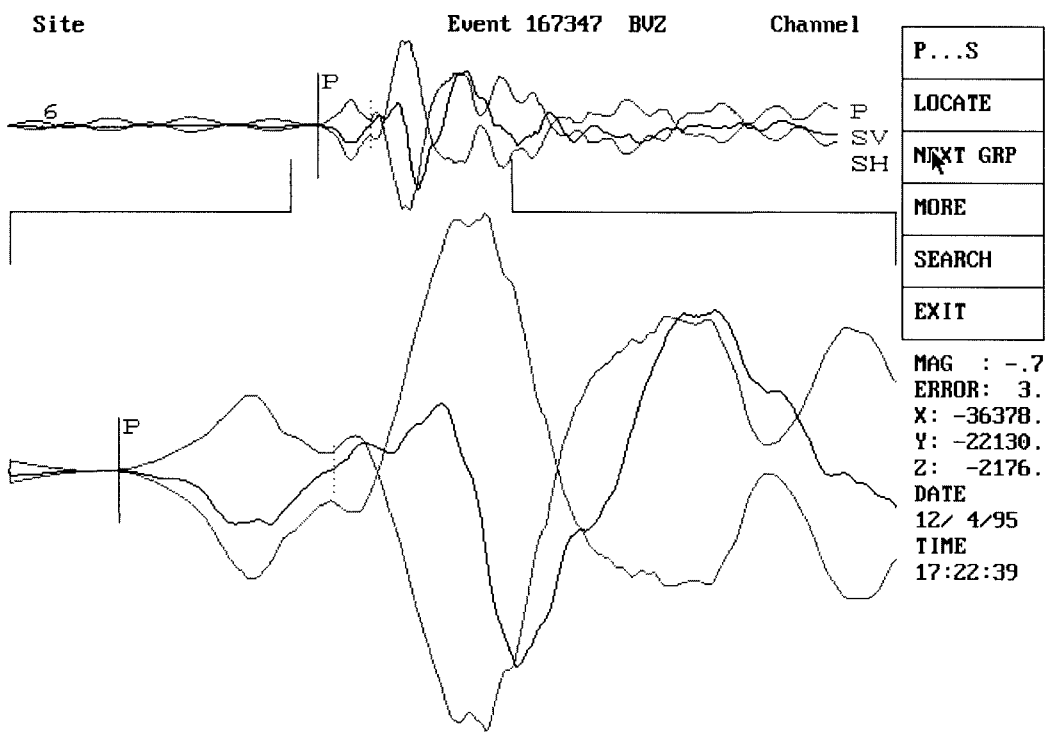

Figure 4.7: Example of a waveform with a low signal-to-noise ratio. Displacement trace (time-integrated velocity trace).

Chapter 5

RMTI STABILITY TESTS

Before applying the relative inversion program (RMTI) to a case study situation, several stability tests are carried out to determine the limitations of the relative inversion technique described by Dahm (1996) and possible sources of error. The tests are not strictly 'tests' in the rigorous sense, but are better described as observations of the behaviour of the relative inversion (and resultant output moment tensor components) under particular conditions. In another sense, these tests are an optimisation exercise to determine which input situations give rise to stable results.

In contrast to Dahm's synthetic tests, these observations were obtained using seismic data recorded in the mining environment. The seismic waveforms used in these tests were recorded by the Portable Seismic System (PSS) developed by the Chamber of Mines Research Organisation, now the CSIR Division of Mining Technology. The data used in these tests form a subset of a larger data set, on which the case study is based (Appendix J). Since the stability and consistency of the results form the focus of this chapter, the details of the seismic network are not described here, but in Appendix J.

In the thesis thus far, the chapters and sections have been documented in chronological order. Section 5.5 does not follow this order, but is appended to Chapter 5 because the results of the tests have a pivotal role in determining the direction of the research that follows. The results shown in Section 5.5 are computed using the latest version of the moment tensor inversion software (described in Chapter 6) written by the author – this explains the differing appearance of the radiation patterns and associated fault-plane solutions. Another aspect to bear in mind is that the tests in Section 5.5 are performed using synthetic data, in contrast to the previous tests (Sections 5.1 to 5.4) that use recorded data.

5.1 RELATIVE INVERSION VS FORWARD CALCULATION

This test was designed to compare the moment tensors obtained through the relative inversion of measured displacement data to those calculated from synthetic data. The flowchart of Figure 5.1 illustrates the three-step process schematically.

5.1.1 Method

1. In the first step, the relative inversion, as formulated by Equation 4.27 is applied to displacement data $u^{k}_{ij(DATA)}$ (measured from the seismograms for each phase observation j) to obtain the full moment tensor $m_{ri(DATA)}$ for each event i.

2. The output moment tensor components $m_{ri(DATA)}$ for each event i are then used in a forward calculation (Equation 4.8) to calculate synthetic amplitudes $u^k_{ij(SYN)}$ for each phase j.
3. In the final step, the synthetic phase amplitudes $u^k_{ij(SYN)}$ are used as input to the relative inversion (Equation 4.27) to obtain a 'synthetic' moment tensor $m_{ri(SYN)}$ for each event i.

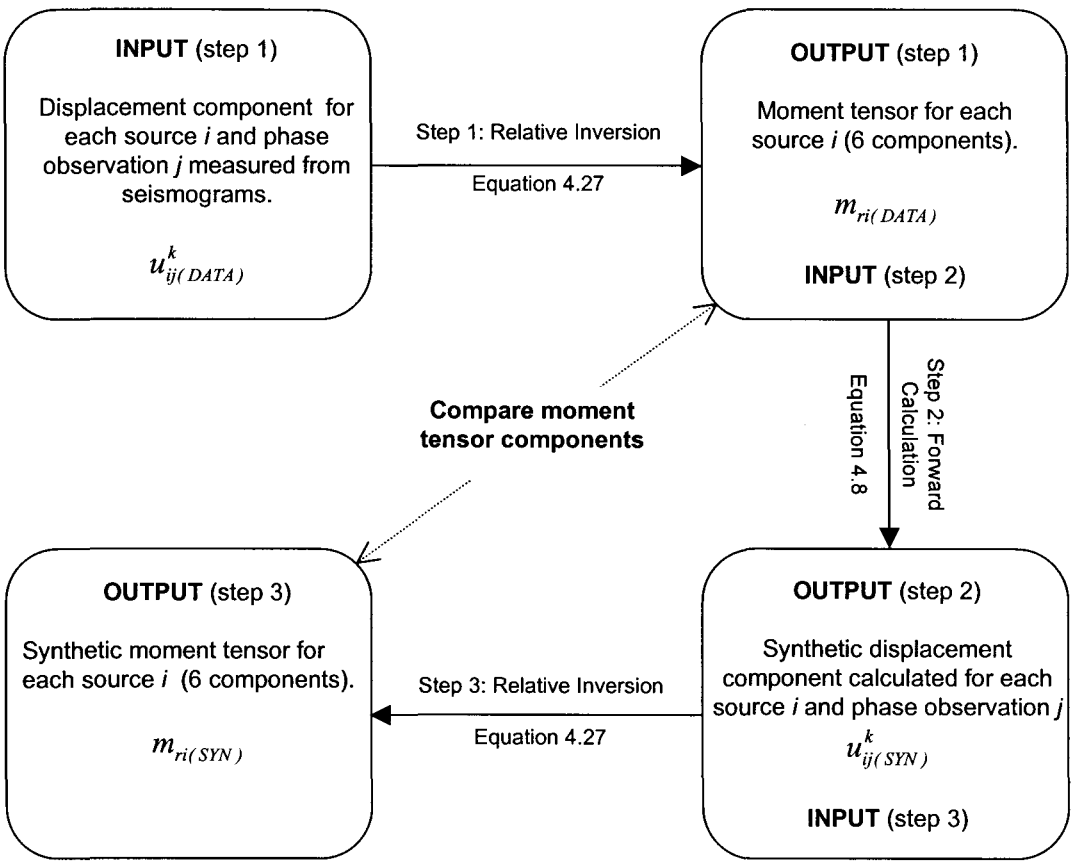

Figure 5.1: Flowchart representing computation sequence.

5.1.2 Results and discussion

The 'synthetic' moment tensor components are plotted against those determined using recorded data (Figure 5.2). Note that the Cartesian moment tensor components represented by a capital '*M*' are discussed in this section (not to be confused with Dahm's components, '*m*'). The graphs show clearly that a strong linear relationship exists between the synthetic moment tensor and the data moment tensor for components in the *xy* plane *viz.* M_{11}, M_{22} and M_{12}. The relationship is not as clear for components M_{13} and M_{23}, and breaks down completely for the M_{33} component, as is evident from the large degree of scatter in the results.

The seismic network in this example has a planar configuration with all recording sites being located in the *xy* plane. As a result, there is incomplete coverage/sampling over the focal sphere. The M_{33} component is oriented perpendicular to the network in the *z*-direction. The variation/error shown by this component is thought to be in consequence to the planar network configuration and inadequate sampling of the radiation pattern.

5.1.3 Conclusions

The moment tensor components oriented perpendicular to the *xy* plane are more susceptible to error/variation than those which lie within the plane of the network. A possible cause could be the planar network configuration and poor sampling of the radiation pattern perpendicular to the plane of the network.

The relationship between the synthetic and computed moment tensor components can be used as a qualitative measure of error. This technique is applied in the following test.

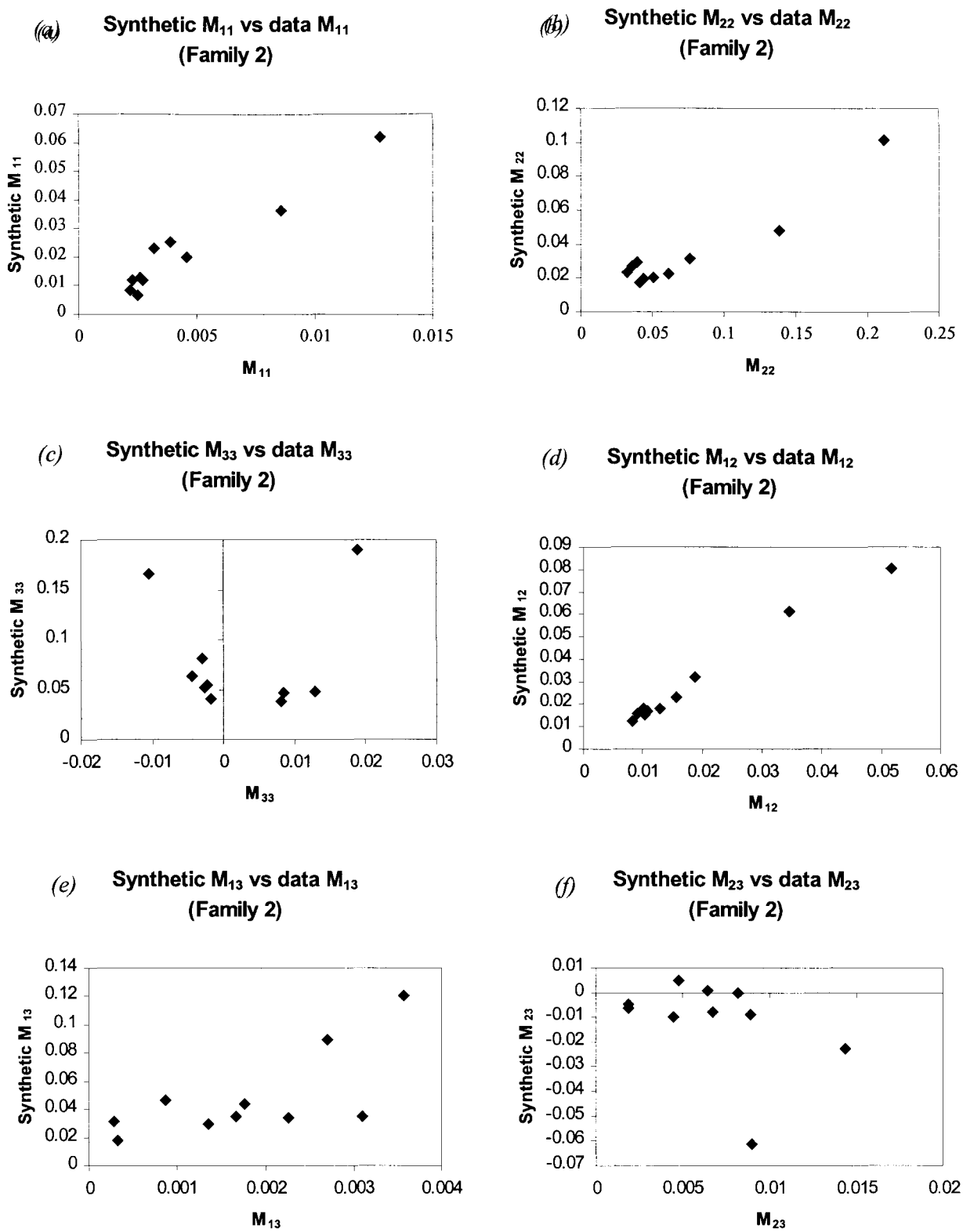

Figure 5.2: Comparison of moment tensor components calculated from measured and synthetic data. (a), (b) and (d) show a directly proportional relationship for the components in the x y plane (plane of the seismic network). A less obvious, but similar relationship exists in (e) and (f). This does not hold for (c).

5.2 SOURCE CLUSTER POSITION

Dahm (1996) specifies that the relative method is only applicable to seismic sources from clusters, provided the spacing between the sources does not exceed the dominant wavelength of the phases used. This test goes one step further, and investigates the effect of the position of the cluster relative to the plane of the seismic network on the output moment tensor components.

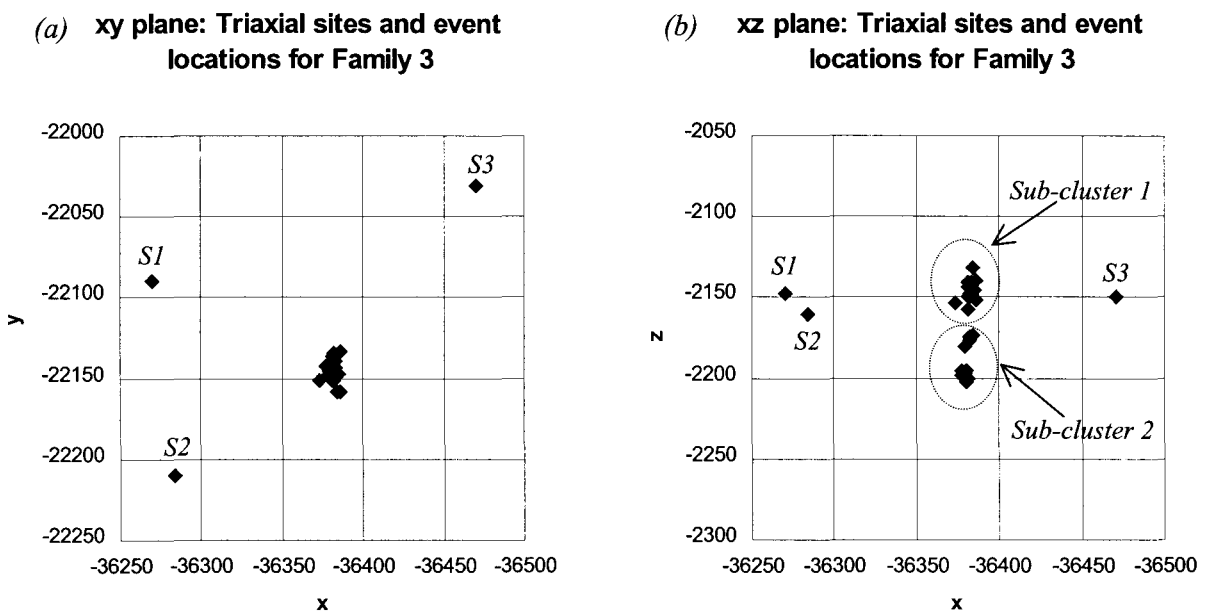

Figure 5.3: Seismic network layout and event locations in the (a) xy and (b) xz plane. Triaxial geophone sites are labelled S1, S2 and S3. Solid symbols represent the position of each event in the source cluster.

5.2.1 Method

1. The relative moment tensor inversion is performed on a cluster of events which are tightly clustered in the *xy* plane (the plane of the seismic network, Figure 5.3a), but have a spread of ~75 m in the *z*-direction (perpendicular to the plane of the network, Figure 5.3b). Using the approach described in section 5.2, the moment tensors computed from the observed displacements are compared with those computed from synthetic data. In addition, radiation patterns for the strike-slip and dip-slip components are plotted.

2. The source cluster is then divided into two sub-clusters. Sub-cluster 1 lies within the plane of the network, and sub-cluster 2 lies below (Figure 5.3b). The relative inversion was applied to each sub-cluster separately. Radiation patterns for the strike-slip and dip-slip components are plotted for each sub-cluster.

5.2.2 Results and discussion

The graphs of synthetic moment tensors *versus* those computed from observations are given in Figure 5.4. Note that the inversion was performed on all events in the source cluster. On each graph, two trends may be observed. Each trend correlates with a particular sub-cluster, and is therefore represented by a particular symbol (sub-cluster 1 = solid symbols, sub-cluster 2 = open symbols). Sub-cluster 1 exhibits a clearly linear relationship for moment tensor components M_{11}, M_{12}, M_{22} and M_{23}. In contrast, the graphs for all components of the events in sub-cluster 2 are scattered.

The radiation patterns for the strike-slip and dip-slip components of the source cluster are shown in Figures 5.6 and 5.7. The strike-slip radiation patterns are constant for all events in the source cluster (Figure 5.6), whereas there is some variation in the dip-slip components (Figure 5.7). Two dip-slip radiation pattern groups can be recognised, each of which corresponds to a particular sub-cluster.

The graphs of synthetic moment tensors *versus* those computed from observations of sub-cluster 1 are given in Figure 5.5. Note that the relative inversion was performed on each sub-cluster separately. The graphs show a directly proportional relationship for components M_{11}, M_{12}, M_{22} and M_{23}, similar to those plotted for sub-cluster 1 in Figure 5.4, but showing a general decrease in the error.

The radiation patterns for each sub-cluster are shown in Figures 5.8 and 5.9. The strike-slip and dip-slip radiation patterns are more or less consistent within each sub-cluster.

5.2.3 Conclusions

The graphs of synthetic tensor *versus* data tensor may be used as a qualitative measure of error. When all events in the source cluster are used in one relative inversion, sub-cluster 1 shows less variation/error in the moment tensor components (linear relationship) than sub-cluster 2. It appears that sub-cluster 2 is subject to greater error than sub-cluster 1, possibly as a result of being located approximately 30 m below the plane of the seismic network. However, since each event is used in turn as a reference event during the inversion, sub-cluster 2 introduces errors into sub-cluster 1.

When two separate relative inversions are performed, the error in the moment tensor components decreases for sub-cluster 1, but shows little improvement for sub-cluster 2. The decreased error is a result of the smaller source separations and improved common ray path assumption for the cluster within the network. In the case of sub-cluster 2, the improvement in the common ray path assumption is counteracted by the increased error introduced by the increased distance of the sub-cluster from the network. In general the strike-slip radiation patterns show less variation than the dip-slip patterns, probably because they are subject to smaller error.

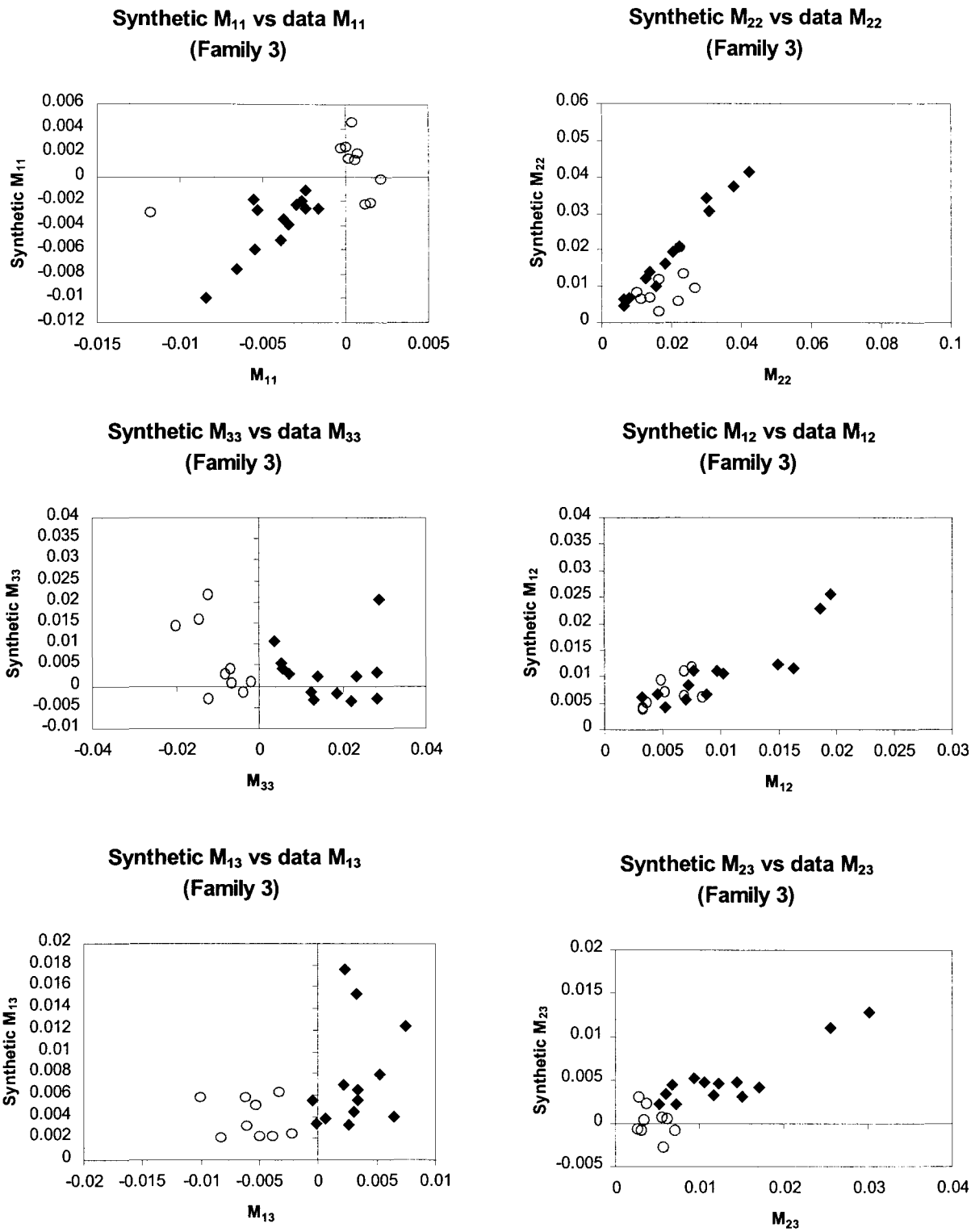

Figure 5.4: Results of relative inversion of source cluster. Synthetic moment tensor components are plotted versus those computed from observed amplitudes. Solid diamonds represent sub-cluster 1, open circles represent sub-cluster 2.

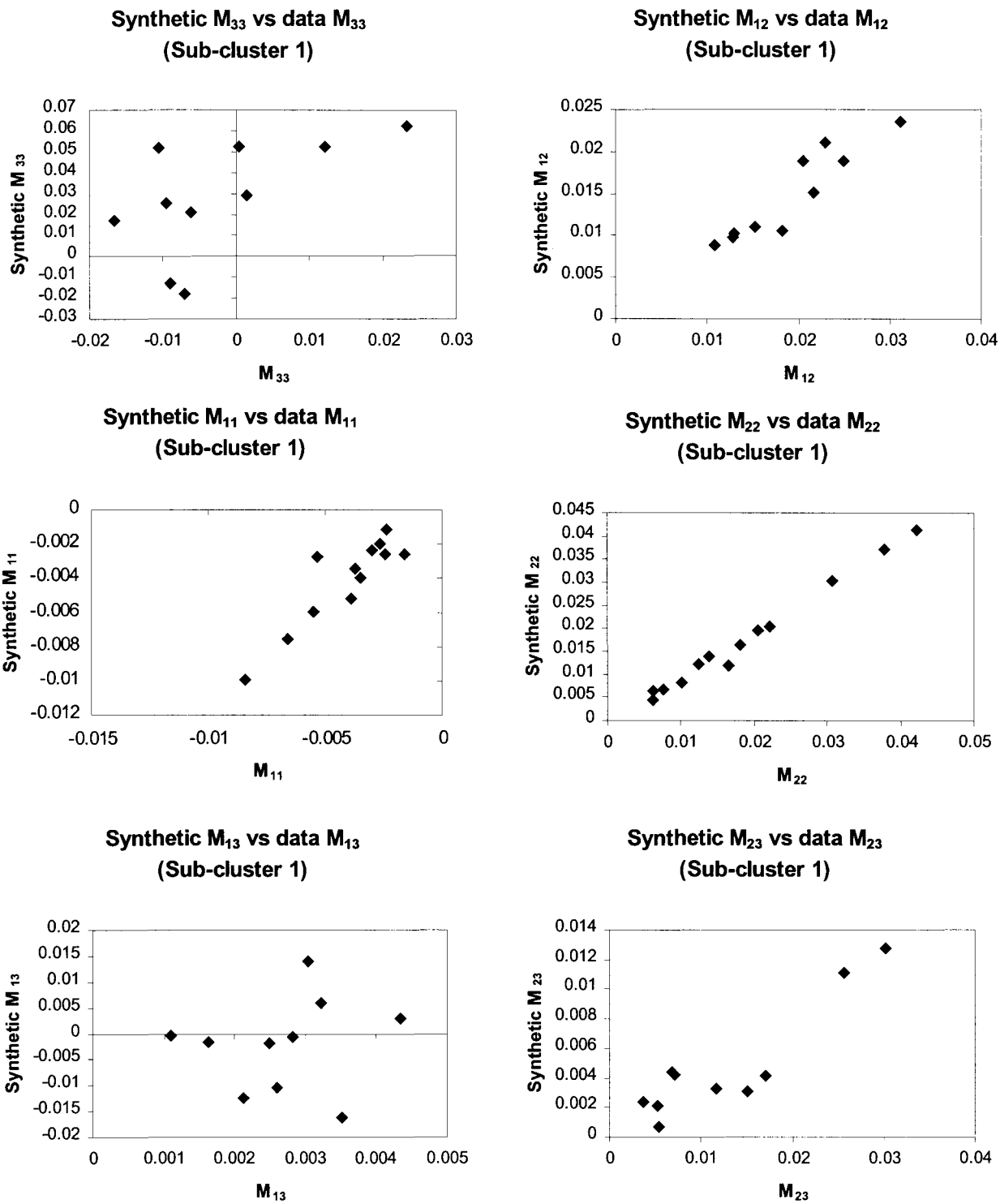

Figure 5.5: Results of relative inversion of sub-cluster 1. Synthetic moment tensor components are plotted versus those computed from observed amplitudes.

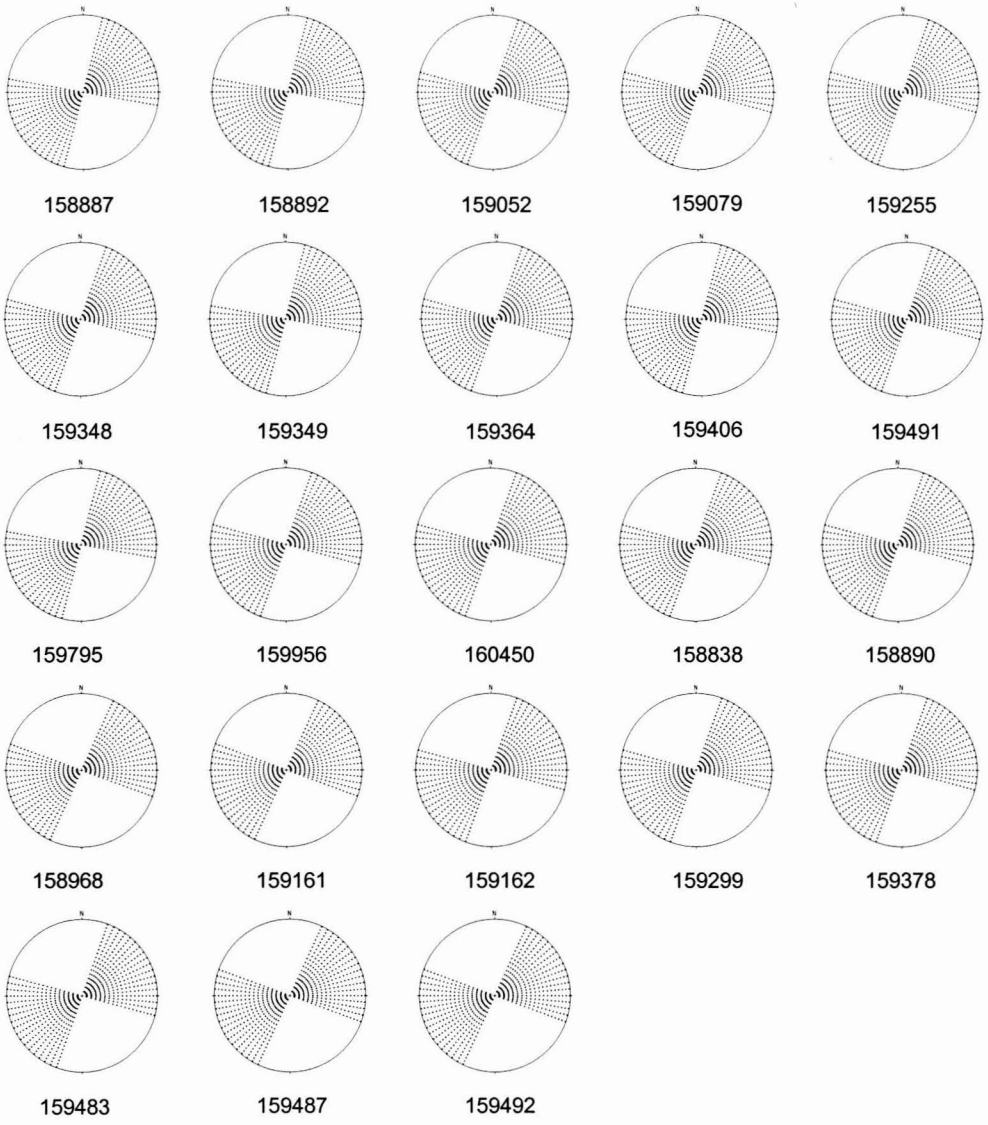

Figure 5.6: Radiation patterns computed for the strike-slip moment tensor components resulting from the relative inversion of all 23 events in the source cluster. Event numbers are given below each pattern.

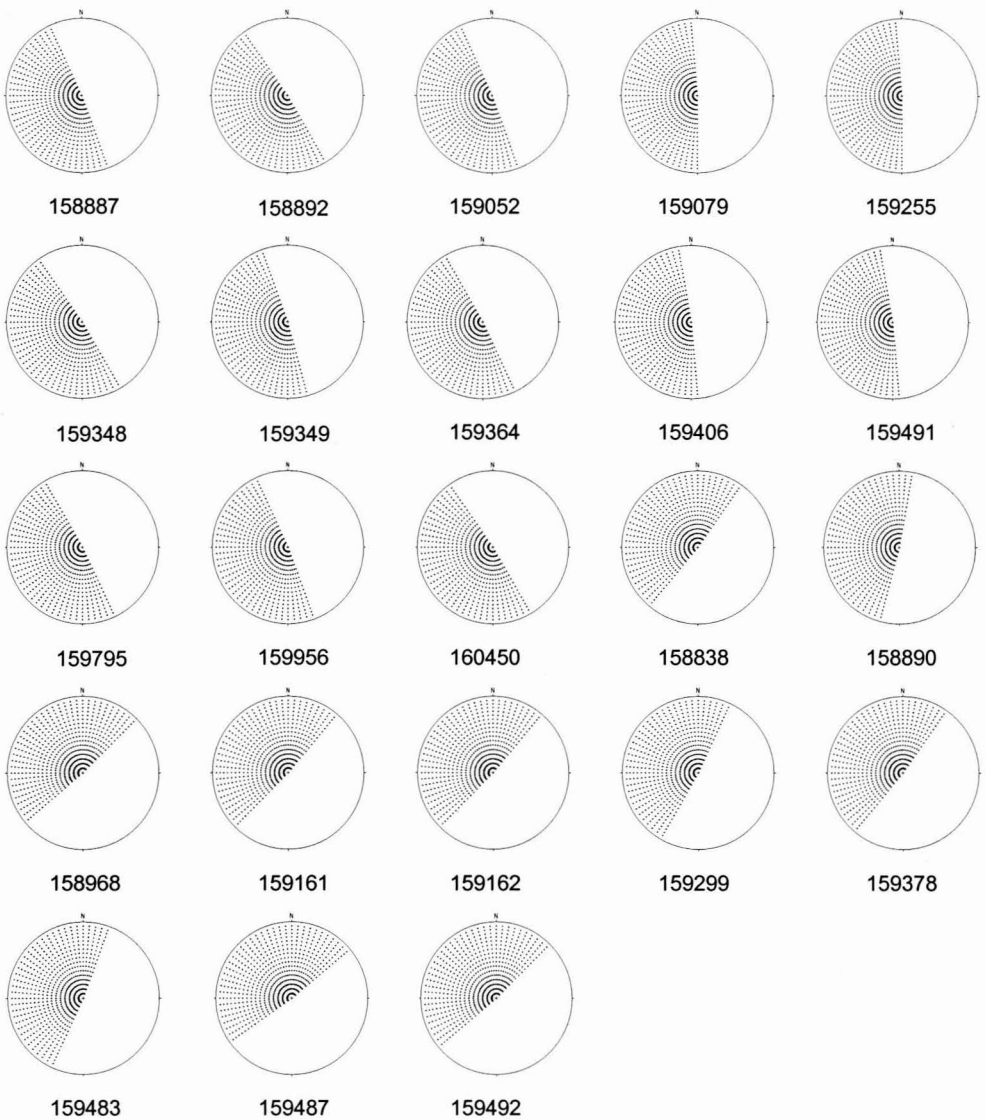

Figure 5.7: Radiation patterns computed for the dip-slip moment tensor components resulting from the relative inversion of all 23 events in the source cluster. Note the change in strike from NNW (first 13 events) to NNE (last 10 events). Event numbers are given below each pattern.

Sub-cluster 1

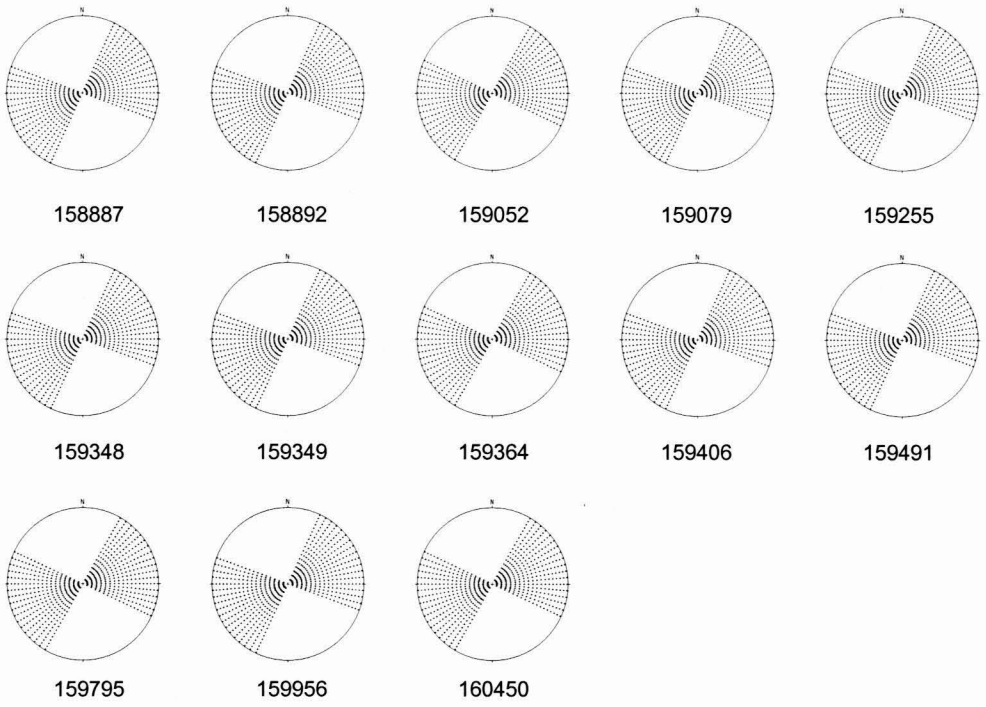

Sub-cluster 2

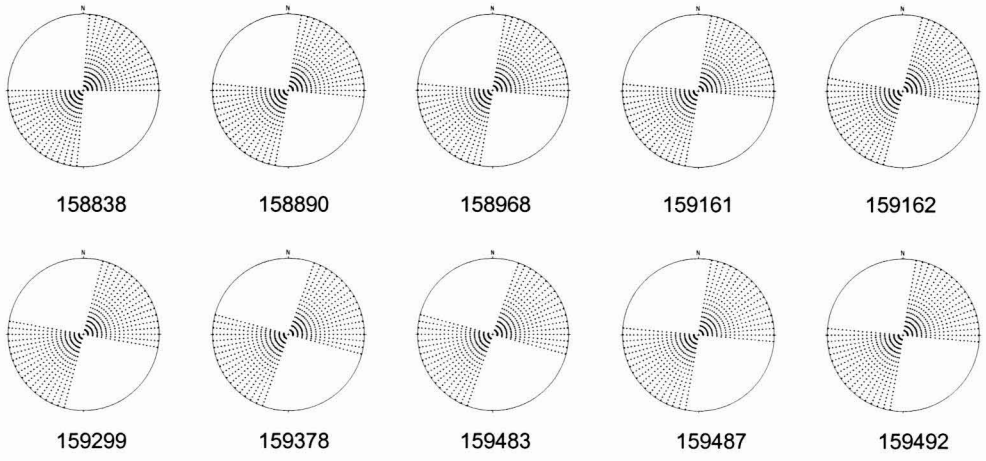

Figure 5.8: Radiation patterns computed for the strike-slip moment tensor components resulting from the relative inversion of sub-cluster 1 (13 events) and sub-cluster 2 (10 events). Event numbers are given below each pattern.

Sub-cluster 1

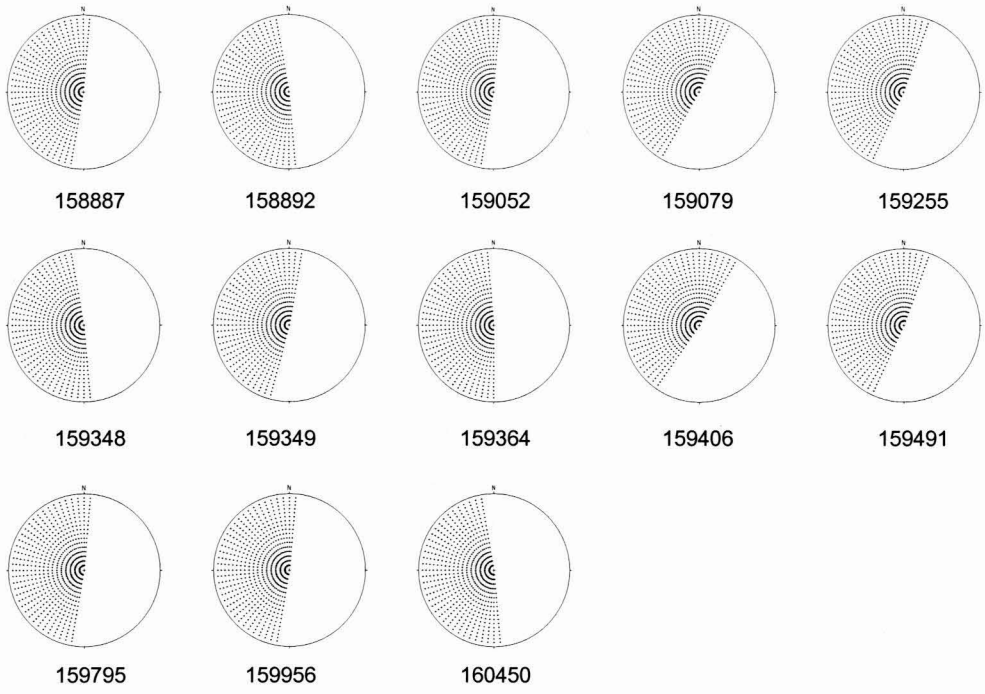

Sub-cluster 2

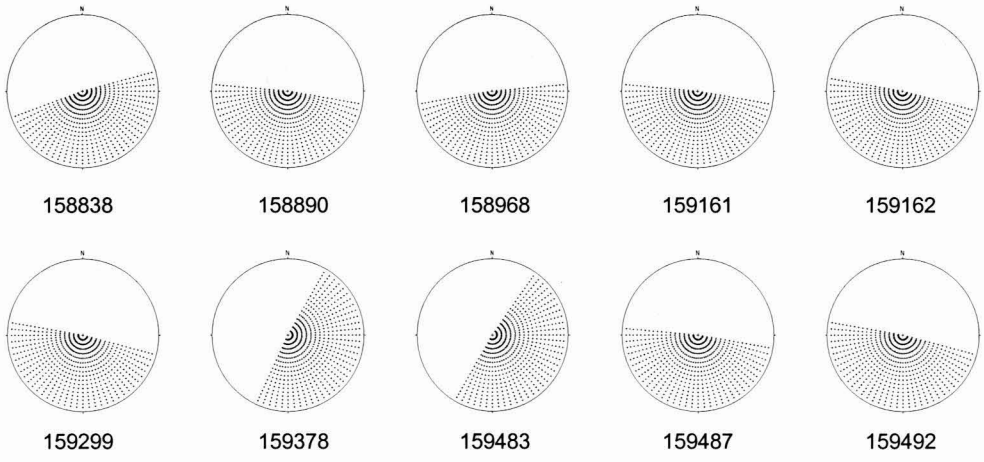

Figure 5.9: Radiation patterns computed for the dip-slip moment tensor components resulting from the relative inversion of sub-cluster 1 (13 events) and sub-cluster 2 (10 events). Event numbers are given below each pattern.

5.3 RELATIVE INVERSION *VERSUS* ABSOLUTE INVERSION

The objective of this test is to compare the results from the relative inversion to those from an absolute inversion of the same data. The source cluster used in the inversion is located on a well-documented geological fault, with known orientation and sense of displacement.

5.3.1 Method

1. The relative inversion method was applied to a source cluster (sub-cluster 1, identified in section 5.2) consisting of thirteen events.
2. An absolute inversion routine written by Brawn (1991), and incorporated into the PSS suite of software, was applied to the same thirteen events individually.
3. Radiation patterns were generated for each output moment tensor (computed using relative and absolute methods). The output radiation patterns were compared with the theoretical radiation pattern produced by a fault of known orientation and sense of displacement.

5.3.2 Results and discussion

The geological fracture mapping (described in Appendix J) indicates that the source cluster used in both inversions (i.e. relative and absolute methods) is located on a Group III fracture with a NNE strike and steep easterly dip of ~80° (Figure 5.10a). Slickensides on the fault plane indicate a left-lateral sense of displacement. The theoretical radiation pattern produced by this fault type is shown in Figure 5.10b.

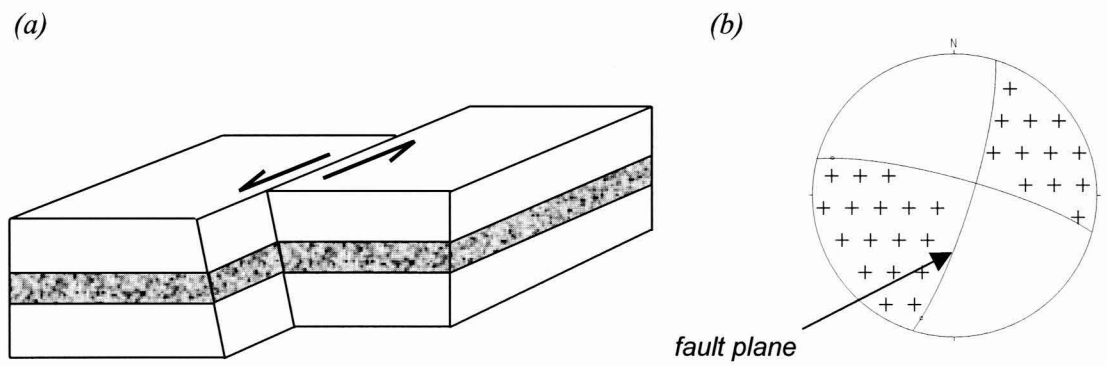

Figure 5.10: (a) Block diagram and (b) focal mechanism projection of a left-lateral strike-slip fault, with a dip of ~80° and NNE strike. + denotes compressional P-wave first arrivals.

Radiation patterns were computed for the double-couple components of the output moment tensors from the relative and absolute inversion. The relative inversion radiation patterns are similar to the predicted pattern (Figure 5.11) and the fault-plane solutions show a NNE left-lateral strike-slip fault mechanism with dips in the range 79° to 89°. These results correlate quite well with those obtained from the fracture mapping.

The radiation patterns produced by the absolute inversion of the same thirteen events are variable (Figure 5.12). The fault-plane solutions of three of the thirteen events show a steeply dipping fault plane with a NNE strike (events 159795, 159956 and 160450), which may be correlated with the observed fault plane. Only one of the radiation patterns (event 159491) matches the predicted pattern (but not completely, since the fault plane has a NS strike and the auxiliary plane dips too shallowly). It follows that the focal mechanisms deduced from these patterns should differ, ranging from steeply dipping normal-slip to oblique-slip fault mechanisms. To summarise, the focal mechanisms and radiation patterns determined using the absolute inversion method do not correlate well with those described by the fracture mapping.

5.3.3 Conclusions

The results computed using the relative inversion show a strong correlation with those obtained from the fracture mapping. The focal-plane solutions and radiation patterns indicate a left-lateral strike-slip fault mechanism, where the fault plane has a NNE strike, and dips steeply towards the East.

The results from the absolute inversion are variable, and the fault-plane solutions for the thirteen events in sub-cluster 1 do not correlate with the fault plane observed and mapped underground. The radiation pattern of only one event correlated with the predicted radiation pattern. The type of faulting (normal, thrust, strike-slip, etc.) could not be resolved from the absolute inversion results.

Sub-cluster 1

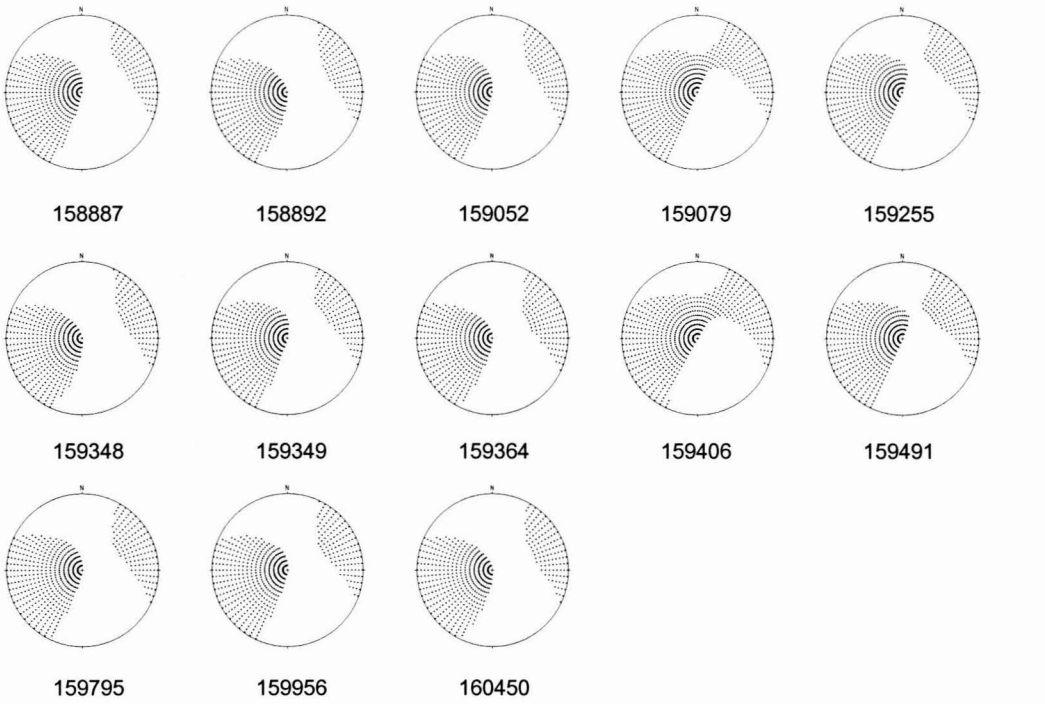

Figure 5.11: P-wave radiation patterns calculated for double-couple (strike-slip and dip-slip) moment tensor components computed using the relative inversion method applied to sub-cluster 1 (13 events of Family 3). + denotes compressional arrivals. Lower hemisphere equal-area projection. Event numbers are given below each pattern.

Sub-cluster 1

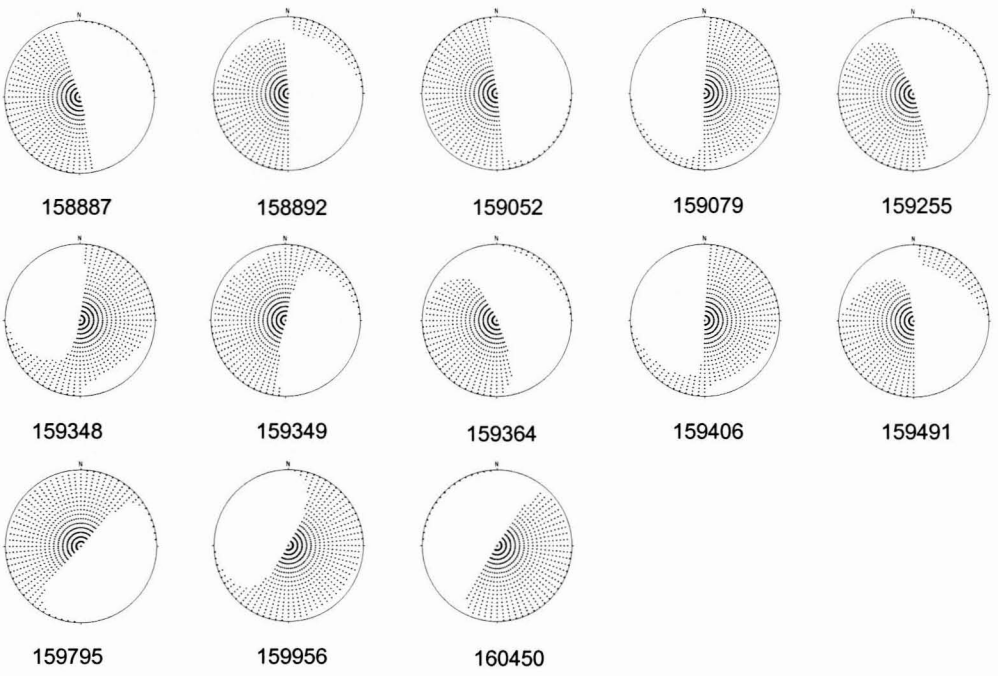

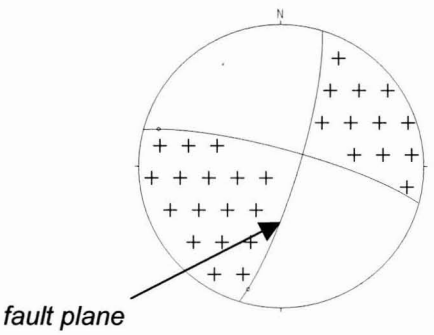

Figure 5.12: P-wave radiation patterns for moment tensors calculated using an absolute inversion method, applied to sub-cluster 1 (13 events of Family 3). + denotes compressional arrivals. Lower hemisphere equal-area projection. Event numbers are given below each pattern.

5.4 SENSITIVITY ANALYSIS

The objective is to investigate the effect of random noise on the output moment tensor components, i.e. to investigate the sensitivity of the inversion result to noise by artificially perturbing the input. This sensitivity analysis is a preliminary one, whereby only the observed displacements are perturbed. A comprehensive analysis would also include perturbations in the event locations, which would in turn influence the azimuth and take-off angles of each raypath. This is a non-trivial exercise, considered to be beyond the scope of this work.

5.4.1 Method

1. Uniformly distributed pseudo-random numbers were used to add a specified level of noise to the displacement data of ten recorded events. The perturbed displacement u_{ij}^{*} is given by:

$$u_{ij}^{*} = u_{ij} + \left(R\frac{P}{100} \right) u_{ij} \qquad 5.1$$

   where u_{ij} is the measured displacement for each event i and phase observation j. The quantity in brackets describes the noise used to perturb u_{ij} where R is the pseudo-random number ($-1 \le R \le 1$), and P is the required noise level in per cent.

2. Five different levels of noise were added to the data: 2%, 10%, 20%, 30%, 40% and 50%. In all cases, the noise was applied to all three displacement input quantities, i.e. to u_{ij}^{P}, u_{ij}^{SH} and u_{ij}^{SV}.

3. The relative inversion was performed on a base case (no added noise) and on each of the five perturbed input data sets.

4. The condition number $\mathcal{K}$ (defined in Equation 4.36) is computed for each relative inversion.

5. The moment tensor components m_{ri}^{*} resulting from the relative inversion of the five perturbed data sets are then compared with the base case moment tensor components m_{ri} by computing the linear correlation coefficient ρ between m_{ri} and m_{ri}^{*}. For pairs of quantities $\left(m_{ri}, m_{ri}^{*}\right)$ where $1 \le i \le n$ and $1 \le r \le 6$, the linear correlation coefficient ρ_r is given by applying the correlation formula given by Press *et al.* (1992):

$$\rho_r = \frac{\sum_{i=1}^{n}\left(m_{ri} - \overline{m}_{ri}\right)\left(m_{ri}^{*} - \overline{m}_{ri}^{*}\right)}{\sqrt{\sum_{i=1}^{n}\left(m_{ri} - \overline{m}_{ri}\right)^2 \sum_{i=1}^{n}\left(m_{ri}^{*} - \overline{m}_{ri}^{*}\right)^2}} \qquad 5.2$$

where $\overline{m}_{ri}$ and $\overline{m}_{ri}^{*}$ are the means of the unperturbed and perturbed moment tensor components, respectively. The correlation coefficient is defined such that $-1 \leq \rho \leq 1$. It takes on a value of 1, termed 'complete positive correlation', when the data points lie on a perfect line with positive slope, with m_{ri} and m_{ri}^{*} increasing together. If the data points lie on a perfect straight line with negative slope, m_{ri}^{*} decreasing as m_{ri} increases, then ρ has a value of -1; this is known as 'complete negative correlation'. A value of ρ near zero indicates that the variables m_{ri} and m_{ri}^{*} are uncorrelated.

6. The percentage relative error ε_{ri} between each of the perturbed moment tensor components m_{ri}^{*} relative to the base case moment tensor components m_{ri} is calculated according to:

$$\varepsilon_{ri} = \left|\frac{m_{ri} - m_{ri}^{*}}{m_{ri}}\right| \cdot 100 \qquad 5.3$$

5.4.2 Results and discussion

Figure 5.13 shows the variation in condition number $\mathcal{K}$ with noise. From the graph it is evident that the system becomes increasingly ill-conditioned as the level of noise increases. However, even though $\mathcal{K}$ increases, these numbers remain relatively low (pers. comm. Napier, 1998; pers. comm. Pierce, 1998) indicating a low-sensitivity to noise.

The linear correlation coefficients ρ are given in Table 5.1. Note that the coefficients computed between the base case (referred to as the 'control' case in the table) and each of the perturbed moment tensors are given in the first (left) column of each of the six tables. The remaining six columns are given for interest and show the correlation between the various combinations of perturbed moment tensor components (e.g. the second column gives the correlation between the moment tensor components perturbed by 2% noise with the remaining five cases: 5%, 10%, 20%, 30% and 40% noise).

For all six components, it is evident that the correlation between the base case m_{ri} and the perturbed moment tensors m_{ri}^{*} decreases with increasing noise levels. However, the system is remarkably insensitive to noise because ρ is in all cases (except for m_{6i}) greater than 0.9.

The relative errors are given in Table 5.2. Each of the six columns show the error computed between the m_{ri}^{*} perturbed by a particular percentage of noise and the base case m_{ri}. For all six moment tensor components, the average relative error increases with increasing levels of noise. It also appears that certain components, on average, are more sensitive to noise than others, i.e. m_{2i} and m_{4i}. On closer inspection of the individual errors, it is evident that the high average for these two components is due to the dominating effect of one particular event. In the case of the m_{2i} component, event 166596 shows the highest relative error and has a swamping effect on the average error. Event 166673 has a large influence on the average error for the m_{4i} component. The source of these high relative errors for events 166596 and 166673 could be a result of inaccurate phase amplitude measurements due to wrong phase identification on the seismogram, high signal-to-noise ratios or large location errors.

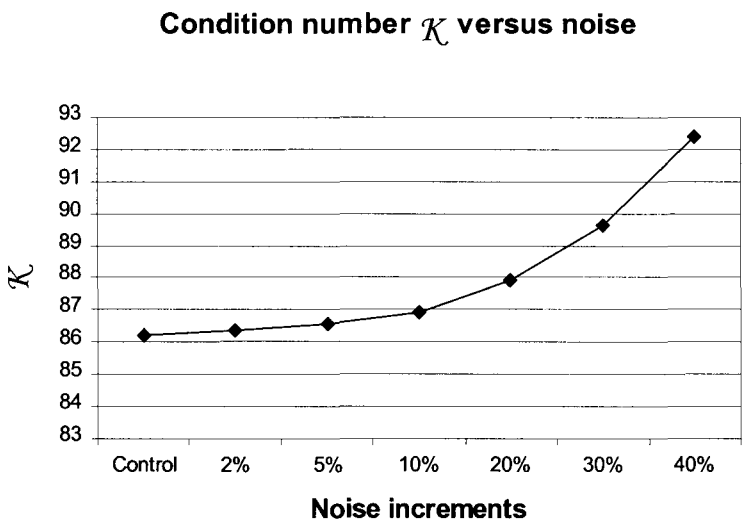

Figure 5.13: Variation in condition number $\mathcal{K}$ with noise.

5.4.3 Conclusions

In general, the relative inversion technique displays a low sensitivity to pseudo-random noise. This conclusion is based on the generally high (>0.9) linear correlation coefficients computed between the unperturbed moment tensor components and those calculated from displacement data to which varying levels of noise was added. However, the system becomes increasingly ill-conditioned as the level of noise increases.

The average relative error for the event cluster for all six moment tensor components increases with increasing levels of noise. Inaccurate phase amplitude measurements, low signal-to-noise ratios or large location errors could be the cause of the large relative errors observed for the m_{2i} and m_{4i} components of events 166596 and 166673, respectively.

Table 5.1 (a): Linear correlation coefficients ρ computed for varying noise levels.

m_{1i}	*Control*	*2% noise*	*5% noise*	*10% noise*	*20% noise*	*30% noise*	*40% noise*
Control	1.0000						
2% noise	0.9999	1.0000					
5% noise	0.9996	0.9999	1.0000				
10% noise	0.9986	0.9991	0.9997	1.0000			
20% noise	0.9949	0.9960	0.9973	0.9989	1.0000		
30% noise	0.9897	0.9912	0.9931	0.9958	0.9989	1.0000	
40% noise	0.9828	0.9847	0.9873	0.9909	0.9961	0.9989	1.0000

m_{2i}	*Control*	*2% noise*	*5% noise*	*10% noise*	*20% noise*	*30% noise*	*40% noise*
Control	1.0000						
2% noise	0.9999	1.0000					
5% noise	0.9997	0.9999	1.0000				
10% noise	0.9985	0.9990	0.9996	1.0000			
20% noise	0.9919	0.9931	0.9948	0.9974	1.0000		
30% noise	0.9754	0.9775	0.9806	0.9859	0.9954	1.0000	
40% noise	0.9425	0.9456	0.9505	0.9590	0.9769	0.9928	1.0000

m_{3i}	*Control*	*2% noise*	*5% noise*	*10% noise*	*20% noise*	*30% noise*	*40% noise*
Control	1.0000						
2% noise	0.9999	1.0000					
5% noise	0.9993	0.9997	1.0000				
10% noise	0.9972	0.9982	0.9993	1.0000			
20% noise	0.9892	0.9913	0.9939	0.9973	1.0000		
30% noise	0.9762	0.9792	0.9834	0.9893	0.9972	1.0000	
40% noise	0.9572	0.9611	0.9667	0.9750	0.9881	0.9967	1.0000

Table 5.1 (b): Linear correlation coefficients ρ computed for varying noise levels.

m_{4i}	*Control*	*2% noise*	*5% noise*	*10% noise*	*20% noise*	*30% noise*	*40% noise*
Control	1.0000						
2% noise	0.9998	1.0000					
5% noise	0.9986	0.9995	1.0000				
10% noise	0.9947	0.9966	0.9987	1.0000			
20% noise	0.9793	0.9832	0.9884	0.9948	1.0000		
30% noise	0.9543	0.9601	0.9680	0.9794	0.9947	1.0000	
40% noise	0.9183	0.9258	0.9364	0.9524	0.9778	0.9941	1.0000

m_{5i}	*Control*	*2% noise*	*5% noise*	*10% noise*	*20% noise*	*30% noise*	*40% noise*
Control	1.0000						
2% noise	0.9999	1.0000					
5% noise	0.9998	0.9999	1.0000				
10% noise	0.9989	0.9993	0.9997	1.0000			
20% noise	0.9938	0.9946	0.9958	0.9978	1.0000		
30% noise	0.9790	0.9804	0.9827	0.9869	0.9955	1.0000	
40% noise	0.9431	0.9452	0.9489	0.9563	0.9736	0.9909	1.0000

m_{6i}	*Control*	*2% noise*	*5% noise*	*10% noise*	*20% noise*	*30% noise*	*40% noise*
Control	1.0000						
2% noise	0.9997	1.0000					
5% noise	0.9982	0.9994	1.0000				
10% noise	0.9929	0.9954	0.9982	1.0000			
20% noise	0.9710	0.9761	0.9830	0.9921	1.0000		
30% noise	0.9322	0.9397	0.9504	0.9667	0.9909	1.0000	
40% noise	0.8726	0.8823	0.8967	0.9199	0.9607	0.9892	1.0000

Table 5.2 (a): Percentage relative error ε_{ri} computed for moment tensor components at different noise levels.

Event no.	**% Relative error: m_{1i}**					
	2% noise	*5% noise*	*10% noise*	*20% noise*	*30% noise*	*40% noise*
166232	3.2	7.8	15.1	26.1	30.0	25.9
166233	3.7	9.1	17.2	28.7	32.5	28.6
166240	5.2	13.1	25.8	47.4	60.1	61.3
166490	8.3	20.5	40.2	73.7	95.9	105.1
166504	4.1	10.0	19.3	34.1	42.1	43.5
166578	3.8	9.3	17.6	29.1	32.3	27.4
166596	4.4	10.8	20.8	36.4	43.9	42.3
166646	6.2	15.4	29.7	51.9	62.4	60.2
166663	3.4	8.3	15.6	25.4	27.7	22.8
166673	5.8	14.6	29.2	55.9	76.5	89.2
Average	4.8	11.9	23.0	40.9	50.3	50.6

Event no.	**% Relative error: m_{2i}**					
	2% noise	*5% noise*	*10% noise*	*20% noise*	*30% noise*	*40% noise*
166232	0.3	1.1	3.2	10.6	21.1	32.4
166233	0.8	1.8	3.0	2.8	0.4	5.4
166240	0.8	1.8	2.9	3.3	1.7	0.6
166490	3.8	9.9	21.3	48.1	78.9	112.1
166504	6.4	16.5	34.4	72.2	110.6	148.6
166578	0.6	1.4	2.7	4.6	5.8	6.3
166596	115.5	304.7	661.0	1512.8	2537.0	3731.3
166646	1.8	4.6	9.9	22.0	35.9	51.1
166663	1.2	3.0	6.1	11.7	17.2	23.5
166673	3.0	7.7	15.6	32.0	48.2	63.9
Average	13.4	35.3	76.0	172.0	285.7	417.5

Event no.	**% Relative error: m_{3i}**					
	2% noise	*5% noise*	*10% noise*	*20% noise*	*30% noise*	*40% noise*
166232	1.0	2.4	5.0	11.3	19.5	29.2
166233	0.5	1.2	2.1	3.0	3.4	4.6
166240	0.0	0.0	0.3	2.4	6.5	11.6
166490	0.8	2.0	4.0	7.6	10.3	12.4
166504	0.5	1.2	2.0	1.8	0.8	5.0
166578	0.9	2.4	6.0	17.1	34.2	56.8
166596	2.2	5.5	10.4	18.0	22.5	23.9
166646	0.3	0.7	1.2	2.5	4.6	7.7
166663	1.0	2.3	4.2	6.8	7.9	8.3
166673	0.0	0.2	0.8	3.7	9.4	17.0
Average	0.7	1.8	3.6	7.4	11.9	17.7

Table 5.2 (b): Percentage relative error ε_{ri} computed for moment tensor components at different noise levels.

Event no.	**% Relative error: m_{4i}**					
	2% noise	*5% noise*	*10% noise*	*20% noise*	*30% noise*	*40% noise*
166232	27.4	72.0	156.1	361.8	614.9	902.2
166233	2.4	6.0	12.2	25.0	36.9	45.2
166240	15.0	38.4	80.1	173.0	275.4	378.5
166490	6.2	16.0	33.6	72.7	114.7	156.7
166504	17.5	44.3	91.1	191.9	301.3	415.3
166578	13.4	34.5	72.6	161.9	270.8	397.6
166596	8.1	20.3	40.8	82.3	124.8	168.7
166646	4.6	12.1	26.8	63.1	108.0	159.5
166663	19.4	48.8	98.5	199.6	298.9	388.6
166673	247.8	636.7	1332.9	2907.9	4701.5	6624.3
Average	36.2	92.9	194.5	423.9	684.7	963.6

Event no.	**% Relative error: m_{5i}**					
	2% noise	*5% noise*	*10% noise*	*20% noise*	*30% noise*	*40% noise*
166232	0.3	0.8	2.0	5.1	8.4	10.8
166233	0.7	1.7	3.3	6.2	8.2	9.0
166240	1.2	3.3	7.0	15.5	24.5	33.6
166490	0.5	1.2	2.7	5.9	8.5	9.8
166504	0.4	0.9	1.3	0.9	2.1	9.0
166578	0.1	0.3	0.8	1.6	1.3	2.2
166596	1.7	4.3	8.7	18.2	28.9	43.2
166646	0.6	1.3	2.2	3.3	4.4	6.8
166663	0.8	2.1	4.5	9.8	15.1	19.8
166673	0.4	1.1	2.6	5.8	8.9	10.7
Average	0.7	1.7	3.5	7.2	11.0	15.5

Event no.	**% Relative error: m_{6i}**					
	2% noise	*5% noise*	*10% noise*	*20% noise*	*30% noise*	*40% noise*
166232	0.1	0.2	0.1	0.5	0.1	2.6
166233	0.6	1.3	1.5	1.2	7.6	16.2
166240	1.9	4.9	9.8	18.6	24.9	28.2
166490	0.7	1.9	3.9	9.1	16.6	26.9
166504	0.0	0.1	1.0	5.6	15.3	31.6
166578	0.2	0.3	0.2	4.4	14.2	30.0
166596	0.5	0.3	3.3	25.1	70.0	140.7
166646	0.7	1.8	3.6	7.7	13.3	21.4
166663	0.2	0.5	0.9	1.1	0.9	6.3
166673	0.5	1.3	2.6	5.6	10.0	17.0
Average	0.6	1.2	2.7	7.9	17.3	32.1

5.5 NOISE SIMULATIONS

This test is similar to that outlined in Section 5.4 in that both tests investigate the sensitivity of the inversion result to pseudo-random noise by artificially perturbing the input. The important difference is that this test is performed on two clusters of synthetic double-couple events in contrast to the previous test, which was performed using real, recorded data. The main objective is to investigate the effect of various levels of noise on (1) a cluster of events having different mechanisms, and, (2) on a cluster of events having very similar mechanisms.

5.5.1 Method

1. Synthetic data for two clusters of pure double-couple events were computed using Equations 2.15-2.21 and 2.47 in Chapter 2). The source was assumed to be synchronous and a step function was used to estimate the displacements. An isotropic velocity structure was assumed, with a P-wave velocity of 5.9 km/s and an S-wave velocity of 3.8 km/s. A density of 2700 kg/m^3 was assumed.
2. The first cluster consisted of 6 double-couple events having variable mechanisms (Figure 5.14). The second cluster consisted of 6 double-couple events having very similar mechanisms – identical dip and strike, and varying only in dip (Figure 5.15).
3. Uniformly distributed pseudo-random numbers were used to add a specified level of noise to the displacement data. The perturbed displacement is given by Equation 5.1.
4. Seven different levels of noise were added to the data: 2%, 5%, 10%, 20%, 30%, 40% and 50%. In all cases, the noise was applied to all three displacement input quantities, i.e. to u_{ij}^{P}, u_{ij}^{SH} and u_{ij}^{SV}. The same random seed was used in all runs, for both event clusters.
5. The relative inversion was performed on a base case (i.e. no added noise) and on each of the five perturbed input data sets for both clusters.
6. Radiation patterns and corresponding fault-plane solutions were computed for group of events, for each level of applied noise.
7. The radiation patterns for each cluster for each noise level are compared to the noise-free patterns on a purely qualitative level (this is to avoid repetition because the tests in Chapter 7, which are similar, are described comprehensively).

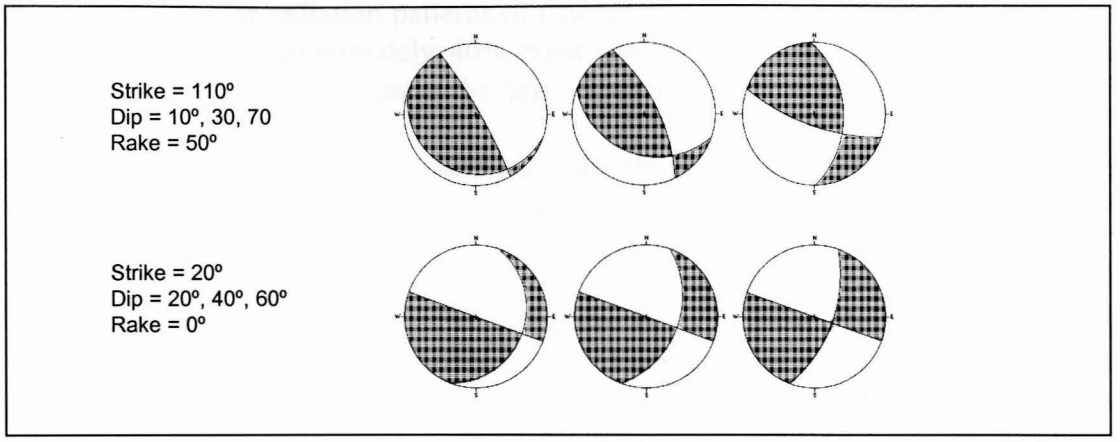

Figure 5.14: Focal mechanism diagrams of the synthetic cluster (Cluster A) consisting of mixed mechanisms. The six events are pure double-couple sources having variable dip, strike and rake. Shaded regions indicate positive (compressional) P-wave first motions.

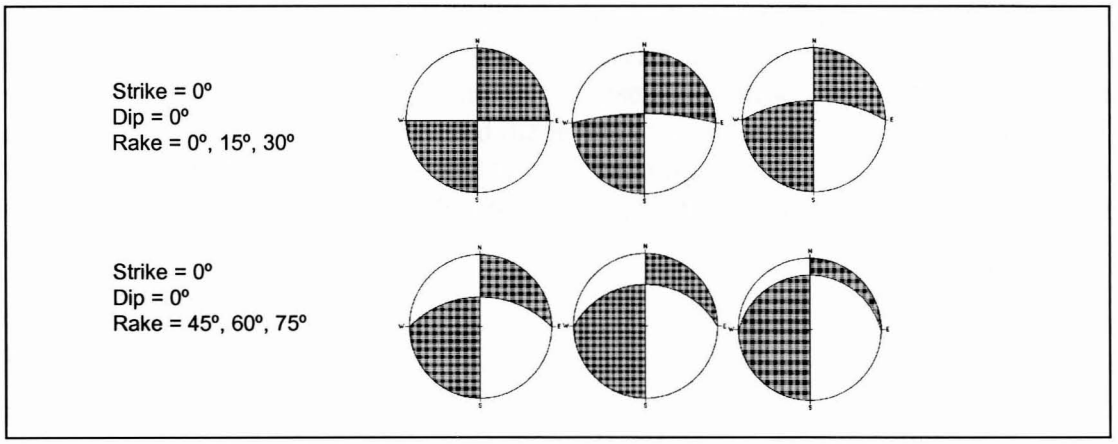

Figure 5.15: Focal mechanism diagrams of the synthetic cluster (Cluster B) consisting of similar mechanisms. The six events are pure double-couple sources having identical dip and strike, and variable rake. The rake varies in 15° increments. Shaded regions indicate positive (compressional) P-wave first motions.

5.5.2 Results and discussion

The radiation patterns and fault-plane solutions computed using RMTI for the cluster of mixed mechanisms for the various applied noise levels are shown in Figure 5.16, and those for the cluster of similar mechanisms are given in Figure 5.17. In this discussion, for the sake of brevity, the cluster of mixed mechanisms is referred to as Cluster A, and that for the similar mechanisms as Cluster B.

It is evident from Figures 5.16 and 5.17 that inversion of the noise free data (0% noise) gives almost perfect resolution of the mechanisms for both clusters. As the level of noise is increased there is a corresponding decrease in the resolution of the mechanisms for both clusters. There is however, one important difference – the

resolution of Cluster B decays far for rapidly than that of Cluster A, for comparable levels of noise. The radiation patterns of Cluster A match those of the noise-free case very closely until approximately 40% noise. Even then, there still is a fairly good resemblance of the mechanisms to the noise-free case.

In stark contrast, the increasing noise has a devastating effect on the resolution of the mechanisms of Cluster B. The radiation patterns show a poor resemblance to those of the noise-free case, even for very low levels (as low as 10%) of noise.

The reason for these observations is thought to be as follows. The relative inversion without a reference mechanism is highly dependent on there being significant differences in the mechanisms of the events in a cluster. When the level of noise is comparable to the differences in the mechanisms, a singular system of equations results, giving rise to the unreliable results. This phenomenon is also discussed in Chapter 7.

These observations have an important bearing on the potential for routine application of RMTI to seismograms recorded in the underground mining environment. Very often, clusters of events recorded underground show similar waveforms, and are therefore the result of similar fracture processes (i.e. similar mechanisms). A case such as this is described in some detail in the case study presented in Chapter 8. RMTI could be used in these cases, provided the levels of noise are extremely low. However, since this is hardly ever the case, RMTI must be applied with caution. This realisation shaped the path of the research that follows – the development of a hybrid moment tensor inversion method.

5.5.3 Conclusions

The relative moment tensor inversion method without a reference mechanism, when applied to a cluster of events having significantly different mechanisms, shows a low sensitivity to pseudo-random noise. The radiation patterns of events contaminated by as much as 40% noise correlate well with the noise-free patterns.

However, the relative method without a reference mechanism must be applied to clusters of events having similar mechanisms with extreme caution, because if the differences between the mechanisms are of the same order as the noise level, the coefficient matrix becomes singular, and the results of the inversion are extremely unreliable.

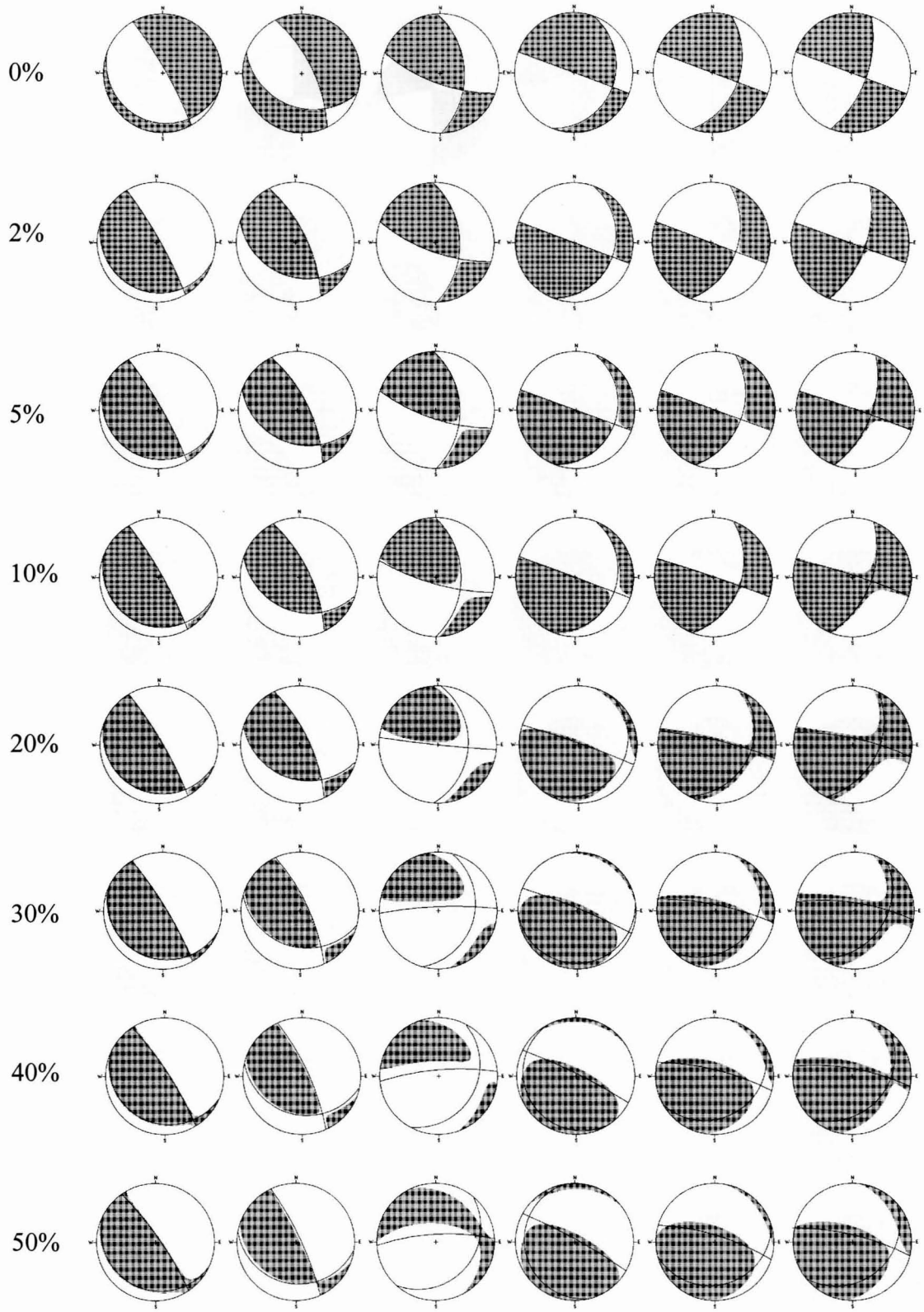

Figure 5.16: Radiation patterns of moment tensors computed using RMTI (relative moment tensor inversion without a reference mechanism) for various levels of pseudo-random noise. Synthetic events in this cluster have different mechanisms

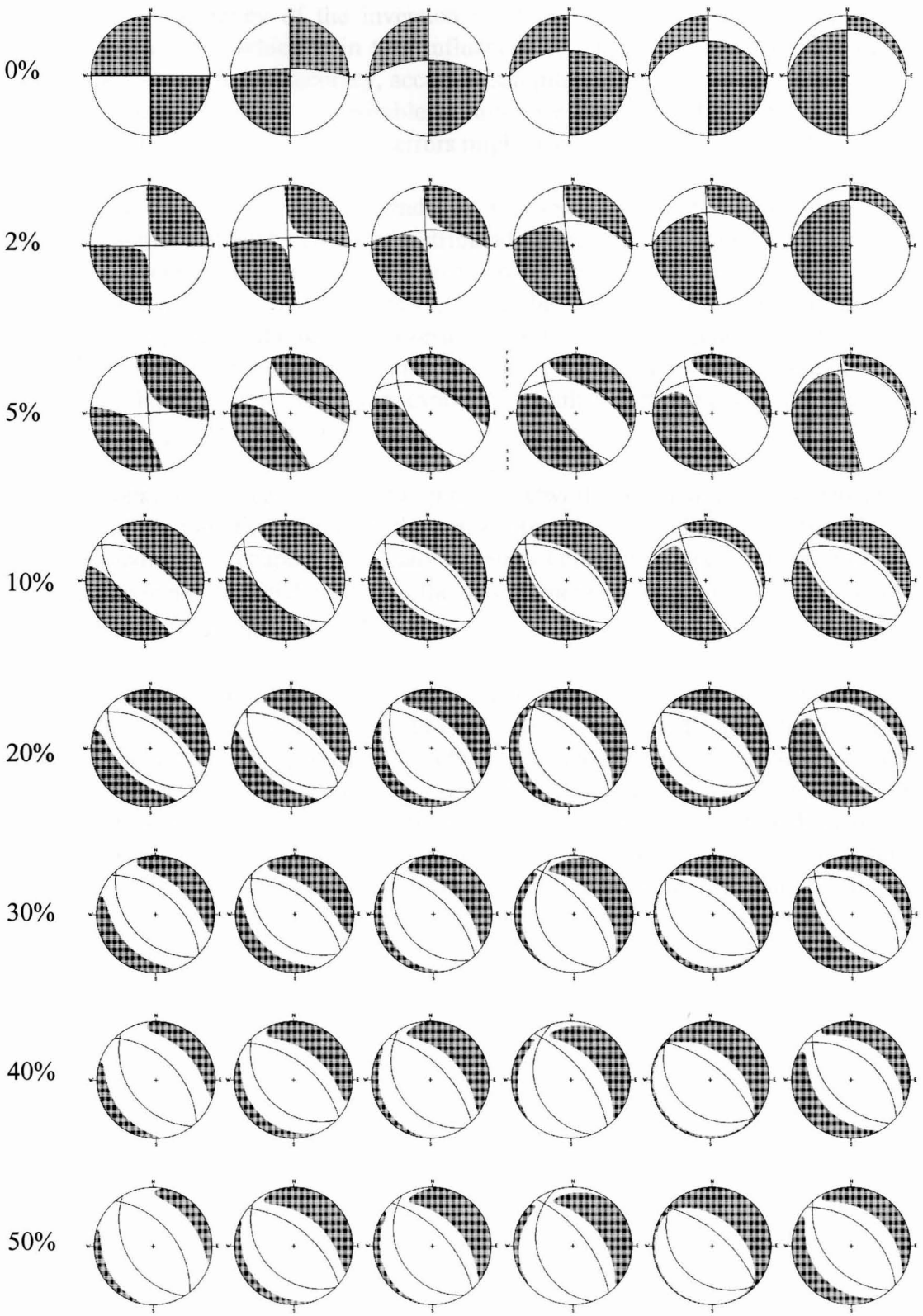

Figure 5.17: Radiation patterns of moment tensors computed using RMTI (relative moment tensor inversion without a reference mechanism) for various levels of pseudo-random noise. Synthetic events in this cluster have similar mechanisms.

5.6 SUMMARY OF CONCLUSIONS

The degree of accuracy of the inversion depends on the quality of the data (i.e. signal-to-noise ratio) which is in turn influenced by the spatial configuration of the seismic network, location accuracy, accuracy/sampling of the station recordings of the waveforms, etc. Clearly, it is desirable to minimise these potential sources of error, and to have insight into where/when errors might occur.

The quality of data recorded depends on the seismic layout. In the ideal case, recording stations should be evenly distributed around the hypocentre, ensuring full spherical coverage. The mining geometry/environment limits the coverage of the network to a plane i.e. usually it is only possible to position the seismic stations parallel to the plane of the reef. As a result, location errors are generally small in the plane of the reef, but large perpendicular to the reef. Since the location of the events is a necessary input parameter, we can expect the results of the inversion to reflect the location errors present in the input data.

An additional effect caused by the planar network configuration is inadequate sampling of the radiation pattern in the z-direction (i.e. perpendicular to the reef). As demonstrated in this chapter, this leads to errors being introduced into the moment tensor components oriented normal to the seismic network (e.g. the M_{33} component, and to a lesser extent, M_{13} and M_{23}).

The relative inversion technique displays a low sensitivity to pseudo-random noise provided the mechanisms of the events in the cluster are significantly different. The radiation patterns of events contaminated by as much as 40% noise correlate well with the noise-free patterns. However, if the differences between the mechanisms are of the same order as the noise level, the coefficient matrix becomes singular, and the results of the relative inversion become extremely unreliable. For this reason, the relative inversion without a reference mechanism should not be used in isolation, and the results should always be compared with those provided by an independent moment tensor inversion technique.

Chapter 6

HYBRID MOMENT TENSOR INVERSION METHODS

In this chapter, a number of 'hybrid' moment tensor inversion methods are developed and described. These revised techniques attempt to capitalise on the strengths of both the absolute and relative moment tensor inversion methods in order to achieve a robust measure of the seismic moment tensor. The hybrid methods are in essence weighting schemes that aim to increase the accuracy of the computed moment tensor by diminishing the effect of noisy data on the system of equations and correct for site effects.

Various weighting schemes have been proposed in the literature, two of which were outlined in Chapter 3 (Udias & Baumann, 1969, Šílený *et al.*, 1992). The schemes investigated were applied to individual events and the corrections (or weightings) were determined using the residuals computed for the event of interest. The new aspect of the hybrid methods proposed herein is that the correction applied to a particular observation is based on the residuals (for a particular geophone site, channel and phase) calculated using all of the events in the cluster – this constitutes the relative component of the hybrid methods. The weighting schemes are non-linear and are applied iteratively.

The reason for developing the hybrid techniques is to attempt to compensate for the various types of systematic error (or noise) influencing the waveforms recorded in the underground environment. For example, raypath focussing and defocussing as a result of inhomogeneities in the rockmass, the degradation of the velocity model due to mining-induced fractures, low signal-to-noise ratios, poor P- and S-wave picks, and various other factors can adversely affect the fidelity of the seismograms. These methods can also be used to enhance signals recorded near a nodal plane in the radiation pattern or to decrease the influence of a low quality observation.

An analogous approach has been applied to the seismic location problem, *viz.* the so-called 'JHD method' (joint hypocentral determination). The relative locations obtained through JHD are usually better than those determined by inversion of more complete and complex velocity models, and the resulting hypocentral locations often give a more focussed picture of the seismicity. Chapter 7 will investigate in depth whether comparable benefits will accrue when similar principles are applied to the moment tensor inversion problem.

In this chapter, three different implementations of the hybrid schemes are developed and outlined in this chapter. However, before elaborating on these methods, the absolute and relative moment tensor inversion approaches are briefly summarised, and their respective strengths and weaknesses enumerated. Since the hybrid methods are

aimed at reducing the level of noise present in a seismogram, the more common possible sources of noise are discussed and the effects of various types of noise on moment tensor solutions are briefly demonstrated. The last part of this chapter describes the code written by the author to implement the hybrid inversion schemes.

6.1 Pros & Cons Of Conventional MTI Methods

At the risk of over-emphasising the point, it is important to state once again that the absolute methods apply to *individual* events whereas the relative method requires a tightly clustered (in space) *group* of events. The relative method must not be confused with joint inversions, where a cluster of events is used to solve for a single source mechanism, which describes all of the events in the cluster. The strengths and weakness of both the absolute and relative approaches are summarised in Table 6.1.

Table 6.1: Strengths and weaknesses of the absolute and relative moment tensor inversion techniques.

	Strengths	**Weaknesses**
Absolute moment tensor inversion	• Apply to individual events. • By using the polarity of the first-motion, the sign of each quadrant in the resultant radiation pattern can be unambiguously determined.	• Dependent on accurate determination of the Green's function. • Requires a denser seismic network for accurate results, i.e. information scarcity. • Sensitive to noise if no outlier rejection scheme is incorporated in the inversion.

Table 6.1(continued): Strengths and weaknesses of the absolute and relative moment tensor inversion techniques.

	Strengths	Weaknesses
Relative moment tensor inversion with reference mechanism	• Apply to clusters of weak events. • Provided the moment tensor of one of the events in the cluster is available, the moment tensors of neighbouring weak events can be computed. • If the polarity of the first motion of the reference event is used in the inversion, the sign of each quadrant in the resultant radiation pattern can be determined. • Reliable and stable in extreme situations concerning sparse coverage of the focal sphere, and noise contamination (shown in Chapter 7).	• Require a cluster of events i.e. not useful in a single event situation. • The moment tensor of at least one event in the cluster (calculated using an independent method) is needed. • Danger exists of the solutions for the individual events being biased towards the reference event. • If the reference event is subject to systematic error, all the other events in the cluster are affected.
Relative moment tensor inversion without reference mechanism	• No reference event or reference mechanism is necessary when the method is applied to events in a cluster with different radiation patterns. • The Green's functions are not required. • The biases introduced by the over-simplification of complex crustal structure are reduced.	• Resolving power of method depends on the variability of mechanisms in a cluster i.e. nearly identical mechanisms result in a singular inversion problem (shown in Chapters 5 and 7). • Although the polarity of the first-motion is used in the system of equations, the signs of the output moment tensors depend on the sign of the constant in the linear constraint (Equation 4.22). • The moment tensors of each of the events in the cluster are estimated, with the exception of a constant factor. Neither the magnitude not the sign of this constant is immediately evident. A scaling procedure (based on the scalar seismic moment) can be introduced to counteract the magnitude, but the same approach cannot be applied in the case of the sign. Thus, there is ambiguity inherent in the method. • Extremely sensitive to noise if source mechanisms are very similar (shown in Chapters 5 and 7).

6.2 NOISE

The most important factor determining the quality of a given seismogram is the signal-to-noise ratio. Aki and Richards (1980) define the signal as the desired part of the data and the noise as the unwanted part. Conventionally, noise is filtered out of the trace in question as expediently as possible, and little thought is given to its origins. However, the sources of noise are fascinating and deserve a brief review.

This section describes the possible sources of noise affecting seismograms recorded by regional and local (i.e. mine) networks. The effects of various types of noise on moment tensor solutions are briefly demonstrated to highlight the need for noise reduction techniques (a detailed study of the effects of noise on moment tensor solutions is presented in Chapter 7).

6.2.1 Sources of noise

In earthquake seismology, seismic noise with periods of $\leq$ 0.1s is mainly of local origin and limited extent. Wind, traffic, machinery, surf, waterfalls, running water, volcanic activity, etc., cause this noise. In a seismological study of the Western Cape, traffic noise was almost mistakenly attributed to the diurnal activities of geckoes in the recording station!

Another group of seismic noise widely observed and discussed by earthquake seismologists has periods ranging from 3s to 10s. These are known as microseisms. On the seismograms these appear as groups in each of which the amplitude increases and then decreases, suggesting a beat frequency. Microseismic storms lasting often for 1 to 2 days are strong enough (ground amplitudes on the coast of 10-20μm, inland 1-2μm) to render some seismograms useless. Microseisms of this sort are caused by cyclonic storms over oceans, and are propagated with gradual loss of energy into the central areas of continents. Some with shorter periods (1.5 to 2s) are observed near large lakes.

Mining seismologists have other sources of noise to contend with: 50Hz noise from the mains AC supply (Figure 6.1), noise due to machinery and underground traffic, poor coupling of geophones situated in old, highly fractured sites, water in the boreholes, badly oriented geophones (Figure 6.2), non-linear effects related to the dynamic range of the recording instruments, etc. In addition, the recorded waveforms are often complex, which compounds the difficulty of accurately identifying individual wave phases (Figure 6.3). Complex events are of great interest since they are the result of several superimposed or near-simultaneous source rupture processes. However, to a signal processor who is only interested in identifying the various wave phases of an individual event as quickly as possible (owing to the huge daily data turnover – 500 or more events *per day* is not unusual), the added complexity of multiple events interfering with one another complicates the location process enormously.

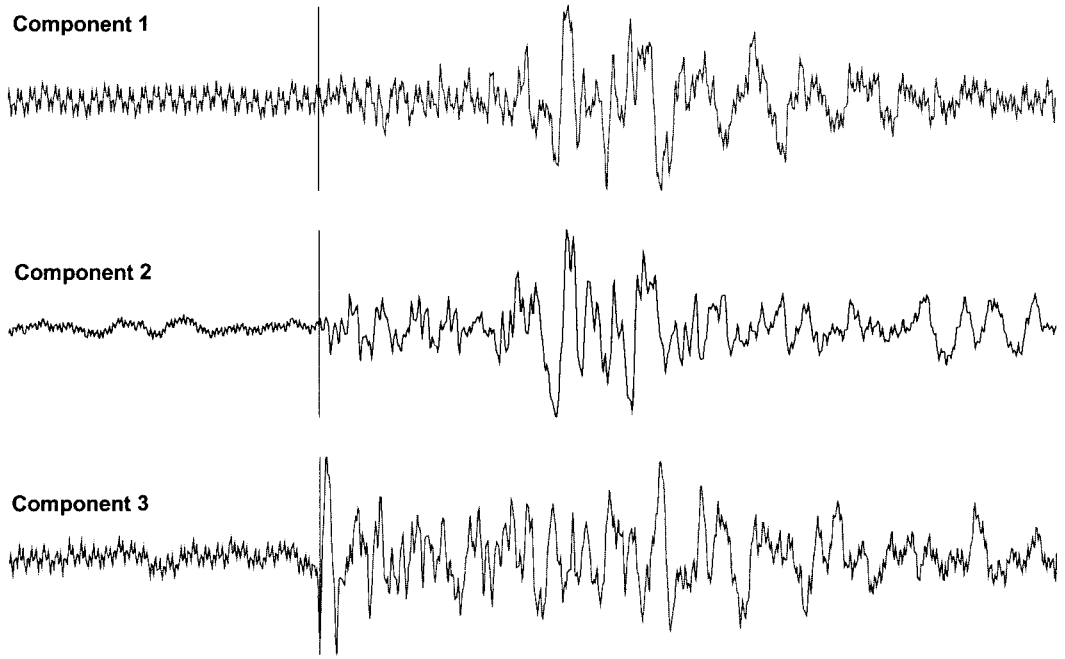

Figure 6.1: Complete waveforms recorded at a station. Component 1 is contaminated by 50 Hz noise. Note the higher frequency harmonic.

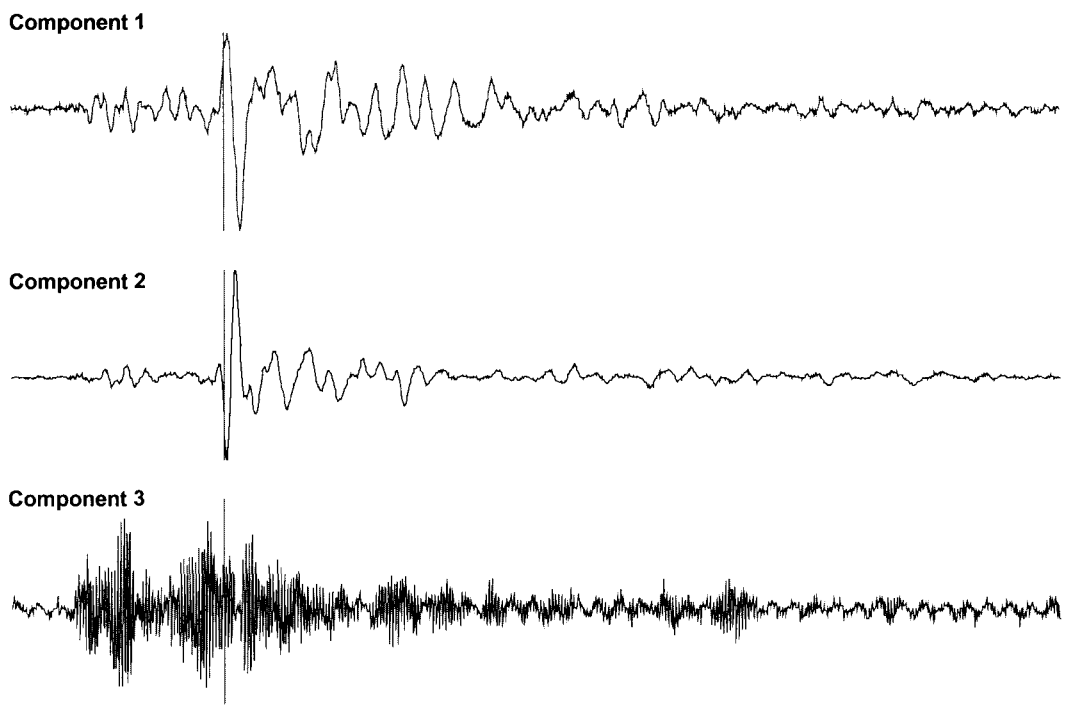

Figure 6.2: Complete waveforms recorded at a station. Note noisy channel (component 3). Since only one of the components is noisy, the source of noise is probably due to a tilted sensor rather than poor coupling of the sensor with the borehole. Coupling problems would affect all three components.

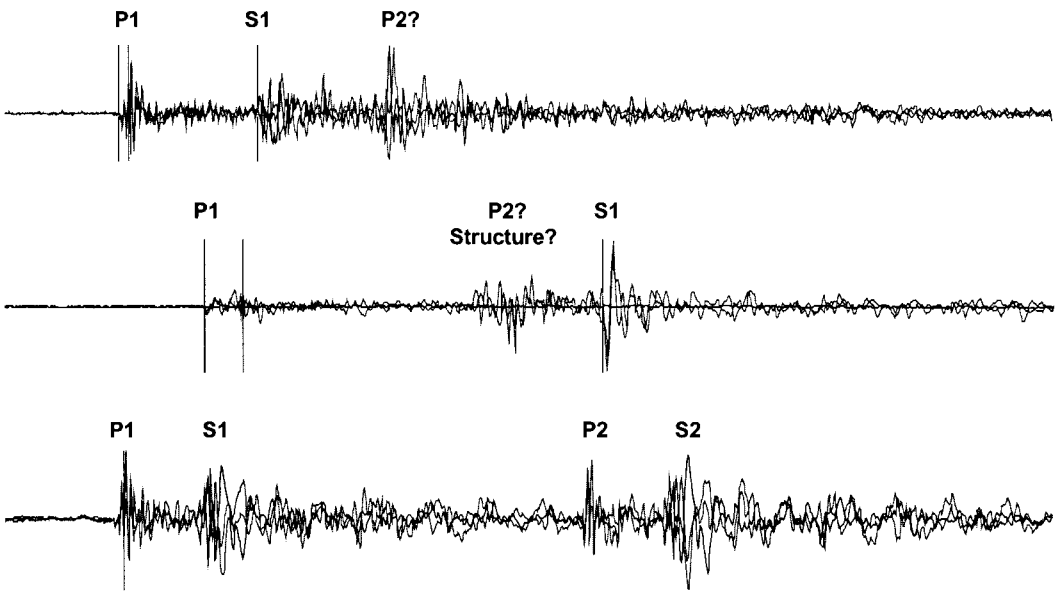

Figure 6.3: Examples of three different complex events. P1 and P2 indicate the P-picks for the first and second events, respectively. Similarly, S1 and S2 indicate the S-picks.

6.2.2 Classification of noise

These different noise sources can be classified in numerous ways, one of which is based on predictability. Noise of a predictable nature is often described as deterministic whereas unpredictable noise is known as stochastic or random noise. Some noise may appear to be stochastic but is actually deterministic. If a large number of varied but predictable noise sources are combined, the result may be sufficiently complex for the resulting combination to seem entirely random.

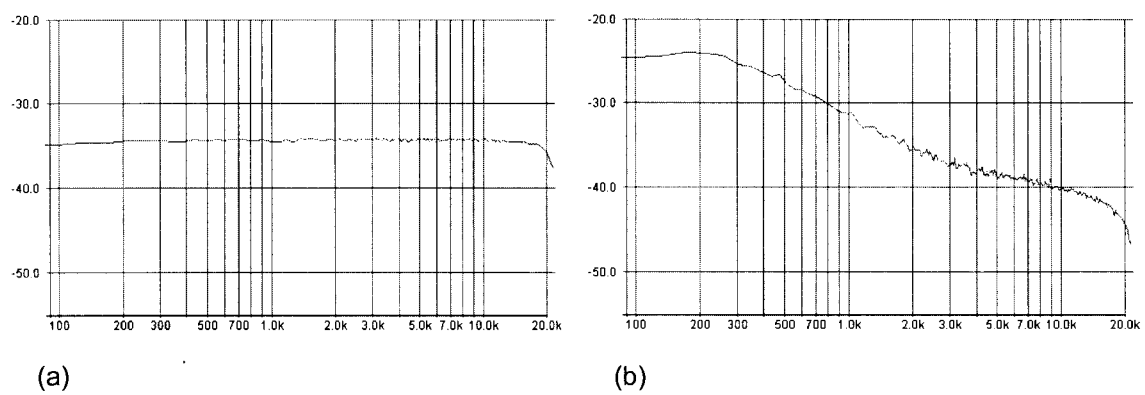

Figure 6.4 Examples of the spectra computed from two types of random noise: (a) An almost 'white' spectrum (b) 'Pink' spectrum (modified from Ritter, 1999).

Figure 6.4 (a) shows the frequency response of a digital sound card for a computer and is an example of an almost 'white' spectrum. A white spectrum would be completely flat for all frequencies. (The dip at the high end is due to the application of a low-pass filter to prevent aliasing effects from the 44.1 kHz sampling rate).

Figure 6.4 (b) is an example of a 'pink' spectrum. Note that the spectrum is not flat but shows higher amplitudes for the lower frequency range. In this example, there is more low-frequency noise than high-frequency noise.

Figure 6.5 shows the spectrum computed from a seismogram contaminated by a 50Hz noise signal. Note the spike in the spectrum at 50Hz, as well as the higher frequency harmonic (150Hz). This is an example of deterministic noise.

Figure 6.6 shows another example of deterministic noise, in this case the spectrum computed from a seismogram where one of the channels is poorly oriented. Since only one of the components is noisy, the source of noise is probably due to a tilted sensor rather than poor coupling of the sensor with the borehole – coupling problems would affect all three components (pers. comm. Van Zyl Brink, 2001).

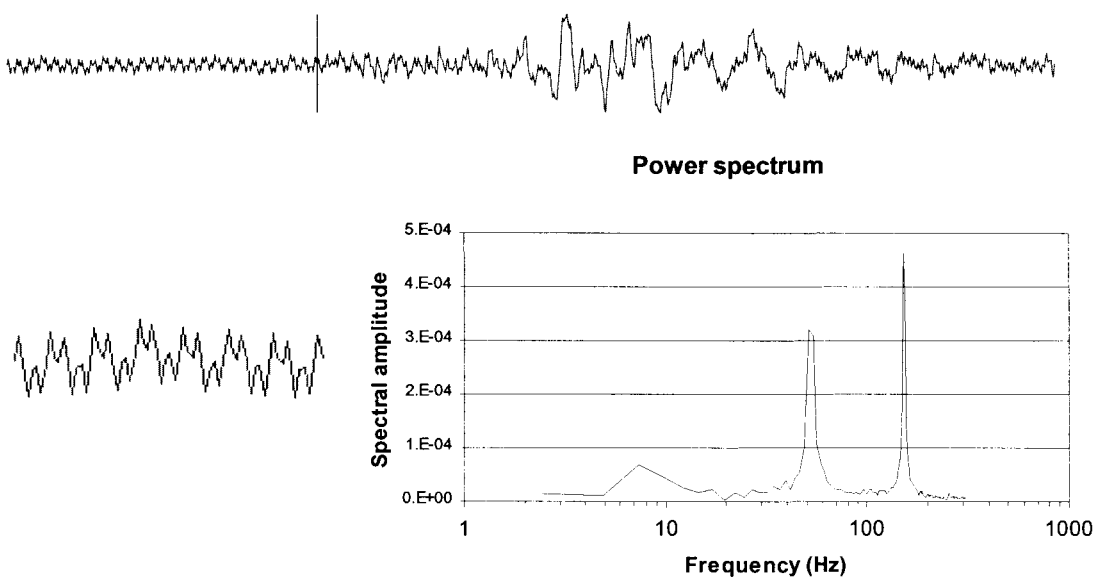

Figure 6.5: Examples of the spectrum computed from a seismogram contaminated by 50Hz noise signal. (a) Complete seismogram showing various arrivals (b) Section of seismogram showing 50Hz noise (c) Power spectrum computed from trace section shown in (b).

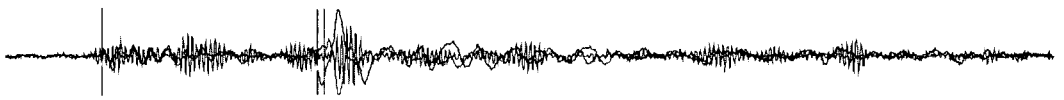

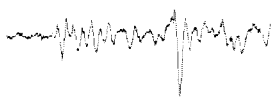

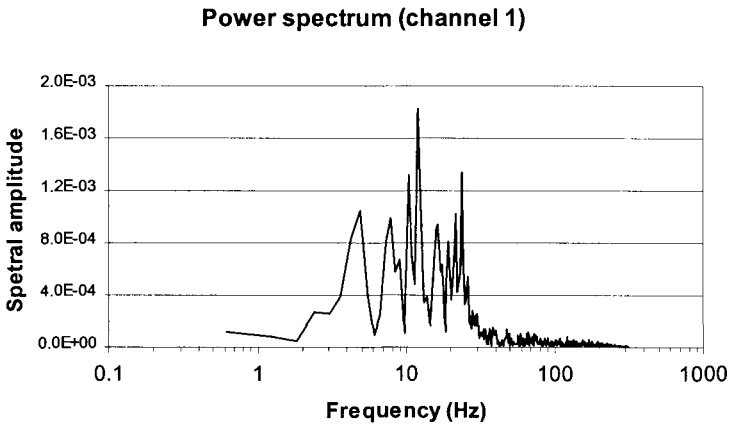

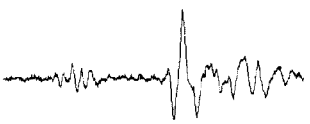

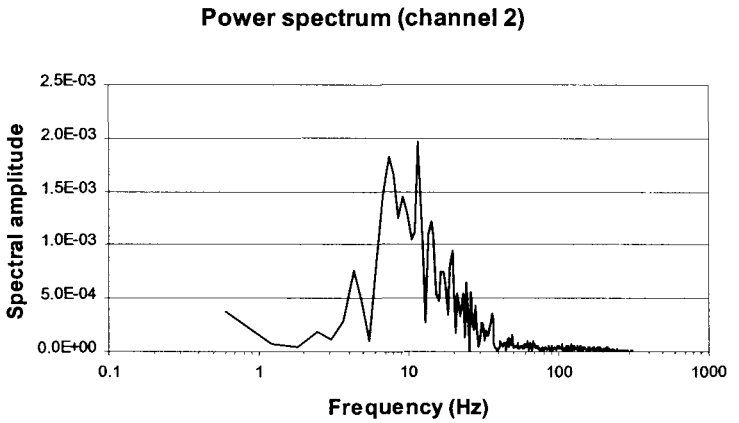

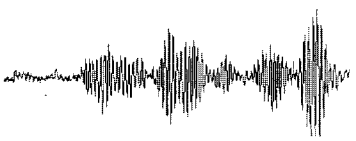

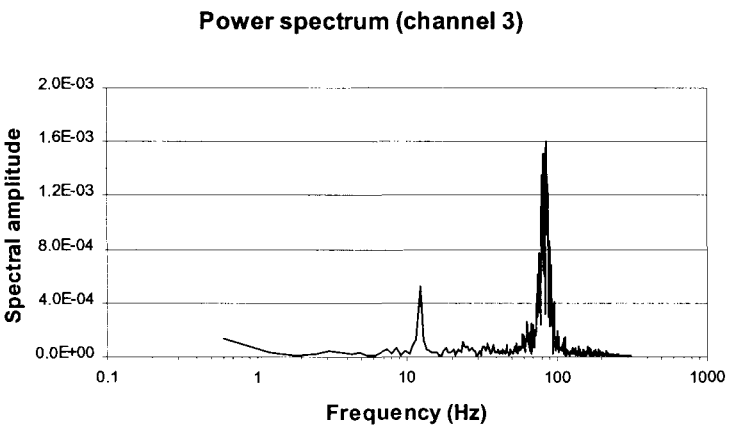

Figure 6.6: Examples of spectra computed for a seismogram where channel 3 shows a poorly oriented signal. (a) Complete 3-component seismogram (b) Waveform and power spectrum for component 1 (c) Waveform and power spectrum for component 2 (d) Waveform and power spectrum for component 3.

6.2.3 Effects of noise on moment tensor solutions

Noisy data has a considerable effect on moment tensor inversions, and results in the appearance of 'false' components in the solutions. Other unwanted effects are blurring of the radiation pattern and variations in the fault-plane solutions. These effects are briefly demonstrated using both synthetic and recorded data.

Figure 6.7(a) shows the radiation pattern and fault-plane solutions resulting from the absolute moment tensor inversion of synthetic data of a pure double-couple source having a strike of 20 degrees, dip of 60 degrees and rake of 0 degrees. The synthetic data is computed using Equations 2.15-2.21 and 2.47 for a network of seven triaxial geophones. The fault-plane solutions and three quantities (%ISO, %DC and %DC) describing the source mechanism are calculated from the moment tensor and are listed in the figures. %ISO is the percentage isotropic component (Equation 2.40), %DC is the percentage double-couple component (Equation 2.41) and %CLVD is the percentage compensated linear vector dipole (Equation 2.42) of the six component moment tensor. The percentage of 'false components' is calculated by adding magnitudes of %ISO and %CLVD because for a pure double-couple source, %DC should be ~100%, and %ISO and %CLVD should both be approximately zero.

It is evident from Figure 6.7(b) that the percentage of false components is ~8% (this value is not zero because of the less than perfect coverage of the focal sphere that results in a relatively poorly conditioned system of equations). In Figure 6.7(b), pseudo-random noise at a level of 40% (following the formulation given in Equation 7.1) has been applied to the input data. When this solution is compared with that of the noise-free case, the most obvious change is the blurring of the radiation pattern, indicating an increase in non-double-couple components. The percentage of false components increases from ~8% to ~22%. In addition, there is a slight decrease in the accuracy of the fault-plane solutions.

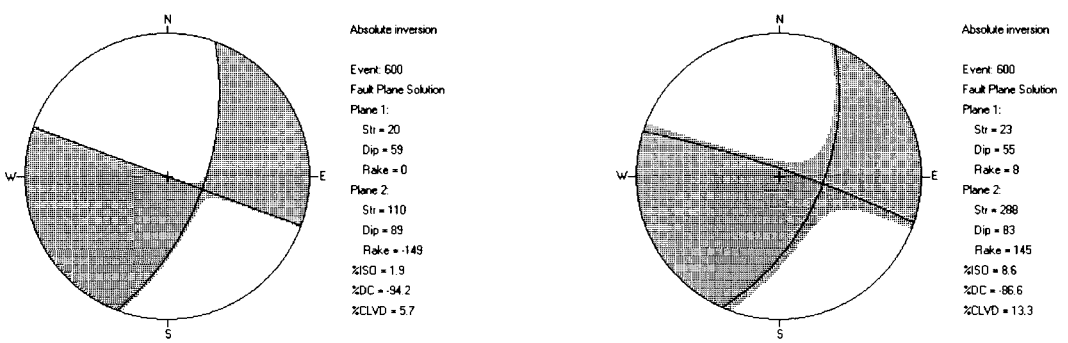

Figure 6.7: Radiation patterns and source parameters computed from synthetic data using the absolute moment tensor inversion technique. (a) Noise free case. (b) 40% random noise applied to all channels.

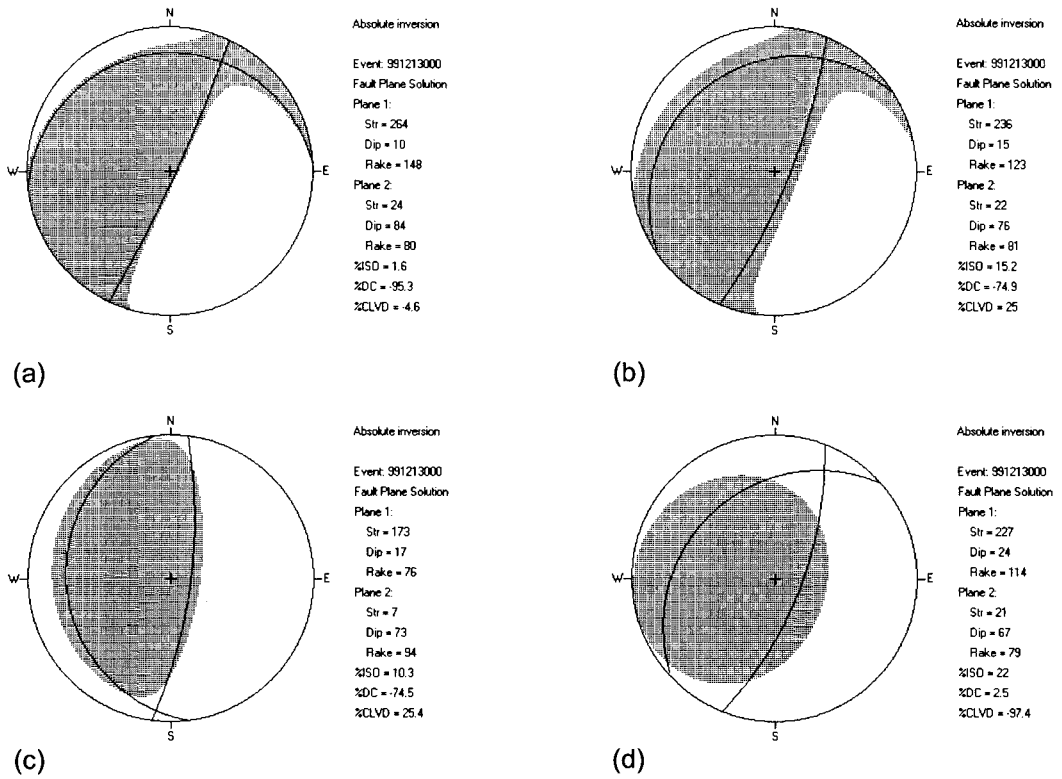

Figure 6.8: Radiation patterns and source parameters computed from recorded data using the absolute moment tensor inversion method (a) Control case, (b) 40% random noise applied to all channels, (c) reversed P- and S-wave polarities for site 1, and, (d) bad phase picks for P- and S-wave for site 1, component 1.

In Figure 6.8, a number of different forms of noise are inflicted on the input of the absolute moment tensor inversion. The results shown are computed using recorded data. Figure 6.8(a) shows the radiation pattern, fault-plane solutions and source parameters of the control case i.e. the solution computed from seismograms having accurate P- and S-wave picks where no synthetic noise has been applied. The percentage of false components is ~6%. The radiation pattern of this event becomes slightly blurred when 40% pseudo-random noise (Equation 7.1) is applied to the input data (Figure 6.8b). In Figure 6.8(c), the polarities of the waveforms recorded by site 1 have been reversed, and, Figure 6.8 (d) shows the effect that incorrect P-and S-wave picks have on the moment tensor solution (for site 1 and component 1). In all cases, except for the control case, the percentage of false components present in the solution increases as a result of the applied noise. This is accompanied by a blurring of the radiation pattern and change in the fault-plane solution.

6.3 HYBRID MTI METHODS

In this section, the aforementioned hybrid moment tensor inversion schemes are developed and described in greater detail. Before describing the mechanics of the methods, it is necessary to highlight the more important underlying assumptions that are involved.

6.3.1 Assumptions

All of the following hybrid schemes share a similar set of basic assumptions, which are summarised below.

1. Each seismic source in the cluster is deemed to be a point source. This is valid provided both the distance D of the recording site or observer from the source and the wavelength λ are much greater than the linear source dimension.

2. The source has the same time dependence at frequencies below the corner frequency, i.e. the usual synchronous source approximation is assumed.

3. The measurements (i.e. seismogram recordings) are made in the far-field.

4. The events in the cluster are not separated by more than one wavelength so that the raypath between each event in the source cluster and any particular recording site may be considered to be common to all the events in the cluster.

5. There is an adequate number of samples or measurements so that the problem is not underdetermined.

6. The majority of the measurements are sufficiently accurate.

7. A Gaussian distribution ('white' spectrum) of residuals or errors (difference or ratio between theoretical and recorded data) indicates that the parametric model is accurate, whereas a deterministic component (peak in spectrum) to the residuals indicates that the model is not accurate.

Two consequences arise from assumptions 5, 6 and 7. It is important to mention them since they are central to the hybrid methods. They are:

1. The degree to which a measurement is in error can be effectively estimated and, consequently, measurements can be corrected. In this study, the level of error for a particular observation is estimated by comparing the observed data to theoretical data. The residuals can be computed in a number of ways. For example, in Equation 6.12, the residual is defined as the ratio of theoretical to observed data, whereas, in Equation 6.17, it is defined as the difference between the observed and theoretical values. The observed data are then 'corrected' by means of a weighting scheme that is related (although indirectly) to the residuals. In the first and second schemes, the weighting factor is derived from the mean or median of the residuals (Equations 6.11 and 6.16). In the last scheme, the weighting factor is determined from the standard deviation of the residuals (Equation 6.19). The aim of these weighting schemes is to decrease the effect of a noisy observation on the system of equations and to attempt to correct for site effects (i.e. either amplification or damping of the signal due to local conditions at a particular site).

2. The corrections can be scaled according to the estimated magnitude of the errors. This concept can be illustrated by inspection of the weighting factor defined by

Equation 6.19. This weighting factor is inversely proportional to the square of the number of standard deviations the residual for that observation is away from the mean residual. Consequently, a noisy observation having a residual that lies 'far' from the mean residual would have a relatively small weighting, whereas a less noisy observation, having a residual lying closer to the mean residual, would have a higher weighting.

6.3.2 Conceptual outline of hybrid methods

The proposed hybrid methods involve computing the moment tensor components for each event in the cluster using absolute techniques (i.e. evaluating the Green's function) and subsequently applying a correction (or weighting), which is ascertained in a relative sense by considering all the events in the cluster. The relative aspect of the method is that a common raypath between each event in the source cluster and a particular receiver is assumed. For each source-receiver combination, each wavefront will experience similar wave propagation effects, however, some of the measurements at the receiver may be more accurate than others, for reasons previously discussed in this chapter.

This section describes the hybrid methods conceptually and the relevant equations are given in sections 6.3.3, 6.3.4 and 6.3.5. For a particular geophone site, channel and wave phase (P or S), it is reasonable to assume that the recordings of some events in the cluster are more accurate than others. Therefore, in order to increase the accuracy of each moment tensor, three weighting schemes are developed to downgrade the effect of the less accurate input data on the system of equations. Obviously, deciding which data points are more or less accurate than others is potentially highly subjective. In this study, the criterion is based on the distribution of the computed errors or residuals when measured data are compared with theoretical data. In this context, the term 'residual' is used rather loosely and refers to some relationship between the measured and observed data, for example a difference, ratio, or relative error.

Statistical theory shows that the distributions of the errors of measurement are remarkably regular, i.e. the distributions can be closely approximated by continuous curves referred to as normal error curves. Using this knowledge, the effect of outliers (data points whose residuals lie 'far' from the mean or median error) can be downgraded by the application of the relevant weighting. The errors or residuals indicate the extent of 'misfit' of the solution with the measured data, and are the result of a number of error sources. Such sources would include the errors originating from incorrect picks and/or poor identification of the various wave phases, low signal-to-noise ratios, deviations in the raypaths, and amplification or damping of the signal due to local site conditions, etc.

The concept of a weighting scheme is not a new one, and various schemes have been described in the literature. The method proposed by Udias & Baumann (1969) is perhaps the most relevant to this work. Their weighting scheme is based on the standard deviation of the residuals of the polarisation angles of the S-wave (Equation

3.13), and on the number of stations with inconsistent P-wave data. These two values are combined into a total error whose minimum is sought (Equation 3.14). The weighting scheme developed by these workers is based on the distribution of errors for individual events. In contrast to Udias & Baumann (1969), the weighting schemes proposed in this thesis are based on the residuals computed when measured data are compared with theoretical data (for a particular geophone site, channel and phase) and are calculated (for a particular geophone site, channel and phase) using all of the events in a cluster, rather than an individual event.

The weighting factors are computed in three different ways. In Scheme A, the weights are related to the mean of the distribution of residuals. This approach is probably the least robust of all the proposed schemes, since a single large outlying value can dominate the mean (and often does so, owing to the relatively small number of observations or 'data points'). Because of the problems associated with outliers, Scheme A is merely of academic interest but is included for comparative purposes and to emphasise the need for the schemes that follow. In Scheme B, the weights are related to the median of the distribution of residuals, so that the effect of a solitary outlier is diminished. In Scheme C, a weighting scheme is used which is based on a data point's distance (measured in standard deviations) from the mean error.

Once the weightings have been applied to the observations, a new set of moment tensor components is computed using the absolute technique. From the new set of moment tensors, a new set of weights is computed. The weights are then applied to the corrected observations, which are subsequently used as input to the absolute moment tensor inversion as before. (In addition to the weights determined from the residuals, Schemes A and B incorporate a second weighting factor to control the proportion of the weights applied with each iteration. The motivation for applying this secondary weighting factor is described in the sections to follow.) The process is applied iteratively until a predefined criterion or set of criteria is satisfied. Schemes A, B and C are illustrated conceptually in Figure 6.9.

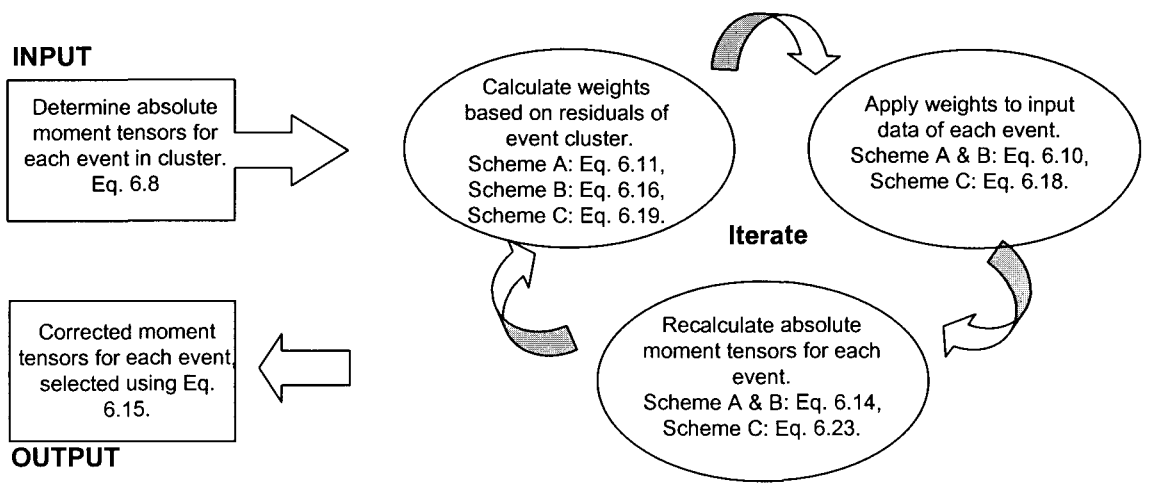

Figure 6.9: Conceptual flowchart illustrating the hybrid moment tensor inversion methods.

Each of the following weighting schemes are based on the absolute inversion method described in Chapter 3 by Equation 3.1 through to Equation 3.11. However, it is important to note that in this section the notation is extended slightly, to indicate that the equations are applied to an event (the i^{th} event) in a cluster (of N events), rather than to a solitary event. Accordingly, Equation 3.10 is rewritten as:

$$\mathbf{u}_i^{obs} = \mathbf{G}_i \mathbf{m}_i \qquad 6.1$$

where the subscript i indicates that Equation 6.1 applies to the i^{th} event in a cluster and the superscript *obs* indicates that the data contained in the $\mathbf{u}_i$ vector are observed values (to distinguish between theoretical values computed later in this section) . In this equation, $\mathbf{u}_i^{obs}$ is a vector of dimension M containing the observed ground displacements or spectral displacements for the i^{th} event, depending on whether the inversion is being in the time- or frequency-domain. $\mathbf{G}_i$ is a $M\times6$ matrix containing the Green's function's components describing the propagation effects between source and receiver for event i, and, $\mathbf{m}_i$ is a vector of dimension 6 containing the moment tensor components of the i^{th} event in the cluster.

Vectors or matrices are denoted using **bold** letters, and vector or matrix elements are given using the same letter but in *italics*. For example, $\mathbf{u}_i^{obs}$ is a vector of observed amplitude data for event i containing M elements of the form u_{ijkl} where:

- the first subscript i indicates the event number and $i = (1, 2, 3, \ldots, N)$ where N is the maximum number of events in the cluster;
- the second subscript j denotes the site number where $j = (1, 2, 3, \ldots, p)$ and p is the maximum number of geophone or observation sites;
- the third subscript k describes the component of the three component sensor and $k = (1, 2, 3)$;
- the fourth subscript l indicates the indicates wave phase such $l = 1$ for the P-phase and $l = 2$ for the S-phase.

Applying the conventions listed above, the elements contained in vector $\mathbf{u}_i^{obs}$ may be written explicitly as:

$$\mathbf{u}_i^{obs} = \left[u_{i111} \quad u_{i112} \quad u_{i121} \quad \cdots \quad u_{i132} \quad \cdots \quad u_{ip11} \quad u_{ip12} \quad u_{ip21} \quad \cdots \quad u_{ip32}\right]^T \qquad 6.2$$

The Green's function matrix $\mathbf{G}_i$ for the i^{th} event is comprised of elements of the form $G_{ijkl1}, G_{ijkl2}, G_{ijkl3}, \ldots, G_{ijkl6}$ where the first, second, third and fourth subscripts are as originally defined, and the fifth subscript describes the component of the Green's function that corresponds to a particular moment tensor component. This matrix is written explicitly as:

$$\mathbf{G}_i = \begin{bmatrix} G_{i1111} & G_{i1112} & G_{i1113} & \cdots & G_{i1116} \\ G_{i1121} & G_{i1122} & G_{i1123} & \cdots & G_{i1126} \\ G_{i1211} & G_{i1212} & G_{i1213} & \cdots & G_{i1216} \\ G_{i1221} & G_{i1222} & G_{i1223} & \cdots & G_{i1226} \\ G_{i1311} & G_{i1312} & G_{i1313} & \cdots & G_{i1316} \\ G_{i1321} & G_{i1322} & G_{i1323} & \cdots & G_{i1326} \\ G_{i2111} & G_{i2112} & G_{i2113} & \cdots & G_{i2116} \\ G_{i2121} & G_{i2122} & G_{i2123} & \cdots & G_{i2126} \\ \vdots & \vdots & \vdots & \ddots & \vdots \\ G_{ip321} & G_{ip322} & G_{ip323} & \cdots & G_{ip326} \end{bmatrix} \qquad 6.3$$

Each Green's function element can be evaluated using Equation 2.10 (and remembering that the total displacement is equal to the vector sum of the displacement components). For example,

$$G_{i1111} = \frac{1}{4\pi\rho\alpha^3 r} \cdot \left[\eta_{11} (\gamma_{i11})^3 + \eta_{12} (\gamma_{i11})^2 \gamma_{i12} + \eta_{13} (\gamma_{i11})^2 \gamma_{i13} \right] \qquad 6.4$$

where $\gamma_{ij1} = (x_{i1} - \xi_{j1})/r_{ij}$, $\gamma_{ij2} = (x_{i2} - \xi_{j2})/r_{ij}$, $\gamma_{ij3} = (x_{i3} - \xi_{j3})/r_{ij}$ are the direction cosines of the source-receiver vector where the source i is positioned at $x_i = (x_{i1}, x_{i2}, x_{i3})$ and the receiver j at $\xi_i = (\xi_{i1}, \xi_{i2}, \xi_{i3})$; $\eta_{k1}, \eta_{k2}, \eta_{k3}$ are the direction cosines describing the orientation of each component comprising the triaxial geophone where index k indicates the component of the sensor; ρ indicates density; α is the P-wave velocity; and, r is the source-receiver distance such that $r = |x - \xi|$.

The vector of moment tensor components of the i^{th} event, $\mathbf{m}_i$, are given by:

$$\mathbf{m}_i = \begin{bmatrix} m_{i1} & m_{i2} & m_{i3} & \ldots & m_{i6} \end{bmatrix} \qquad 6.5$$

where

$$m_{i1} = M_{11}, m_{i2} = M_{12}, m_{i3} = M_{13}, m_{i4} = M_{22}, m_{i5} = M_{23}, m_{i6} = M_{33} \qquad 6.6$$

and M_{11}, M_{12}, M_{13} etc. are the Cartesian moment tensor components defined by Equation 2.22 and illustrated in Figure 2.11 in the coordinate system of the seismic network.

Considering each equation of the system of equations given by Equation 6.1, the displacement of the i^{th} event recorded at the j^{th} site for geophone component k and phase observation l is related to the components of the Green's functions and moment tensor components by:

$$u_{ijkl}^{obs} = \sum_{r=1}^{6} G_{ijklr} m_{ir} \qquad 6.7$$

where the G_{ijklr} and m_{ir} are as defined in Equations 6.3 and 6.5.

6.3.3 Scheme A - mean correction

1. Consider a cluster of N events. The components of the moment tensor $\mathbf{m}_i$ of the i^{th} event in the cluster can be computed by writing Equation 6.1 as an inverse problem and solving for the vector $\mathbf{m}_i$ such that:

$$\mathbf{m}_i = \mathbf{G}_i^{-1} \mathbf{u}_i^{obs} \qquad 6.8$$

where $\mathbf{G}_i^{-1}$ is a $6 \times M$ matrix and is the generalised inverse of $\mathbf{G}_i$. Since M > 6 the system of equations is overdetermined and Equation 6.8 is solved using the method of least-squares (Appendix C). This approach fits the set of known amplitude data of event i, $\mathbf{u}_i^{obs}$, to a Green's function matrix, $\mathbf{G}_i$, by computing the most statistically suitable moment tensor $\mathbf{m}_i$ for that event.

2. Once the moment tensors $\mathbf{m}_i$ are computed for each event i in the cluster, the theoretical displacements are $\mathbf{u}_i^{th}$ computed using the forward calculation:

$$\mathbf{u}_i^{th} = \mathbf{G}_i \mathbf{m}_i \qquad 6.9$$

In general, $\mathbf{u}_i^{th} \neq \mathbf{u}_i^{obs}$ because the system is overdetermined, and the $\mathbf{m}_i$ are the results of the least-squares fit. This fact plays a critical role in the process of hybrid inversion because if $\mathbf{u}_i^{th} = \mathbf{u}_i^{obs}$ the weighting scheme would have no effect (since the correction would equal zero).

3. A correction or weighting determined by consideration of all the events in the cluster is applied to the input displacements such that:

$$u_{ijkl}^{new} = u_{ijkl}^{old} + \underbrace{a_{jkl} \cdot u_{ijkl}^{old}}_{\text{Correction factor}} \qquad 6.10$$

where a_{jkl} is a compound weighting function and $u_{ijkl}^{old} = u_{ijkl}^{obs}$ for the first iteration only since u_{ijkl}^{old} will be different for each iteration as a result of the correction applied in Equation 6.10.

The compound weighting function a_{jkl} is defined according to:

$$a_{jkl} = w_{IterNo} \cdot \left(\bar{r}_{jkl} - 1\right) \qquad 6.11$$

In Equation 6.11, w_{IterNo} is an attenuation function that ranges between 0 and 1 and controls the amplitude of the applied correction or weighting. The term in brackets $\left(\bar{r}_{jkl} - 1\right)$ is a smoothing function determined from the mean ratio $\bar{r}_{jkl}$ between the theoretical $\mathbf{u}_i^{th}$ and observed $\mathbf{u}_i^{obs}$ displacements for the j^{th} site, k^{th} component and l^{th} phase and is computed according to:

$$\bar{r}_{jkl} = \frac{1}{N_{eq}} \sum_{i=1}^{N_{eq}} \left(\frac{u_{ijkl}^{th}}{u_{ijkl}^{obs}} \right) \qquad 6.12$$

where N_{eq} is the number of equations and is less than or equal to the number of events N in the cluster. N_{eq} would be less than the total number of events in the cluster if one or more of the geophones were inactive during the occurrence of an event, as is often the case in a mine seismic network. Since the mean ratio $\bar{r}_{jkl}$ is computed using all the events in the cluster (for i = 1 to N_{eq}) for each site (subscript j), component (subscript k) and phase (subscript l) the $\left(\bar{r}_{jkl} - 1\right)$ term may be thought of as a 'site correction'.

The motivation for using w_{IterNo} is to introduce the correction or weighting gradually in order to gauge the smoothness (or otherwise) of the method's convergence. The selection of w_{IterNo} is subjective and a number of other functions could be used. In this study, w_{IterNo} is calculated using:

$$w_{IterNo} = \frac{10^{(IterNo-1)/10}}{10} \qquad 6.13$$

i.e. w_{IterNo}= {0.10, 0.12, 0.15, 0.19, 0.25, 0.32, 0.40, 0.50, 0.63, 0.79, 1.0}. It is evident from the formulation that the maximum number of iterations is 11 and that the weight of the applied correction increases slowly at the beginning of the iterative procedure, and accelerates during the final stages.

The usage of w_{IterNo} could be controversial if it were defined as a decreasing function. If the function were defined such that it decreased from 1 to 0 with increasing iteration number *IterNo*, and the residuals were also noted to decrease, it could be argued that the sympathetic decrease in residuals was a consequence of the attenuation function w_{IterNo}, rather than due to the smoothing function $\left(\bar{r}_{jkl} - 1\right)$. However, this is not the case in this study since w_{IterNo} is defined such that it increases with increasing iteration number. The decrease in residuals with increasing iteration number for five different recording sites is shown in Figure 6.10(a). This graph is discussed in more detail in section 6.3.6.

The $(\bar{r}_{jkl} - 1)$ term of Equation 6.11 behaves like a smoothing function. When $u_{ijkl}^{th} = u_{ijkl}^{obs}$ for all events in the cluster (i.e. for i = 1 to N_{eq}), $\bar{r}_{jkl}$ would equal 1, and as a result, $a_{jkl} = 0$. In other words, when the theoretical and observed values of displacement are equal, no correction would be applied. This is hardly ever the case for recorded data and would only occur using synthetic data.

When $u_{ijkl}^{th} \approx u_{ijkl}^{obs}$ for most of the events in the cluster, $\bar{r}_{jkl} \approx 1$ resulting in a_{jkl} being a small value close to zero. In this case, since the observed and theoretical displacements are so similar, the observed data can be considered to have a high degree of accuracy. A very small correction would be applied to the relatively more accurate observed data.

If $u_{ijkl}^{th} > u_{ijkl}^{obs}$ for most of the observed and theoretical displacements, then $\bar{r}_{jkl} > 1$ (Equation 6.12). As a result, a_{jkl} will be positive and the correction will be added to the observation. This assumes $u_{ijkl}^{th} > u_{ijkl}^{obs}$ implies that the observations at the geophones are being underestimated (due to site effects, noise, etc.) and therefore require amplification.

The reverse is true if $u_{ijkl}^{th} < u_{ijkl}^{obs}$ for most of the equations. In this case, $\bar{r}_{jkl} < 1$ and a_{jkl} will be negative. Consequently, the correction will be subtracted from the observation. It is assumed that $u_{ijkl}^{th} < u_{ijkl}^{obs}$ implies that the observations are being overestimated and therefore require damping.

Since the correction factors (which are different for each observation) applied to the input data in Equation 6.12 differ from iteration to iteration, u_{ijkl}^{new} is not a linear function of u_{ijkl}^{old}, and as a result, the weighting scheme is non-linear. The implication of the non-linearity is that the end result of the multi-step process having a variable weighting (described by the attenuation function, Equation 6.13) will not be the same as the results determined directly using a constant weight.

The non-linearity is evident when the moment tensor components given in Tables 6.2(a) and 6.2(b) are compared. Table 6.2(a) gives the moment tensor components and associated normalised standard error computed using the multi-step process having weights that vary according to Equation 6.13. The results reported in Table 6.2(a) are those at iteration 8 (i.e. where w_{IterNo} = 0.5). The moment tensor solutions listed in Table 6.2(b) were computed using a constant weight, w_{IterNo} = 0.5. Comparison of the results in the two tables shows that the results differ and illustrate the non-linearity of the iterative system.

Table 6.2(a): Moment tensor solutions of six synthetic events computed using the multi-step iterative process at $w_{IterNo} = 0.5$ (iteration 8).

Event ID	Ratio*	Cartesian moment tensors (10^9 N.m) rotated into geographical (North, East, Down) system					
		M_{11}	M_{12}	M_{13}	M_{22}	M_{23}	M_{33}
100	0.24	-1.434	-0.964	1.071	-1.385	-2.695	-5.215
200	0.26	-2.468	-1.731	2.491	-2.900	-1.541	-4.223
300	0.20	-1.311	-4.033	3.745	-5.787	4.017	0.202
400	0.21	-0.894	1.665	2.317	1.902	-6.890	-3.221
500	0.27	-3.782	3.457	-2.684	3.918	-2.956	-0.459
600	0.27	-4.149	4.772	2.757	4.924	-3.836	-2.032

* Ratio = Standard error normalised to scalar seismic moment (Equation 6.15)

Table 6.2(b): Moment tensor solutions of six synthetic events computed using a single step and $w_{IterNo} = 0.5$ (non-iterative process).

Event ID	Ratio*	Cartesian moment tensors (10^9 N.m) rotated into geographical (North, East, Down) system					
		M_{11}	M_{12}	M_{13}	M_{22}	M_{23}	M_{33}
100	0.25	-1.424	-0.945	0.760	-1.355	-2.756	-5.265
200	0.26	-2.424	-1.671	2.012	-2.817	-1.583	-4.215
300	0.20	-1.216	-3.874	3.341	-5.580	4.017	0.266
400	0.21	-0.894	1.607	2.340	1.837	-6.885	-3.271
500	0.27	-3.763	3.363	-2.509	3.814	-2.966	-0.503
600	0.27	-4.134	4.683	2.755	4.829	-3.816	-2.043

* Ratio = Standard error normalised to scalar seismic moment (Equation 6.15)

4. A new set of moment tensors is then recomputed for each event using the corrected data:

$$\mathbf{m}_i^{new} = \mathbf{G}_i^{-1}\mathbf{u}_i^{new} \qquad 6.14$$

5. Return to step 2 and recompute the theoretical displacements using Equation 6.9, from which a revised correction can be computed as in steps 3 and 4. If the attenuation function w_{IterNo} is used, the maximum number of iterations is 11. If w_{IterNo} is set to a constant, any number of iterations can be performed. Iterating through this sequence, the 'best' solution is identified on the basis of the minimum standard error normalised against the scalar moment:

$$\frac{E}{M_o} \qquad 6.15$$

where the scalar seismic moment M_o is computed from the moment tensor components according to Equation 2.23, and the standard error E is calculated using Equation C.3 (Appendix C). Equation 6.15 has no influence on the iterative procedure and is merely a normalisation procedure introduced to allow comparisons of the standard errors between iterations. It is necessary because the amplitudes of the linear equations are affected by the weighting scheme, causing changes in the magnitude of the standard error.

Since the *mean* error ratio contributes to the site correction, this scheme is very sensitive to outliers (outliers are defined as the minimum or maximum values of the ratio described by Equation 6.12). Outliers with large magnitudes will tend to swamp the correction, biasing it towards the less accurate data. For this reason, a Scheme B is developed, where the site correction is based on the median.

6.3.4 Scheme B – median correction

This scheme is almost identical to Scheme A, with one exception: Equation 6.12 is replaced by:

$$\bar{r}_{jkl} = median\left(\frac{u^{th}_{ijkl}}{u^{m}_{ijkl}}\right)_{i=1,Neq} \qquad 6.16$$

where $\bar{r}_{jkl}$ is the *median* ratio (in contrast to the *mean* ratio) of the residuals between the theoretical $\mathbf{u}^{th}$ and measured $\mathbf{u}^{m}$ displacements for the j^{th} site, k^{th} component and l^{th} phase. N_{eq} is the number of equations and is less than or equal to the number of events in the cluster, as before.

In the case of a normal distribution of residuals, the mean and median will be the same, and Scheme B will give the same results as Scheme A. However, if the distribution is skewed, the mean and median residuals will differ and the methods will give different results.

Note that all the points of discussion (most importantly, those in Step 3 of Section 6.3.3) apply to this section, and the variation of the residuals with increasing iteration number for five different recording sites is shown in Figure 6.10(b). As alluded to earlier, this graph is discussed in more detail in section 6.3.6.

6.3.5 Scheme C – weighted mean correction

Schemes A and B are very similar, differing only in the definition of $\bar{r}_{jkl}$. This scheme differs from the previous two schemes because the residuals are computed from the differences between the observed and theoretical displacements (rather than the ratio of theoretical to observed displacement) and the weighting function is relatively simple (in contrast to the complex weighting function that consisted of an attenuation

function and a smoothing function). As before, the scheme is described in a stepwise fashion.

1. Calculate the theoretical displacements $\mathbf{u}^{th}$ from Equation 6.9 after solving Equation 6.8 in a least-squares sense (as for steps 1 and 2 in Scheme A and B).

2. For the i^{th} event in the cluster, j^{th} site, k^{th} component and l^{th} phase, the residuals ε_{ijkl} between the theoretical and measured or observed displacements are calculated according to:

$$\varepsilon_{ijkl} = u_{ijkl}^{obs} - u_{ijkl}^{th} \qquad 6.17$$

3. A weighting factor (ω_{ijkl}) is determined from the residuals of all the events in the cluster and is applied to the input data in the following way:

$$u_{ijkl}^{new} = \omega_{ijkl} \cdot u_{ijkl}^{old} \qquad 6.18$$

where $u_{ijkl}^{old} = u_{ijkl}^{obs}$ for the first iteration and ω_{ijkl} is computed using:

$$\omega_{ijkl} = \frac{1}{1 + d_{ijkl}^2} \qquad 6.19$$

In Equation 6.19, d_{ijkl} is the number of standard deviations the residual ε_{ijkl} is away from the mean residual $\bar{\varepsilon}_{jkl}$ (for event i, site j, component k and phase l) defined by:

$$d_{ijkl} = \frac{\varepsilon_{ijkl} - \bar{\varepsilon}_{jkl}}{s_{jkl}} \qquad 6.20$$

where s_{jkl} is the unbiased standard deviation of the residuals. The mean residual $\bar{\varepsilon}_{jkl}$ and unbiased standard deviation s_{jkl} of the residuals are computed using Equations 6.21 and 6.22, respectively:

$$\bar{\varepsilon}_{jkl} = \frac{1}{N_{eq}} \sum_{i=1}^{N_{eq}} \varepsilon_{ijkl} \qquad 6.21$$

$$s_{jkl} = \sqrt{\frac{1}{(N_{eq} - 1)} \sum_{i=1}^{N_{eq}} \left(\varepsilon_{ijkl} - \bar{\varepsilon}_{jkl}\right)^2} \qquad 6.22$$

If $u_{ijkl}^{th} = u_{ijkl}^{obs}$ for all events in the cluster (i = 1 to N_{eq}) for a particular site (and component and phase), the standard deviation s_{jkl} will be zero, and ω_{ijkl} = 1. (When s_{jkl} = 0, Equation 6.20 is undefined and some exception handling in the

computer code is necessary). Since $\omega_{ijkl}=1$, no change will be made to the observed data in Equation 6.18 (as mentioned before, this will rarely be the case for real, recorded data).

If $u_{ijkl}^{th} \approx u_{ijkl}^{obs}$ for most of the events in the cluster, the standard deviation s_{jkl} will be small, and ω_{ijkl} will be close to 1 (such that $\omega_{ijkl} < 1$), and very little change will be made to the observed data.

If some of the data are noisy, and $u_{ijkl}^{th} \neq u_{ijkl}^{obs}$ for several events in the cluster, the standard deviation will be larger, and $\omega_{ijkl} << 1$. As a result, ω_{ijkl} will have a damping effect on the noisy data.

The variation of the residuals with increasing iteration number for five different recording sites is shown in Figure 6.10(c) to illustrate the decrease in residuals after application of the correction. More detail is given in Section 6.3.6.

4. A new set of moment tensor components is then recomputed for each event using the corrected data:

$$\mathbf{m}_i^{new} = \mathbf{G}_i^{-1}\mathbf{u}_i^{new} \qquad 6.23$$

5. As with the other schemes, this one can be applied iteratively by returning to step 2 and repeating the process. However, in contrast, the maximum number of iterations is not limited. Once again, the 'best' solution is identified on the basis of the minimum standard error normalised against the scalar moment (Equation 6.15).

This scheme shares a common characteristic with Scheme A – a sensitivity to outliers because the correction or weighting is dependent on the standard deviation of the normal distribution.

6.3.6 Comparison of the variation of the residuals with iteration

In this section, a comparison of the behaviour of the residuals of Schemes A, B and C is presented. The three schemes are applied to the same set of synthetic data (computed using Equations 2.15-2.21 and 2.47, Chapter 2) to which 20% pseudo-random noise (defined by Equation 7.1) had been applied.

Figures 6.10(a), 6.10(b) and 6.10(c) shows the variation of the residuals of event 1, component 1 and phase 1 (i.e. the P-wave) for five recording sites computed using Scheme A, Scheme B and Scheme C. In the figures, the dashed line represents the point on the y-axis where the theoretical displacements are equal to the observed displacements (i.e. $u_{ijkl}^{th} = u_{ijkl}^{obs}$ for all events in the cluster). This is the point where no correction would be applied to the observed data (because the compound weighting function of Schemes A and B would equal zero, and the weighting factor of Scheme C would equal 1).

(a)

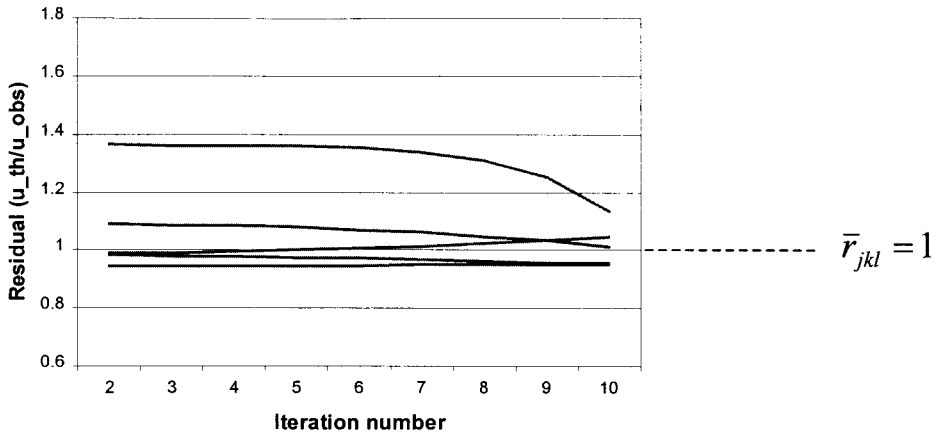

(b)

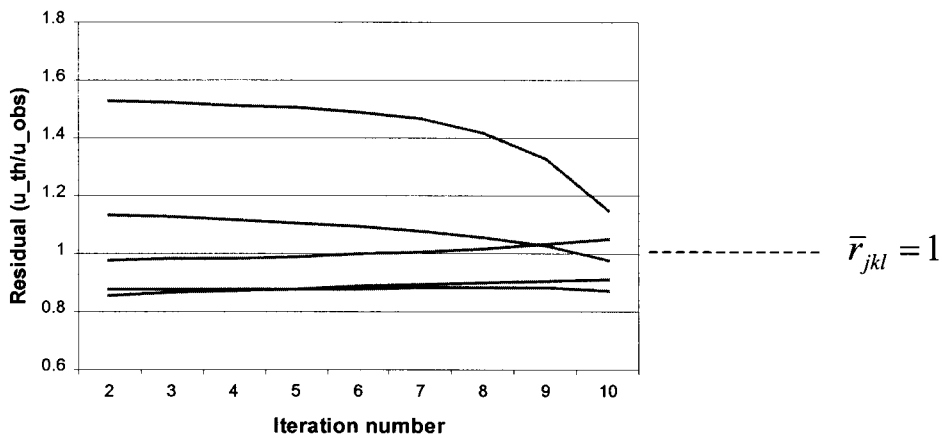

(c)

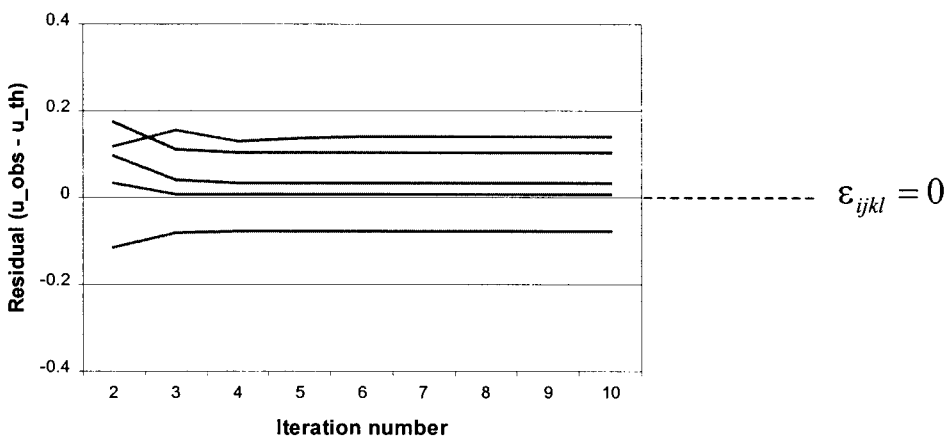

Figure 6.10: Variation in residuals of event 1, component 1 and the P-phase for five recording sites for (a) Scheme A - mean correction, (b) Scheme B - median correction, and, (c) Scheme C - weighted mean correction.

The trends of the residuals shown in Figures 6.10(a) and 6.10(b) are very similar. In both figures, the residuals above and below the dashed line converge towards the point where the theoretical displacements would equal the observed displacements for all events in the cluster at some point during the iterations. The convergence accelerates towards the end of the iterations because of the increased weights of the attenuation function.

As with the previous figures, the residuals shown in Figure 6.10(c) converge towards the point where the theoretical displacements would equal the observed displacements for all events in the cluster. The most rapid change occurs at the beginning of the iterations, after which the residuals remain more or less constant.

6.4 MOMENT TENSOR INVERSION TOOLBOX

The author has written a computer program that performs a number of different moment tensor inversions – the moment tensor inversion toolbox (Figure 6.11). This program performs was written using Delphi 5. The moment tensor inversion toolbox performs six moment tensor inversion methods, *viz.* absolute (single event) moment tensor inversions, relative moment tensor inversion with and without reference mechanisms, and hybrid moment tensor inversion using mean, median and weighted mean corrections.

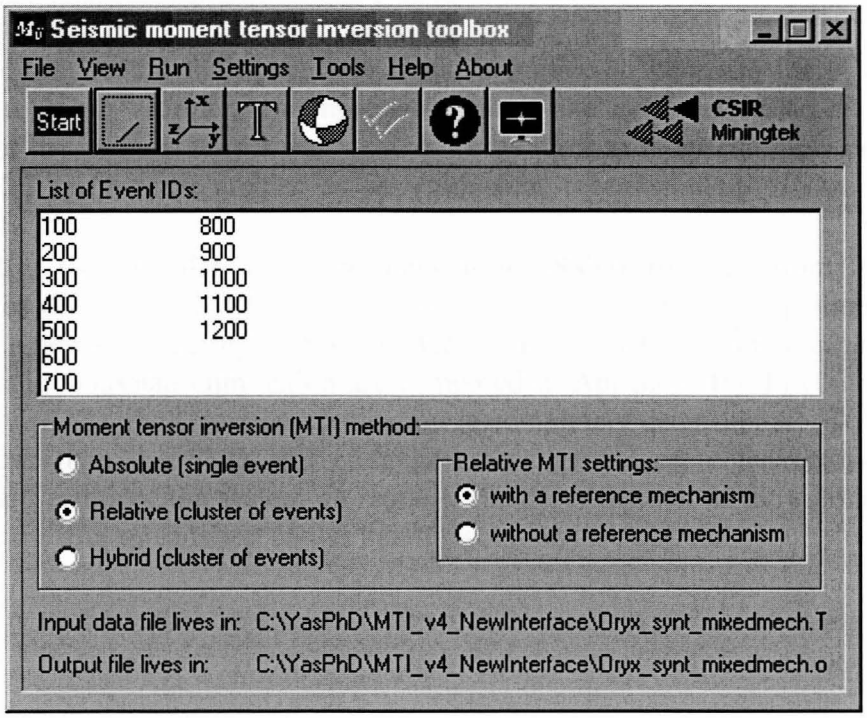

Figure 6.11: Interface of the moment tensor inversion toolbox

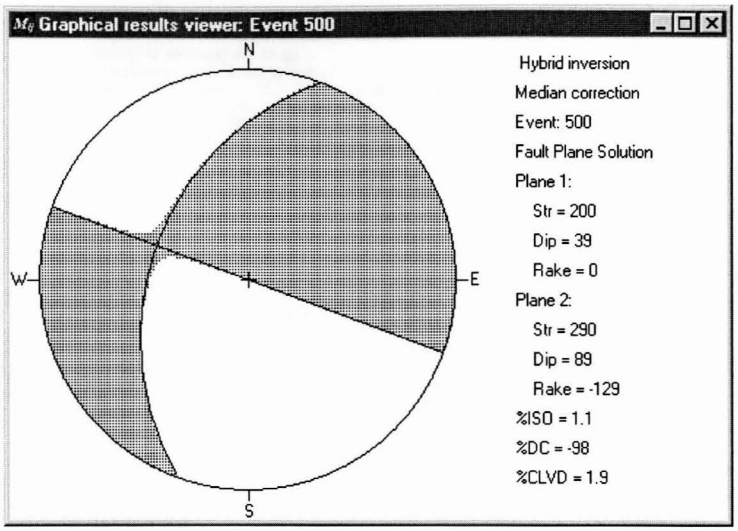

Figure 6.12: An example of an image generated by the MTI toolbox. The images can be saved to disc as bitmaps or copied to the Windows clipboard and pasted into documents.

- A text file viewer was added for rapid viewing of the output text files (Figure 6.13).
- The different moment tensor inversion methods could now be easily tested and compared with one another (these comparisons form the bulk of Chapter 7). This aided the research tremendously.
- A procedure to compute the fault-plane solution (strike, dip and rake of the fault plane and auxiliary plane) for a particular moment tensor was written.
- In addition to the fault-plane solutions, a routine to compute the P (principal tension axis), T (principal compressional axis) and B (intermediate or null axis) axes of the moment tensor was written. These three axes are routinely determined in focal mechanism studies as an equivalent representation of double-couple sources.
- Initially, the singular value decomposition (SVD) routines from Numerical Recipes (Press *et al.*, 1990) were used to solve the system of equations. In this work, a new solution engine based on Gaussian elimination techniques is used (the SVD and Gaussian elimination are compared in Appendix H). In contrast to the iterative SVD, the Gaussian elimination is completely deterministic. This method is faster than the SVD and computes the eigenvalues, eigenvectors and the standard errors of the system on request. Hand verification of the solution engine by means of a spreadsheet shows that the solutions are correct.

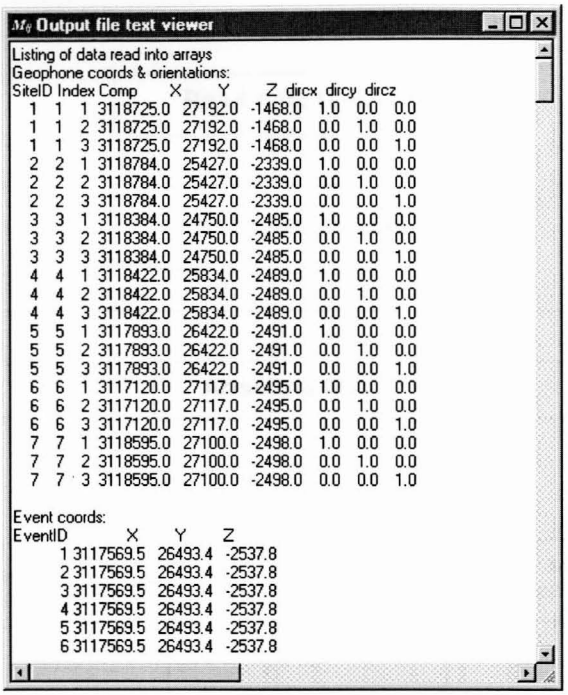

Figure 6.13: An example of an output file displayed by the text viewer

6.4.2 Program structure

The structure of the program is given in the flowchart in Figure 6.14. The structure of the moment tensor inversion toolbox is modular, written using a top-down design technique. The program may be divided into four main steps. In the first step, the data are read into various arrays and records, and the values of some constants are determined (e.g. number of events in the cluster, number and orientation of geophones). The next step involves performing some preliminary calculations (e.g. computing the azimuth and take-off angle of each ray, rotating the wave phases, computing the Green's functions where necessary) in order to set up the system of equations. The system of equations for each of the methods is solved in the third step using the same generic solution engine. The final step is to facilitate interpretation of the moment tensor components computed in the previous step. The moment tensors are rotated into the geographical coordinate system, the fault-plane solutions are determined, a number of source parameters are computed and, at the request of the user, the corresponding radiation patterns are plotted.

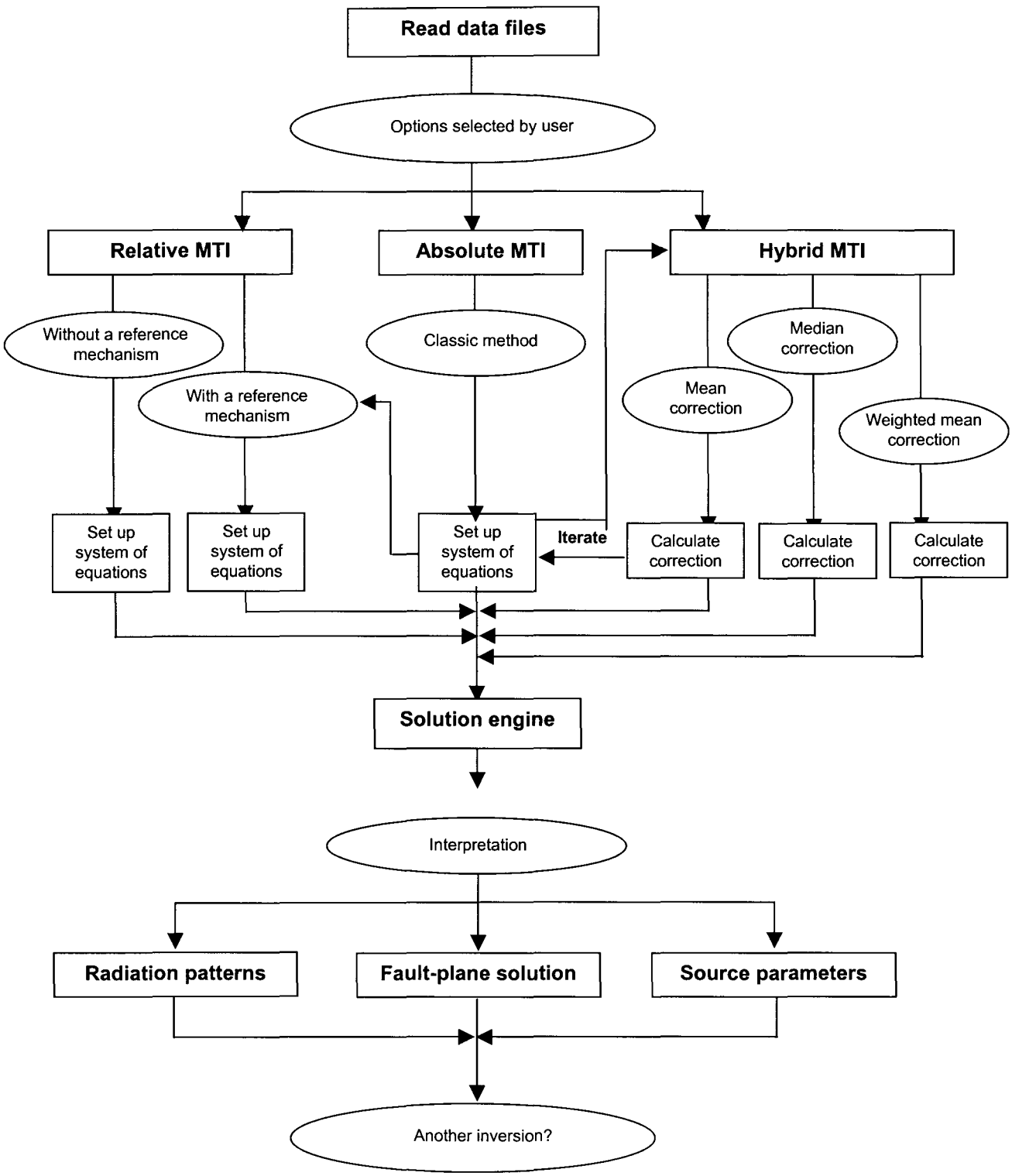

Figure 6.14: Flowchart illustrating the main computational steps (units) in the MTI toolbox

6.4.3 Equations implemented in program

Before outlining the equations implemented in the moment tensor inversion toolbox, some salient points are reiterated.

- In all methods, it is assumed that the point source approximation holds so that all equivalent forces occur at a seismic point source (Pujol & Herrmann, 1990). It also assumed that the equivalent forces act very simply in time, as a pure impulse (i.e. a delta function). As a result, the moment tensor components are time-independent and describe a static source mechanism.
- These assumptions have the effect of simplifying the problem tremendously. The trade-off is that the inversion methods do not apply to complex events, or to those recorded in the near-field. However, since the purpose of this section is to investigate the performance and resolving power of the hybrid methods under various conditions and not to resolve complex sources, the assumptions are satisfactory.
- The relative and hybrid methods apply to tightly clustered groups of events, so that the common raypath assumption holds.
- All the inversions are performed in the frequency-domain.
- The solution engine is based on the Gaussian elimination scheme described in Appendix E and used by RMTI (Chapter 4).

Absolute moment tensor inversion

The absolute method treats each event separately and, therefore, can be performed on single events or on groups of events that are not necessarily clustered. The system of equations given in Equation 6.1 forms the basis of this method. The Green's functions are computed using the far-field portion of Equation 2.10 (see Equation 6.3).

Relative MTI with a reference mechanism

The relative inversion using a reference mechanism relies on at least one event in the cluster having a 'good' solution. Two inversions are applied: a preliminary absolute inversion is performed on all events in the cluster, and the event with the lowest condition number is used as a reference event in the relative inversion. The magnitude of the condition number is dependent on the number of equations for that event, and the number of equations present is, in turn, dependent on the number of geophone sites triggered and the signal-to-noise ratio (seismograms with very poor signal-to-noise ratios are not written to the input data file). Therefore, using this criterion as the basis for the selection of a reference event is relatively robust. Other selection criteria included choosing the event with the lowest standard error normalised to scalar seismic moment. The problem with this, however, was that those events having insufficient equations and resulting in poorly conditioned systems, showed the lowest normalised standard error. The relative moment tensor inversion coded follows the formulation given by Dahm (1995) in Equation 4.20.

Relative MTI without a reference mechanism

The relative moment tensor inversion without a reference mechanism can be applied to groups of events having different radiation patterns. (This can be ascertained by a preliminary run using the absolute method.) However, this method shows limited success when the data are noisy, the source mechanisms similar, or when the coverage of the focal sphere is sparse.

The relative moment tensor inversion without a reference mechanism coded for the MTI toolbox follows the formulation given by Dahm (1995) (Equation 4.23). In contrast, RMTI (described in Chapter 4, Section 4.4) applied the system of equations given by Equation 4.27. Inspection of the formulation given by Equation 4.23 reveals that the source event occurring along the diagonal plays a dominant role in the solution. In fact, the solutions for the other sources in the cluster will be biased towards that of the reference event. To counteract this biasing effect, Dahm (1996) proposes an unweighted relative inversion without a reference mechanism. However, this formulation (Equation 4.27) has extensive memory requirements (Appendix H), limiting the number of events that can be processed at one time in a source cluster. To reduce the memory requirements, the author applies Equation 4.23, N times where N is the number of events in the cluster, each time using a different event as a reference mechanism. Only the solution of the reference event is accepted each time (the first six elements of the solution vector given by Equation 4.26). In this way, the biasing effect caused by the reference event is not problematical because the solution for each event is weighted towards itself.

Several other modifications are applied. A root-mean-square normalisation procedure is introduced to prevent the larger magnitude events from 'swamping' the smaller magnitude events.

In addition, the constraint to avoid a null solution is modified – instead of setting the constant in the constraint given by Equation 4.22 to an arbitrary value, it is computed by summing the moment tensor components calculated by the absolute method according to:

$$\text{constant} = \sum_{j=1}^{n} \sum_{i=1}^{6} m_{ij} \qquad 6.24$$

where n is the number of events in the source cluster and m_{ij} are the moment tensor components computed for the i^{th} event for the j^{th} component using the absolute moment tensor inversion method (Equation 6.1).

Hybrid MTI

The three hybrid methods developed and applied in the thesis are iterative. The starting point is to perform an absolute inversion (Equation 6.1) on each event in the cluster, and use the distribution of residuals in a relative sense to determine a correction or weighting. The residuals are computed using Equation 6.12 for the mean

and median weighting schemes, and using Equation 6.17 for the weighted mean correction scheme. For mean and median weighting schemes, the mean and median ratios are computed according Equation 6.12 and Equation 6.16. From these ratios, the weighting factor is determined according to Equation 6.11. For the third scheme, the weighting factor is calculated using Equation 6.19.The weighting factors are applied according to Equation 6.10 for the first two schemes, and using Equation 6.18 for the third scheme. The corrections are then applied to the observations and a new set of moment tensor components is computed using the absolute methods. A new relative correction is determined and the process is repeated. This process is applied repeatedly and the solution having the minimum standard error of the least-squares matrix (normalised to the scalar seismic moment) is selected as the most accurate solution (Equation 6.15).

6.4.4 Input data file generation

In contrast to the RMTI code, the moment tensor inversion toolbox reads all the required information from one file generated by AURA. The basic input required by the toolbox consists of: the positions and orientations of the geophones in local coordinates, the event locations in local coordinates, the spectral plateaus of the displacement spectrum for the P- and S-phases, and, the polarities of these phases. At this point, a comment on the polarities is pertinent. The polarities of the dominant motion of the wave phase are used in the inversion because the spectral plateaus reflect the frequencies dominating the signal. As a result, the output moment tensor describes the dominant source mechanism. The polarities are automatically determined by cross-correlating the observed and theoretical seismograms following the method proposed by Spottiswoode (1984).

It is also important to mention how the input required by the moment tensor inversion toolbox (which is generated using AURA) differs from that required by RMTI (created partly by hand and partly by various PSS programs). The input to RMTI consisted of the peak or peak-to-peak amplitudes of the P-, SV- and SH-phases measured from the time-integrated displacement traces to which a low-pass filter had been applied. In addition to the amplitudes, the polarities of these phases were also used. Both P and S-phases were used simultaneously to assist in constraining the moment tensor components by adding different types of governing equations to the linear inversion problem.

The RMTI input data files were painstakingly created by hand after careful inspection of each individual waveform. This method of creating a data file in the mining environment would be prohibitively time-consuming - hence the need for the development of more efficient method to generate data files for routine application to mining-induced tremors.

In contrast to the RMTI input data files that used peak displacement amplitudes of the P-, SH- and SH-phases, the input to the moment tensor inversion toolbox consists of the plateaus of the unrotated displacement spectra for the P- and S-phases. An example of the spectra is given in Figure 8.5 in the case study. It was found that using

the spectral plateaus as input gave more stable and repeatable results than those computed from peak phases. The reason for this is that the identification of the peak phases was done by the user, and as a result, was subjective.

The data file read by the moment tensor inversion toolbox consists of a number of fields flagged by various tag identifiers (Figure 6.15).

The 'GEO' tag identifies a text string describing a geophone site: the site ID, component, position (xgeo, ygeo, zgeo) and orientation of the sensor by means of direction cosines (dircxn, dircyn, dirczn) are all given in this string.

The 'EVC' tag identifies a text string containing event information: the event ID and location (xev, yev, zev).

The 'DATA' tag marks a text string containing event amplitude data. The fields are:

- Event ID,
- Site ID,
- Component,
- Phase,
- Moment (computed using the spectral plateau of the displacement spectrum), Energy,
- Pol (the polarity of the dominant motion determined from cross-correlation of observed and synthetic P and S-waves),
- big (peak value of cross-correlation function), big_e (largest 'earlier' peak of cross-correlation),
- big_l (largest 'late' peak of cross-correlation function),
- f0 (corner frequency),
- kappa (attenuation factor),
- qual (quality factor of spectral fit),
- psumy (proportion of energy passed by this bandwidth), and,
- psumyQ (proportion of energy passed by bandwidth and Q).

```
   Site Comp     xgeo      ygeo     zgeo dircxn dircyn dirczn
GEO   1   1 3118725.0   27192.0  -1468.0 1.000  .000  .000
GEO   1   2 3118725.0   27192.0  -1468.0  .000 1.000  .000
GEO   1   3 3118725.0   27192.0  -1468.0  .000  .000 1.000
GEO   2   1 3118784.0   25427.0  -2339.0 1.000  .000  .000
GEO   2   2 3118784.0   25427.0  -2339.0  .000 1.000  .000
GEO   2   3 3118784.0   25427.0  -2339.0  .000  .000 1.000
GEO   3   1 3118384.0   24750.0  -2485.0 1.000  .000  .000

Etc.


      Event      xev      yev      zev
   OR Event Site Comp Phase    Moment   Energy Pol   big  big_e  big_l f0 kappa  qual psumy psumyQ

EVC   991014004 3117569.6   26493.5   -2538.1
DATA  991014004   1   1   1  .54E+11  .11E+05 -1 -1.229  .493  .436  44.7 .006 2.597 .900  .292
DATA  991014004   1   1   2  .91E+10  .84E+04  0 -.981  .207  .847  58.6 .007 2.114 .882  .216
DATA  991014004   1   2   1  .75E+10  .98E+03 -1 -.999  .369  .284  76.1 .005  .697 .853  .244
DATA  991014004   1   2   2  .13E+11  .54E+05  1  .862 -.030 -.541  88.9 .008  .775 .831  .115
DATA  991014004   1   3   1  .59E+11  .27E+05  1 1.222 -.117 -.389  57.7 .008  .897 .884  .192
DATA  991014004   1   3   2  .10E-19  .10E-19  0  .000  .000  .000   .0 .000  .000 .000  .000

EVC   991014004 3117569.6   26493.5   -2538.1
DATA  991014004   2   1   1  .20E+10  .24E+03  1  .709 -.075  .423 117.9 .003  .937 .780  .246
DATA  991014004   2   1   2  .17E+11  .44E+05  0 -.825  .161  .778  68.2 .006 1.319 .829  .220
DATA  991014004   2   2   1  .15E+11  .13E+06  1  .766 -.102 -.064 247.2 .009  .589 .467  .015
DATA  991014004   2   2   2  .99E+09  .23E+04  0 -.632  .551  .217 173.7 .005 2.728 .684  .094
DATA  991014004   2   3   1  .17E+10  .10E+04  0  .575 -.140  .568 208.0 .005  .790 .629  .077
DATA  991014004   2   3   2  .34E+11  .14E+06  1 1.106 -.051 -.168  62.8 .008 4.533 .849  .172

EVC   991014004 3117569.6   26493.5   -2538.1
DATA  991014004   5   1   1  .46E+10  .16E+04 -1 -.599  .302  .416 125.0 .001 3.302 .768  .401
DATA  991014004   5   1   2  .10E-19  .10E-19  0  .000  .000  .000   .0 .000  .000 .000  .000
DATA  991014004   5   2   1  .22E+11  .32E+05 -1 -.659  .259  .354 121.2 .002 2.561 .774  .311
DATA  991014004   5   2   2  .71E+10  .62E+05  0 -.476  .423 -.202 141.4 .002 2.061 .739  .300
DATA  991014004   5   3   1  .11E+11  .11E+05  1  .630 -.013 -.063 135.6 .003 2.855 .749  .198
DATA  991014004   5   3   2  .49E+11  .57E+06  1  .787 -.186 -.022  82.2 .002 4.723 .843  .408

Etc.
```

Figure 6.15: Example of data file created by AURA for input into the moment tensor inversion toolbox

Chapter 7

STABILITY TESTS

In any inversion procedure, it is necessary to demonstrate that the results are reliable and physically meaningful. Before applying the hybrid MTI methods described in Chapter 6 to a case study situation, several stability tests are carried out to determine the limitations of the method and possible sources of error. This knowledge will enable the interpreter to distinguish between artefacts introduced by processing and meaningful output.

To test the source mechanism resolving capability for clustered events of the hybrid methods, the following series of experiments is performed on a synthetic cluster of events:

- In the first set of experiments, the number of recording stations is reduced from 7, in turn, to 5, 3 and 2 in order to explore the resolving power of the methods. No noise is added to the input data.

- In the second set of experiments, the sensitivity of the hybrid inversion methods to random noise is explored. The input synthetic data are artificially contaminated with increasing levels of random noise and the resultant focal mechanisms are compared. In addition, the number of recording stations is reduced from 7, in turn, to 5, 3 and 2.

- Lastly, the sensitivity of the hybrid inversion methods to systematic noise is investigated. The input synthetic data are again contaminated with increasing levels of systematic noise and the resultant focal mechanisms are compared. As before, the number of recording stations is reduced.

In all experiments, the mechanisms computed using the hybrid methods are compared to those calculated using both absolute and relative inversion methods. The mechanisms are expressed as radiation patterns, fault-plane solutions and various source parameters.

7.1 SYNTHETIC DATA

Synthetic data for the double-couple events were computed in a relatively straightforward manner (Equations 2.15-2.21 and 2.47, Chapter 2). A synchronous source in the form of a step function was used to estimate the displacements. An isotropic velocity structure was assumed, with a P-wave velocity of 5.9 km/s and an S-wave velocity of 3.8 km/s. A density of 2700 kg/m^3 was assumed for the metasedimentary rocks in the mining area.

The synthetic events were positioned within a network of 7 triaxial geophones simulating the configuration of the array of sensors operating at Oryx Gold Mine. Rather than using an imaginary seismic network configuration with perfect focal coverage, the tests were performed using an existing network. Since the South African gold bearing reefs are tabular, the mine networks tend to have a planar geometry – the result is less than perfect coverage of the focal sphere. The synthetic clusters were positioned at the location of a real cluster of events recorded by the network. The geometry of the network and the position of the cluster are shown in Figure 7.1a. For the chosen hypocentres (both real and synthetic), the coverage of the focal sphere is shown in Figure 7.1b.

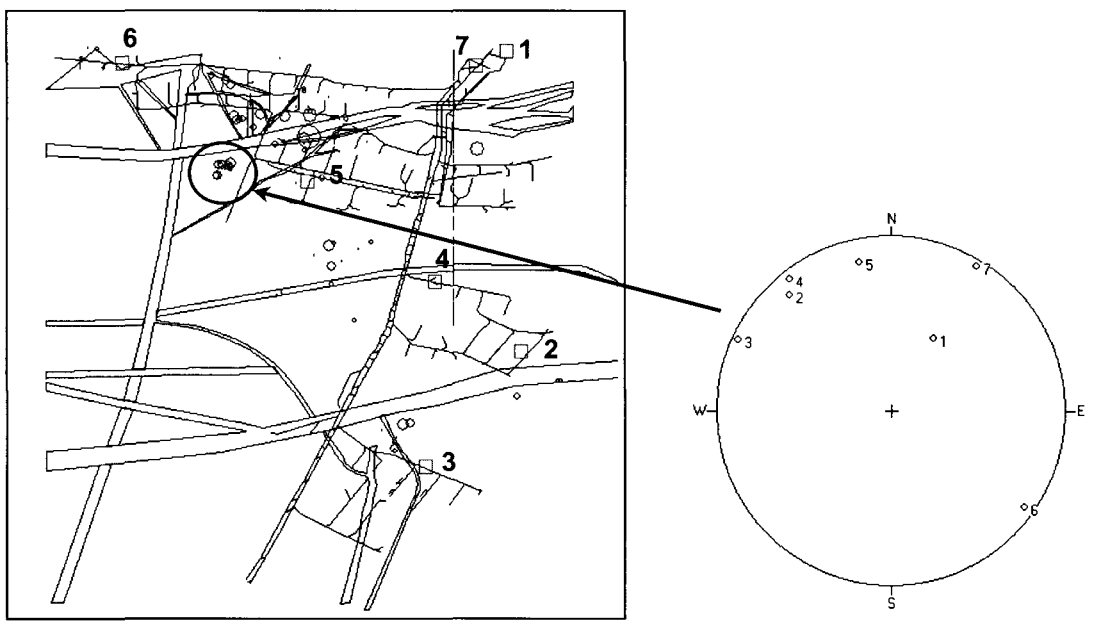

Figure 7.1: (a) Layout of the Oryx seismic network. Note the position of the cluster of events. Solid squares represent triaxial geophone sites, while circles represent locations of those events recorded from May 1999 to June 2000 having local magnitudes > 0. (b) Coverage of the focal sphere for the event cluster.

The set of six events comprising the cluster are pure double-couple sources consisting of vertically dipping fault planes with a strike of 0° (North). The rake varies from 0° to 75° in 15° increments. The focal mechanism diagrams of synthetic cluster diagrams of the six events are shown in Figure 6.2. The diagrams were plotted using FOCAL, a FORTRAN program written by Suetsugu (1994). Circle symbols represent positive (compressional) P-wave first motions. Circle size indicates the amplitude of the wave field at that point in the radiation pattern.

In this study, similar mechanisms were chosen since studies of tightly grouped events recorded underground often show very similar mechanisms. Groups of events having very similar mechanisms may occur, for example, ahead of a development end as a result of mine-induced fracturing or in the vicinity of an active geological feature. However, clusters of events showing a variety of different mechanisms have been observed in areas where pre-existing geological features intersect the mine-induced fracturing or occur in close proximity to one another.

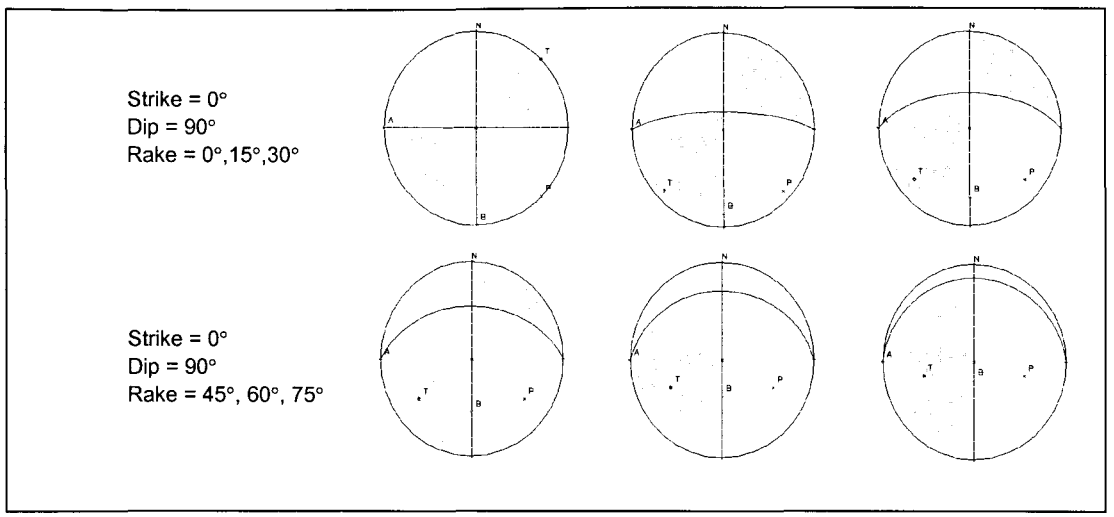

Figure 7.2: Focal mechanism diagrams of the synthetic cluster. The six events are pure double-couple sources consisting of vertically dipping fault planes with a North strike. The rake varies from 0° to 75° in 15° increments. Circle symbols represent positive (compressional) P-wave first motions. Circle sizes indicate the amplitude of the wave field at the relevant point in the radiation pattern.

The quantities used to compare the theoretical mechanisms with those computed via the various methods are as follows:

- percentage isotropic component (%ISO, Equation 2.40);
- percentage double-couple component (%DC, Equation 2.41);
- percentage compensated linear vector dipole (%CLVD, Equation 2.42);
- percentage false components (% False) calculated by summing the %ISO and %CLVD;
- maximum difference between the orientations (strike, dip and rake) of the theoretical and computed fault-plane solutions in degrees;
- total difference between orientations of the theoretical and computed fault-plane solutions in degrees.

In each case, the averages of the parameters were used in the comparative study. Instead of calculating the average difference between the computed and theoretical values of each of the parameters, the computed solution showing the maximum deviation from the theoretical one could have been used to evaluate which of the moment tensor inversion methods performs the best. However, since the parameters are being used in a comparative sense, it is immaterial which are used, as long as they are calculated consistently.

Note that the type of decomposition applied was chosen for the sake of mathematical convenience. The %CLVD does not, in general, correspond to any readily recognisable physical attributes of the source.

The same random seed is used in all the runs to generate the 'random' noise so that to each dataset is added an identical noise level. Alternatively, different seeds could have been used, but this would have necessitated many more runs so that averages could be taken.

It is also important to note that no outlier rejection is applied in these tests. The corrections are based purely on the distribution of the residuals - this is an important aspect to bear in mind, since similar results in the hybrid methods could be obtained artificially, simply by rejecting any equations with large residuals.

7.2 NOISE SIMULATIONS

7.2.1 Random noise

In this study, random noise is simulated using pseudo-random numbers generated by the Delphi (Pascal) runtime library. Formally, the perturbed input displacement u_{ij}^{*} (or moment, depending on whether the computation is being performed in the time or frequency-domain) is given by:

$$u_{ij}^{*} = u_{ij} + \left(R\frac{P}{100} \right) u_{ij} \qquad 7.1$$

where u_{ij} is the measured displacement for each event i and phase observation j. The quantity in brackets describes the noise used to perturb u_{ij} where R is the pseudo-random number ($-1 \leq R \leq 1$), and P is the maximum allowable noise level in per cent. In this study, the random noise represents the background noise present on most seismograms due to various underground activities, as well as that due to imperfect processing, i.e. poor P- and/or S-wave picks.

7.2.2 Systematic noise

The deterministic or systematic noise fraction is simulated by adding (or subtracting) an offset to the wave phase. Such noise would be the result of systematic errors such as poorly calibrated or oriented geophones, bending of the ray-paths resulting in the wave phase arriving earlier or later than expected, etc. In this case, the perturbed input displacement is given by:

$$u_{ij}^{*} = u_{ij} \pm \left(\frac{P}{100} \right) u_{ij} \qquad 7.2$$

where P is the required offset in per cent. It should be noted that the offsets would be the same for all events in a spatial cluster for a particular site, component (i.e. geophone orientation) and phase.

7.3 EXPERIMENT 1 - RESOLVING POWER

This test was designed to explore the resolving power of the hybrid moment tensor inversion methods.

7.3.1 Method

The number of recording stations used in the moment tensor inversions was reduced from 7, in turn, to 5, 3 and 2. The focal coverage ranged from moderate (7 stations) to very poor (2 stations). Refer to Figure 7.3. The tests were applied to data free of noise. Six moment tensor inversion methods were applied, *viz.*:

1. absolute moment tensor inversion (referred to as method A1 in the figures that follow);
2. relative moment tensor inversion with a reference mechanism (B1);
3. relative moment tensor inversion without a reference mechanism (B2);
4. hybrid moment tensor inversion using a mean correction (C1);
5. hybrid moment tensor inversion using a median correction (C2);
6. hybrid moment tensor inversion using a weighted mean correction (C3).

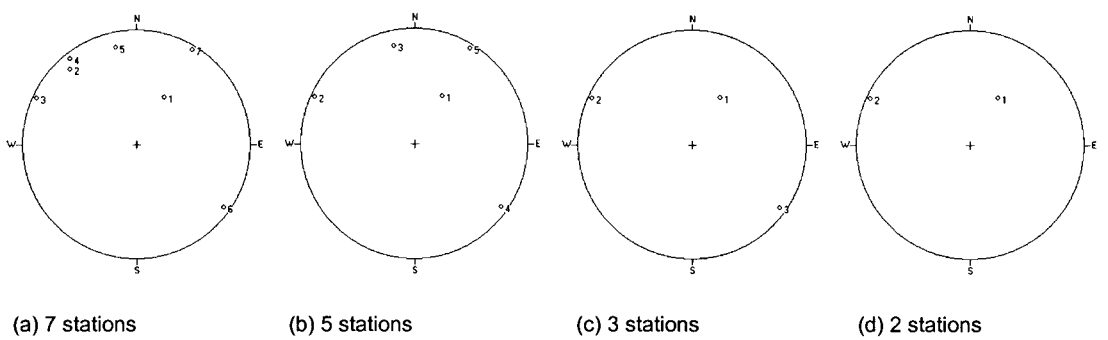

Figure 7.3: Focal sphere coverages used in establishing the resolving power of the methods.

7.3.2 Results and discussion

Refer to Figures 7.4(a) to (d) and Table 7.1. Rather than laboriously describe every observation, only the main trends are highlighted. Inversion of the noise free data gives almost perfect resolution of the mechanisms for all MTI methods for the 7 and 5 station configurations, as can be seen from Figures 7.4a and 7.4b. Method B2 gives the best resolution (~100% DC components, with no difference in the orientations of the computed and theoretical fault-plane solutions), and method C1 gives the lowest (~95% DC components, ~6% false components, and a total average difference in the orientations of ~3°).

However, the quality of the results from method B2 decreases substantially when the inversions are performed using sparse coverage (3 stations) of the focal sphere (Figure 7.4c). In this case method C2 gives the best resolution (~92% DC components, ~11% false components, and an average difference in the orientations of ~2.5°), followed closely by methods A1, B1, C1 and C3. Method B2 performs poorly, giving the lowest resolution (~43% DC components, ~67% false components and an average difference in orientations of ~2.5°). These results are summarised in Table 7.1.

The good resolution shown by all methods (except for B2) up to this point is lost in the extremely sparse coverage by 2 stations (Figure 7.4d). Again, method C2 performs the best overall (~63% DC components, ~52% false components and an average difference in orientations of ~19°). Method B2 performs the worst overall.

Table 7.1: Results of Experiment 1.

	Average source components (%)				Average difference between resolved mechanisms and theoretical mechanisms (degrees)			
7 stations	**%ISO**	**%DC**	**%CLVD**	**%False**	**Strike**	**Dip**	**Rake**	**Total**
A1	0.9	96.8	3.2	4.1	0.3	1.0	0	1.3
B1	0.5	97.4	2.5	3.0	0.5	1.3	0.8	2.6
B2	0.0	100.0	0.0	0.0	0	0	0	0
C1	1.4	95.1	4.8	6.2	0.7	1.0	0	1.7
C2	0.9	97.1	2.9	3.8	0.3	1.0	0	1.3
C3	0.9	96.8	3.2	4.1	0.3	1.0	0	1.3
5 stations								
A1	0.8	97.0	3.0	3.8	0	1.0	0.5	1.5
B1	0.5	97.5	2.5	3.0	0.3	1.3	0.5	2.1
B2	0.0	100.0	0.0	0.0	0	0	0	0
C1	1.4	94.7	5.3	6.8	0.7	1.0	0	1.7
C2	0.9	96.8	3.2	4.0	0.3	1.0	0	1.3
C3	0.8	97.0	3.0	3.8	0.3	1.0	0	1.3
3 stations								
A1	2.9	91.4	8.5	11.4	0.3	1.3	0.7	2.3
B1	3.1	90.9	9.1	12.2	0.5	1.3	0.5	2.3
B2	10.4	42.9	57.0	67.4	46.3	37.3	73.6	>90
C1	3.7	89.4	10.6	14.3	0.5	1.3	0.7	2.5
C2	2.8	91.5	8.5	11.3	0.5	1.5	0.5	2.5
C3	2.8	91.4	8.6	11.4	0.3	1.3	0.7	2.3
2 stations								
A1	19.4	53.1	46.9	66.3	6.0	12.3	5.2	23.4
B1	25.9	66.5	33.5	59.4	8.3	20.0	11.2	39.5
B2	27.1	65.2	34.8	61.9				>90
C1	23.9	53.7	46.3	70.2	7.2	26.0	8.2	41.3
C2	15.6	62.9	37.1	52.7	4.2	10.0	5.0	19.2
C3	19.4	53.1	46.9	66.3	6.0	4.8	4.8	22.8

7.3.3 Conclusions

On the basis of the experimental results, the following can be concluded:

1. The relative method without reference mechanism (method B2) shows the highest resolution of mechanisms, provided that the coverage of the focal sphere is not too sparse (> 3 stations). The relative method with a reference mechanism is more robust than the method without a reference mechanism in situations of sparse coverage (2 stations).

2. The hybrid method (method C2), using a median correction, is the most robust of all the methods tested in the most extreme case of poor coverage (2 stations) of the focal sphere.

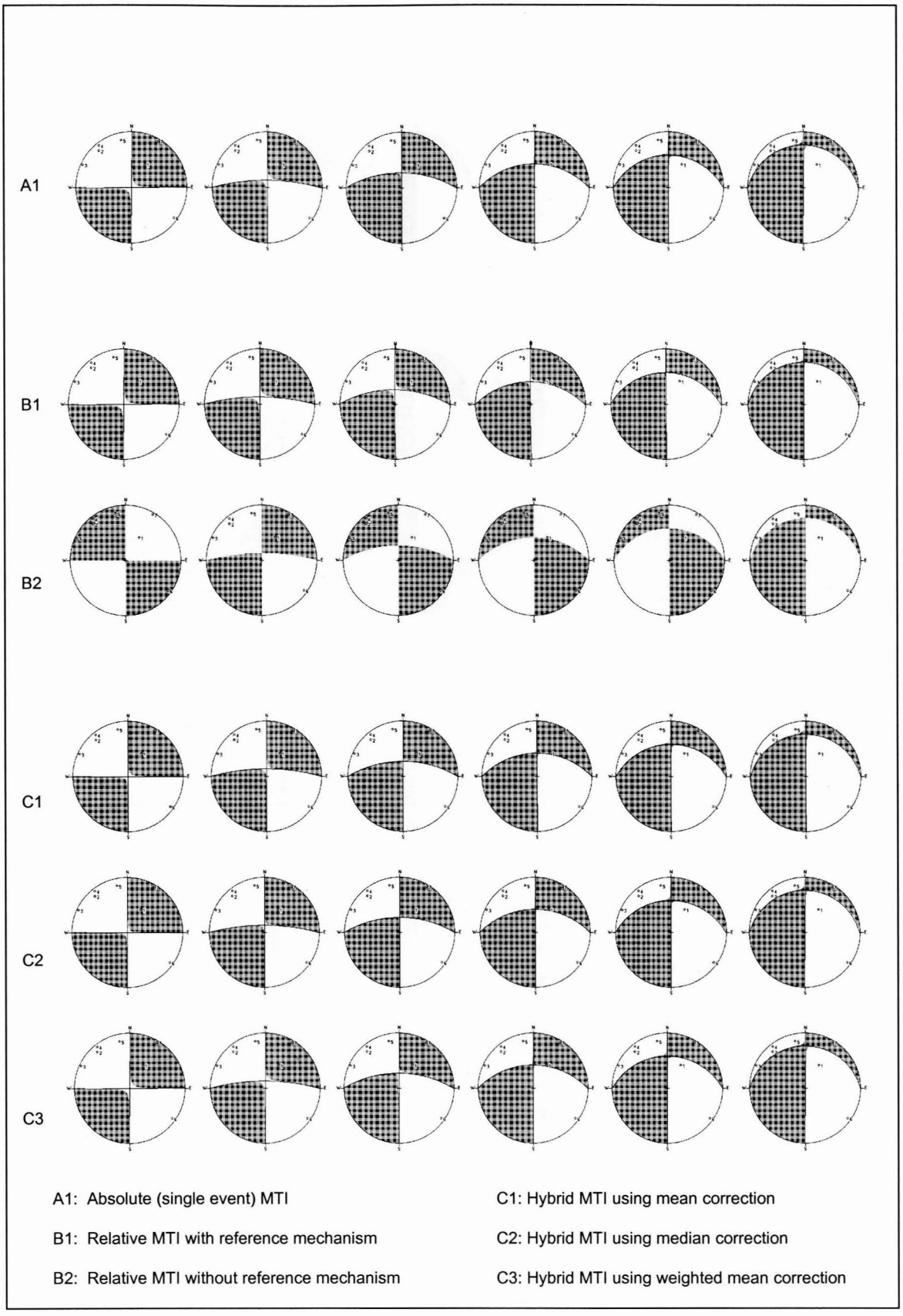

Figure 7.4(a): Radiation patterns of moment tensors computed using 6 different MTI methods. 7 stations. No noise has been added to the input data.

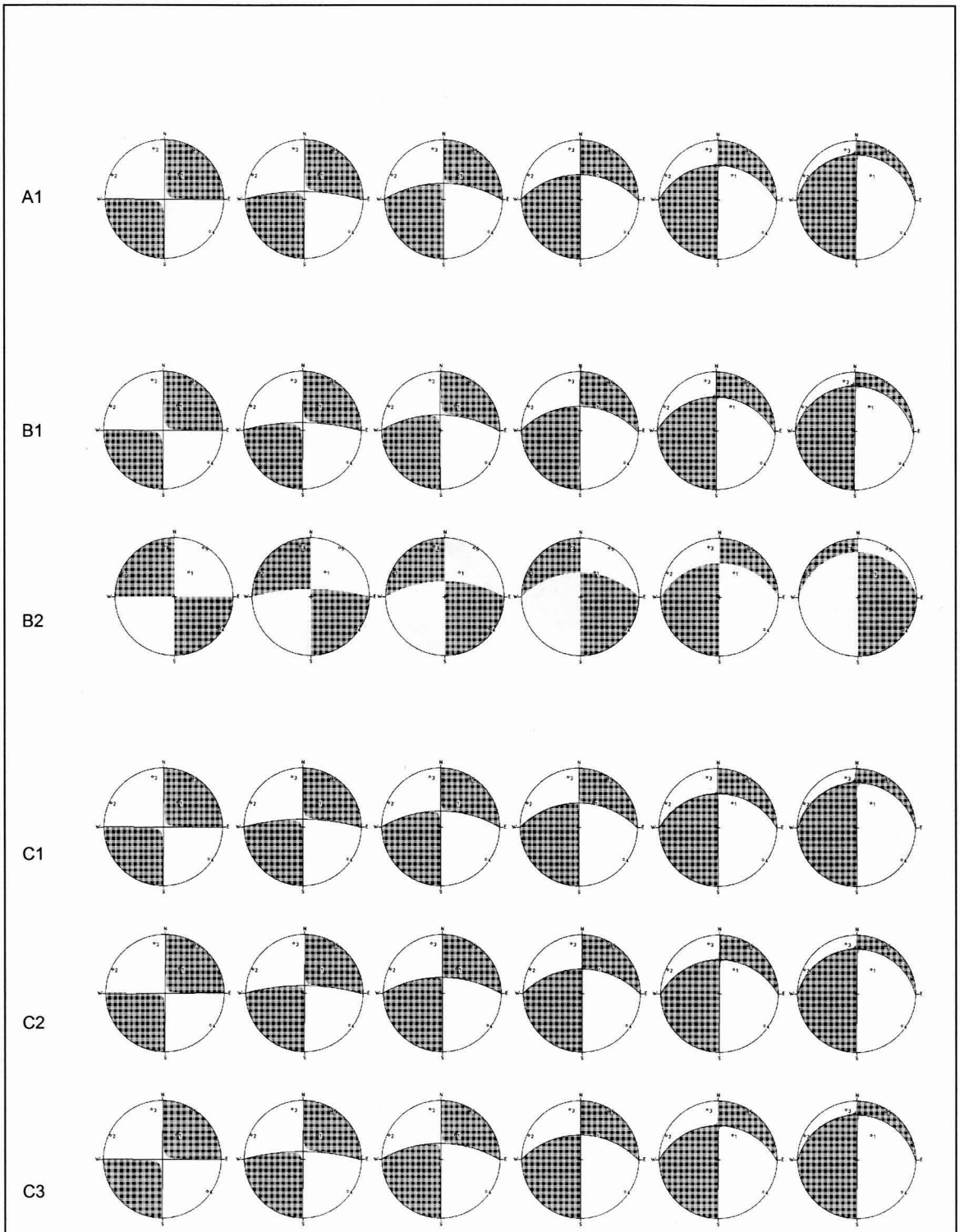

Figure 7.4(b): Radiation patterns of moment tensors computed using 6 different MTI methods. 5 stations. No noise has been added to the input data.

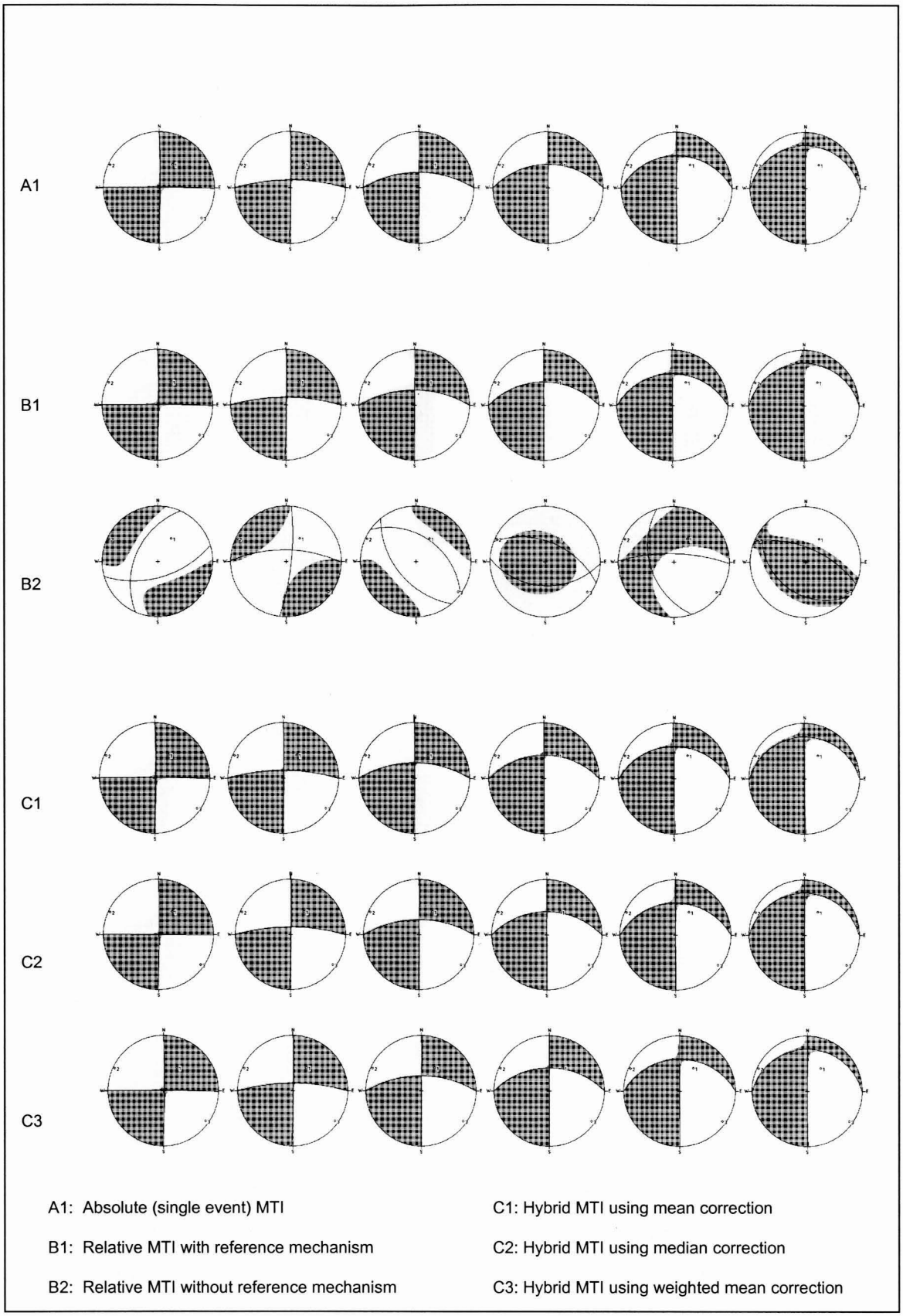

Figure 7.4(c): Radiation patterns of moment tensors computed using 6 different MTI methods. 3 stations. No noise has been added to the input data.

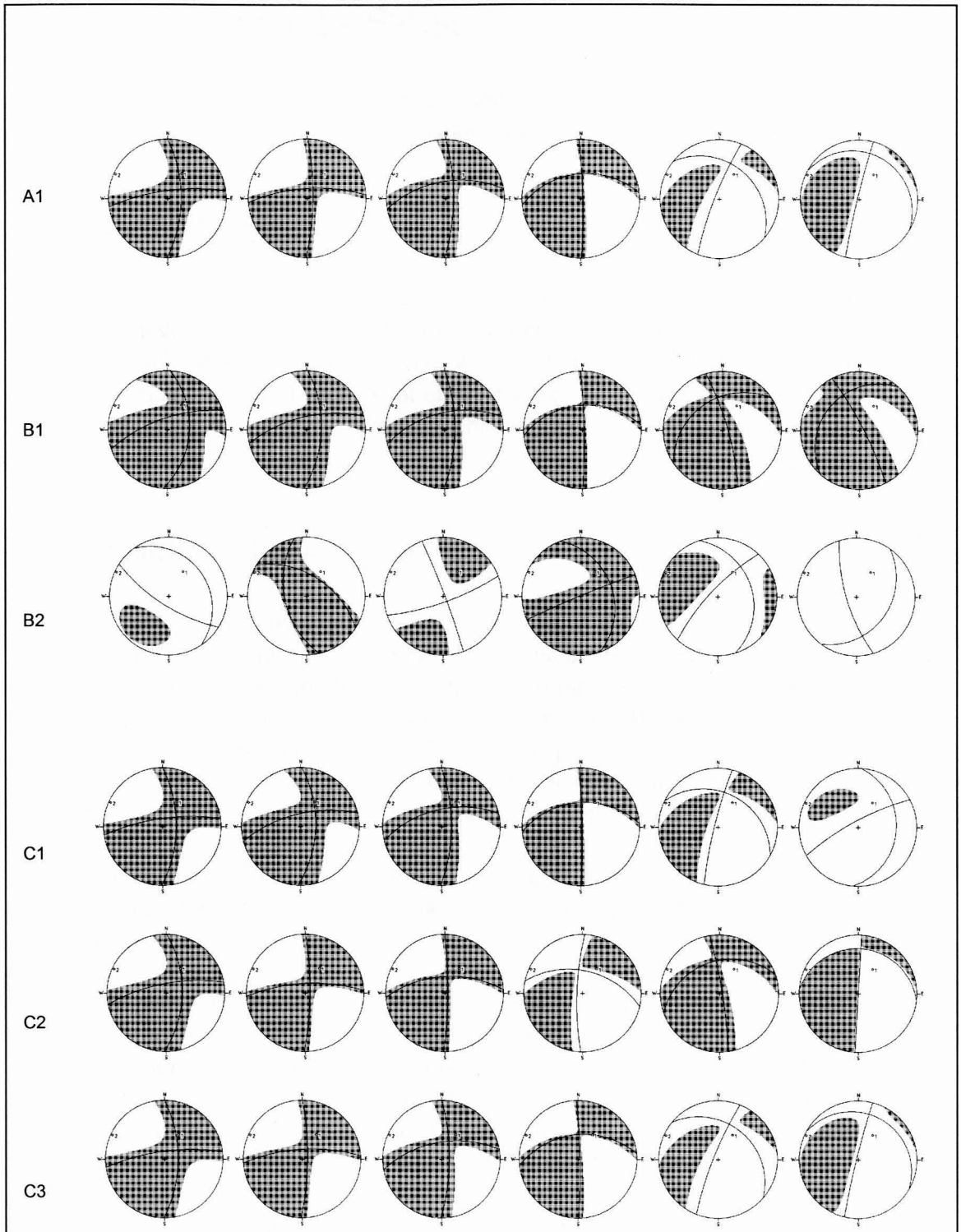

Figure 7.4(d): Radiation patterns of moment tensors computed using 6 different MTI methods. 2 stations. No noise has been added to the input data.

7.4 EXPERIMENT 2 – SENSITIVITY TO RANDOM NOISE

This test was designed to assess the resolving power of the six moment tensor inversion methods in the presence of random noise.

7.4.1 Methodology

In this series of tests, the input data were contaminated by random noise ranging in maximum level from 10% to 50% of the input amplitude and are introduced in increments of 10%. The random noise was calculated using Equation 7.1 and was applied to each channel of each event in the data set. The coverage of the focal sphere was reduced incrementally by decreasing the number of stations from 7, in turn to 5, 3 and finally 2.

7.4.2 Results and discussion

Refer to Table 7.2(a) and Figure 7.5(a). Inversion of the data contaminated by 10% random noise yields good resolution of the mechanisms for the 7-station case for all moment tensor inversion methods with the exception of method B2. The application of 10% random noise has a devastating effect on method B2. This is interesting when contrasted with Experiment 1 where this method provided the best resolution of the mechanisms for the same network configuration and the same set of synthetic mechanisms. The reason for this phenomenon is thought to be that for mechanisms that are alike or very similar, the least-squares matrix of method B2 is near singular and hence produces unreliable results. This is borne out by the condition numbers for this method, which generally are a few orders of magnitude larger than those of the other methods.

The mechanisms in the event cluster were purposely chosen to be similar, since this is very likely to happen in the underground environment. In the noise-free case, the differences amongst these mechanisms are sufficiently large for method B2 to produce realistic results. However, the differences in the mechanisms are of the same order as the level of applied noise and, consequently, the system of equations becomes near-singular, thereby significantly blurring the distinction between mechanisms.

Methods C1 and C3 give the best resolution (95.5% DC components and a total average difference in the orientations between the computed and theoretical fault-plane solutions of 2.1°). As mentioned earlier, method B2 shows the lowest resolution (64.7% DC components and a total average difference in the orientations between the computed and theoretical fault-plane solutions of >90°). As the number of stations is decreased incrementally from 7 down to 2, the resolutions of all the methods deteriorate. In the 5-station configuration (Figure 7.5b) methods A1, C1, C2 and C3 all show the same resolution (93.5% DC components and a total average difference in the orientations between the computed and theoretical fault-plane solutions of 1.6°). Method B1 follows closely (93.1% DC component and a total difference in the

orientations of 2.8°) and method B2 performs poorly (%DC of 41%, total average difference in the orientations between the computed and theoretical fault-plane solutions of >90°). For the 3-station configuration (Figure 7.5c) methods A1 and C3 yield the best resolution (90.7% DC component, 4.6° difference in orientation). For the very sparse coverage 2-station configuration (Figure 7.5d), method C2 shows the best resolution (69.7% DC component and a total average difference in the orientations of the computed and theoretical fault-plane solutions of ~22.5°). Interestingly, method B1 gives the highest percentage DC components (95.3% DC) and lowest false component fraction (37.6%), despite the poor resolution of the fault-plane solution.

Refer to Table 7.2(b) and Figures 7.6(a) to (d). The inversion of the data contaminated by 20% random noise shows generally similar trends to those of the 10% noise tests. For this reason, only the main trends are described. As the number of stations is decreased incrementally from 7 down to 2, each of the methods A1, C1, C2 and C3 shows the same resolution (%DC of 90.9%, and a total average difference in the orientations of the computed and theoretical fault-plane solutions of 2.6°). Methods A1 and C3 show the same resolution for the 3-station configuration (%DC of 85.6, and a total average difference in the orientations of the computed and theoretical fault-plane solutions of 7.3°). In the 2-station configuration, method A1 performs best overall (%DC of 67.7, and a total average difference in the orientations of the computed and theoretical fault-plane solutions of 20.5°). Once again, despite showing the lowest fault-plane resolution, method B1 gives the highest percentage DC components (82.6% DC) for the 2-station configuration. For all the station configurations, method B2 fares worst overall.

Refer to Table 7.2(c) and Figures 7.7(a) to (d). As before, the 30% random noise tests show similar trends to the previous tests. In the 7-station configuration, methods A1, C1, C2 and C3 show the same resolution (%DC of 87.5%, and a total average difference in the orientations of the computed and theoretical fault-plane solutions of 4.9°), followed closely by method B1 (85.9% DC and difference in orientation of 8.3°). In the most extreme 2-station configuration, method C2 again shows the best resolution (67.2 % DC component, and a total average difference in the orientations of the computed and theoretical fault-plane solutions of 24.4°), followed closely by method A1 (55.2 % DC component, and a total average difference in the orientations of the computed and theoretical fault-plane solutions of 25.2°). As with the previous tests, method B1 shows the highest percentage DC components (91.6% DC) for the 2-station configuration, despite having very poor fault-plane resolution. For all the station configurations, method B2 again shows the poorest overall results.

Refer to Table 7.2(d) and Figures 7.8(a) to (d) for the source parameters and radiation patterns of the 40% random noise tests. Once again, methods A1, C1, C2 and C3 show the same performance for the 7-station configuration (84.6% DC component and a total average difference in the orientations of the computed and theoretical fault-plane solutions of 6.9°), followed closely by method B1 (83.2% DC, difference in orientations of 10.2°). In the most extreme 2-station configuration, method C2 shows the best resolution overall (59.4 % DC component and a difference in orientations of 33.4°). As with the previous tests, method B1 shows the highest percentage DC

components (93.3% DC) for the 2-station configuration, despite having poor fault-plane resolution. For all the station configurations, method B2 performs worst overall.

7.4.3 Conclusions

On the basis of the experimental results, it can be concluded that:

1. The absolute moment tensor inversion method (method A1) and the hybrid methods using a median correction (C2) and a weighted mean correction (C3) show similar robustness and stability in extreme configurations concerning network coverage of the focal sphere and random noise. The levels of noise inflicted on the input data in these tests are extremely high – certainly higher than would be expected in reality. Therefore, the prospects of retrieving the source mechanisms of real events by these methods are good.

2. The relative method with a reference mechanism (method B1) exhibited slightly poorer performance in all the tests when compared with the aforementioned methods.

3. The hybrid method using a mean correction (method C1) gave unreliable results and is very sensitive to high noise levels.

4. The relative moment tensor inversion without a reference mechanism (method B2), when applied to events having very similar mechanisms, is extremely sensitive to noise and gave very unreliable results in the situations investigated. Since clusters of events recorded underground are likely to have similar mechanisms, this method must be used with some caution.

Table 7.2(a): Results of Experiment 2 - 10% random noise.

	Average source components (%)				Average difference between resolved mechanisms and theoretical mechanisms (degrees)			
7 stations	**%ISO**	**%DC**	**%CLVD**	**%False**	**Strike**	**Dip**	**Rake**	**Total**
A1	1.4	95.1	4.9	6.3	0.6	1.2	0.3	2.1
B1	1.8	93.7	6.3	8.1	1.0	1.8	0.6	3.4
B2	24.9	64.7	35.3	60.2				>90
C1	1.3	95.5	4.5	5.8	0.6	1.2	0.3	2.1
C2	1.5	95.0	5.0	6.5	0.6	1.2	0.3	2.1
C3	1.4	95.5	4.9	6.3	0.6	1.2	0.3	2.1
5 stations								
A1	1.8	93.5	6.5	8.3	0.3	1.0	0.3	1.6
B1	2.0	93.1	6.9	8.9	0.8	1.7	0.3	2.8
B2	19.4	41.0	59.0	78.4				>90
C1	1.8	93.5	6.5	8.3	0.3	1.0	0.3	1.6
C2	1.8	93.5	6.5	8.3	0.3	1.0	0.3	1.6
C3	1.8	93.5	6.5	8.3	0.3	1.0	0.3	1.6
3 stations								
A1	3.5	90.7	9.3	12.8	1.5	1.9	1.2	4.6
B1	4.2	88.1	11.9	16.1	1.5	3.8	1.2	6.5
B2	27.6	67.3	32.7	60.3				>90
C1	3.8	89.6	10.4	14.2	1.7	2.3	1.0	5.0
C2	3.5	90.5	9.5	13.0	1.5	2.2	1.1	4.7
C3	3.5	90.7	9.3	12.8	1.5	2.0	1.1	4.6
2 stations								
A1	18.5	62.7	37.3	55.8	11.0	10.7	4.8	26.5
B1	32.9	95.3	4.7	37.6	32.0	23.7	10.7	66.4
B2	23.2	59.3	40.7	63.9				>90
C1	21.9	54.8	45.2	67.1	9.0	14.2	7.0	30.2
C2	15.7	69.7	30.3	46.0	3.4	12.8	6.3	22.5
C3	18.5	62.7	37.3	55.8	10.8	10.6	3.8	25.2

Table 7.2(b): Results of Experiment 2 - 20% random noise.

	Average source components (%)				Average difference between resolved mechanisms and theoretical mechanisms (degrees)			
7 stations	**%ISO**	**%DC**	**%CLVD**	**%False**	**Strike**	**Dip**	**Rake**	**Total**
A1	2.6	90.9	9.1	11.7	1.0	1.8	0.8	2.6
B1	3.5	89.3	10.7	14.2	1.0	2.7	2.2	5.9
B2	11.6	63.6	36.4	48.0				>90
C1	2.6	90.9	9.1	11.7	1.0	1.8	0.8	2.6
C2	2.6	90.9	9.1	11.7	1.0	1.8	0.8	2.6
C3	2.6	90.9	9.1	11.7	1.0	1.8	0.8	2.6
5 stations								
A1	3.5	88.5	11.5	15.0	2.5	2.8	1.7	7.0
B1	4.0	87.1	12.9	16.9	1.3	5.5	1.7	8.5
B2	15.5	27.7	72.3	87.8				>90
C1	3.5	88.5	11.5	15.0	2.5	2.8	1.7	7.0
C2	3.4	88.7	11.3	14.7	2.5	1.8	1.7	6.0
C3	3.5	88.5	11.5	15.0	2.5	2.0	1.7	6.2
3 stations								
A1	6.2	85.6	14.4	20.6	2.5	2.8	2.0	7.3
B1	8.8	79.9	20.1	28.9	1.8	5.5	1.7	9.0
B2	26.4	64.4	35.6	62.0				>90
C1	6.6	84.7	15.3	21.9	2.5	3.3	2.3	8.1
C2	6.4	85.2	14.8	21.2	2.5	2.8	2.1	7.4
C3	6.2	85.6	14.4	20.6	2.5	2.8	2.0	7.3
2 stations								
A1	18.7	67.7	32.3	51.0	6.8	11.2	2.5	20.5
B1	24.7	67.9	32.0	56.7	9.3	18.8	5.3	33.4
B2	28.9	82.6	17.4	46.5				>90
C1	26.3	58.4	41.6	67.9	14.0	17.3	8.5	39.8
C2	25.2	72.8	27.2	52.4	12.5	17.3	10.1	39.9
C3	18.7	67.7	32.3	51.0	8.6	11.0	3.5	23.1

Table 7.2(c): Results of Experiment 2 - 30% random noise.

	Average source components (%)				Average difference between resolved mechanisms and theoretical mechanisms (degrees)			
7 stations	**%ISO**	**%DC**	**%CLVD**	**%False**	**Strike**	**Dip**	**Rake**	**Total**
A1	3.7	87.5	12.5	16.3	1.2	2.5	1.2	4.9
B1	5.1	85.9	14.1	19.2	1.5	3.8	3.0	8.3
B2	15.8	56.1	43.9	59.7				>90
C1	3.7	87.5	12.5	16.3	1.2	2.5	1.2	4.9
C2	3.7	87.5	12.5	16.3	1.2	2.5	1.2	4.9
C3	3.7	87.5	12.5	16.3	1.2	2.5	1.2	4.9
5 stations								
A1	5.0	84.7	15.3	20.3	1.2	2.8	3.0	7.0
B1	5.9	82.6	17.4	23.3	2.0	1.3	1.5	4.8
B2	18.7	46.8	53.2	71.9				>90
C1	5.0	84.7	15.3	20.3	1.2	2.5	1.2	4.9
C2	4.9	85.1	14.9	19.8	1.5	2.5	0.5	4.5
C3	5.0	84.7	15.3	20.3	1.2	2.5	1.2	4.9
3 stations								
A1	8.4	73.5	26.4	34.8	3.5	3.7	3.2	10.4
B1	12.2	67.8	32.2	44.4	3.7	6.8	2.8	13.3
B2	24.9	72.9	27.1	52.0				>90
C1	33.3	87.7	12.3	45.6				>90
C2	8.5	72.9	27.1	35.6	3.7	3.7	3.0	10.4
C3	8.3	73.5	26.5	34.8	3.6	4.3	3.2	11.1
2 stations								
A1	19.2	55.2	44.8	64.0	4.2	14.0	7.0	25.2
B1	33.3	91.6	8.4	41.7				>90
B2	31.0	74.1	26.0	57.0				>90
C1	20.3	60.7	39.4	59.7	14.5	13.5	8.0	36.0
C2	23.2	67.2	32.8	56.0	16.2	13.7	4.6	34.5
C3	19.2	55.2	44.8	64.0	4.1	14.0	6.3	24.4

Table 7.2(d): Results of Experiment 2 - 40% random noise.

	Average source components (%)				Average difference between resolved mechanisms and theoretical mechanisms (degrees)			
7 stations	**%ISO**	**%DC**	**%CLVD**	**%False**	**Strike**	**Dip**	**Rake**	**Total**
A1	4.8	84.6	15.3	20.1	1.7	3.3	1.9	6.9
B1	6.5	83.2	16.8	23.3	1.8	5.2	3.2	10.2
B2	20.1	45.4	54.6	74.7				>90
C1	4.8	84.6	15.4	20.2	1.7	3.3	1.9	6.9
C2	4.8	84.6	15.4	20.2	1.7	3.3	1.9	6.9
C3	4.8	84.6	15.4	20.2	1.7	3.3	1.9	6.9
5 stations								
A1	6.4	81.8	18.2	24.6	1.8	3.2	1.5	6.5
B1	7.6	79.2	20.7	28.3	2.8	1.3	1.9	6.0
B2	18.5	43.7	56.3	74.8				>90
C1	6.4	81.8	18.2	24.6	1.8	3.2	1.5	6.5
C2	6.3	82.3	17.7	24.0	1.8	3.0	1.2	6.0
C3	6.4	81.8	18.2	24.6	1.8	3.2	1.5	6.5
3 stations								
A1	10.1	73.7	26.3	36.4	4.3	5.0	4.0	13.3
B1	14.7	68.7	31.3	46.0	3.5	10.7	3.8	18.0
B2	26.1	66.5	33.5	59.6				>90
C1	33.3	90.0	10.0	43.4				>90
C2	10.5	72.7	27.2	37.7	4.2	4.3	4.2	12.7
C3	10.1	73.7	26.3	36.4	4.1	5.0	3.7	12.8
2 stations								
A1	24.6	50.7	49.3	73.9	12.8	28.0	7.5	48.3
B1	32.7	93.3	6.1	38.8				>90
B2	33.2	83.7	16.2	49.4				>90
C1	24.6	50.7	49.3	73.9	12.8	22.2	7.8	42.8
C2	22.4	59.4	40.5	62.9	9.3	16.6	7.5	33.4
C3	24.6	50.7	49.3	73.9	12.8	22.2	7.2	42.2

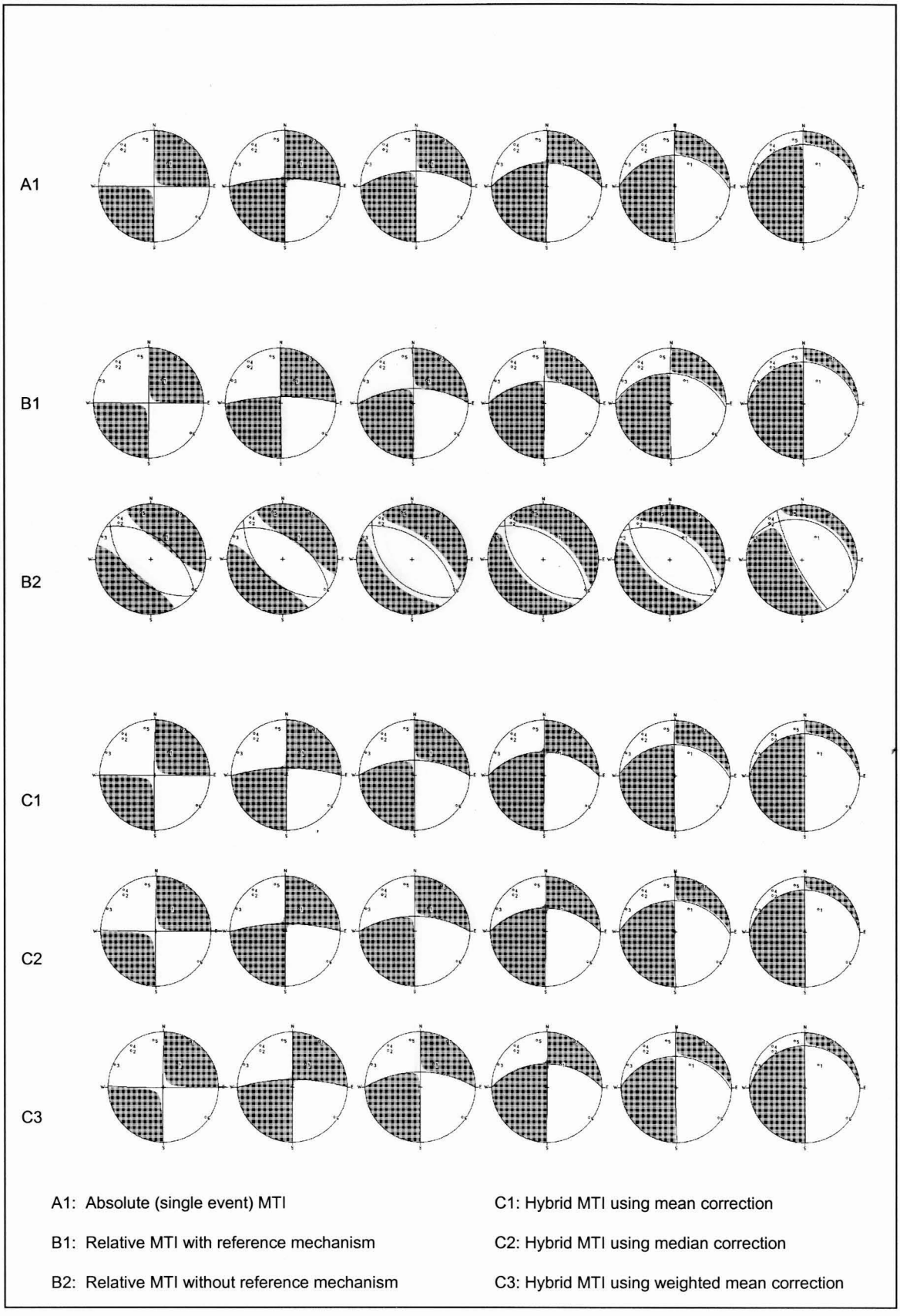

Figure 7.5(a): 10% random noise added to all events - all 7 stations.

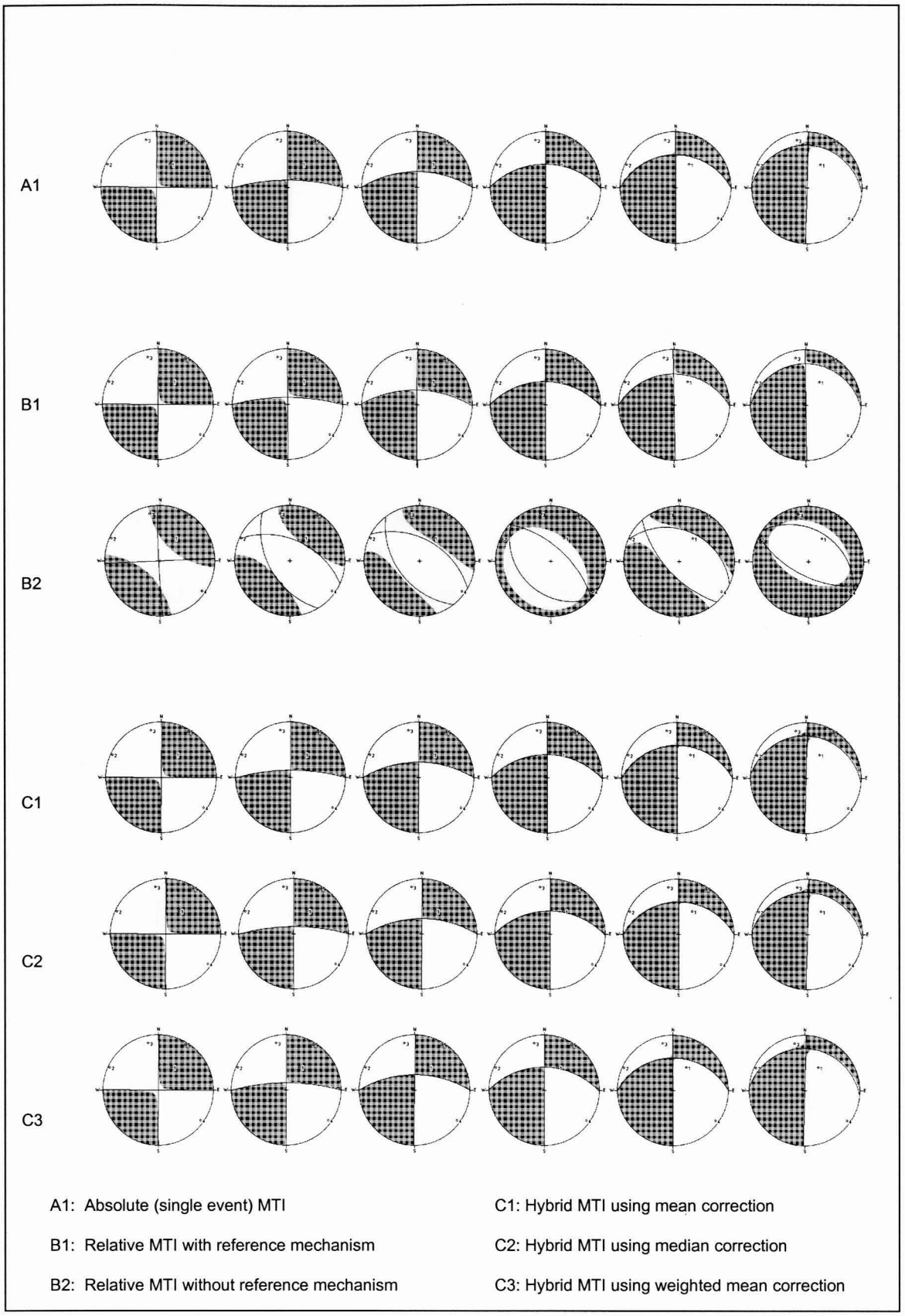

Figure 7.5(b): 10% random noise added to all events - 5 stations (1, 3, 5, 6 and 7).

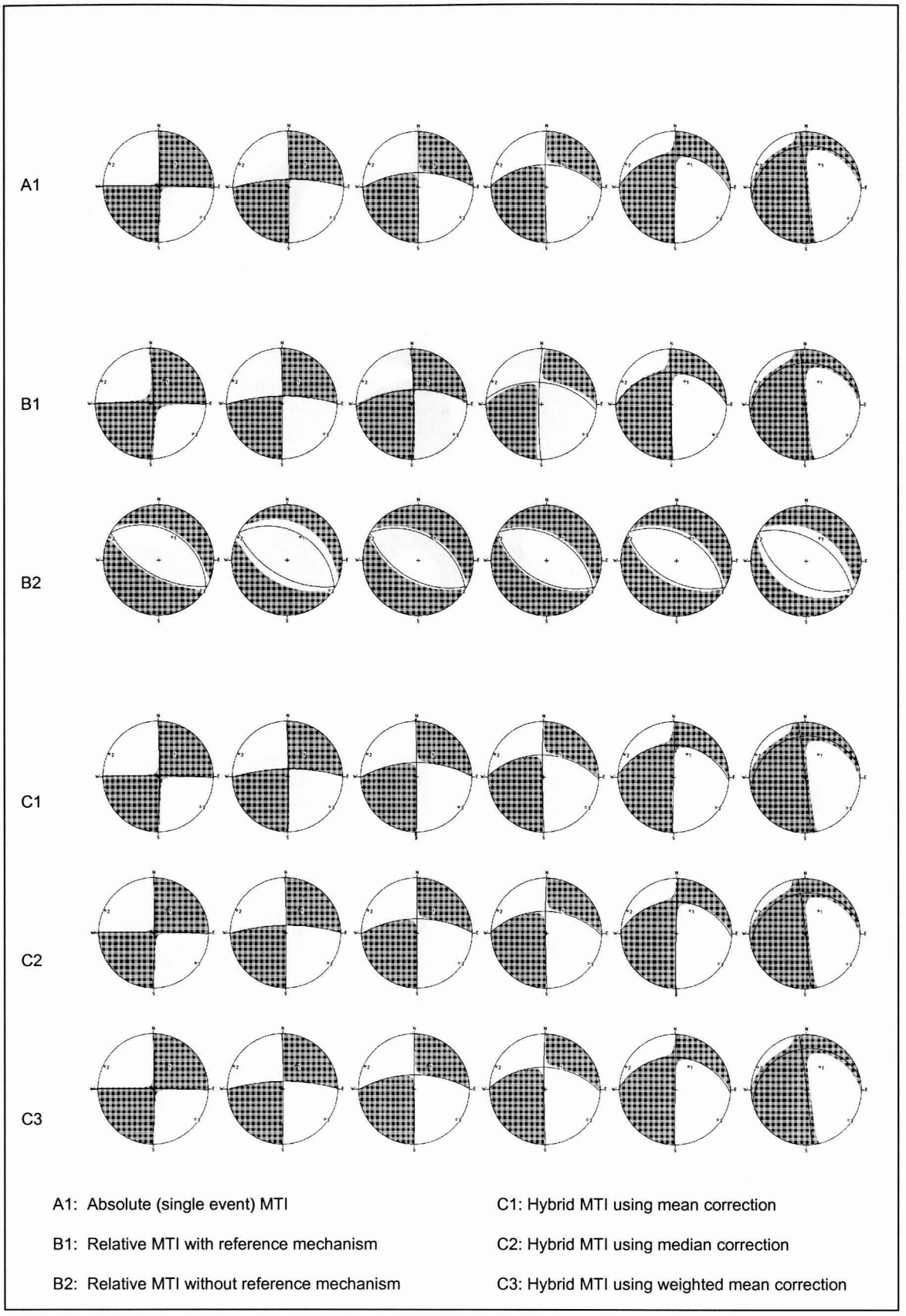

Figure 7.5(c): 10% random noise added to all events - 3 Stations (1, 3 and 6).

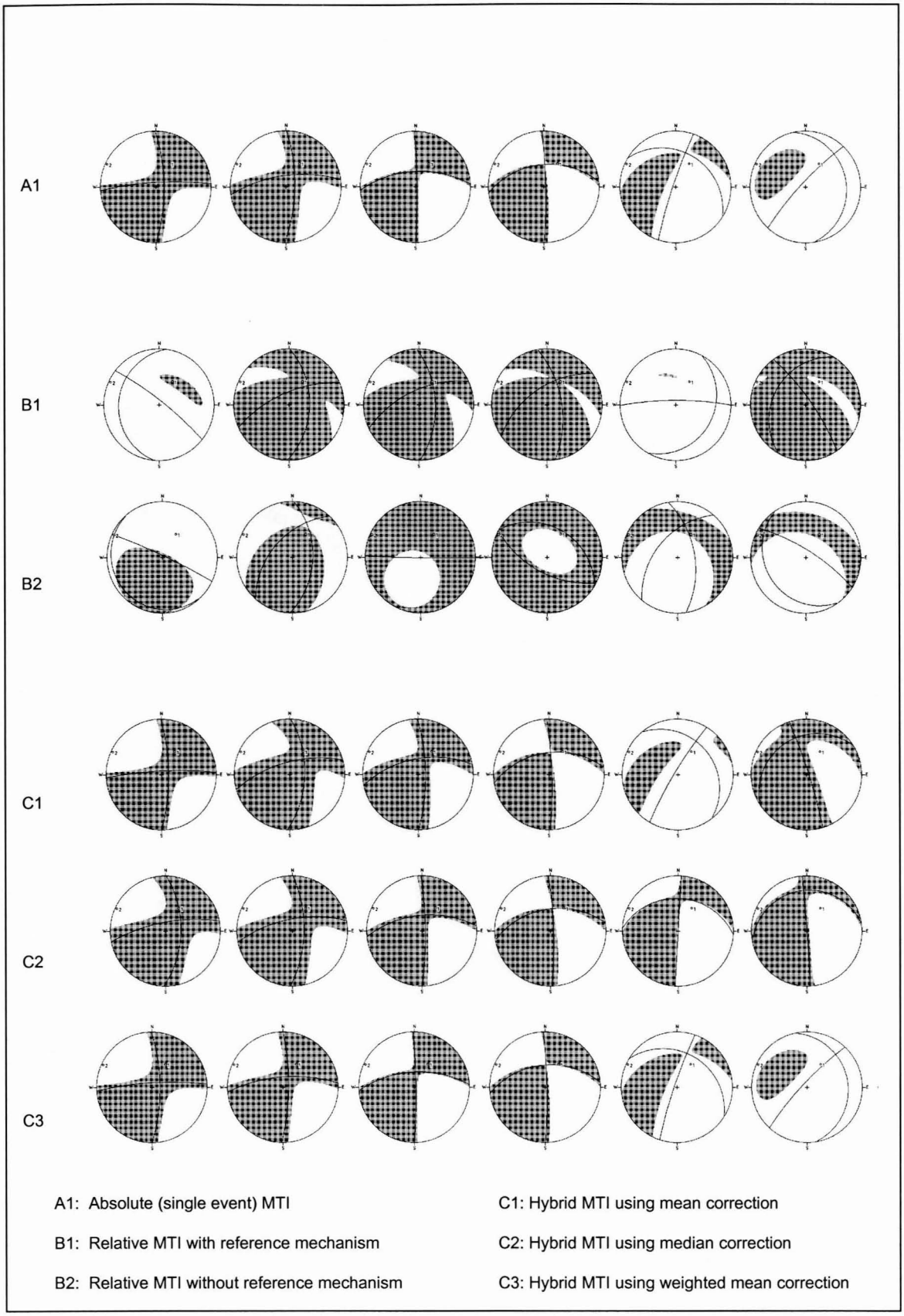

Figure 7.5(d): 10% random noise added to all events - 2 stations (1 and 3).

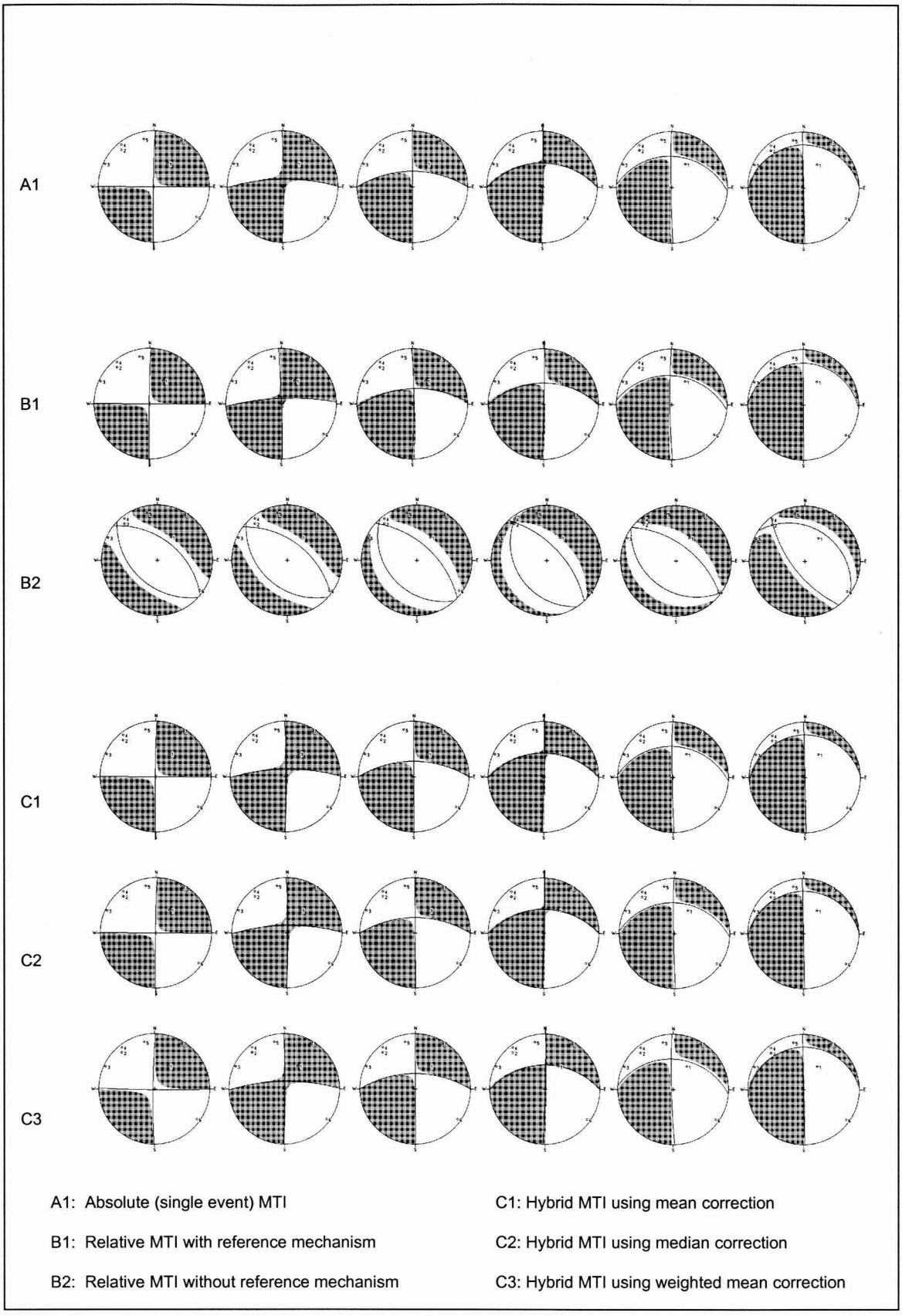

Figure 7.6(a): 20% random noise added to all events - all 7 stations.

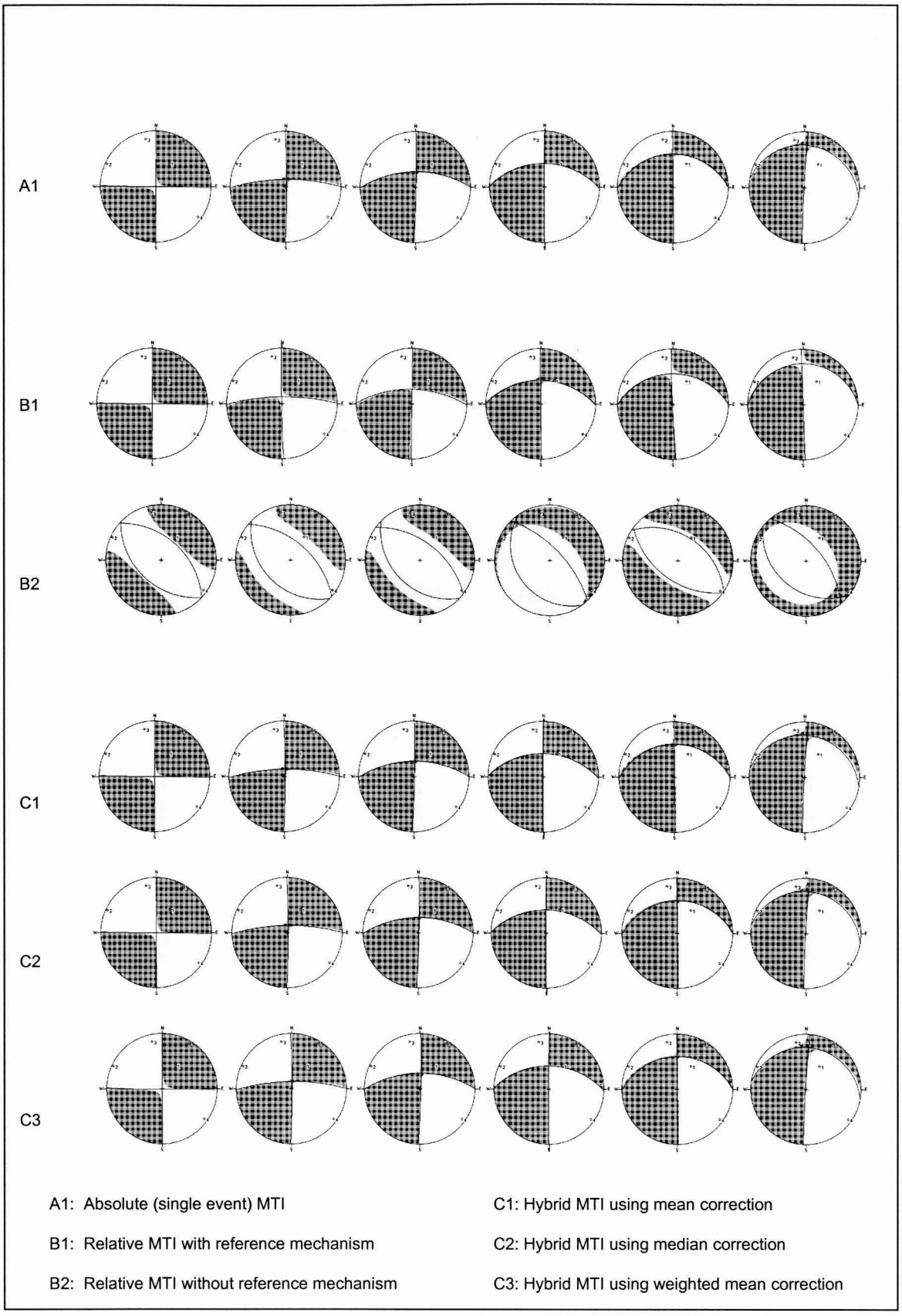

Figure 7.6(b): 20% random noise added to all events - 5 stations (1, 3, 5, 6 and 7).

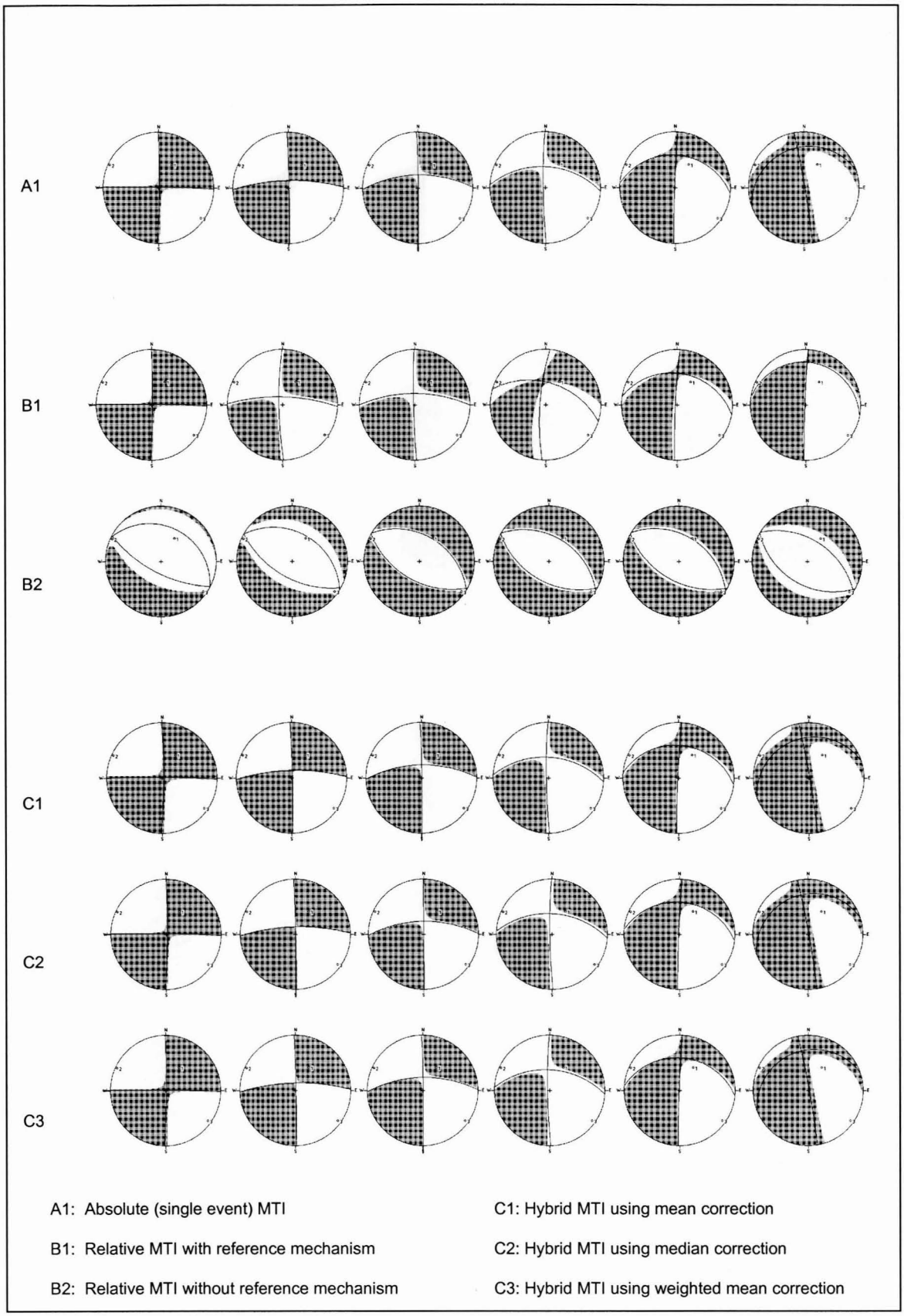

Figure 7.6(c): 20% random noise added to all events - 3 stations (1, 3 and 6).

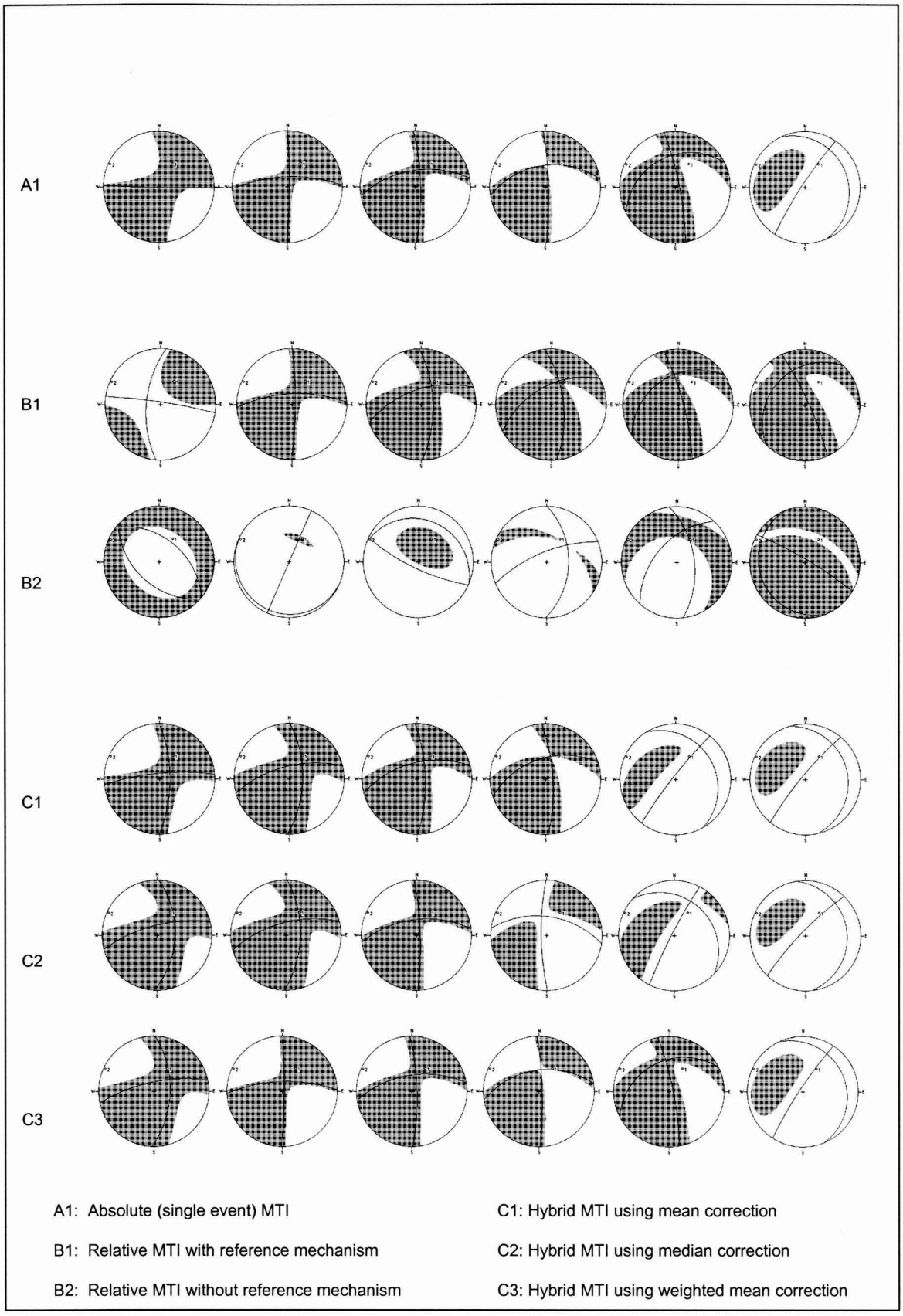

Figure 7.6(d): 20% random noise added to all events - 2 stations (1 and 3).

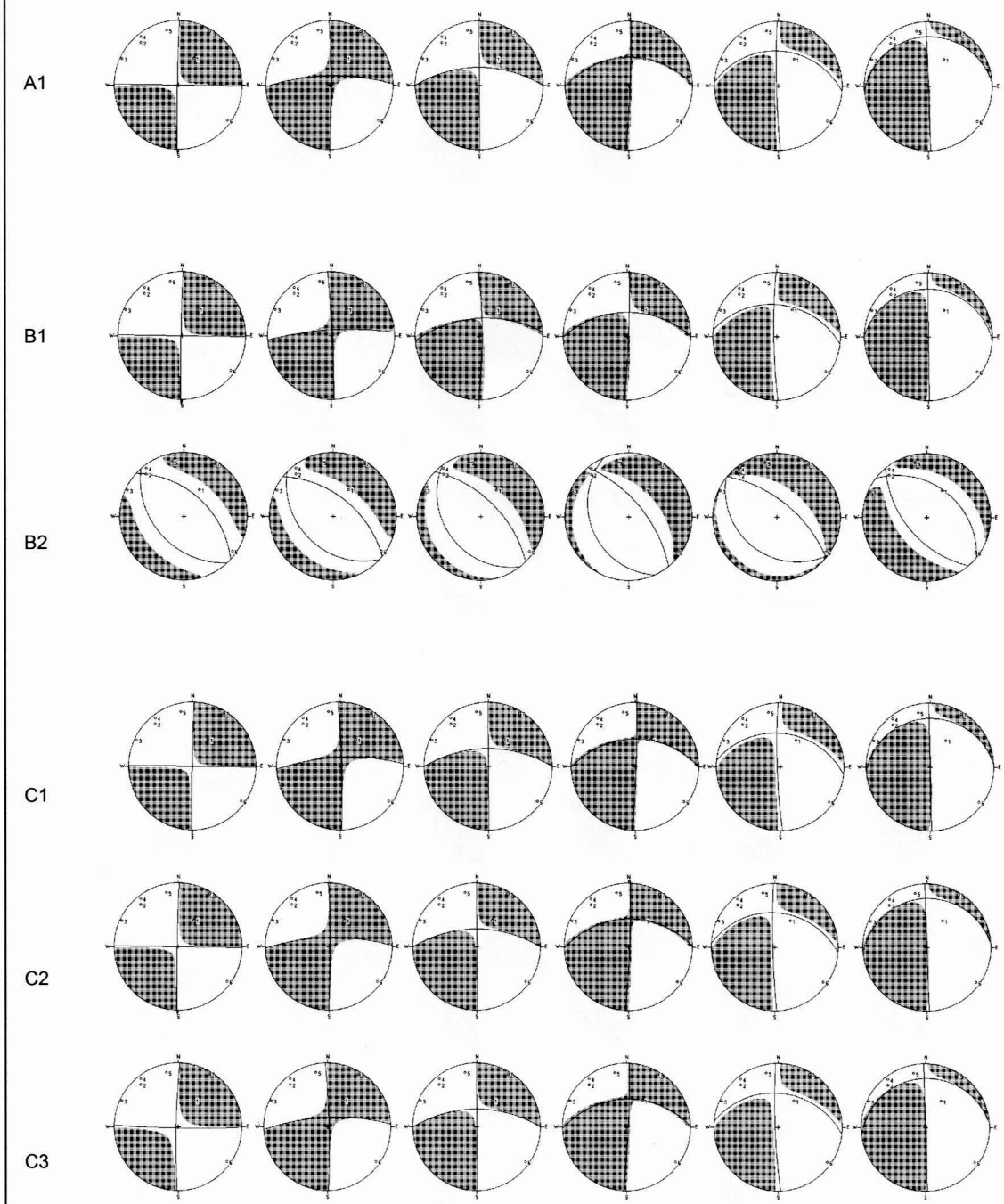

Figure 7.7(a): 30% random noise added to all events - all 7 stations.

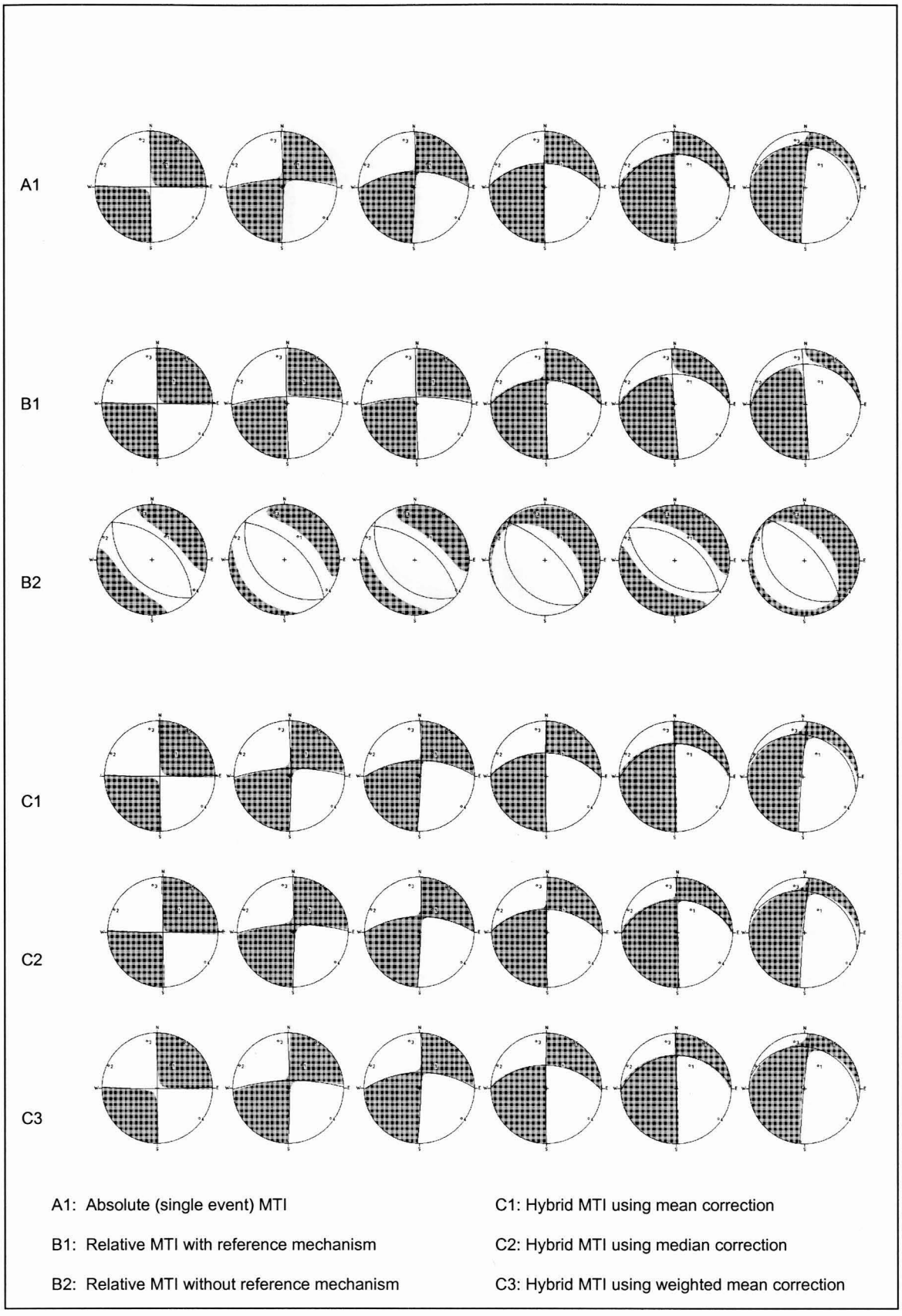

Figure 7.7(b): 30% random noise added to all events - 5 stations (1, 3, 5, 6 and 7).

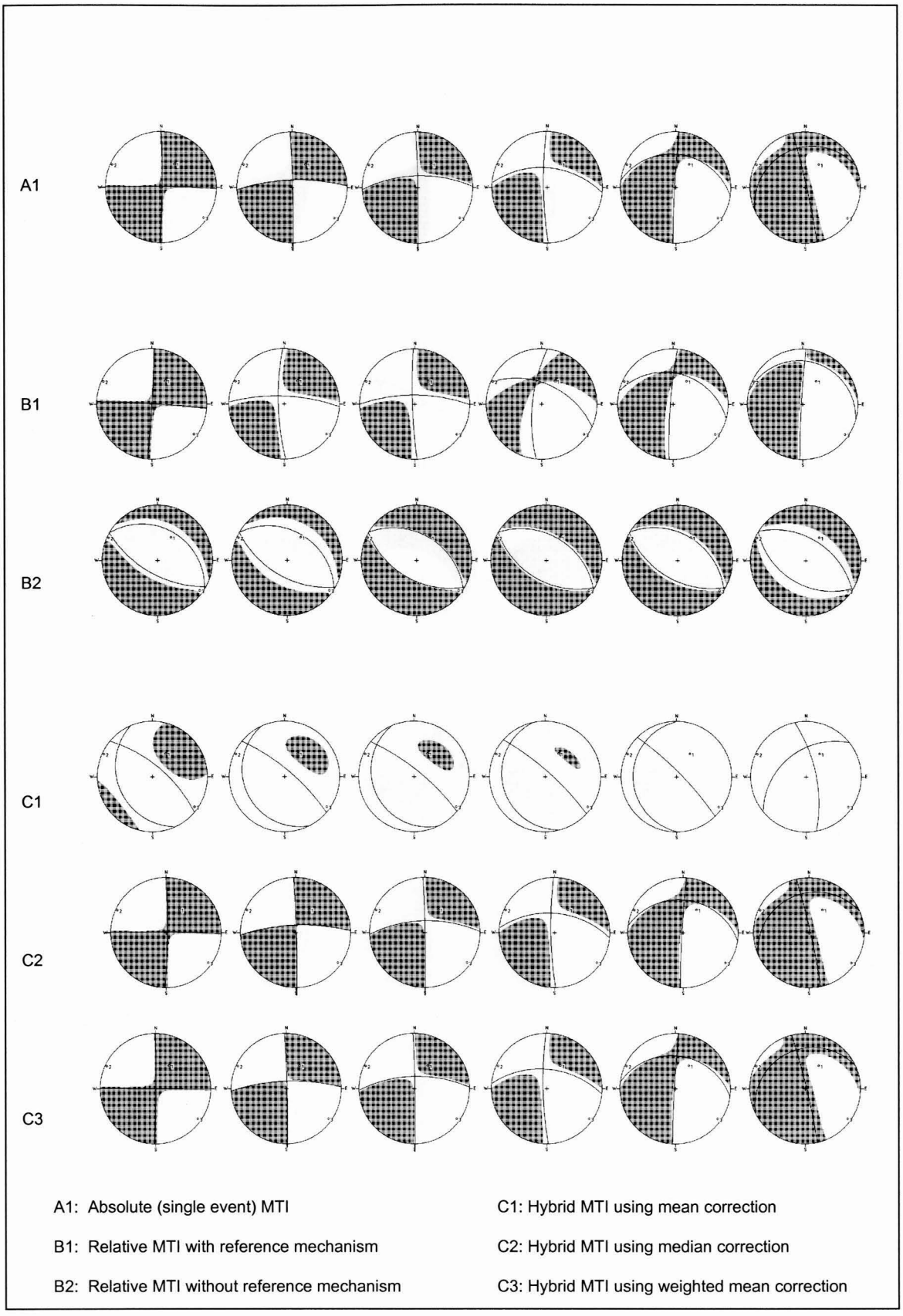

Figure 7.7(c): 30% random noise added to all events - 3 stations (1, 3 and 6).

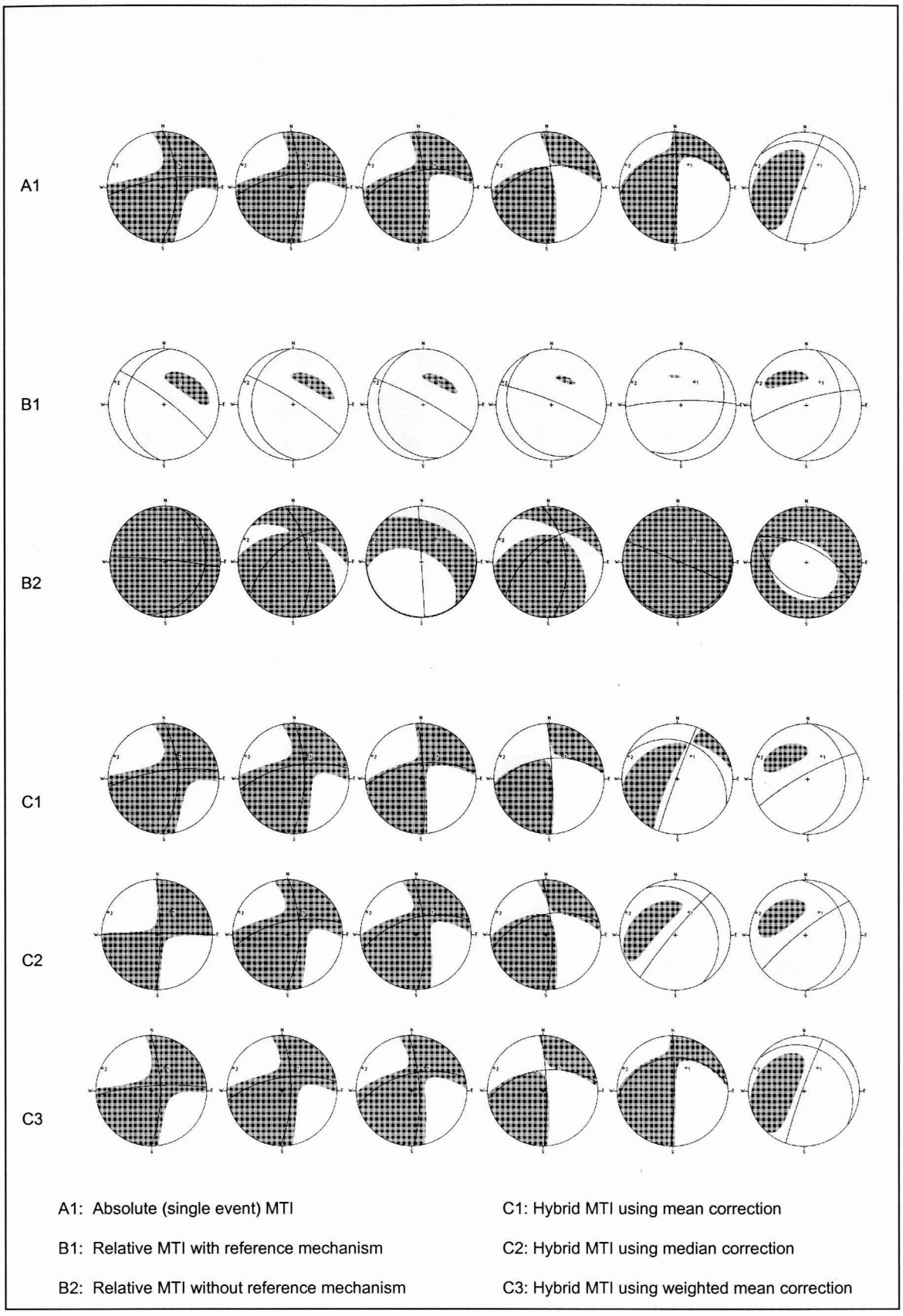

Figure 7.7(d): 30% random noise added to all events - 2 stations (1 and 3).

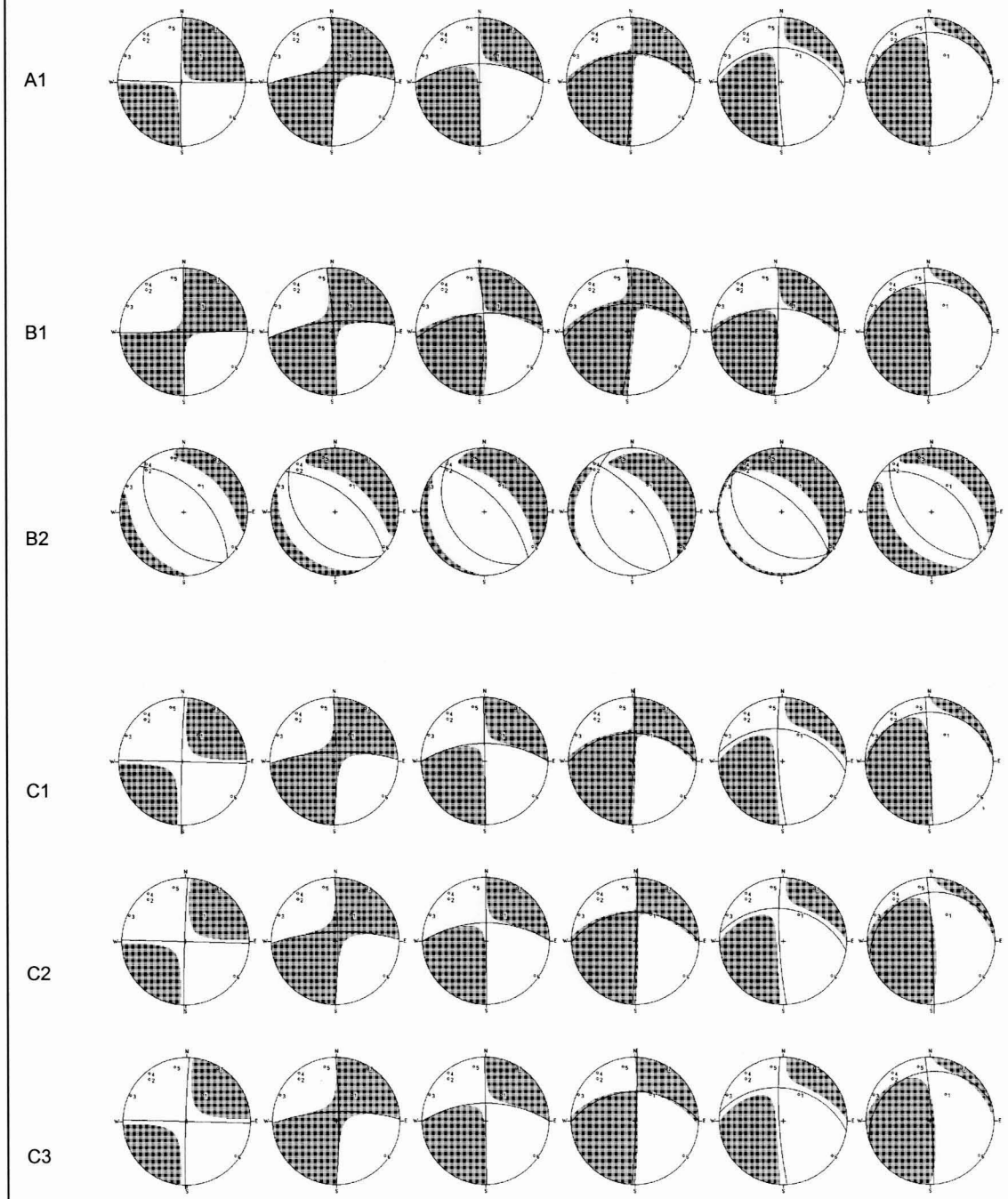

Figure 7.8(a): 40% random noise added to all events - all 7 stations.

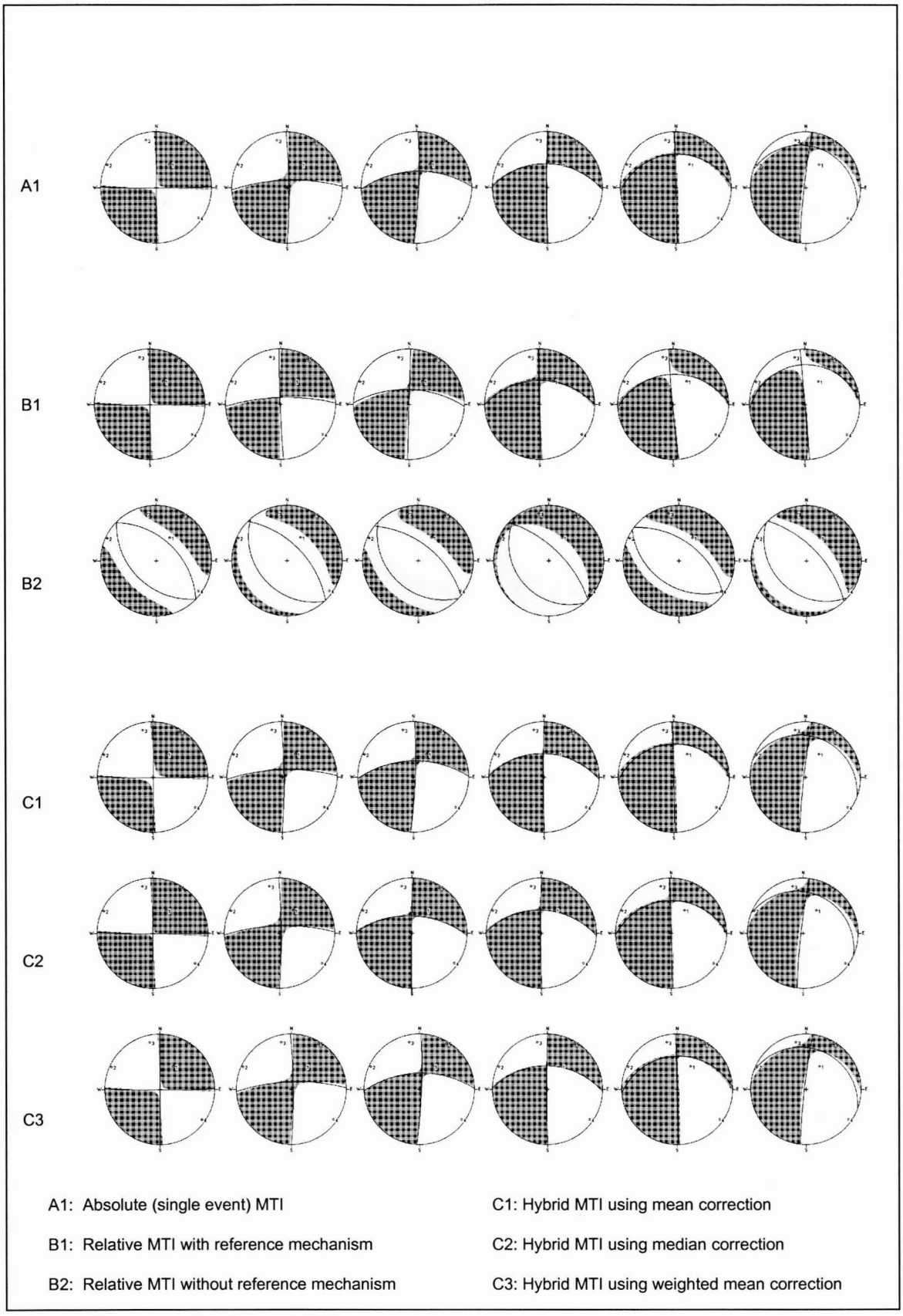

Figure 7.8(b): 40% random noise added to all events - 5 stations (1, 3, 5, 6 and 7).

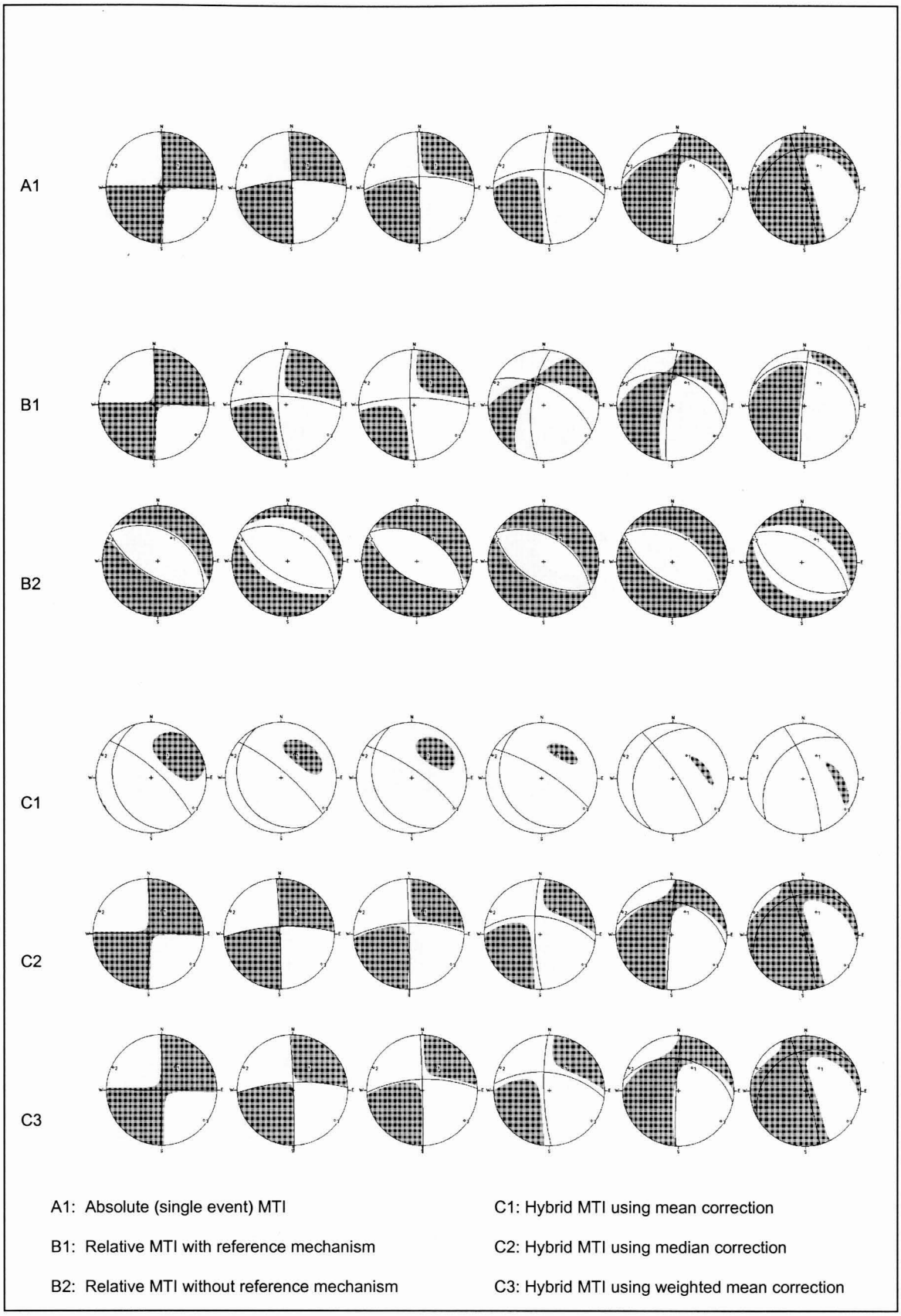

Figure 7.8(c): 40% random noise added to all events - 3 stations (1, 3 and 6).

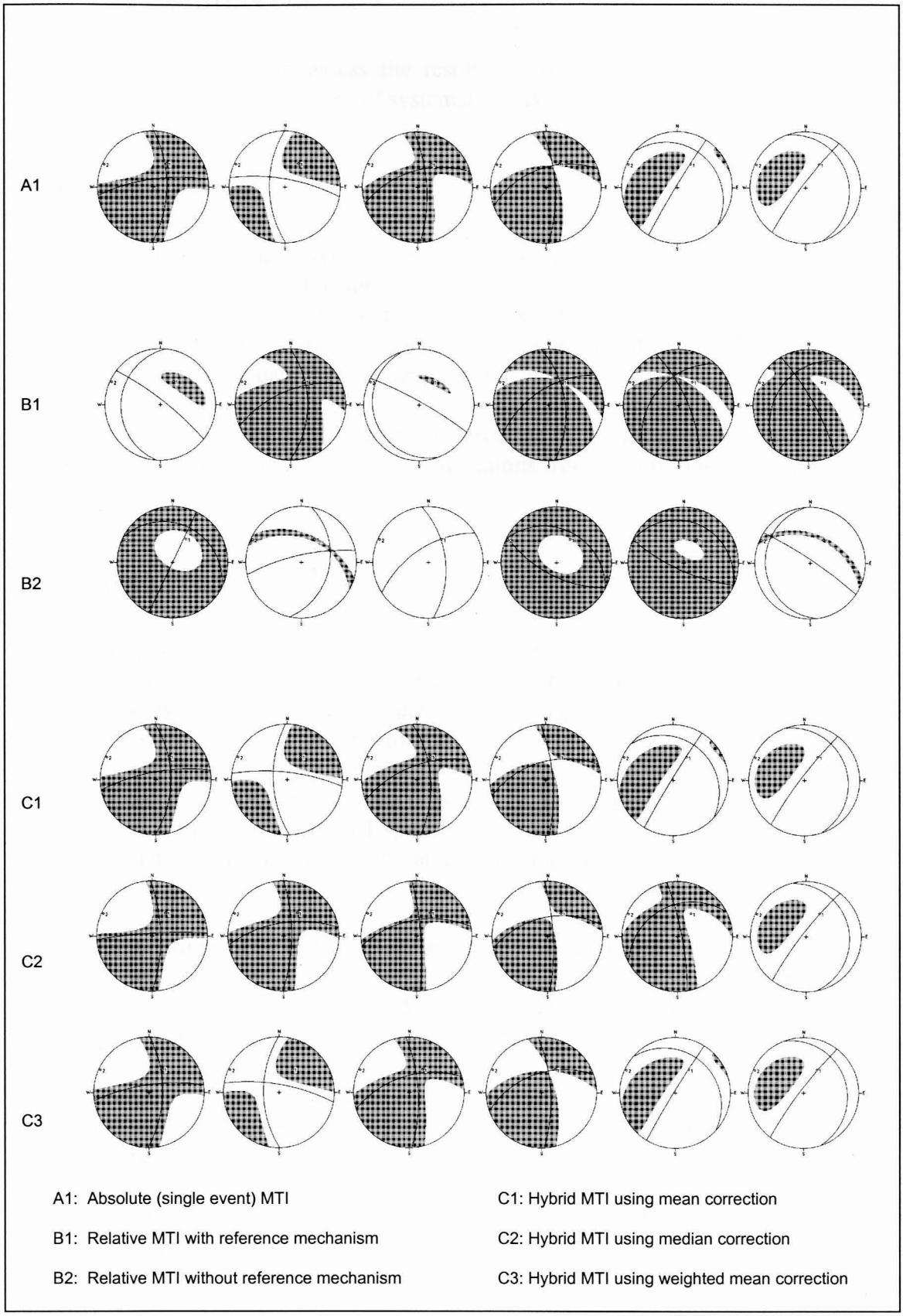

Figure 7.8(d): 40% random noise added to all events - 2 stations (1 and 3).

7.5 EXPERIMENT 3 – SYSTEMATIC NOISE

This test was designed to assess the resolving power of the six moment tensor inversion methods in the presence of systematic noise.

7.5.1 Methodology

In this test, the input data were contaminated by systematic noise. The systematic noise was calculated using Equation 7.2 at a level of 100% of the input amplitude. The noise was applied to all input data (for all events in the cluster) recorded by site 1. The noise was applied only to one channel (or component) of the triaxial site, but to both the P- and S-wave data for that component.

As with the previous two experiments, the coverage of the focal sphere was reduced incrementally, by decreasing the number of stations from 7, in turn to 5, 3 and finally 2.

7.5.2 Results and discussion

Refer to Figures 7.9(a) to (d) and Table 7.3 for the results of Experiment 3. For all of the station configurations, method C3 gives the best resolution in respect of the %DC components as well as the fault-plane solutions. For the 7-station configuration, method C3 yields a DC component of 96.4% and a total average difference between computed and theoretical mechanisms of 4.5°. Methods C2 and B1 follow closely with 88.6 and 88.2% DC components, respectively, and a difference in orientations of 4.6 and 5.9°, respectively. As in Experiment 2, method B2 fares the worst, with a percentage DC component of 42.2% and an average difference in orientations of 43.8°.

As the number of stations is decreased first from 7 to 5 and then to 3, the same trends exhibited earlier by the 7-station configuration are seen again. Method C3 performs the best overall, followed by method C2, then method B1. Method B2 performs poorly, giving the lowest resolution of all the methods.

The performance of all the methods decreases substantially when the inversions are performed using sparse coverage (2 stations) of the focal sphere. Method C3 provides the best resolution overall (57.4% DC components, and a total average difference between resolved and theoretical mechanisms of 20.3°). As in Experiment 2, method B1 yields the highest percentage DC components (72.5% DC) and lowest percentage of false components (46.0%), despite the poor resolution of the fault- plane solution (total average difference between resolved and theoretical mechanisms of 30.1°).

Table 7.3: Results of Experiment 3 - 100% systematic noise added to site 1 and component 1 data (P- and S-waves) for all events in cluster.

	Average source components (%)				Average difference between resolved mechanisms and theoretical mechanisms (degrees)			
7 stations	**%ISO**	**%DC**	**%CLVD**	**%False**	**Strike**	**Dip**	**Rake**	**Total**
A1	4.8	87.6	12.4	17.1	3.0	5.2	1.2	9.4
B1	3.4	88.2	11.8	15.2	1.0	3.8	1.1	5.9
B2	17.1	42.2	57.7	74.8	22.3	18.5	3.0	43.8
C1	6.7	85.3	14.7	21.4	4.0	8.2	1.5	13.7
C2	3.4	88.6	11.4	14.8	1.5	3.8	0.3	4.6
C3	1.5	96.4	3.6	5.1	1.0	2.0	1.5	4.5
5 stations								
A1	4.7	87.7	12.3	17.0	1.8	5.2	0.8	7.8
B1	3.1	85.9	14.1	17.2	1.0	4.0	1.8	6.8
B2	10.9	75.2	24.8	35.7	10.2	9.2	0.7	20.1
C1	6.9	85.2	14.8	21.7	3.7	8.5	2.0	14.2
C2	3.4	88.2	11.8	15.2	1.3	4.8	0.1	6.2
C3	1.6	95.8	4.2	5.8	0.8	2.0	1.8	4.6
3 stations								
A1	5.5	84.3	15.7	21.2	4.3	5.3	0.7	10.3
B1	7.9	85.1	14.9	22.8	4.0	3.8	2.0	9.8
B2	25.5	59.5	40.5	66.0				>90
C1	8.6	77.0	23.0	32.6	5.8	6.0	7.3	19.1
C2	7.0	81.7	18.3	25.3	4.0	4.5	0.5	9.0
C3	3.1	93.8	6.2	9.3	0.8	2.3	1.8	4.9
2 stations								
A1	22.5	48.6	51.4	73.9	6.3	13.0	6.5	25.8
B1	18.5	72.5	27.5	46.0	9.6	14.3	6.2	30.1
B2	21.1	60.5	39.5	60.6				>90
C1	24.2	44.5	55.5	79.7	5.8	11.8	7.3	24.9
C2	20.4	56.9	43.1	63.5	9.0	9.1	4.3	23.4
C3	19.1	57.4	42.6	61.6	3.5	12.0	4.8	20.3

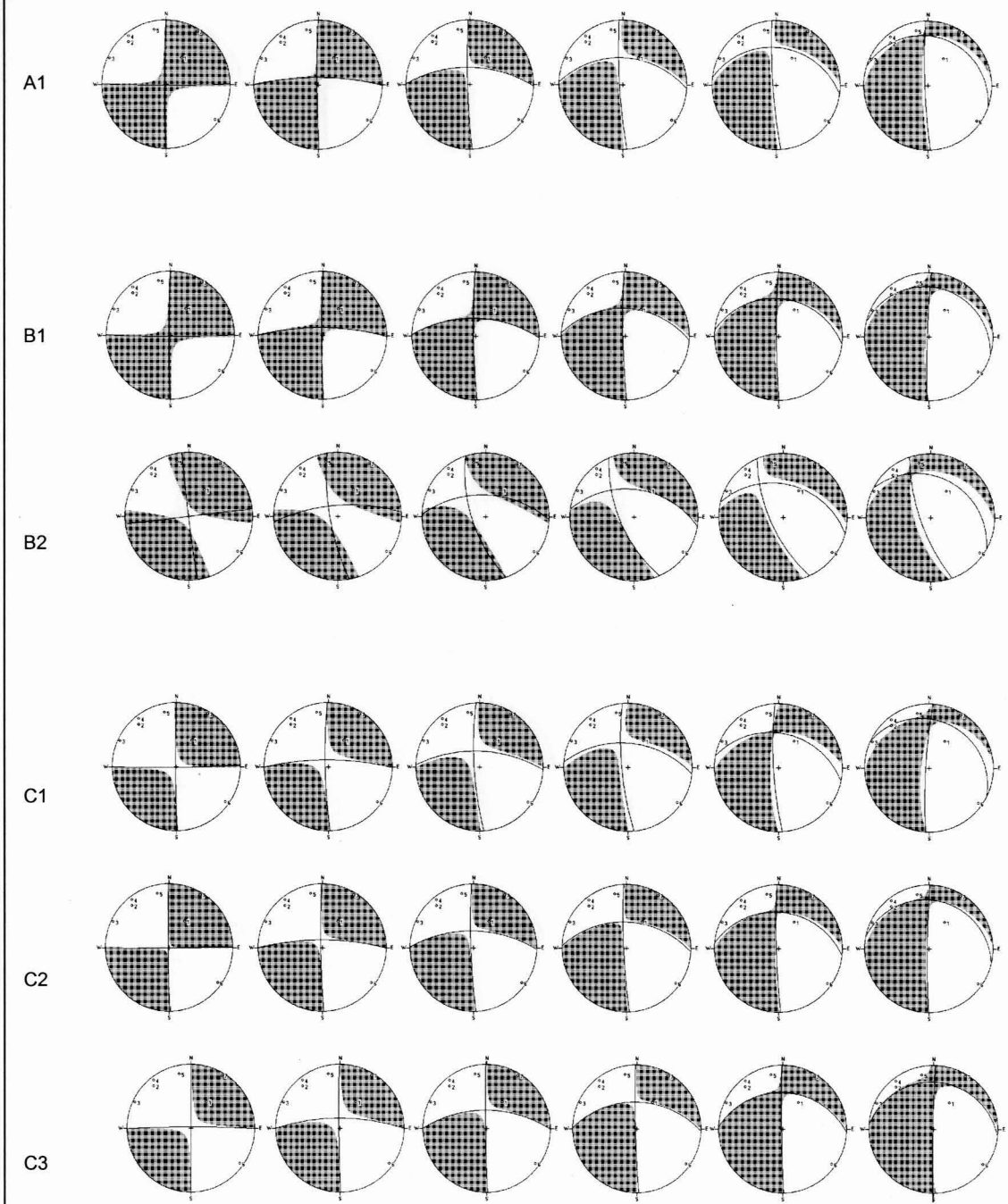

Figure 7.9(a): 100% systematic added to site 1 and component 1 data (P- and S-waves) for all events in cluster - all stations.

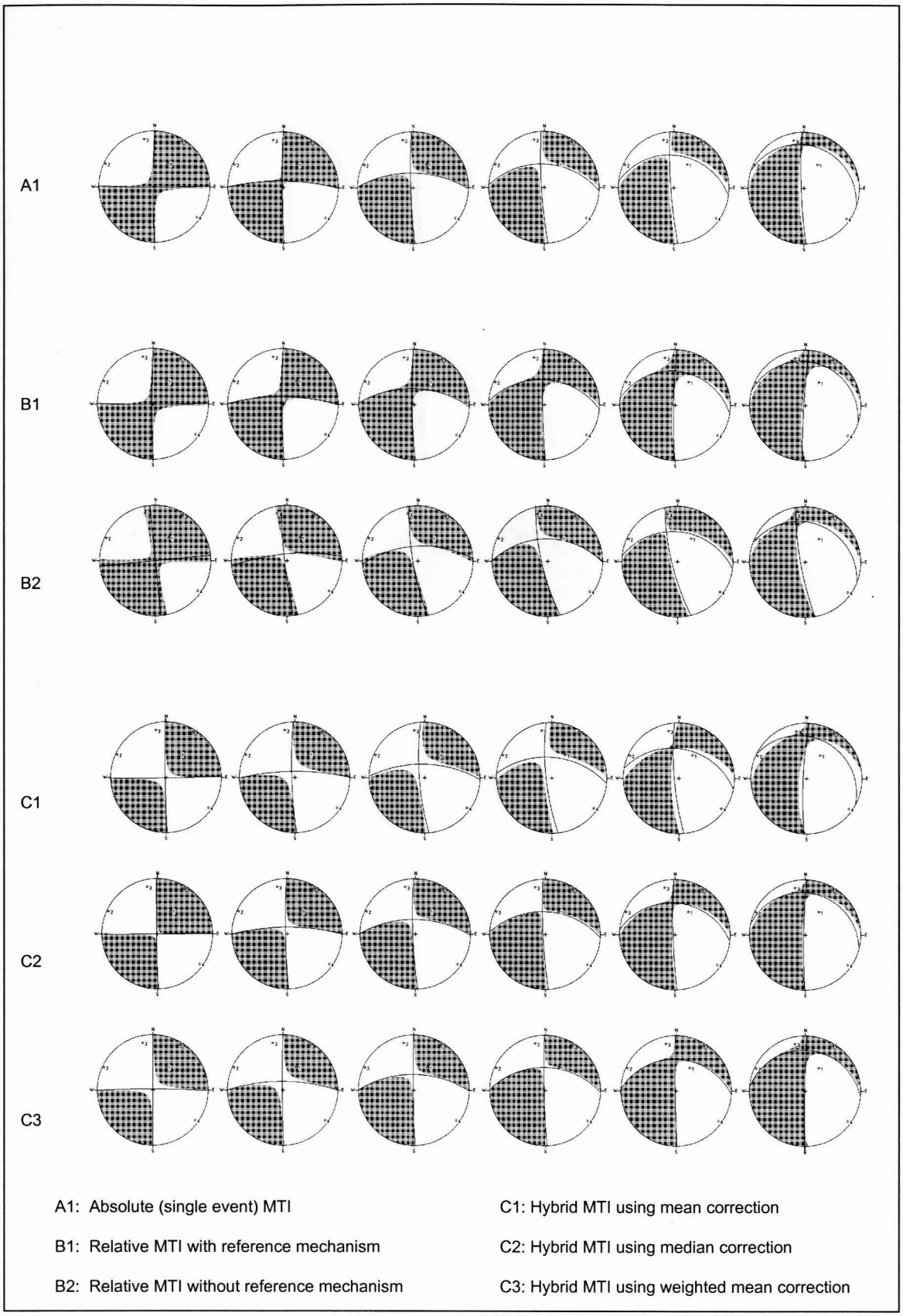

Figure 7.9(b): 100% systematic added to site 1 and component 1 data (P- and S-waves) for all events in cluster - 5 stations.

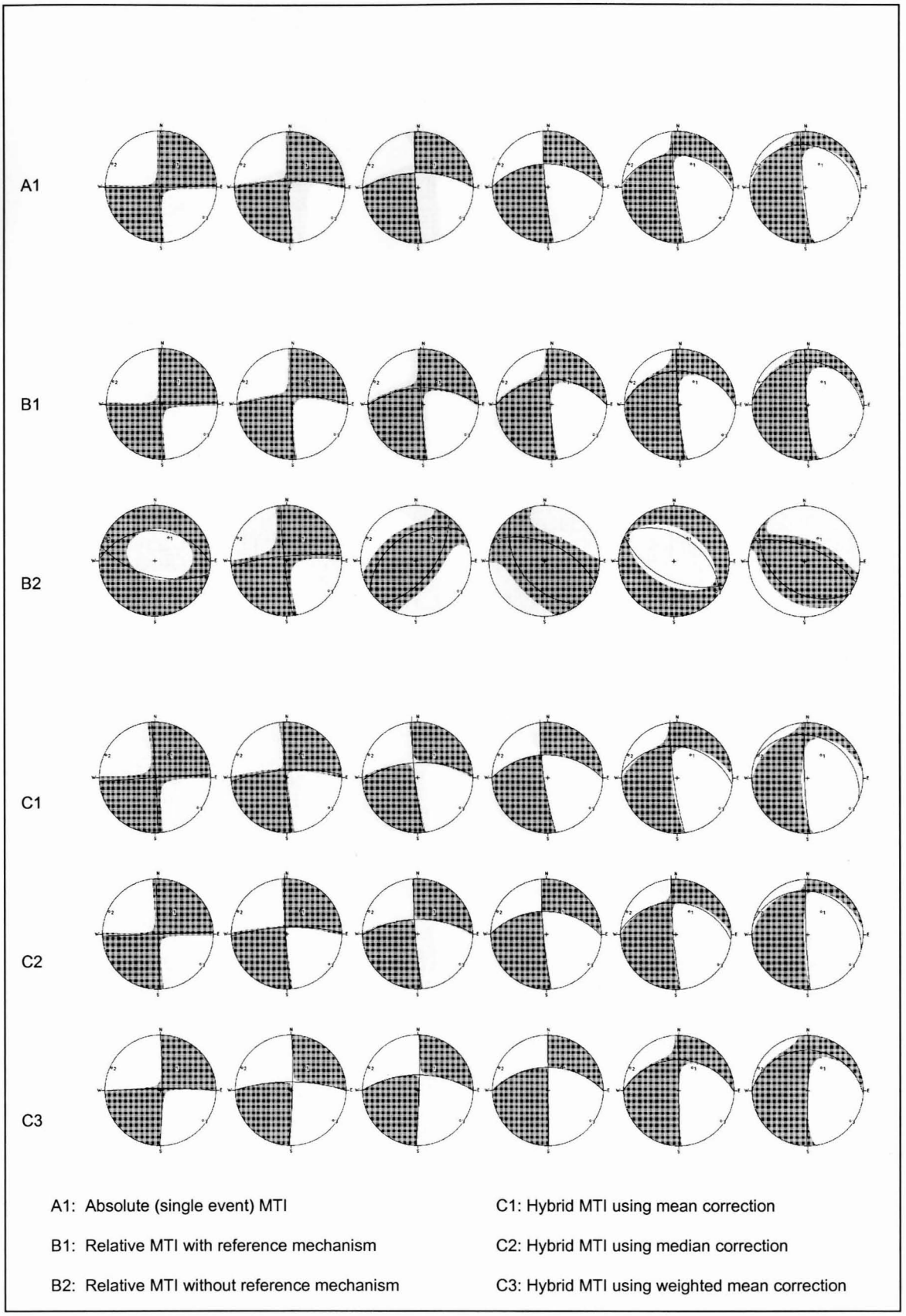

Figure 7.9(c): 100% systematic added to site 1 and component 1 data (P- and S-waves) for all events in cluster - 3 stations.

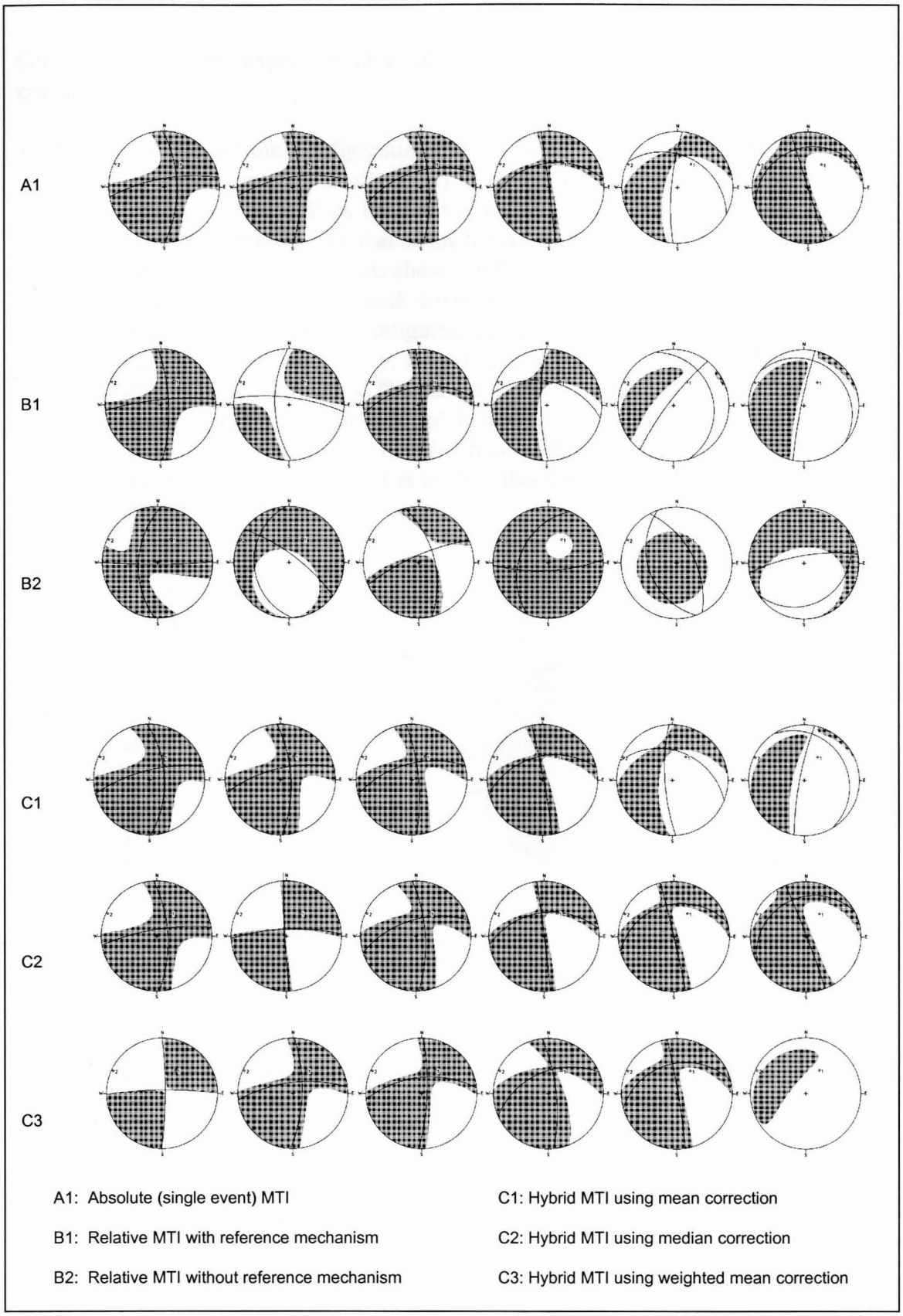

Figure 7.9(d): 100% systematic added to site 1 and component 1 data (P- and S-waves) for all events in cluster - 2 stations.

7.5.3 Conclusions

On the basis of the experimental results described above, the following can be concluded:

1. For all of the station configurations investigated, the hybrid method using a weighted mean correction (method C3) gives the best resolution in respect of the %DC components as well as the fault-plane solutions. The performance of this method is closely matched by that of the hybrid method using a median correction (method C2). These two methods show similar robustness and stability in extreme configurations concerning network coverage of the focal sphere and systematic noise and, in all situations investigated, outperformed the relative and absolute methods. For the sake of brevity, the size of each radiation pattern displayed in this chapter is reduced by 25%. The danger of this, however, is that the full impact of the success of two aforementioned hybrid methods in reducing the level of systematic noise is diminished. For this reason, the radiation patterns of event 5 are given again in Figure 7.10. It is evident that the hybrid method has the effect of 'focussing' the solution.

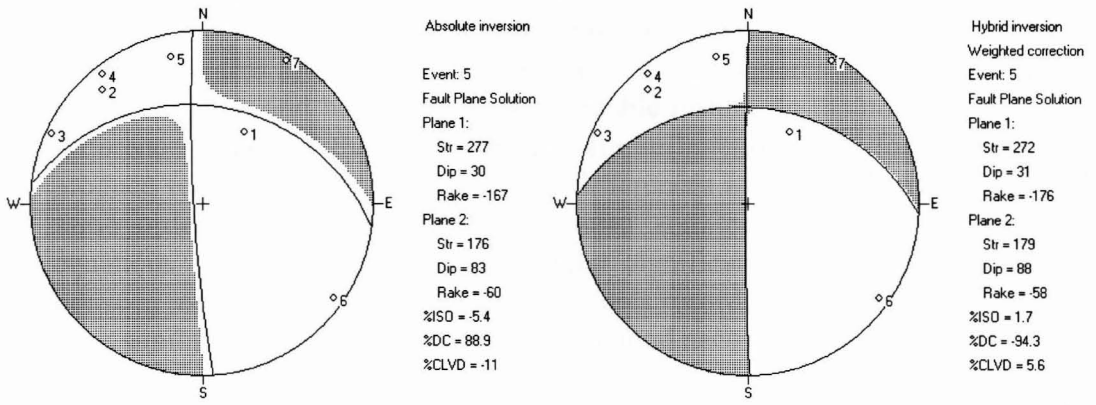

Figure 7.10: Radiation patterns and source parameters of event 5 computed using (a) the absolute moment tensor inversion method, and (b) the hybrid method using a weighted mean correction.

2. As in Experiment 2, the relative method with a reference mechanism (method B1) exhibited slightly poorer performance in all the tests when compared with the aforementioned hybrid methods. However, for the configuration having sparse coverage (2 stations) of the focal sphere, this method yields the highest percentage DC components and lowest percentage of false components of all the methods despite the poor resolution of the fault plane.

3. As before, the hybrid method using a mean correction (method C1) gave unreliable results and is very sensitive to high noise levels.

4. The relative moment tensor inversion without a reference mechanism (method B2), when applied to events having very similar mechanisms, is more sensitive to

noise than the absolute method and hybrid methods using median and weighted mean corrections. As mentioned previously, since clusters of events recorded underground are likely to have similar mechanisms, this method must be used with caution.

7.6 SUMMARY OF CONCLUSIONS

The main findings of the three experiments can be summarised as follows:

1. In the noise-free situation, the relative method without reference mechanism (method B2) shows the highest resolution of mechanisms, provided that the coverage of the focal sphere is not too sparse (> 3 stations). The hybrid method (method C2), using a median correction, is the most robust of all the methods tested in the most extreme case of poor coverage (2 stations) of the focal sphere.

2. In contrast, the application of even low levels of random noise has a devastating effect on the relative method without reference mechanism (method B2). This is of interest because in the noise-free case, this method provides the best resolution of the mechanisms for the same network configuration and the same set of synthetic mechanisms. The reason for this phenomenon is thought to be that for mechanisms that are alike or very similar, the least-squares matrix of method B2 is near-singular and hence produces unreliable results. In the noise-free case, the differences amongst these mechanisms are sufficiently large for method B2 to produce realistic results. However, the differences in the mechanisms are of the same order as the level of applied noise and, consequently, the system of equations becomes near-singular, thereby significantly blurring the distinction between mechanisms. Since clusters of events recorded underground are likely to have similar mechanisms, the use of this method necessitates caution.

3. In the random noise tests, the absolute moment tensor inversion method (method A1) and the hybrid methods using a median correction (C2) and a weighted mean correction (C3) show similar robustness and stability in extreme configurations concerning network coverage of the focal sphere and noise level. The levels of noise inflicted on the input data in these tests are extremely high – certainly higher than would be expected in reality. Therefore, the prospects of retrieving the source mechanisms of real events by these methods are good.

4. The relative method with a reference mechanism (method B1) exhibited slightly poorer performance in all the random noise tests when compared with the aforementioned methods.

5. In the experiment where high levels of systematic noise are applied to the input synthetic data, the hybrid methods using a median correction and weighted mean correction show similar robustness and stability in extreme configurations concerning network coverage of the focal sphere and systematic noise. In all situations investigated, these two hybrid methods outperformed the relative and absolute methods. As seen in the random noise tests, the relative method with a

reference mechanism (method B1) exhibited slightly poorer performance in all the tests when compared with the aforementioned hybrid methods. However, for the configuration having sparse coverage (2 stations) of the focal sphere, this method yields the highest percentage DC components and lowest percentage of false components of all the methods despite the poor resolution of the fault plane.

6. In all the tests involving noise, the hybrid method using a mean correction (method C1) gave unreliable results and is sensitive high noise levels. This is not surprising since the correction applied is based only on the mean residual and, therefore, is extremely sensitive to outliers.

Chapter 8

CASE STUDY

In this chapter, two of the three hybrid moment tensor inversion methods developed and described in Chapter 6 are applied to a cluster of 14 events recorded at Oryx Gold Mine. Because these two hybrid methods (based on the median correction and the weighted mean correction) showed similar robustness and stability in the presence of random and systematic noise, both methods are applied to recorded data to determine which gives the better results. The results are compared with those determined using absolute methods. This case study is described in part in a paper submitted to RaSim5 (Andersen & Spottiswoode, 2001).

8.1 GENERAL INFORMATION

8.1.1 Geological setting

Oryx Gold Mine (originally known as Beisa Mine) is located approximately 340km south-west of Johannesburg at the southern end of the arcuate Witswatersrand basin (Figure 8.1). The following geological description is taken from Tweedie (1986). The area is an open plain 1400m above sea level and underlain by 400-800m of flat-lying Karoo rocks (Carboniferous). Beneath these younger rocks are folded and faulted Precambrian volcanics and sediments, which contain the auriferous conglomerates of the Witwatersrand Supergroup. The Witwatersrand Supergroup consists of thick clastic sediments and shales with some intercalated lava flows and lies unconformably on Archaean granites and schists.

The reef mined at Oryx is known as the Beisa reef and can be correlated with the base of the Johannesburg Subgroup of the Central Rand. The reef varies from a 5cm thick quartz-pebble conglomerate to a unit of loosely packed quartz and chert pebbles 150cm thick. A seam, up to 5cm thick on the basal contact, consisting almost entirely of carbon, carries virtually all of the gold and uranium mineralisation with the latter predominating.

Early exploration efforts along the western edge of the basin were frustrated by the complicated geological structures. Overfolding of the Central Rand beds was first proved by drilling along the basin edge in the northern part of the Orange Free State goldfield. This, in addition to some other evidence, led to the supposition that the reefs in the south of the basin, previously thought to be too deep for exploitation, may be brought nearer to the surface by basin-edge folding. This theory proved to be correct beyond expectation, the magnitude of the overfolding being greater than anything previously known in Witswatersrand rocks (Figure 8.2). The Beira reef, for example, is brought from a depth of 3km to within 400m of the surface.

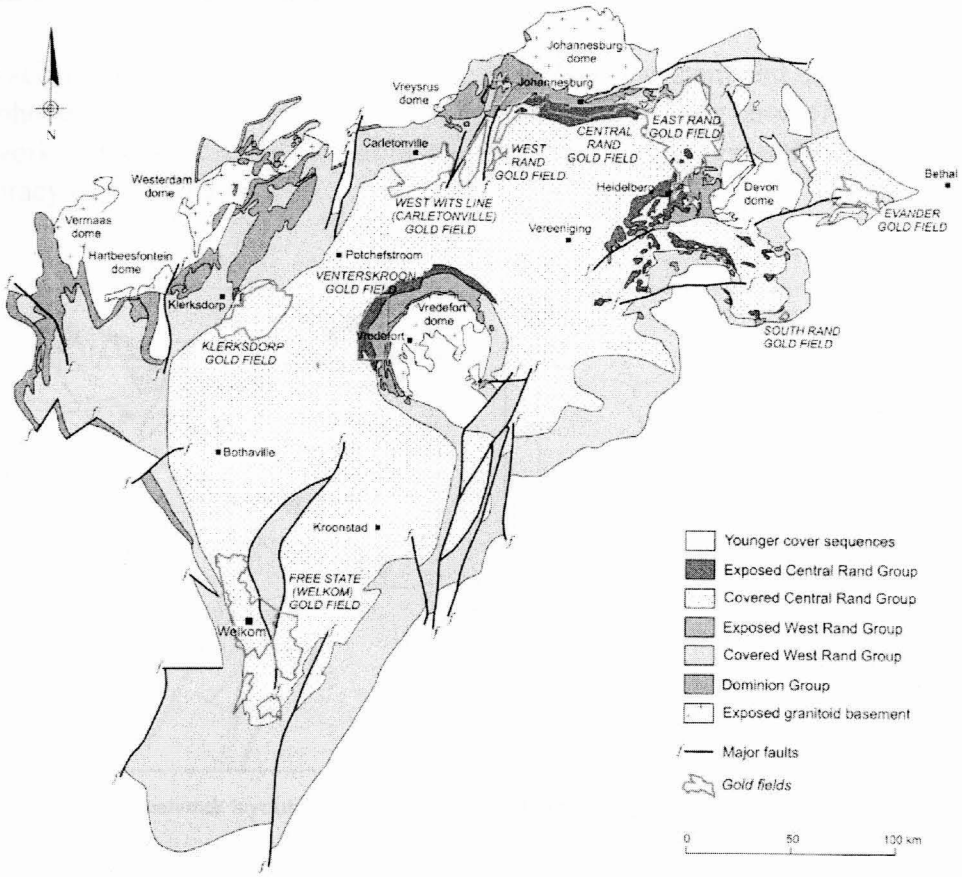

Figure 8.1: Location and regional geology (from Tweedie, 1986).

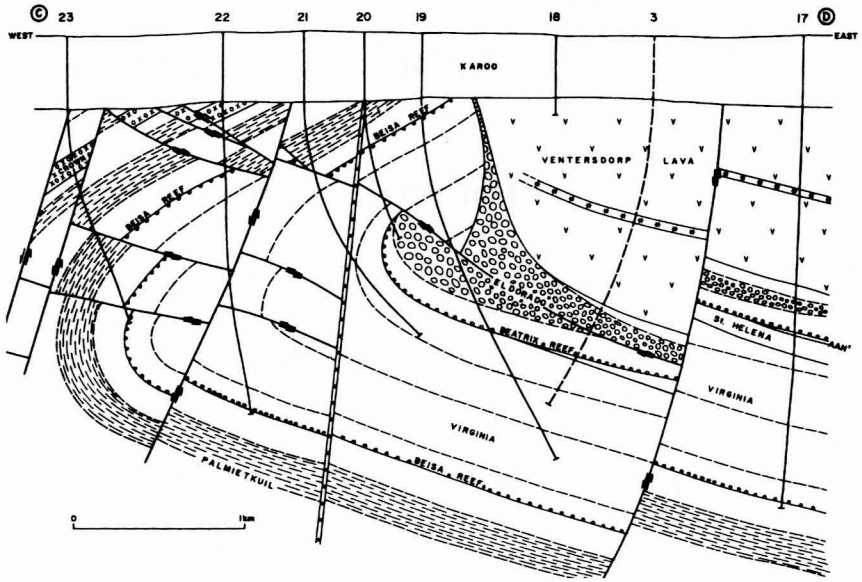

Figure 8.2: East-west section illustrating basin-edge overfolding of a magnitude greater than previously known in Witwatersrand rocks (from Tweedie, 1986).

8.1.2 Seismic network

The seismic network at Oryx Gold Mine is a PRISM system and consists of 7 triaxial geophones located at various depths on the mine's lease area (Figure 8.3a). The network has a sensitivity of approximately M_L = -1 (Figure 8.3b) and a location accuracy of around 20m.

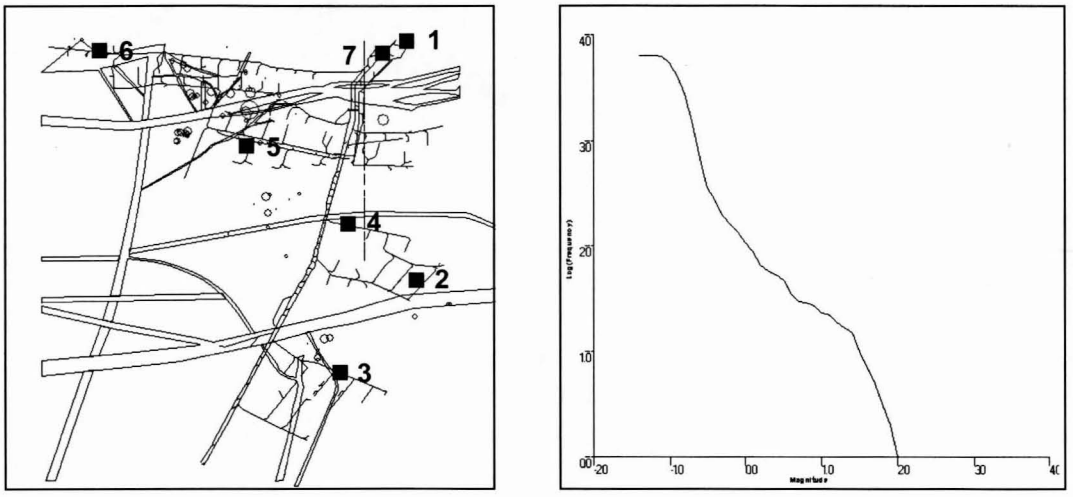

(a) Oryx seismic network layout

(b) Frequency-magnitude relationship

Figure 8.3: Gutenburg-Richter frequency-magnitude relation showing a network sensitivity of about M = -1.

8.2 SEISMIC DATA AND PROCESSING

8.2.1 Seismic event cluster identification

The event cluster considered in this study is positioned ahead of an advancing stope at a depth of approximately 2500m (Figure 8.4b). The cluster was selected for closer study due to the noticeably tight spatial grouping, which becomes even more evident when the data set is filtered with respect to event magnitudes. The entire data set, recorded between March 1999 and June 2000, consists of 6495 events, and is shown in Figure 8.4(a). The filtered data set (displaying events having local magnitudes > 0) consists of 78 events, and is displayed in Figure 8.4(b). Only the seismograms of the filtered data set were available for this study.

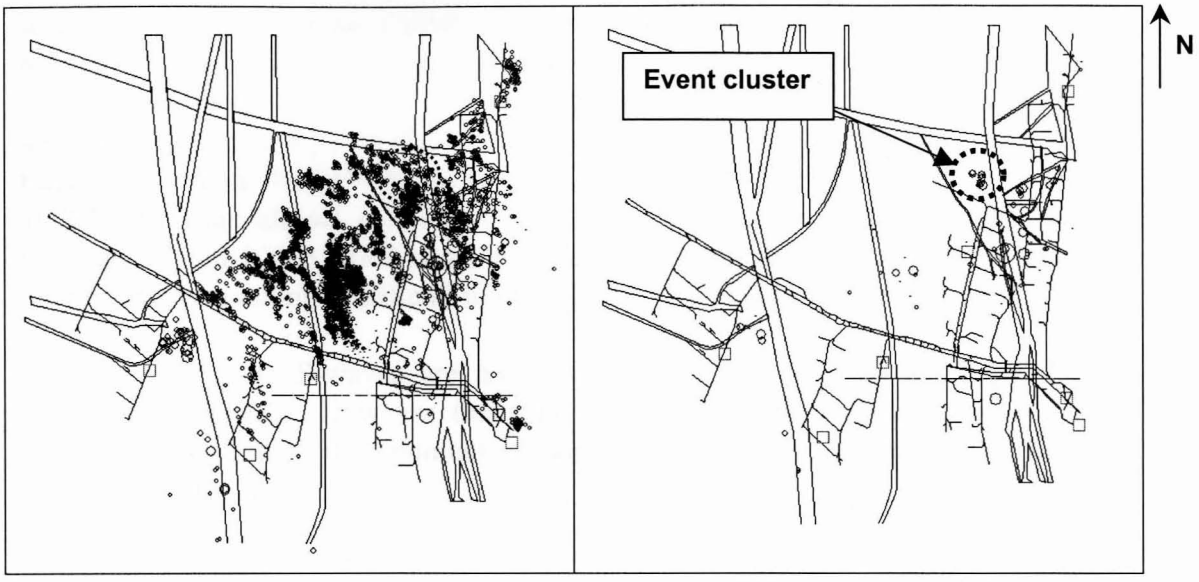

(a) Entire data set (March 1999 – May 2000) (b) Events having M > 0 (March 1999 – May 2000)

Figure 8.4: Plan view of events recorded at Oryx Gold mine (a) Entire data set: 6495 events recorded between March 1999 and May 2000 (b) Filtered data set: 78 events having local magnitudes M > 0 recorded during the same time period. Open squares represent the triaxial geophone sites.

8.2.2 Data description

The cluster selected for investigation consists of 14 of the 78 events, and the local magnitude M_L for these events ranges from 0 to 1.4 (Table 8.1), recorded over a time period of approximately 9 months.

Table 8.1: Event parameters

Event ID	Date	Time	M_L	X	Y	Z	Error
991014004	14/10/1999	08:04:39	0.4	3117569.5	26493.4	-2537.8	13.5
991118076	18/11/1999	16:50:11	0.5	3117572.0	26502.4	-2534.9	11.8
991123066	23/11/1999	17:04:10	0.2	3117549.3	26495.9	-2502.2	5.9
991123074	23/11/1999	17:43:53	1.4	3117571.0	26532.1	-2502.2	6.4
991127024	27/11/1999	13:35:28	0.9	3117570.5	26508.0	-2535.5	10.7
991206128	06/12/1999	17:11:46	1.4	3117562.8	26515.8	-2510.6	7.6
991213000	13/12/1999	04:24:36	0.4	3117573.3	26525.3	-2530.4	7.9
1000112007	12/01/2000	13:53:23	0.0	3117564.3	26519.7	-2528.4	9.4
1000209102	09/02/2000	19:27:11	0.9	3117513.0	26456.3	-2549.1	29.3
1000225001	25/02/2000	03:48:59	1.3	3117517.0	26461.4	-2490.5	5.0
1000316107	16/03/2000	17:45:30	0.4	3117535.8	26525.0	-2516.9	18.0
1000328082	28/03/2000	18:56:44	0.5	3117526.8	26533.5	-2508.9	10.6
1000331112	31/03/2000	23:38:45	0.2	3117523.5	26524.9	-2508.9	15.8
1000512000	12/05/2000	11:45:06	1.4	3117520.5	26539.8	-2516.9	6.9

Not only is the cluster of events tightly grouped in space, but also some of the waveforms of the events are remarkably similar. This implies that the underlying

source mechanisms are very similar. The waveform similarity is illustrated in Figure 8.6. The waveforms shown in the figure are the velocity traces recorded by component 2 of triaxial site 1. The waveforms are plotted using the same time scale on the x-axis and no filters have been applied. Inspection of the traces reveals that some of the traces (for events 991014004, 991118076, 991123066, 991127024, 991206128 and 1000316107) are almost indistinguishable from one another, especially the S-wave packages. Event 1000328082 is complex and the P-arrival is masked by the coda of a previous wave, making it difficult to identify the onset of the P-wave.

In many cases, the S-waves are not simple pulses but have an additional higher frequency component. However, this study assumes a simple impulsive source model and, for this reason, the moment tensor solutions will describe the average or dominant source mechanism.

8.2.3 Moment tensor inversion

The distances from the event cluster to the receivers range from ~350m (site 5) to ~2000m (site 3). The source radius of the largest event is ~ 57m (P-wave radius = 56.5m and S-wave radius = 57.8m for M_L = 1.4). Since the source radius of the largest event in this cluster is much less than the distance to the closest geophone site, the far-field approximation is satisfied.

The hybrid moment tensor inversion method using a median correction coded by the author was applied to the event cluster. Absolute moment tensors were also computed for comparative purposes. The inputs to both inversion methods consist of the spectral plateaus of both P- and S-waves at frequencies below the corner frequency of the time-integrated displacement traces (Figure 8.5). The polarities of dominant motion were used as an additional constraint and were determined from cross-correlation of observed with synthetic P- or S-waves.

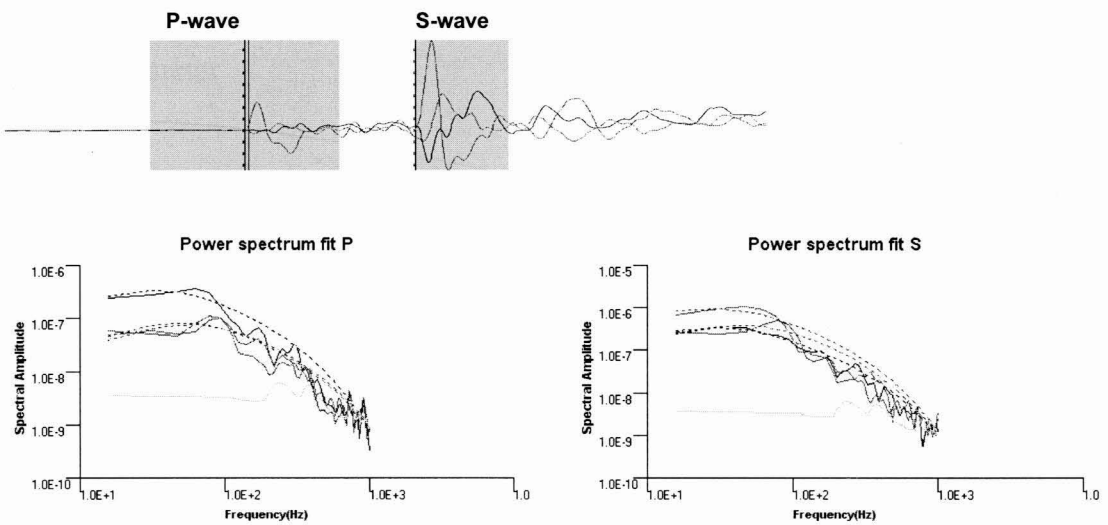

Figure 8.5: Spectra of the low-pass filtered time-integrated displacement traces (a) for the P-wave, and (b) for the S-wave.

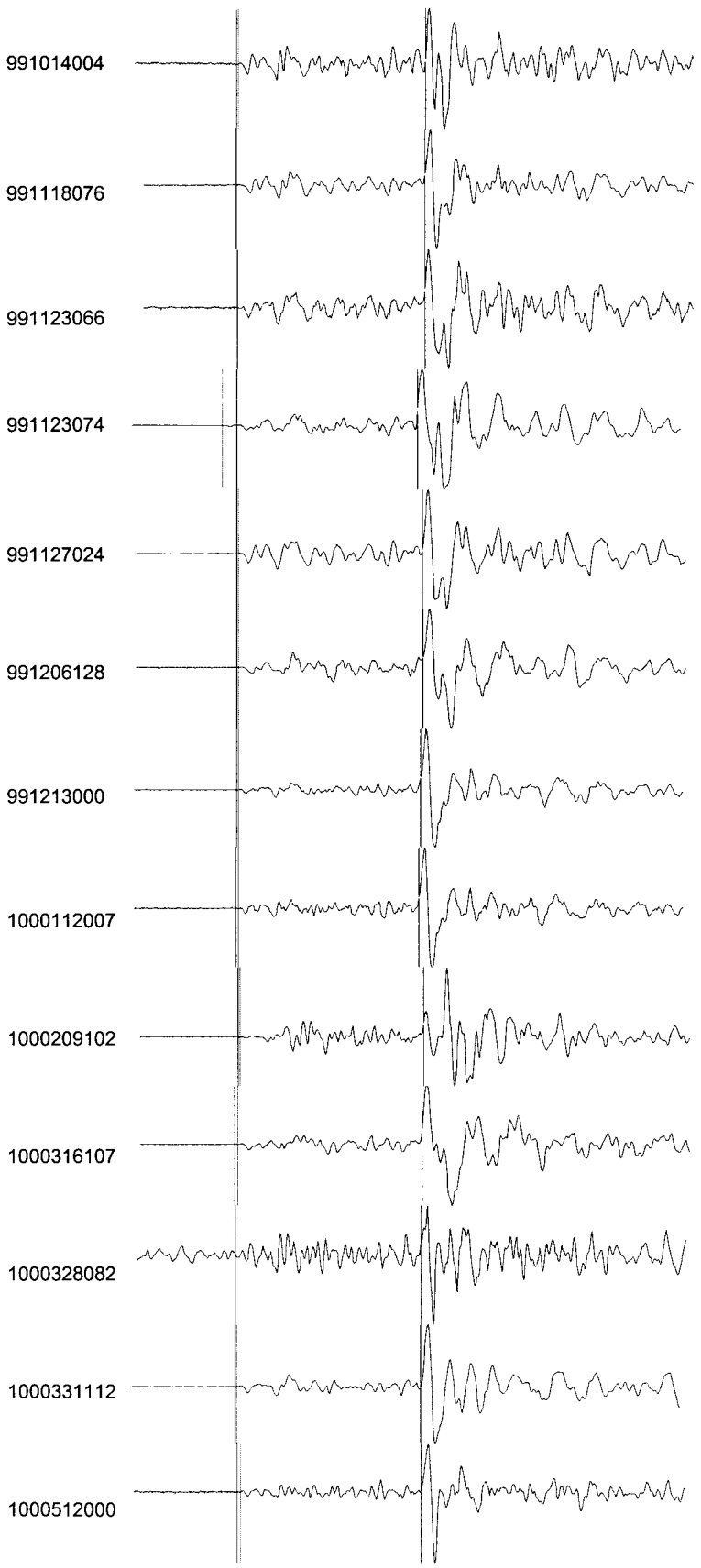

Figure 8.6: Velocity waveforms plotted using the same time axis as recorded by site 1, component 2. Note similarity between events 991014004, 991118076, 991123066, 991127024, 991206128 and 1000316107. Only 13 of the 14 events are displayed since site 1 was inactive when event 1000225001 occurred.

Of the 14 events, only 12 were used in the first hybrid inversion (Table 8.2). Events 1000209102 and 1000225001 were rejected owing to the difficulty in identifying the various wave phases due to source complexity. A further two events were rejected from the cluster in the second hybrid inversion on the basis of their relatively 'poorer' solutions in order to ascertain the effect this would have on the other solutions.

Table 8.2: Qualitative assessment of seismograms

Event ID	Comment	Moment tensor inversion
991014004	Clear P and S-arrivals	Successful
991118076	Clear P and S-arrivals	Successful
991123066	Clear P and S-arrivals	Successful
991123074	Clear P and S-arrivals	Successful
991127024	Clear P and S-arrivals	Successful
991206128	Clear P and S-arrivals	Successful
991213000	Clear P and S-arrivals	Successful
1000112007	Clear P and S-arrivals	Successful
1000209102	Complex	Rejected from cluster
1000225001	Complex	Rejected from cluster
1000316107	Poor signal to noise ratio	Rejected from 2nd hybrid inversion
1000328082	Poor P-picks because P-wave of second event is lost in the coda of a previous event. Clear S-arrivals.	Successful
1000331112	Clear P and S-arrivals	Successful
1000512000	Complex	Rejected from 2nd hybrid inversion

8.3 Results And Discussion

One of the difficulties in moment tensor inversions is proving that the results provide an accurate reflection of reality. The only way this verification can be reliably undertaken is to obtain a detailed fracture mapping of the area of interest and compare the locations and orientations of the computed fault-plane solutions with those of the mapping. Even then, the conclusions often remain speculative. In the absence of such mapping, lesser techniques must be used. In this particular case study, the similarity of the waveforms plays an important role in assessing the integrity of the hybrid moment tensor solutions in the sense of whether or not they are any better than those determined using absolute methods. Since the input waveforms of the cluster show such close similarity, it is reasonable to expect the output moment tensors and their corresponding radiation patterns to exhibit similar likenesses.

8.3.1 Absolute inversion

The radiation patterns and fault-plane solutions of the cluster computed using the absolute moment tensor inversion method are shown in Figure 8.7. The standard errors, Cartesian moment tensors, source parameters (where %ISO, %DC %CLVD and the deviation from the double-couple source ε, are calculated using Equations 2.40 - 2.43) and fault-plane solutions for the cluster are listed in Tables 8.3(a) to (d).

It is evident from the radiation patterns (Figure 8.7) and their corresponding fault-plane solutions that the results computed using the absolute moment tensor inversion are more varied than would be expected from a source cluster having very similar waveforms.

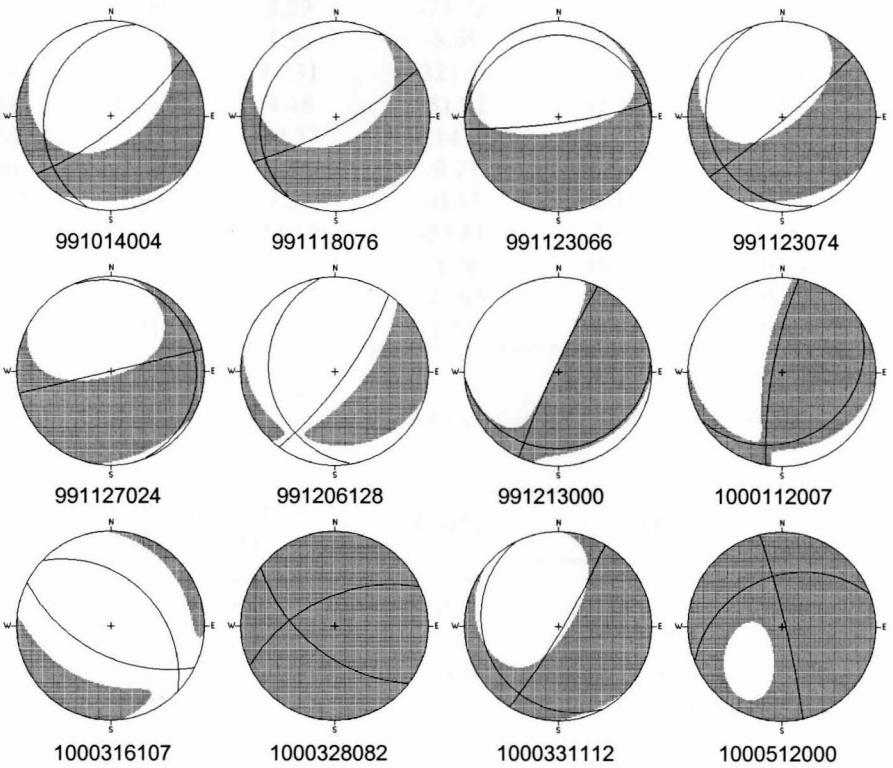

Figure 8.7: Radiation patterns and fault-plane solutions for the cluster computed with an absolute moment tensor inversion.

Table 8.3(a): Standard error normalised to scalar seismic moment for the Oryx cluster (Absolute moment tensor inversion method)

Event ID	Standard error normalised to scalar seismic moment
991014004	0.99
991118076	1.09
991123066	1.27
991123074	0.62
991127024	1.20
991206128	1.00
991213000	1.57
1000112007	1.13
1000316107	0.18
1000328082	1.43
1000331112	1.26
1000512000	1.52

Table 8.3(b): Cartesian moment tensor components for the Oryx cluster (Absolute moment tensor inversion method)

Event ID	Cartesian moment tensors (10^9 N.m) rotated into geographical (North, East, Down) system					
	M_{11}	M_{12}	M_{13}	M_{22}	M_{23}	M_{33}
991014004	-3.00	1.25	-14.29	3.31	6.65	-20.07
991118076	-5.00	3.59	-23.75	5.76	9.22	-28.67
991123066	-3.46	1.53	-8.69	0.90	7.78	-13.61
991123074	-9.76	11.31	-321.47	20.43	47.74	-217.98
991127024	-12.65	9.48	-51.92	15.03	33.60	-28.45
991206128	-9.32	20.77	-114.95	25.90	32.66	-22.99
991213000	-2.49	4.36	-9.21	0.00	20.44	5.15
1000112007	-0.53	2.39	-0.47	0.46	10.94	8.91
1000316107	1.90	14.19	-55.81	2.87	6.15	-247.57
1000328082	4.58	-1.72	-1.20	19.74	10.98	25.66
1000331112	-0.84	18.97	-75.95	32.71	105.03	-51.66
1000512000	3.31	-3.87	1.78	9.17	7.05	4.32

Table 8.3(c): Source parameters for the Oryx cluster (Absolute moment tensor inversion method)

Event ID	Deviation from DC (ε)	ISO%	DC%	CLVD%
991014004	0.58	-20.0	-12.4	87.6
991118076	0.66	-19.2	-19.7	80.3
991123066	0.33	-25.1	34.2	65.8
991123074	0.43	-14.5	68.5	-31.5
991127024	0.55	-10.5	65.7	-34.3
991206128	0.28	-1.00	-43.4	-56.6
991213000	0.02	1.71	-95.4	-4.7
1000112007	0.45	18.9	-67.8	32.3
1000316107	0.3	-25.1	40.2	59.8
1000328082	0.36	33.3	-70.4	29.6
1000331112	0.19	0.8	-62.7	-37.3
1000512000	0.12	33.3	-83.7	16.3

Table 8.3(d): Fault-plane solutions for the Oryx cluster (Absolute moment tensor inversion method)

Event ID	Fault-plane solution 1 (degrees)			Fault-plane solution 2 (degrees)		
	Strike	Dip	Rake	Strike	Dip	Rake
991014004	194.9	19.5	-125.3	51.8	74.2	-78.4
991118076	211.0	14.4	-118.9	60.7	77.5	-82.9
991123066	170.7	19.4	-133.4	35.8	76.1	-76.4
991123074	270.4	8.9	-82.0	82.3	81.2	-91.2
991127024	161.0	12.3	-158.5	50.0	85.5	-78.6
991206128	337.6	5.1	-8.9	76.5	89.2	-95.1
991213000	84.2	10.9	148.8	204.9	84.4	80.6
1000112007	57.7	17.3	136.3	190.0	78.2	77.3
1000316107	313.9	36.7	-76	116.7	54.5	-100.2
1000328082	245.0	55.9	42.4	127.9	56.1	137.5
1000331112	152.0	12.6	-148.0	30.6	83.4	-79.3
1000512000	248.9	33.1	-9.4	346.8	84.9	-122.7

8.3.2 Hybrid inversion using a median correction

The hybrid moment tensor inversion method using a median correction gives radiation patterns and fault-plane solutions showing a high degree of similarity (Figure 8.8), indicating that these solutions are very probably more accurate reflections of reality than the absolute moment tensor solutions. The standard errors, Cartesian moment tensor components, source parameters and fault-plane solutions for the cluster are listed in Tables 8.4(a) to (d). The variation in standard error normalised to scalar seismic moment (Equation 6.15) for each event is shown graphically in Figure 8.11(a).

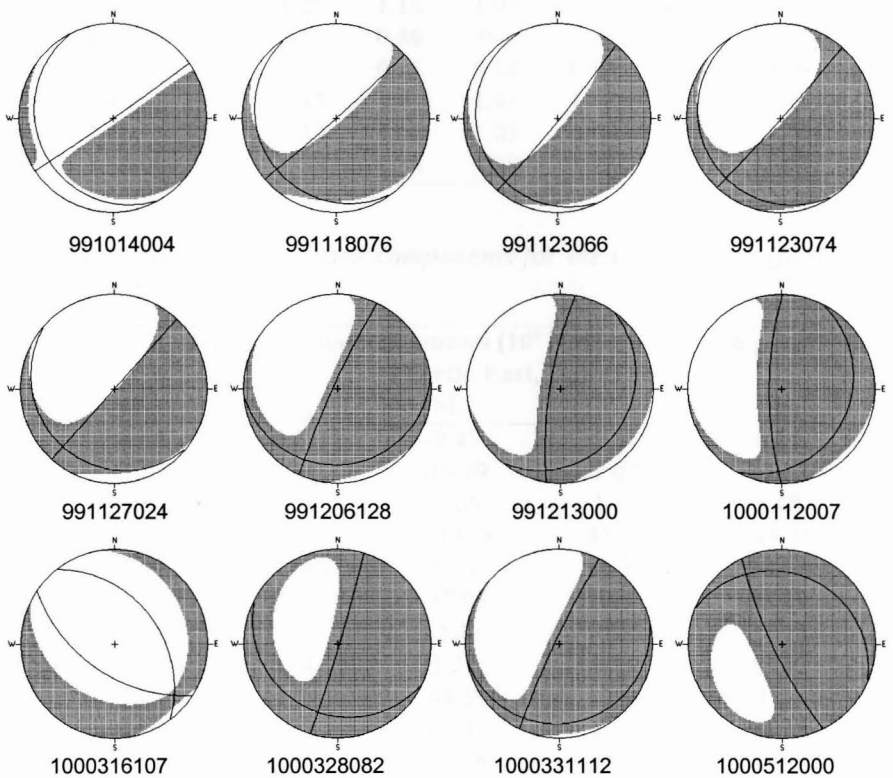

Figure 8.8: Radiation patterns and fault-plane solutions for the cluster computed with the hybrid moment tensor inversion using a median correction.

Table 8.4(a): Standard error normalised to scalar seismic moment for the Oryx cluster (first hybrid moment tensor inversion)

Event ID	Standard error normalised to scalar seismic moment									
	Iteration number									
	1	2	3	4	5	6	7	8	9	10
991014004	0.99	0.96	0.95	0.93	0.91	0.89	0.85	0.78	0.69	0.50
991118076	1.09	1.02	1.00	0.98	0.94	0.9	0.84	0.76	0.64	0.50
991123066	1.27	1.16	1.13	1.09	1.03	0.96	0.87	0.75	0.58	0.40
991123074	0.62	0.59	0.58	0.57	0.56	0.54	0.51	0.48	0.42	0.30
991127024	1.20	1.08	1.05	1.01	0.96	0.9	0.81	0.71	0.57	0.40
991206128	1.00	0.95	0.94	0.92	0.89	0.85	0.79	0.70	0.56	0.40
991213000	1.57	1.32	1.26	1.18	1.09	0.97	0.84	0.67	0.50	0.30
1000112007	1.13	0.96	0.91	0.86	0.8	0.72	0.62	0.50	0.37	0.30
1000316107	0.18	0.16	0.15	0.15	0.14	0.13	0.12	0.10	0.08	0.10
1000328082	1.43	1.43	1.43	1.43	1.43	1.42	1.4	1.38	1.31	1.20
1000331112	1.26	1.15	1.12	1.08	1.03	0.96	0.87	0.76	0.60	0.40
1000512000	1.52	1.4	1.37	1.33	1.28	1.22	1.13	1.03	0.91	0.80

Table 8.4(b): Cartesian moment tensor components for the Oryx cluster (first hybrid moment tensor inversion method)

Event ID	Cartesian moment tensors (10^9 N.m) rotated into geographical (North, East, Down) system					
	M_{11}	M_{12}	M_{13}	M_{22}	M_{23}	M_{33}
991014004	-3.12	-0.27	-9.47	1.41	6.11	-2.53
991118076	-4.13	1.78	-15.79	3.04	12.82	-4.25
991123066	-1.31	1.17	-7.65	1.10	8.48	-3.79
991123074	-10.58	18.93	-139.78	43.12	144.36	-31.42
991127024	-8.27	6.46	-37.07	10.33	38.13	-2.90
991206128	-2.82	13.67	-37.95	19.76	93.29	47.69
991213000	1.03	3.77	-2.40	-0.55	27.71	26.12
1000112007	1.07	1.74	1.29	0.10	13.42	15.63
1000316107	3.43	11.27	-44.59	10.16	4.24	-196.72
1000328082	0.88	1.32	-2.50	8.69	11.56	4.82
1000331112	-4.05	7.86	-45.58	20.07	106.57	54.85
1000512000	1.18	-0.56	2.25	3.55	6.98	8.83

Table 8.4(c): Source parameters for the Oryx cluster (first hybrid moment tensor inversion)

Event ID	Deviation from DC (ε)	ISO%	DC%	CLVD%
991014004	0.27	-12.9	74.0	-26.0
991118076	0.30	-9.0	72.5	-27.5
991123066	0.33	-10.4	71.7	-28.3
991123074	0.10	3.0	-79.6	-20.4
991127024	0.14	-0.4	-72.1	-27.9
991206128	0.32	18.3	-71.7	28.2
991213000	0.44	21.3	-12.6	-87.4
1000112007	0.33	24.7	-34.5	-65.5
1000316107	0.43	-15.6	68.5	-31.5
1000328082	0.18	28.7	-64.9	-35.1
1000331112	0.36	17.4	-70.4	29.6
1000512000	0.03	32.7	-94.9	-5.1

Table 8.4(d): Fault-plane solutions for the Oryx cluster (first hybrid moment tensor inversion)

Event ID	Fault-plane solution 1			Fault-plane solution 2		
	Strike	Dip	Rake	Strike	Dip	Rake
991014004	152.9	11.3	-172.2	55.2	88.5	-78.8
991118076	145.4	9.5	-172.9	48.3	88.8	-80.6
991123066	155.7	7.9	-153.6	39.6	86.5	-82.9
991123074	147.5	8.6	-164	41.8	87.7	-81.8
991127024	130.4	10.5	178.2	222.2	89.7	79.5
991206128	83.7	11.5	148.4	204.7	84.0	80.2
991213000	36.5	15.0	116.5	189.2	76.6	83.2
1000112007	27.2	16.9	115.7	180.5	74.8	82.5
1000316107	322.6	38.0	-74.9	123.7	53.6	-101.5
1000328082	116.5	15.4	-169.9	16.7	87.3	-74.9
1000331112	77.4	9.0	141.6	205.4	84.4	82.9
1000512000	292.6	15.6	49.1	154.6	78.3	100.3

A second hybrid moment tensor inversion using a median correction is performed on the cluster, rejecting a further two events, namely 1000316107 and 1000512000. These two events were excluded because their radiation patterns (Figure 8.8) are noticeably different when compared to the rest of the cluster. This is not surprising because event 1000316107 has an extremely poor signal-to-noise ratio, and the resulting system of equations is poorly conditioned (event 1000316107 has a condition number of ~639, Table 8.5). Event 1000512000, on the other hand, is not poorly conditioned (condition number of ~17, Table 8.5). However, as is clear from the complexity of the waveforms given in Figure 8.10, a more complicated source-time function is needed to model this event accurately.

The radiation patterns of the moment tensors computed in the second hybrid inversion are given in Figure 8.9. The standard errors, source parameters and fault-plane solutions for the cluster are listed in Tables 8.6(a) to (d). As is evident from Tables 8.4(a) and 8.6(a) and Figures 8.11(a) and (b), removing the two events from the cluster has a minimal effect on the convergence of the solutions. This is demonstrated in Figure 8.12 which shows the variation in the total standard error with iteration for both the first and second inversions because both trends show a steady decrease with increasing iteration.

Regarding Figures 8.11(a) and (b), which show the variations of the standard errors (normalised against the scalar moment) for each event with the iteration number, it is clear that the errors decrease as the processing continues. More subtly, the largest errors in the cluster, on the whole, decrease most rapidly. The decrease in the errors is, of course, inherent in the solution process itself since corrections are applied to the input data, which are assumed to be in error, even if only marginally so. However, the 'sharpening up' of the solutions described earlier is an encouraging phenomenon, and is a strong indicator of the method's potential for use as a standard processing tool for mine seismicity.

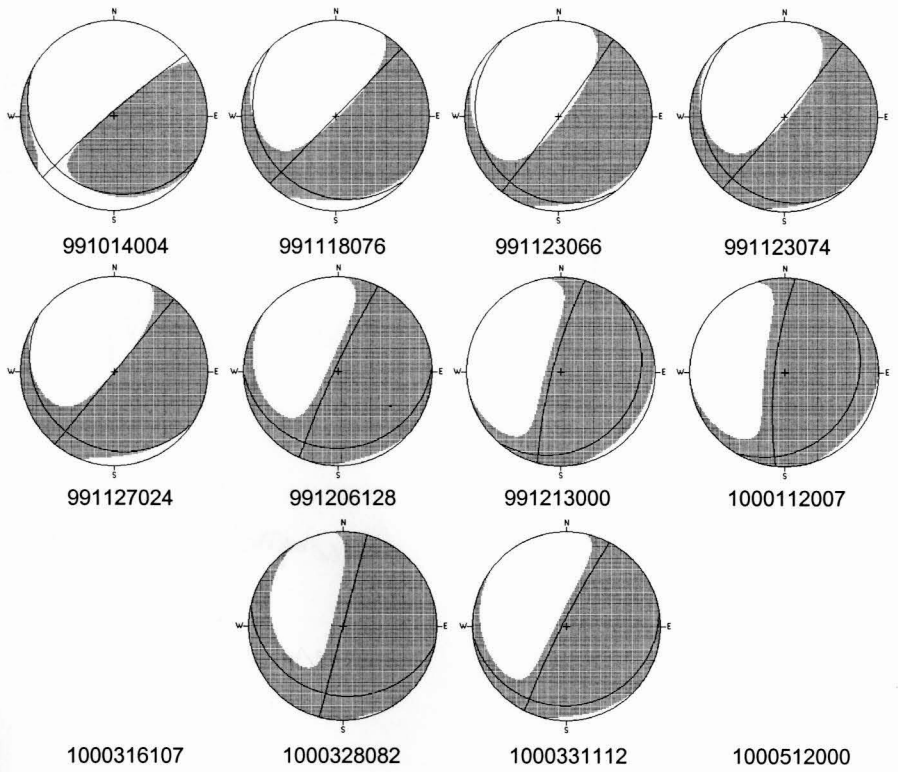

Figure 8.9: Radiation patterns and fault-plane solutions for the cluster computed with the hybrid moment tensor inversion using a median correction. Events 1000316107 and 1000512000 were not included in the inversion.

Table 8.5: Condition numbers for Oryx cluster

Event ID	Condition number
991014004	36.8
991118076	47.6
991123066	23.5
991123074	39.7
991127024	29.1
991206128	46.2
991213000	44.1
1000112007	29.7
1000316107	638.6
1000328082	76.3
1000331112	24.0
1000512000	17.3

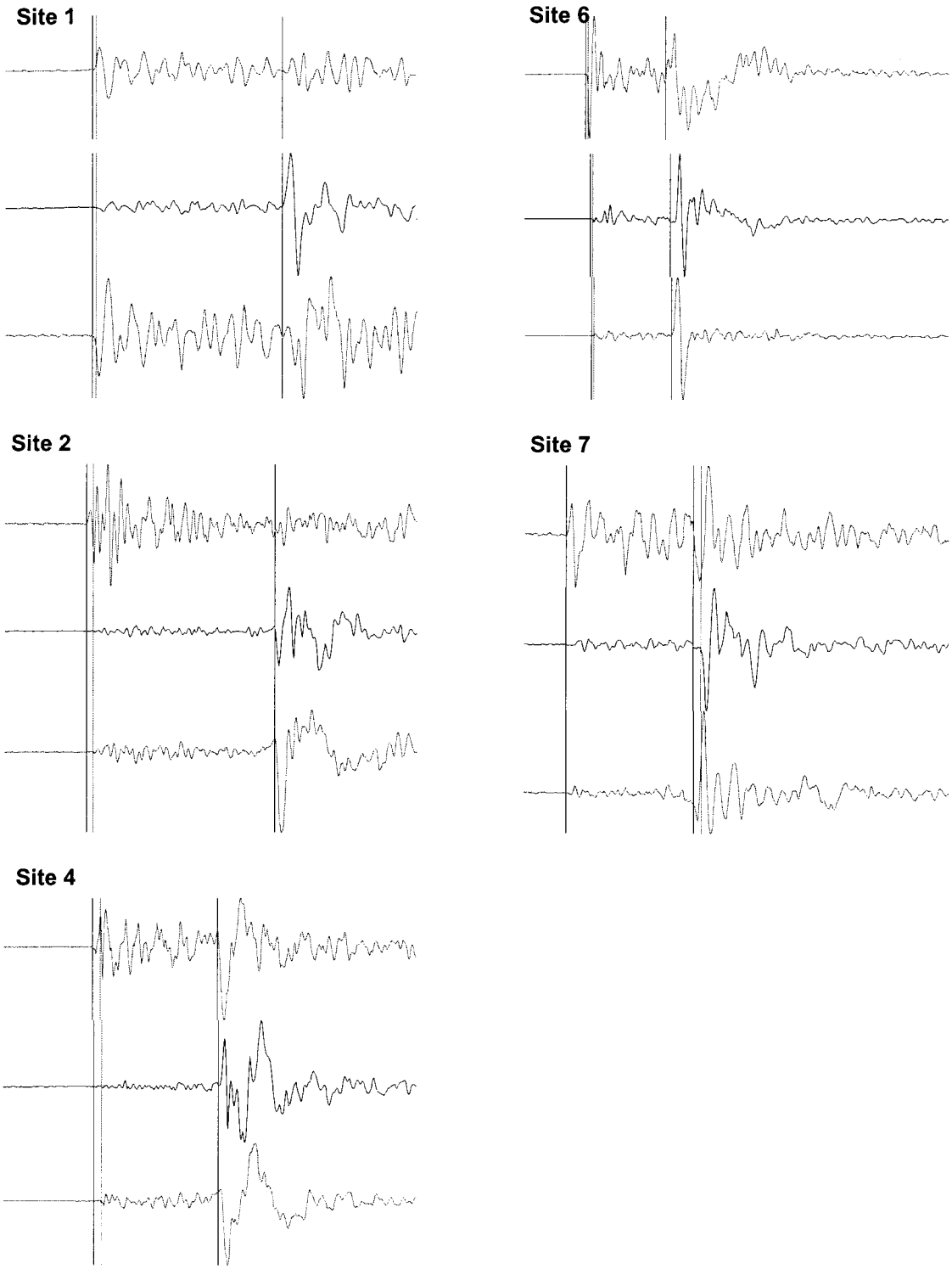

Figure 8.10: Low-pass filtered velocity traces for event 1000512000. Note the complexity of the waveform. Site 5 was not active when this event occurred.

The effect of rejecting the two events is to 'focus' the remaining solutions, as can be seen by comparing the radiation patterns of Figures 8.8 and 8.9. There is also a noticeable decrease in the isotropic components (compare ISO% of Tables 8.4(c) and 8.6(c)), leading one to hope that the second set of results is closer to what is happening in reality than the first set. There has been much discussion in the literature about the interpretation of non double-couple components (i.e. the presence of isotropic components and deviations from the pure double-couple model). Most of the debate is centred on whether the non double-couple components are intrinsic to the source rupture process or artefacts of processing (due to inappropriate modelling of the raypath, the presence of noise, invalid source models, etc.). This study shows that the percentage of isotropic component can be decreased significantly by application of the hybrid moment tensor inversion method with median correction.

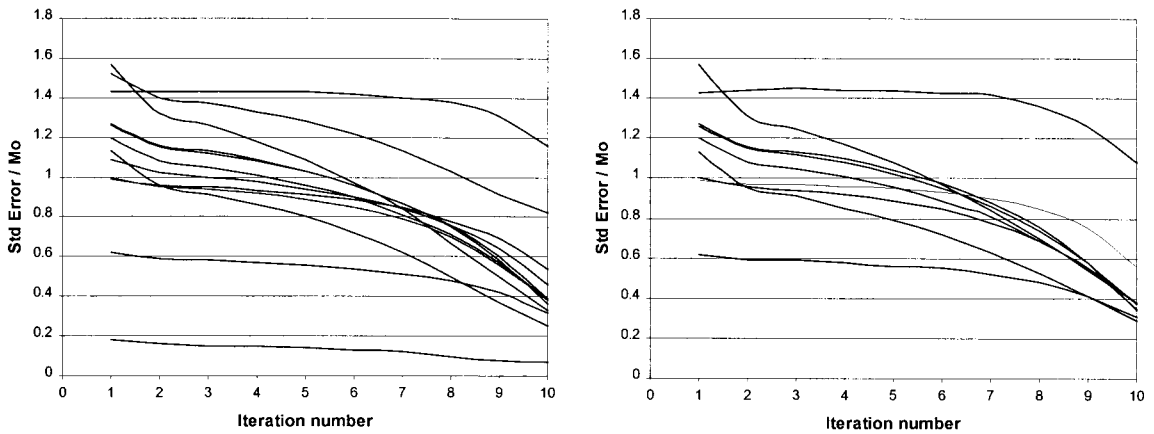

Figure 8.11: Graphs showing the variation of normalised standard error with iteration number (a) for first hybrid inversion performed on 14 events and (b) second hybrid inversion performed on 12 events (both using a median correction).

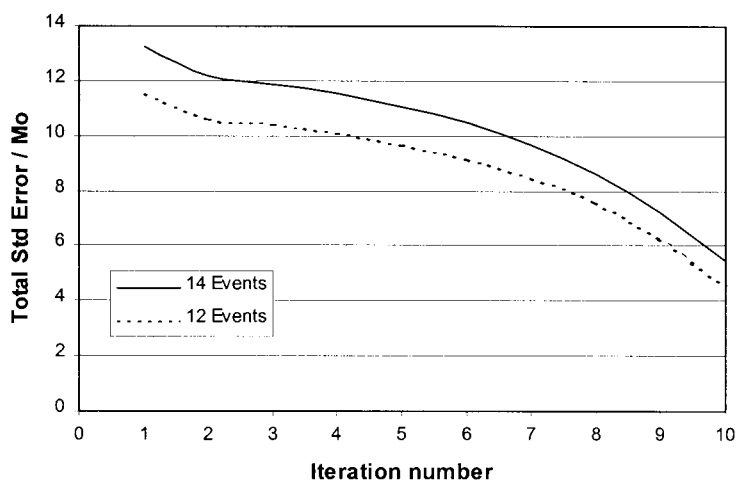

Figure 8.12: Graph showing the variation of total normalised standard error with iteration number for both hybrid inversions (using a median correction).

Table 8.6(a): Standard error normalised to scalar seismic moment for the Oryx cluster (second hybrid moment tensor inversion)

Event ID	Standard error normalised to scalar seismic moment									
	Iteration number									
	1	2	3	4	5	6	7	8	9	10
991014004	0.99	0.97	0.97	0.96	0.95	0.93	0.90	0.85	0.75	0.60
991118076	1.09	1.03	1.01	0.99	0.96	0.92	0.86	0.78	0.64	0.40
991123066	1.27	1.16	1.13	1.10	1.04	0.98	0.88	0.76	0.58	0.30
991123074	0.62	0.59	0.59	0.58	0.56	0.55	0.52	0.48	0.41	0.30
991127024	1.20	1.08	1.05	1.01	0.96	0.89	0.81	0.69	0.55	0.40
991206128	1.00	0.96	0.94	0.92	0.89	0.85	0.78	0.69	0.55	0.40
991213000	1.57	1.31	1.25	1.17	1.08	0.97	0.84	0.70	0.54	0.40
1000112007	1.13	0.95	0.91	0.85	0.79	0.72	0.63	0.53	0.41	0.30
1000316107										
1000328082	1.43	1.44	1.45	1.44	1.44	1.43	1.42	1.36	1.26	1.10
1000331112	1.26	1.15	1.12	1.08	1.02	0.95	0.86	0.74	0.58	0.40
1000512000										

Table 8.6(b): Cartesian moment tensor components for the Oryx cluster (second hybrid moment tensor inversion)

Event ID	Cartesian moment tensors (10^9 N.m) rotated into geographical (North, East, Down) system					
	M_{11}	M_{12}	M_{13}	M_{22}	M_{23}	M_{33}
991014004	-2.84	0.05	-8.21	1.31	7.39	2.28
991118076	-3.77	2.09	-15.22	3.78	14.32	-1.87
991123066	-1.09	1.38	-7.52	1.58	9.37	-2.55
991123074	-14.72	21.83	-138.73	41.87	153.77	-29.32
991127024	-7.91	7.70	-37.38	11.31	42.51	-0.37
991206128	-2.07	13.75	-40.22	23.58	98.23	46.23
991213000	1.01	3.04	-6.02	-1.05	26.32	17.97
1000112007	0.95	1.39	-0.56	-0.21	12.40	11.49
1000316107						
1000328082	0.41	2.45	-2.11	7.23	12.81	6.07
1000331112	-5.26	10.33	-50.49	19.93	109.61	51.84
1000512000						

Table 8.6(c): Source parameters for the Oryx cluster (second hybrid moment tensor inversion)

Event ID	Deviation from DC (ε)	ISO%	DC%	CLVD%
991014004	0.03	-0.21	93.5	6.5
991118076	0.19	-3.5	-62.3	-37.7
991123066	0.23	-5.0	76.1	-23.9
991123074	0.11	1.8	-77.5	-22.5
991127024	0.09	2.4	-82.31	-17.7
991206128	0.33	18.6	-71.7	28.3
991213000	0.32	16.9	-71.9	28.1
1000112007	0.41	22.0	-18.2	-81.8
1000316107				
1000328082	0.27	26.1	-46.8	-53.2
1000331112	0.31	16.2	-72.1	27.9
1000512000				

Table 8.6(d): Fault-plane solutions for the Oryx cluster (second hybrid moment tensor inversion)

Event ID	Fault-plane solution 1			Fault-plane solution 2		
	Strike	Dip	Rake	Strike	Dip	Rake
991014004	116.9	11.4	156.7	229.8	85.5	79.6
991118076	134.6	10.3	179.8	224.7	90.0	79.7
991123066	142.4	8.3	-164.0	36.5	87.7	-82.0
991123074	142.0	9.0	-167.7	39.8	88.1	-81.2
991127024	125.2	10.9	175.6	219.6	89.2	79.1
991206128	88.0	11.2	152.9	204.6	84.9	80.0
991213000	38.2	11.3	113.1	194.6	79.6	85.5
1000112007	30.0	14.1	113.4	185.9	77.1	84.3
1000316107						
1000328082	101.6	16.5	176.7	194.8	89.1	73.5
1000331112	82.2	9.4	145.0	206.8	84.6	82.3
1000512000						

8.3.3 Hybrid inversion using a weighted mean correction

The radiation patterns computed through the hybrid moment tensor inversion method using a weighted mean correction show a lower degree of similarity than those computed the hybrid inversion using a median correction (Figure 8.13). In fact, the radiation patterns show a very strong resemblance to the absolute moment tensor solutions (compare Figures 8.7 and 8.13).

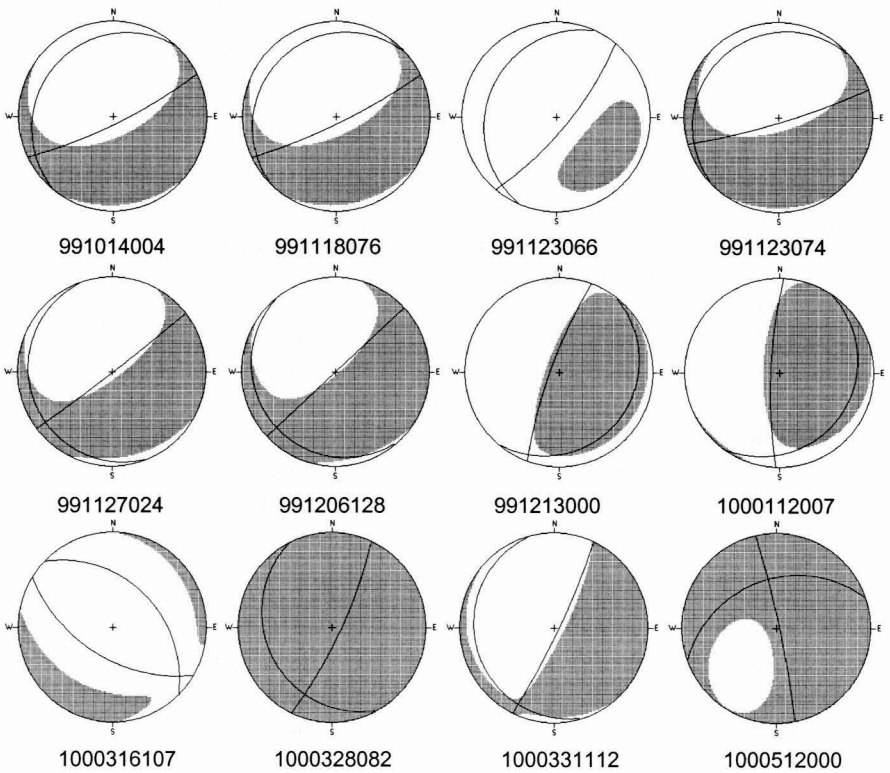

Figure 8.13: Radiation patterns and fault-plane solutions for the cluster computed with the hybrid moment tensor inversion using a weighted mean correction.

The standard errors, Cartesian moment tensor components, source parameters and fault-plane solutions for the cluster are listed in Tables 8.7(a) to (d). The variations of the standard errors (normalised against the scalar moment) for each event with iteration number are shown in Figure 8.14. It is immediately evident that the iterative procedure shows poorer convergence that the hybrid method using a median correction (compare Figures 8.11a and 8.14a). Specifically, the standard error of event 991123074 actually increases, showing that the solutions for this event are, in fact, worsened by the correction (Table 8.7a).

Table 8.7(a): Standard error normalised to scalar seismic moment for the Oryx cluster (first hybrid moment tensor inversion)

Event ID	Standard error normalised to scalar seismic moment									
	Iteration number									
	1	2	3	4	5	6	7	8	9	10
991014004	0.99	1.01	1.11	1.11	1.11	1.11	1.11	1.11	1.11	1.10
991118076	1.09	1.12	1.20	1.19	1.19	1.19	1.19	1.19	1.19	1.20
991123066	1.27	0.98	0.76	0.78	0.78	0.78	0.78	0.78	0.78	0.80
991123074	0.62	0.50	0.51	0.51	0.51	0.51	0.51	0.51	0.51	0.50
991127024	1.20	1.18	1.15	1.16	1.16	1.16	1.16	1.16	1.16	1.20
991206128	1.00	1.01	0.99	0.98	0.98	0.98	0.98	0.98	0.98	1.00
991213000	1.57	1.43	1.22	1.21	1.21	1.21	1.21	1.21	1.21	1.20
1000112007	1.13	1.01	0.87	0.87	0.87	0.87	0.87	0.87	0.87	0.90
1000316107	0.18	0.17	0.15	0.15	0.15	0.15	0.15	0.15	0.15	0.20
1000328082	1.43	1.43	1.96	1.95	1.96	1.96	1.96	1.96	1.96	2.00
1000331112	1.26	0.91	0.92	0.92	0.92	0.92	0.92	0.92	0.92	0.90
1000512000	1.52	1.18	1.22	1.21	1.21	1.21	1.21	1.21	1.21	1.20

Table 8.7(b): Cartesian moment tensor components for the Oryx cluster (first hybrid moment tensor inversion)

Event ID	Cartesian moment tensors (10^9 N.m) rotated into geographical (North, East, Down) system					
	M_{11}	M_{12}	M_{13}	M_{22}	M_{23}	M_{33}
991014004	-1.79	0.66	-13.56	1.98	5.59	-13.07
991118076	-3.27	1.85	-22.74	2.69	9.98	-19.54
991123066	-4.18	-0.75	-8.14	-1.98	8.77	-16.71
991123074	-31.47	5.71	-307.49	52.06	80.81	-183.64
991127024	-9.57	6.87	-51.65	8.46	36.55	-17.87
991206128	-10.05	14.83	-84.01	23.37	71.80	-11.90
991213000	-2.19	2.33	-7.48	-2.85	22.73	14.83
1000112007	-0.75	1.42	0.34	-0.90	11.94	8.58
1000316107	-0.03	10.74	-55.40	3.69	1.66	-295.20
1000328082	5.83	-1.36	-3.42	15.71	8.66	6.55
1000331112	-8.96	6.29	-66.12	20.00	128.27	-60.04
1000512000	3.17	-4.89	2.61	8.44	7.67	3.65
991014004	-1.79	0.66	-13.56	1.98	5.59	-13.07
991118076	-3.27	1.85	-22.74	2.69	9.98	-19.54

Table 8.7(c): Source parameters for the Oryx cluster (weighted hybrid moment tensor inversion method)

Event ID	Deviation from DC (ε)	ISO%	DC%	CLVD%
991014004	0.60	-17.7	64.7	-35.3
991118076	0.59	-17.7	64.8	-35.2
991123066	0.02	-32.6	95.2	4.8
991123074	0.47	-12.1	67.3	-32.7
991127024	0.38	-9.5	69.9	-30.1
991206128	0.17	1.7	-66.7	-33.3
991213000	0.25	9.7	-75.1	24.9
1000112007	0.39	14.1	-69.5	30.5
1000316107	0.25	-26.8	49.9	50.1
1000328082	0.26	33.3	-75.2	24.8
1000331112	0.18	-7.9	78.8	-21.2
1000512000	0.04	33.3	-92.7	7.3

Table 8.7(d): Fault-plane solutions for the Oryx cluster (weighted hybrid moment tensor inversion method)

Event ID	Fault-plane solution 1 (degrees)			Fault-plane solution 2 (degrees)		
	Strike	Dip	Rake	Strike	Dip	Rake
991014004	221.0	11.7	-112.5	63.9	79.2	-85.5
991118076	226.0	9.4	-107.9	64.1	81.1	-87.1
991123066	203.4	16.3	-105.4	39.5	74.3	-85.5
991123074	226.7	7.7	-116.3	73.2	83.1	-86.6
991127024	159.3	6.7	-162.9	52.2	88.0	-83.6
991206128	140.0	8.1	-177.0	46.9	89.6	-81.9
991213000	38.9	11.5	108.7	199.9	79.1	86.3
1000112007	34.3	12.9	121.3	182.3	79.0	83.2
1000316107	314.7	37.6	-79.1	121	53.2	-98.3
1000328082	152.1	19.1	-141.5	25.2	78.3	-74.9
1000331112	163.9	9.1	-131.2	25.4	83.2	-84.0
1000512000	250.6	34.9	-8.8	347.8	85.0	-124.5

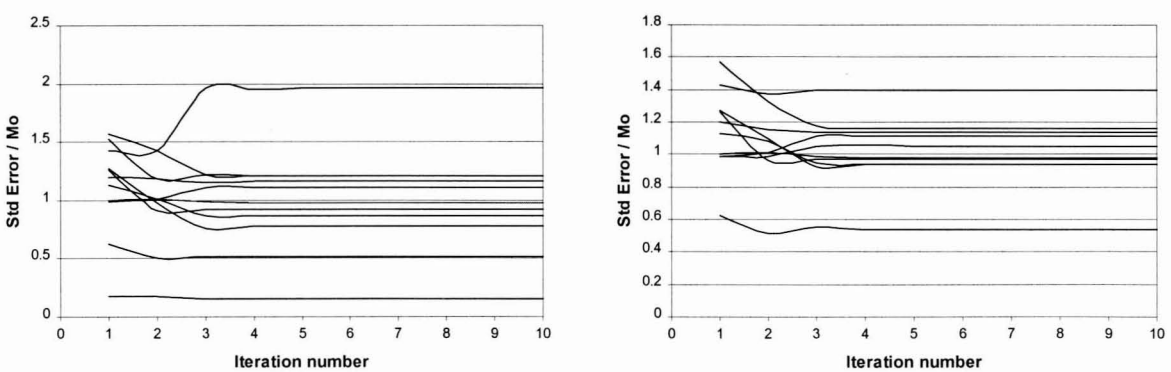

(a) (b)

Figure 8.14: Graphs showing the variation of normalised standard error with iteration number for each event in the cluster (a) for first hybrid inversion performed on 14 events and (b) second hybrid inversion performed on 12 events (both using a weighted mean correction).

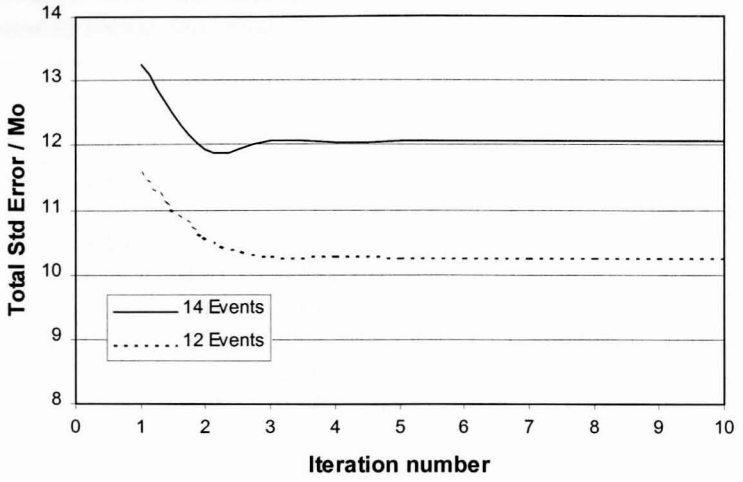

Figure 8.15: Graph showing the variation of total normalised standard error with iteration number for both hybrid inversions (using a weighted mean correction)

As before, two events (1000316107 and 1000512000) are rejected from the cluster, and a second hybrid inversion using a weighted mean correction is performed. The radiation patterns are shown in Figure 8.16. The standard errors, Cartesian moment tensor components, source parameters and fault-plane solutions for the cluster are listed in Tables 8.8(a) to (d).

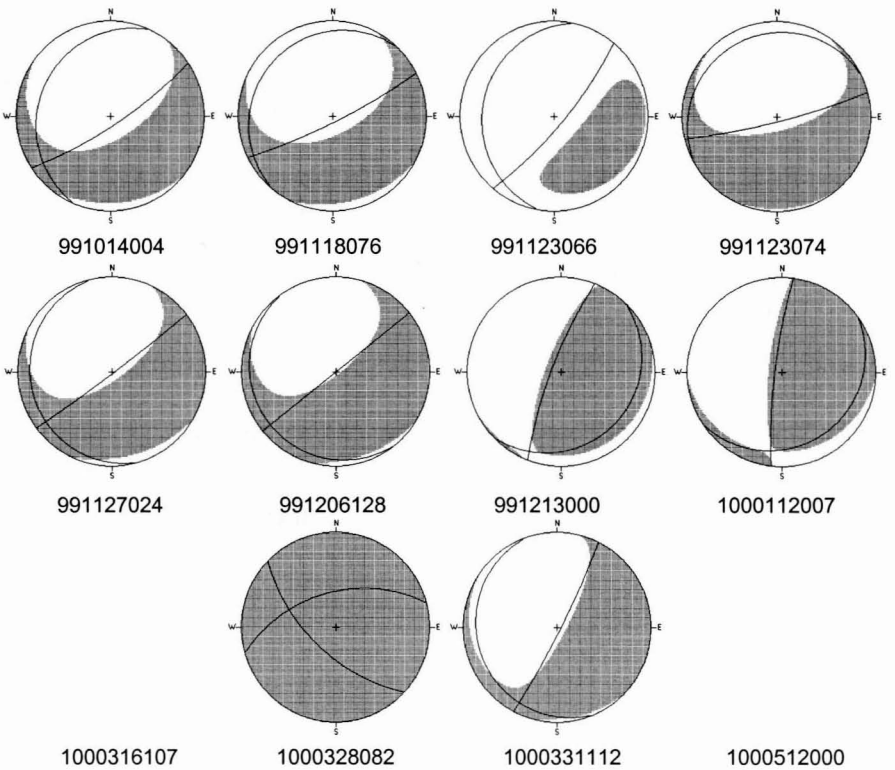

Figure 8.11(b): Radiation patterns and fault-plane solutions for the cluster computed with the hybrid moment tensor inversion using a weighted mean correction. Events 1000316107 and 1000512000 were not included in the inversion.

Table 8.8(a): Standard error normalised to scalar seismic moment for the Oryx cluster (second hybrid moment tensor inversion)

Event ID	Standard error normalised to scalar seismic moment									
	Iteration number									
	1	2	3	4	5	6	7	8	9	10
991014004	0.99	0.99	1.05	1.06	1.05	1.05	1.05	1.05	1.05	1.10
991118076	1.09	1.12	1.16	1.16	1.15	1.15	1.15	1.15	1.15	1.20
991123066	1.27	1.10	0.92	0.94	0.94	0.94	0.94	0.94	0.94	0.90
991123074	0.62	0.51	0.55	0.54	0.54	0.54	0.54	0.54	0.54	0.50
991127024	1.20	1.15	1.14	1.14	1.14	1.14	1.14	1.14	1.14	1.10
991206128	1.00	0.98	0.98	0.98	0.98	0.98	0.98	0.98	0.98	1.00
991213000	1.57	1.33	1.18	1.16	1.16	1.16	1.16	1.16	1.16	1.20
1000112007	1.13	1.08	0.95	0.94	0.94	0.94	0.94	0.94	0.94	0.90
1000316107										
1000328082	1.43	1.37	1.40	1.40	1.40	1.40	1.40	1.40	1.40	1.40
1000331112	1.26	0.96	0.97	0.97	0.97	0.97	0.97	0.97	0.97	1.00
1000512000										

Table 8.8(b): Cartesian moment tensor components for the Oryx cluster (second hybrid moment tensor inversion)

Event ID	Cartesian moment tensors (10^9 N.m) rotated into geographical (North, East, Down) system					
	M_{11}	M_{12}	M_{13}	M_{22}	M_{23}	M_{33}
991014004	-2.48	0.81	-13.86	2.50	6.82	-15.67
991118076	-3.75	2.75	-23.27	3.73	10.32	-19.71
991123066	-3.33	0.39	-8.58	-0.52	8.46	-13.62
991123074	-22.23	7.53	-310.43	41.23	73.71	-187.53
991127024	-9.37	7.84	-52.70	11.05	34.85	-22.22
991206128	-9.55	16.27	-90.15	22.17	66.91	-14.04
991213000	-2.20	2.89	-7.89	-1.97	23.69	17.80
1000112007	-0.43	2.06	-0.52	-0.08	11.97	7.04
1000316107	5.64	-2.58	-0.53	17.18	9.15	24.80
1000328082	-5.76	10.01	-68.59	18.38	124.13	-51.72
1000331112						
1000512000	-2.48	0.81	-13.86	2.50	6.82	-15.67
991014004	-3.75	2.75	-23.27	3.73	10.32	-19.71
991118076						

Table 8.8(c): Source parameters for the Oryx cluster (Weighted hybrid moment tensor inversion method)

Event ID	Deviation from DC (ε)	ISO%	DC%	CLVD%
991014004	0.60	-18.9	-13.9	86.1
991118076	0.64	-17.0	64.0	-36.0
991123066	0.22	-27.5	56.8	43.2
991123074	0.45	-12.5	67.9	-32.1
991127024	0.44	-9.3	68.1	-31.9
991206128	0.21	0.3	-57.3	-42.7
991213000	0.32	13.2	-72.1	27.9
1000112007	0.34	14.2	-71.3	28.7
1000316107				
1000328082	0.42	33.3	-68.6	31.4
1000331112	0.20	-6.3	77.8	-22.2
1000512000				

Table 8.8(d): Fault-plane solutions for the Oryx cluster (weighted hybrid moment tensor inversion method)

Event ID	Fault-plane solution 1 (degrees)			Fault-plane solution 2 (degrees)		
	Strike	Dip	Rake	Strike	Dip	Rake
991014004	203.7	14.7	-122.0	56.6	77.6	-82.1
991118076	222.7	8.9	-110.6	63.5	81.6	-86.8
991123066	190.9	14.8	-118.4	40.1	77.1	-82.9
991123074	243.3	7.4	-102.3	75.7	82.7	-88.4
991127024	165.9	7.6	-157.0	53.1	87.0	-83.0
991206128	143.0	6.1	-178.2	51.3	89.8	-83.9
991213000	44.4	12.8	112.8	201	78.2	84.9
1000112007	54.7	13.2	137.2	186.7	81.1	80.2
1000316107						
1000328082	254.7	49.0	42.7	133.5	59.2	130.2
1000331112	158.8	8.5	-137.8	26.9	84.3	-83.7
1000512000						

The removal of the two events from the system of equations has a marked effect on the convergence of the solutions. The iterative procedure shows better convergence than for the first inversion (compare Figures 8.14(a) and (b)). The effect of removing the two events is very clearly shown in Figure 8.15. This graph shows the variation of total normalised standard error with iteration number for both hybrid inversions. An interesting feature of the graph is that the trend for the first inversion (using 14 events) shows a minimum, after which it increases to a constant level. It is this minimum which is accepted as the final solution in this method. This behaviour, which is not evident in the second inversion, hints at the potential of this method for chaotic instability in certain pathological cases, i.e. it may happen that the solutions jump around erratically without converging on any readily identifiable final point. The flat region of the convergence profile for the first inversion shows that the mathematical system has a stable attractor which is not the minimum of the objective function, and the mere presence of this phenomenon warns against injudicious use of the method, even if the attractor is quite close to the desired minimum.

As noted in the set of results for the hybrid inversion using a median correction, the radiation patterns appear to be slightly more focussed. Compared with the hybrid inversion using a median correction, the effect of removing the two noisy events on the isotropic components is less, since, while some of the ISO% decrease, others show an increase (Table 8.8c). However, the effect of removing the two events has a dramatic effect on the percentage DC component of event 991014004, causing this source parameter to decrease from ~65% to ~14%.

Comparison of the graphs of the variation in total standard error with iteration number (Figures 8.12 and 8.15) reveals that the hybrid inversion using a weighted mean correction shows a higher total standard error (normalised to scalar moment) for the cluster compared with that of the method using the median correction. Despite this, the results are encouraging, since this total error is less than that computed for the absolute inversion.

From these results it can be concluded that the noisy events have a greater impact on the system of equations of the hybrid inversion using a weighted mean correction than on the method using a median correction. Therefore, despite the weighting, outliers with large magnitudes still appear to have a large influence on the correction. This method thus shows less potential as a useful tool in the routine processing of mining-induced seismic events.

8.4 CONCLUSIONS

The conclusions fall into two main categories: those related to the accuracy of the solutions, and those concerning the interpretation of the computed mechanisms.

8.4.1 Solution accuracy

At the risk of repetition, it is important to stress that the similarity of the waveforms played an important role in assessing the integrity of the hybrid moment tensor solutions. Since the input waveforms of the cluster showed such close similarity, it is reasonable to expect the output moment tensors and their corresponding radiation patterns to be similar as well.

The solutions computed using the absolute moment tensor inversion method are considered to show a relatively low accuracy because they exhibit more variation than would be expected from a source cluster having very similar waveforms.

The solutions computed using the hybrid moment tensor inversion using a median correction displayed a distinct improvement after the iterative residual correction procedure was applied. The radiation patterns and fault-plane solutions show a high degree of similarity and are probably more accurate reflections of reality that those computed using the absolute moment tensor inversion method. Compared to the absolute methods, there is a noticeable decrease in the percentage of the isotropic component. This is of importance in the light of the recent discussions in the literature about the interpretation of non double-couple components (i.e. the presence of isotropic components and deviations from the pure double-couple model). Most of the debate is centred on whether the non double-couple components are intrinsic to the source rupture process or artefacts of processing (due to inappropriate modelling of the raypath, the presence of noise, invalid source models, etc.). This study shows that the percentage of isotropic component can be decreased significantly by application of the hybrid moment tensor inversion method with median correction. Compared to the hybrid moment tensor inversion using a weighted mean correction, this method shows a lower sensitivity to noisy events. These observations are very encouraging and point towards the method's potential for use as a standard processing tool for mine seismicity.

The hybrid method using a weighted mean correction showed a slight improvement in the solutions since the radiation patterns appeared to be more crisply focussed.

However, this method is more sensitive to noisy data than the median corrected method and shows less promise for use as a standard processing tool in mine seismicity assessments.

8.4.2 Interpretation

The solutions computed using the hybrid moment tensor inversion indicate that the dominating source mechanisms for most of the events in the cluster are of the shear type and show near-vertical and near-horizontal nodal-planes. The solutions also display a distinct rotation with time of a subvertical nodal-plane.

In addition, the isotropic component of the source mechanism shows a systematic change. In the early part of the time sequence of events, the isotropic component is negative implying an implosive contribution to the total mechanism – this would be consistent with the crushing of fault gouge on the failure plane. The isotropic component becomes positive towards the later part of the time sequence, and increases systematically. The positive isotropic component could be a result of over-riding of asperities on the fault plane (due to irregularities in the rock mass, or fault infill material) which results in a volume increase (Figure 8.12). The shear dilatancy of materials such as rock was first discussed by Reynolds[27] . This term refers to the change in volume associated with the shear distortion of an element in the material. Consider, for instance, a pack of incompressible spheres arranged in a state of packing as dense as possible. If any shear distortion is applied, the relative positions of the spheres must change, and the total volume of the pack must increase. A possible contributing factor to the volumetric expansion could be the decrease in the confinement as the stope advances, which allows expansion towards the free surface

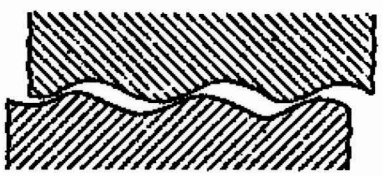

Cemented granular material
(rock, concrete, etc.)

Figure 8.12: Dilatant volume increase caused by frictional sliding along microcracks (from Vermeer & de Borst, 1984).

Evidence from laboratory tests suggests that the internal friction angle decreases with increasing confining stress. This observation is confirmed by the shape of the Hoek & Brown failure envelope. As the dilation angle is related to the internal friction angle, the dilation decreases with increasing confining stresses. The results of this study appear to be in agreement with the laboratory observations because this study suggests that an increasing amount of dilation occurs (i.e. the isotropic component increases) as the confinement decreases due to mining.

Chapter 9

SYNOPSIS

In this final chapter, a brief overview of the project is given and the principal conclusions reached at various points during this study are summarised.

9.1 PROJECT OVERVIEW

The main focus of this thesis was the development and application of a robust moment tensor inversion technique to be applied to clusters of mining-induced seismic events. To achieve this objective, a number of different moment tensor inversion methods applicable to clusters were explored, and revised techniques, referred to in this work as the hybrid methods, were developed. The hybrid methods are essentially weighting schemes where the weights (or corrections) are determined from the residuals for a particular geophone site, component and wave phase, calculated by considering all of the events in the cluster. The main advantage of the hybrid methods is that they are able to compensate for various types of systematic noise and/or error present in seismograms recorded in the underground mining environment.

Three hybrid methods were proposed in this study. In the first and second methods, the weights were related (although indirectly) to the mean and median of the residuals (computed for a particular geophone site, component and wave phase) where the residual was defined as the ratio of the theoretical to observed data. In these two methods, the correction was introduced gradually in order to gauge the smoothness (or otherwise) of the methods' convergence. The third method differed from the aforementioned ones in that the weighting scheme was based on a data point's distance as measured in standard deviations from the mean error. Additionally, the residuals were defined as the difference between the observed and theoretical data. All three methods were iterative and non-linear.

After extensive testing of the methods on synthetic data contaminated by increasing levels of random and systematic noise, two of the three methods were found to be robust and potentially applicable to real data. These were the hybrid methods using a median correction, and the weighted mean correction. To test the relevance of these methods to a real-world case, these two remaining hybrid procedures were applied to a cluster of real events recorded at Oryx gold mine. This part of the study proved to be the deciding one, since the hybrid method using a median correction displayed a higher degree of success at resolving the mechanisms of the events than the method using a weighted mean correction. This method resulted in more 'focussed' moment tensor solutions and enhanced the interpretation of the focal mechanisms of the cluster.

9.2 PRINCIPAL FINDINGS AND CONCLUSIONS

For clarity and ease of reference, the findings and conclusions of the first phase (the application of the relative method without a reference mechanism) and second phase (the development and application of the hybrid methods) of this study are kept separate.

9.2.1 Phase I - relative method without a reference mechanism

A number of tests were performed to assess the performance of the algorithm described by Dahm (1996) and to determine the limitations of the relative inversion and possible sources of error or deficiency.

The first set of tests was carried out using seismic data recorded at the Blyvooruitzicht Gold Mine experimental preconditioning site, where a strike-stabilising pillar was in the process of being extracted. The site was extensively monitored and geologically mapped to gauge the effectiveness of preconditioning, and hence provided an ideal setting in which to assess the capabilities and limitations of the relative inversion technique. These tests are essentially observations of the behaviour of the relative inversion (and resultant moment tensor components) in particular circumstances. In these tests, the input data consisted of the peak amplitudes of the P, SH and SV-phases, measured from the time-integrated displacement traces to which a low-pass filter had been applied. The main observations are summarised below.

1. It was found that the planar configuration of the seismic network used in this study led to a variation in the moment tensor components oriented normal to the plane of the network, which coincided with that of the reef. The variation was thought to result from inadequate sampling of the radiation pattern in the z-direction (i.e. perpendicular to the reef) and from the location errors, which are generally small in the plane of the reef, but large perpendicular to the reef. In this work, the relationship between the synthetic and computed moment tensor components was used as a qualitative measure of error.

2. The position of the source cluster relative to the plane of the reef was found to have an effect on the moment tensor components. Source clusters located within the plane of the seismic network showed less variation in the moment tensor components than those located below the reef. As before, the relationship between the synthetic and computed moment tensor components was used to assess the errors.

3. In general, the relative inversion technique displayed a low sensitivity to pseudo-random noise when applied to events having different radiation patterns. This conclusion was based on the generally high (>0.9) linear correlation coefficients computed between the unperturbed moment tensor components and those calculated from displacement data to which varying levels of noise had been

applied. Unsurprisingly, the system became increasingly ill-conditioned as the level of noise was increased.

A second set of tests was performed on two clusters of synthetic double-couple events in contrast to the previous set of tests, which were performed using real, recorded data. The first synthetic cluster consisted of events having different mechanisms, and the second was comprised of events having very similar mechanisms. The main observations are summarised below.

1. The relative inversion technique showed a low sensitivity to pseudo-random noise provided that the mechanisms of the events in the cluster were significantly different. The radiation patterns of events contaminated by as much as 40% noise were found to correlate well with the noise-free patterns. These conclusions match those of Dahm (1996).

2. In contrast, when the mechanisms of the events in the cluster were similar, the relative inversion technique was extremely sensitive to pseudo-random noise. When the differences between the mechanisms were of the same order as the noise level, the coefficient matrix became singular, and the results of the relative inversion became extremely unreliable. The radiation patterns showed a poor resemblance to those of the noise-free case, even for very low levels (as low as 10%) of noise.

Since the success of Dahm's relative method is highly dependent on the events in a cluster having significantly different mechanisms (and this cannot always be guaranteed for clusters of events recorded underground) it is recommended that the method not be used in isolation - the results should always be compared with those provided by an independent moment tensor inversion technique.

9.2.2 Phase II - hybrid methods

The principal findings made during the secondary phase of this study are divided into three general categories, *viz.* observations of the stability of the methods made when synthetic data were perturbed by various levels and types of noise; observations of the stability of the methods when applied to data recorded by a mine seismic network, and observations that refer specifically to the interpretation of the focal mechanisms determined in the case study.

Stability test observations (synthetic data)

A series of stability tests was carried out to assess the source mechanism resolving capabilities of the hybrid methods, and to determine the limitations of the hybrid methods and possible sources of error. In these tests, the hybrid techniques were applied to a cluster of synthetic events having very similar mechanisms. The input data were artificially contaminated by high levels of random and systematic noise, while the focal coverage was systematically decreased. The results of the three hybrid

inversion methods were compared with those computed using absolute and relative methods.

The main findings of the three experiments are summarised below.

1. In the noise-free situation, the relative method without reference mechanism (proposed by Dahm, 1995) displayed the highest resolution of mechanisms, provided that the coverage of the focal sphere was not too sparse (> 3 stations). The hybrid method where the correction was based on the median of the distribution of residuals was found to be the most robust of all the methods tested in the most extreme case of poor coverage (2 stations) of the focal sphere.

2. When the synthetic data were contaminated by increasing levels of random noise, slightly different trends were observed. Low levels of random noise were found to have a devastating effect on the results computed using the relative method without reference mechanism (Dahm, 1995). This was of particular interest for two reasons. Firstly, in the noise-free case, this method provided the best resolution of the mechanisms for the same network configuration and the same set of synthetic mechanisms. Secondly, this method was applied successfully to data recorded at Blyvooruitzicht Gold Mine (Appendix J). It was concluded that the reason for this unexpected behaviour was that the level of applied noise was of the same order as the differences between the mechanisms in the cluster, which resulted in a near-singular least-squares matrix. In the noise-free case, the differences amongst these mechanisms were sufficiently large for the relative method without a reference mechanism to produce realistic results. It was concluded that since clusters of events recorded underground are likely to have similar mechanisms, this method must be used with caution.

3. In the random noise tests, when the performance of the six different moment tensor inversion methods was compared, it was found that the absolute moment tensor inversion method and those hybrid methods using the median correction and the weighted mean correction showed similar robustness and stability in severely sub-standard configurations in respect of network coverage of the focal sphere and noise level.

4. In the systematic noise tests, the hybrid methods using a median correction and weighted mean correction showed similar robustness and stability. In all situations investigated, these two hybrid methods outperformed the relative and absolute methods. As was observed in the random noise tests, the relative method with a reference mechanism (Dahm, 1995) exhibited slightly poorer performance in all the tests when compared with the aforementioned hybrid methods. However, for the configuration having sparse coverage (2 stations) of the focal sphere, this method yielded the highest percentage double-couple components and lowest percentage of false components of all the methods, despite the poor resolution of the fault plane. The prospects of retrieving the source mechanisms of real events by the hybrid methods using a median and a weighted mean correction were thought to be good because the levels of noise inflicted on the input data in these tests were high – certainly higher than would be expected in reality.

5. In all the tests involving noise, the hybrid method using a mean correction gave unreliable results and was found to be sensitive to high noise levels. The reason for this behaviour is that the correction based on the mean residual is extremely sensitive to outliers. This method, therefore, proved to be of academic interest only, since real data sets often have large outlying values.

Stability test observations (recorded data)

The hybrid moment tensor inversion methods based on the median correction and weighted mean corrections were applied to a cluster of 14 events recorded at Oryx Gold Mine. Because these two hybrid methods showed similar robustness and stability in the presence of random and systematic noise, both methods were applied to determine which gave the better results. The results were compared with those determined using absolute methods. The waveforms of the events in the cluster displayed a remarkable degree of similarity. This similarity played an important role in the assessment of the accuracy of the hybrid moment tensor solutions, since it was reasonable to expect the output moment tensors and their corresponding radiation patterns to exhibit similar likenesses.

The main observations can be summarised as follows:

1. The solutions computed using the absolute moment tensor inversion method exhibited more variation than would be expected from a source cluster having very similar waveforms, and thus a relatively low level of accuracy was indicated.

2. The solutions computed using the hybrid moment tensor inversion using a median correction showed a considerable improvement after the iterative residual correction procedure was applied and the radiation patterns and fault-plane solutions showed a high degree of similarity.

3. When the results of the hybrid methods (using a median correction) were compared to those computed using the absolute methods, a noticeable decrease in the percentage of the isotropic component was observed. This is of importance in the light of the recent discussions in the literature about the interpretation of non-double-couple components (i.e. the presence of isotropic components and deviations from the pure double-couple model). A common topic in these debates is whether the non-double couple components are intrinsic to the source rupture process or artefacts of processing (due to inappropriate modelling of the ray-path, the presence of noise, invalid source models, etc.). This study showed that the percentage of isotropic component could be decreased significantly by application of the hybrid moment tensor inversion method with median correction. An additional important observation was made: compared to the hybrid moment tensor inversion using a weighted mean correction, the method using a median correction showed a lower sensitivity to noisy events. These observations are very encouraging and point towards the method's potential for use as a standard processing tool for mine seismicity.

4. The hybrid method using a weighted mean correction showed a slight improvement in the solutions since the radiation patterns appeared to be more crisply focussed. However, this method is more sensitive to noisy data than the median corrected method, and shows less promise for use as a standard processing tool in mine seismicity assessments

Case study at Oryx Gold Mine

The solutions of the cluster of events recorded at Oryx Gold Mine computed using the hybrid moment tensor inversion indicate that the dominating source mechanisms for most of the events in the cluster are of the shear type and show near-vertical and near-horizontal nodal-planes. The solutions also display a distinct rotation with time of a subvertical nodal-plane.

The isotropic component of the source mechanism changes systematically during the time sequence of events. In the early part of the time sequence, the isotropic component is negative implying an implosive contribution to the total mechanism – this would be consistent with the crushing of fault gouge on the failure plane. The isotropic component becomes positive towards the later part of the time sequence, and increases systematically. It is thought that the positive isotropic component is a result of over-riding of asperities on the fault plane (due to irregularities in the rock mass, or fault infill material) which results in a volume increase. A factor contributing to the volumetric expansion could be the decrease in the confinement as the stope advances, which allows expansion towards the free surface

Evidence from laboratory tests suggests that the internal friction angle decreases with increasing confining stress. The shape of the Hoek & Brown failure envelope confirms this observation. Since the dilation angle is related to the internal friction angle, the dilation decreases with increasing confining stresses. The results of this study appear to be in agreement with the laboratory observations because this study suggests that an increasing amount of dilation occurs (i.e. the isotropic component increases) as the confinement decreases due to mining.

REFERENCES

Aki, K. & Richards, P.G. (1980). *Quantitative Seismology,* Freeman, San Francisco.

Andersen, L.M. & Spottiswoode, S.M. (2001). A hybrid relative moment tensor methodology. Paper submitted to RaSim5.

Backus, G.E. (1977). Interpreting the stress glut moments of total degree two or less, *Geophys. J. R. Astr. Soc.* **51**, 1 – 25.

Barker, J.S. & Langston, C.A. (1982). Moment tensor inversion of complex earthquakes, *Geophys. J. R. Astr. Soc.* **46**, 341–371.

Ben-Menahem, A. & Singh, S.J. (1981). *Seismic waves and sources,* Springer Verlag, New York.

Bulland, R. (1976). The mechanics of locating earthquakes. *Bull. Seism. Soc. Am.* **70**, 149 – 170.

Burden, R.L. & Faires, J.D. (1985). *Numerical Analysis*, PWS Publishers, United States of America.

Bolt, B.A. (1988). *Earthquakes*, Freeman, San Francisco.

Bowers, D. (1997). The October 30, 1994, seismic disturbance in South Africa: Earthquake or large rock burst? *J. Geophys. Res.* **102,** 9843–9857.

Brawn, D.R. (1991). *Unpublished computer code (Fortran): Moment tensor inversion*, CSIR Miningtek, Auckland Park, South Africa.

Brawn, D.R. (1989). *A maximum entropy approach to underconstraint and inconsistency in the seismic source inverse problem; Finding and interpreting seismic source moments*, Ph.D. Thesis, University of the Witwatersrand, Johannesburg.

Burridge, R. & Knopoff, C. (1964). Body force equivalents for seismic dislocations, *Bull. Seism. Soc. Am.* **77**, 1875–1888.

Dahm, T. (1996). Relative moment tensor inversion based on ray theory: theory and results, *Geophys. J. Int.* **124**, 245–257.

de Natale, G., Iannaccone, M., Martini, M. & Zollo, A. (1987). Seismic sources and attenuation properties at the Campi Flegreei volcanic area, *Pure Appl. Geophys.* **125**, 883–917.

Dornboos, D. J. (editor) (1988). *Seismological Algorithms, Computational Methods and Computer Programs*, Academic Press, London.

Dufumier, H. (1996). On the limits of linear moment tensor inversion of teleseismic body wave spectra, *Pageoph*, **147**, 467-482.

Dziewonski, A.M & Gilbert, F. (1974). Temporal variation of the seismic moment tensor and the evidence for precursive compression for two deep earthquakes, *Nature*, **247**, 185 – 188.

Dziewonski, A.M. & Woodhouse, J.H. (1983). An experiment in systematic study of global seismicity: centroid-moment tensor solutions for 201 moderate and large earthquakes of 1981, *J. Geophys. Res.* **88**, 3247 – 3271.

Dziewonski, A.M., Chou T.A. & Woodhouse, J.H. (1981). Determination of earthquake source parameters from waveform data for studies of local and regional seismicity, *J. Geophys. Res.* **86**, 2825 – 2852.

Ebel, J.E. & Bonjer, K.P. (1990). Moment tensor inversion of small earthquakes in southwestern Gemany for the fault plane solution, *Geophys. J. Int.* **101**, 133–145.

Fan, G.W & Wallace, T.C. (1995). The determination of source parameters for small earthquakes from a single very broadband seismic station, *Geophys. Res. Lett.* **18**, 1385–1388.

Feignier, B. & Young, R.P. (1992). Moment tensor inversion of induced microseismic events: Evidence of nonshear failures in the $-4 < M < -2$ moment magnitude range, *Geophys. Res. Lett.* **19**, 1503 – 1506.

Fitch, T.J., McCowan, D.W. & Shields, M.W. (1980). Estimation of seismic moment tensor from teleseismic body wave data with application to intraplate and mantle earthquakes, *J. Geophys. Res.* **85**, 3817–3828.

Fitch, T.J., North, R.G. & Shields, M.W. (1981). Focal depths and moment tensor representations of shallow earthquakes associated with the great Sumba earthquake, *J. Geophys. Res.* **86**, 9357–9374.

Gay, N.C. & Ortlepp, W.D. (1979). Anatomy of a mining-induced fault zone, *Bull. Geol. Soc. Am.* **90**, 47–58.

Gibowicz, S.J. (1990). Keynote lecture: The mechanism of seismic events inducd by mining, in *Rockbursts and Seismicity in Mines,* C. Fairhurst (Editor), Balkema, Rotterdam, 3–23.

Gibowicz, S.J. & Kijko, A. (1994). *An Introduction to Mining Seismology*, Academic Press, San Diego, California.

Gilbert, F. (1970). Excitation of the normal modes of the earth by earthquake sources, *Geophys. J. R. Astr. Soc.* **77**, 223–226.

Gilbert, F. (1973). Derivation of source parameters from low-frequency spectra. *Phil. Trans. Roy. Soc. A.* **274**, 369 – 371.

Grodner, M. (1998). Personal communication. CSIR Miningtek, Auckland Park, South Africa.

Hamming, R.W. (1962). *Numerical methods for Scientists and Engineers: International Series in Pure and Applied Mathematics*, McGraw-Hill Book Company, New York.

Hasegawa, H. S., Wetmiller & R.J., Gendzwill, D.J. (1989). Induced seismicity in mines in Canada - An overview, *Pure Appl. Geophys.* **129**, 423–453.

Herrmann, R.B. (1975). A student's guide to the use of P- and S-wave data for focal mechanism determination, *Earthquake Notes,* **46**, 29–39.

Hudson, J. (1980). *The excitation and propagation of elastic waves,* Cambridge Univiversity Press, Cambridge, United Kingdom.

Hutchings, L. (1994). Kinematic earthquake models and synthesised ground motion using empirical Green's functions, *Bull. Seism. Soc. Am.* **84**, 1028–1050.

Hutchings, L. & Wu, F. (1990). Empirical Green's functions from small earthquakes - A waveform study of locally recorded aftershocks of the San Fernando earthquake, *J. Geophys. Res.* **95**, 1187–1214.

Jager, A.J. (1998). Personal communication. CSIR Miningtek, Auckland Park, South Africa.

Jager, J.C. & Cook, N.G.W. (1976). *Fundamentals of Rock Mechanics*, Chapman and Hall, London.

Johnston, D.E. & Langston, C.A. (1984). The effect of assumed source structure on inversion of earthquake source parameters: The eastern Hispaniola earthquake of 14 September 1981, *Bull. Seism. Soc. Am.* **74**, 2115–2134.

Jost, M.L. & Herrmann, R.B. (1989). A student's guide and review of moment tensors, *Seism. Res. Lett.* **60**, 37–57.

Kanamori, H. & Given, J.W. (1981). Use of long-period surface waves for rapid determination of earthquake source parameters, *Phys. Earth Planet. Interiors,* **27**, 8–31.

Kanamori, H., Mori, J. & Heaton, T.H. (1990). The 3 December 1988 Pasadena earthquake (M_L = 4.9) recorded with the very broadband system in Pasadena, *Bull. Seism. Soc. Am.* **80**, 483–487.

Kasahara, K. (1981). *Earthquake Mechanics*, Cambridge University Press, Cambridge, United Kingdom.

Kataka, M. (1998). Personal communication. University of the Witwatersrand, Johannesburg, South Africa.

Kikuchi, M. & Kanamori, H. (1986). Inversion of complex body waves – II, *Phys. Earth Planet. Interiors,* **43**, 205–222.

Kikuchi, M. & Kanamori, H. (1991). Inversion of complex body waves – III, *Bull. Seism. Soc. Am.* **81**, 2335–2350.

Knopoff, L. & Randall, M.J. (1970). The compensated linear vector dipole: a possible mechanism for deep earthquakes, *J. Geophys. Res.* **75**, 4957–4963.

Kullman, D.H., Stewart, R.D. & Grodner, M. (1996). A pillar preconditioning experiment on a deep-level South African mine, in *Proceedings of the 2nd North American Rock Mechanics Symposium: NARMS '96: Rock Mechanics Tools and Techniques,* M. Aubertin, F. Hassani, & H. Mitri (Editors), Balkema, Rotterdam, 375–380.

Lanczos, C. (1970). *Linear Differential Operators*, Van Nostrand, London.

Lawson, C.H. & Hanson, R.J. (1974). *Solving Least Squares Problems*, Prentice-Hall, Engelwood Cliffs, New Jersey.

Lay, T. & Wallace, T.C. (1995). *Modern Global Seismology,* Academic Press, San Diego.

Linzer, P. (1998). *Unpublished computer code (Pascal): Gaussian elimination,* CSIR Miningtek, Auckland Park, South Africa.

McGarr, A. (1993). Keynote address: Factors influencing the strong ground motion from mining-induced tremors, in *Rockbursts and Seismicity in Mines,* R.P. Young (Editor), Balkema, Rotterdam, 3–12.

McGarr, A. (1992a). An implosive component in the seismic moment tensor of a mining-induced tremor, *Geophys. Res. Lett.* **19**, 1579–1582.

McGarr, A. (1992b). Moment tensors of ten Witwatersrand mine tremors, *Pageoph.* **139**, 781–800.

McGarr, A. (1984). Some applications of seismic source mechanism studies to assessing underground hazard, in *Rockbursts and Seismicity in Mines,* N.C. Gay & E.H. Wainwright (Editors), S. Afr. Inst. Min. Metal. Symp. **6**, 199–208.

McGarr, A. (1971). Violent deformation of rock near deep-level tabular excavations - seismic events, *Bull. Seism Soc. Am.* **61**, 1453–1446.

McGarr, A., Bicknel, J., Sembera, E. & Green, R.W.E. (1989). Analysis of exceptionally large tremors in two gold mining districts of South Africa, *Pure Appl. Geophys.* **129**, 295–307.

Menke, W. (1989). *Geophysical Data Analysis: Discrete Inverse Theory,* Academic Press, Orlando.

Nabelek, J.L. (1984). *Determination of earthquake source parameters from inversion of body waves.* PhD Thesis, MIT.

Napier, J.A.L. (1998). Personal communication. CSIR Miningtek, Auckland Park, South Africa.

Oncescu, M.C. (1986). Relative seismic moment tensor determination for Vrancea intermediate depth earthquakes, *Pure Appl. Geophys.* **124**, 931–940.

Panza, G.F. (1985). Synthetic seismograms: the Rayleigh waves modal summation, *J. Geophys.* **58**, 125–145.

Patton, H. (1980). Reference point equalisation method for determining the source and path effects of surface waves, *J. Geophys. Res.* **85**, 821–848.

Pierce, A.P. (1998). Personal communication. University of British Columbia, Canada.

Press, W.H., Flannery, B.P., Teukolsky, S.A. & Vetterling, W.T. (1990). *Numerical recipes: The Art of Scientific Computing,* Cambridge University Press, New York.

Press, W.H., Teukolsky, S.A., Vetterling, W.T. & Flannery, B.P. (1992). *Numerical recipes in C,* Cambridge University Press, New York.

Pujol, J. & Herrmann, R.B. (1990). A student's guide to point sources in homogeneous media, *Seism. Res. Lett.* **61**, 209–220.

Reynolds, O. (1885). On the dilantancy of media composed of rigid particles in contact, *Phil. Mag.* 5^{th} *Ser.* **20**.

Ritter, T. Professional Engineer, Austin, Texas, USA, http://www.io.com/~ritter/NOISE/NOISRC.HTM

Scholz, C.H. (1990). *The Mechanics of Earthquakes and Faulting*, Cambridge University Press, United Kingdom.

Šílený, J., & Psencik, I. (1995). Mechanisms of local earthquakes in 3-D inhomogeneous media determined by waveform inversion, *Geophys. J. Int.*, **121**, 459-474.

Šílený, J., Panza, G.F. & Campus, P. (1992). Waveform inversion for point source moment retrieval with variable hypocentral depth and structural model. *Geophys. J. Int.* **109**, 259–274.

Šílený, J., Campus, P., and G.F. Panza (1996). Seismic moment tensor resolution by waveform inversion of a few local noisy records - I. Synthetic tests, *Geophys. J. Int.*, **126**, 605-619.

Silver, P.G. & Jordan, T.H. (1982). Optimal estimation of scalar sesimic moment, *Geophys. J. R. Astr. Soc.* **70**, 755 – 787.

Spottiswoode, S.M. (1998-2001). Personal communication. CSIR Miningtek, Auckland Park, South Africa.

Spottiswoode, S.M. (1984). Source mechanisms of mine tremors at Blyvooruitzicht gold mine, in *Rockbursts and Seismicity in Mines,* N.C. Gay & E.H. Wainwright (Editors), S. Afr. Inst. Min. Metal. Symp. **6**, 29–37.

Spottiswoode, S.M. & McGarr, A. (1975). Source parameters of tremors in a deep level gold mine, *Bull. Seism. Soc. Am.* **65**, 93–112.

Spottiswoode, S.M. & Milev, A. (1998). The use of waveform similarity to define planes of mining-induced seismic events, *Tectonophysics.* **289**, 51 – 60.

Stickney, M.C. & Sprenke, K.F. (1993). Seismic events with implosional focal mechansims in the Coeur d'Alene Mining District Northern Idaho, *J. Geophys. Res.* **98**, 6523 – 6528.

Strelitz, R.A. (1978). Moment tensor inversions and source models, *Geophys. J.* **52**, 359–364.

Strelitz, R.A. (1980). The fate of the downgoing slab: A study of the moment tensors from body waves of complex deep-focus earthquakes, *Phys. Earth. Planet. Int.* **21**, 83–96.

Stump, B.W. & Johnson, L.R. (1977). The determination of source properties by the linear inversion of seismograms, *Bull. Seism. Soc. Am.* **67**, 1489–1502.

Tarantolla, A. (1987). *Inverse Problem Theory*. Elsevier, Amsterdam.

Tweedie, K.A.M. (1986). The discovery and exploration of Beisa and Beatrix gold and uranium mines in the southern extension of the Welkom gold field in *Mineral deposits of Southern Africa I,* C.R Anhaeusser & S. Maske (Editors), Geological Society of South Africa, Johannesburg, 541-547.

Udias, A. (1964). A least squares method of earthquake mechanism determination using S-wave data, *Bull. Seism. Soc. Am.* **55**, 2036–2047.

Udias, A. & Baumann, D. (1969). A computer program for focal mechanism determination combining P and S wave data. *Bull. Seism. Soc. Am.* **59**, 503–519.

Vermeer, P.A. & de Borst, R. (1984). Non-associated plasticity for soils, concrete and rock, *Heron*, **21**, 1–64.

Wallace, T.C., Velasco, A., Zhang, J. & Lay, T. (1991). A broadband seismological investigation of the 1989 Loma Prieta, California earthquake: Evidence for slow slip? *Bull. Seism. Soc. Am.* **81**, 1622–1646.

Weidner, D.J. & Aki, K. (1973). Focal depth and mechanism of mid-ocean ridge earthquakes, *JGREA*, **78**, 1818.

Wiejacz, P. (1991). *Investigation of focal mechanisms of mine tremors by the moment tensor inversion*, Ph.D. Thesis, Instit. Geophys., Pol. Acad. Sci., Warsaw.

Wong, I. & McGarr, A. (1990). Implosional failure in mining-induced seismicity: A critical review, in *Rockbursts and Seismicity in Mines,* C. Fairhurst (Editor), Balkema, Rotterdam, 45–51.

LIST OF APPENDICES

Appendix A

FAULT-PLANE SOLUTION

A spherical surface, referred to as the focal sphere, is envisaged surrounding the hypocentre of the source (Figure A.1, bottom).

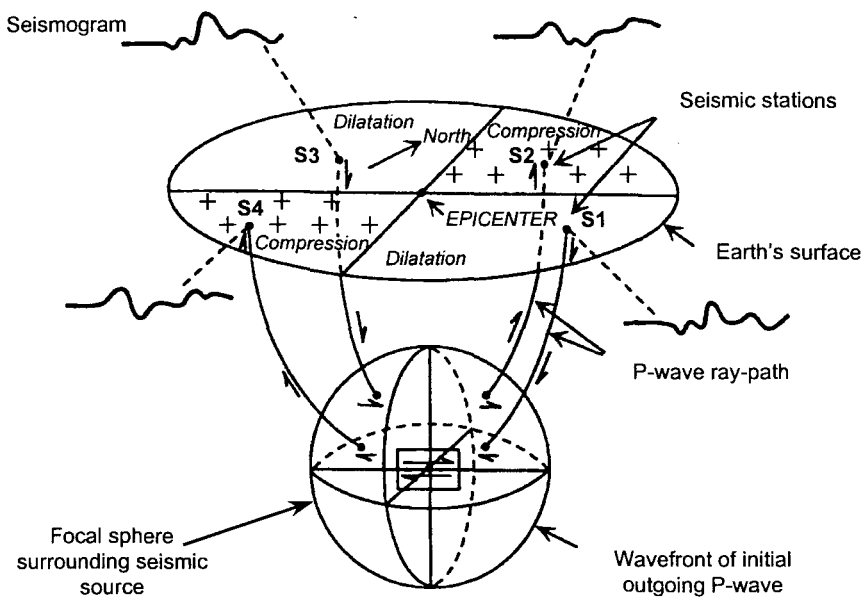

Figure A.1: First motions of P-wave at seismometers located in various directions about an earthquake to allow determination of the fault plane orientation (modified from Lay & Wallace, 1995).

Seismic stations (labelled S_1 to S_4) are projected as points on the surface of the focal sphere by ray tracing back to the source. Their positions on the focal sphere are given by two parameters, *viz.* the take-off angle θ at the source, measured from the vertical axis, and the azimuth ϕ, measured from North. Each combination of θ and ϕ describes a unique ray-path from the source to a point on the surface of the focal sphere. The P-wave polarity of the wavefront corresponding to the ray-path is plotted on the surface of the sphere. For example, the seismometers located at positions S_2 and S_4 will record compressional first motions.

Repeating this procedure for all the data available from all the recording stations for a seismic event gives a comprehensive view of wave radiation from the hypocentre provided the source is sufficiently surrounded by seismometers. Nodal planes can be

constructed to separate the wave radiation (projected onto the surface of the focal sphere) into compressional and dilatational quadrants.

The focal sphere is a three-dimensional body, so the polarity data on the sphere are distributed in three dimensions and, therefore, difficult to interpret visually (Figure A.1). For ease of interpretation, the three-dimensional data are projected onto a two-dimensional diagram, called a focal mechanism diagram (Figure A.2).

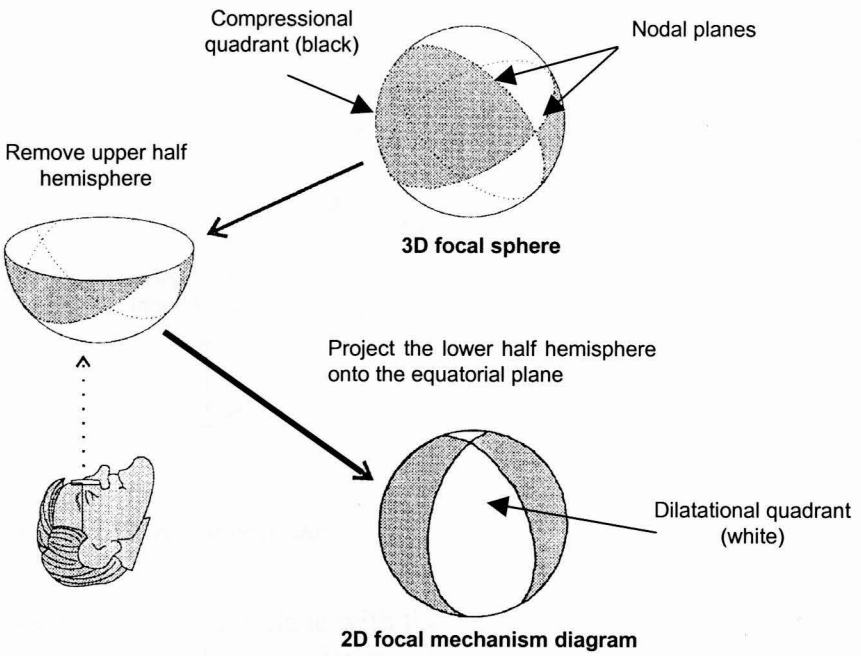

Figure A.2: Projection of the focal sphere onto an equatorial plane to produce a focal mechanism diagram (from Suetsuga, 1994).

Appendix B

FAULT-PLANE NOMENTCLATURE

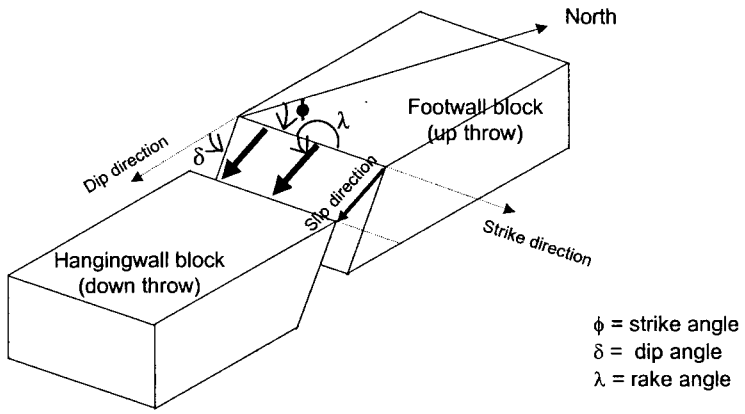

Figure B.1: Fault nomenclature conventions.

The line of intersection of the fault plane with the surface of the earth is known as the strike direction (Figure B.1). The orientation of the strike direction is expressed in terms of an angle known as the strike angle $\left(0 \le \phi_S \le 360^\circ\right)$. The strike angle is measured clockwise from North. The strike direction is defined according to the right-hand rule which states: if you orient the thumb on your right hand along the strike, and rotate your hand downward from the horizontal to the fault plane so that your hand pivots through an angle less than 90°, your thumb will point in the strike direction. The strike direction is arbitrarily either orientation for a vertically dipping fault.

A line drawn on the surface of the earth, perpendicular to the strike direction, drawn in the direction in which the fault plane dips is known as the dip direction. The dip angle, δ, of the fault is the angle between the dip direction and the fault plane, and is measured downwards from the horizontal plane $\left(0 \le \delta \le 90^\circ\right)$.

The relative motion of the two fault blocks on either side of the fault is defined by a slip vector, which can have any orientation on the fault plane. The direction of the slip vector is given by the angle of slip, the rake λ. The rake is the angle between the strike direction and the slip vector, measured counter-clockwise in the plane of the fault, showing the motion of the hangingwall relative to the footwall $\left(0 \le \lambda \le 360^\circ\right)$.

The block diagram in Figure 2.5 shows some common fault types. In strike-slip faulting, the two sides of a fault slip horizontally relative to one another. If $\lambda = 0^\circ$ or

180° the motion is called pure strike-slip. For $\lambda = 0°$ or 180° and vertical dip ($\delta = 90°$) the geometry is called vertical strike-slip. If $\lambda = 0°$ the motion is called left-lateral strike-slip, and if $\lambda = 180°$ the motion is called right lateral strike-slip.

In dip-slip faulting, the two sides of the fault slip vertically relative to one another. For $\lambda = 90°$ the hangingwall moves upwards relative to the footwall causing reverse faulting. If $\lambda = 270°$ the hangingwall moves downwards relative to the footwall causing normal faulting.

In general, λ will have a different value than these special cases, and the motion then is called oblique-slip, with the predominant character being described by stringing together the appropriate descriptors (e.g. right–lateral oblique normal faulting, for $180° < \lambda < 270°$).

Appendix C

METHOD OF LEAST-SQUARES

It is important to note that this section is self-contained and that the symbols do not follow those used in the main body of the thesis. Consider the following linear system of equations written in matrix notation as:

$$\mathbf{y} = \mathbf{Bx} \qquad C.1$$

where **y** is a vector of dimension R (number of observations), **x** is a vector of dimension C (number of unknowns, i.e. the moment tensor components or the model parameters), and **B** is the $R \times C$ coefficient matrix. For an overdetermined system, $R > C$.

For any vector **y** the error, or residual, **E** is given by:

$$\mathbf{E} = [\mathbf{y} - \mathbf{Bx}] \qquad C.2$$

where **E** is a vector of dimension R.

Using the least-squares approach, we seek to find the values of **x** for which the sum of the squared errors is a minimum. This sum is given by:

$$E^2 = \sum_{i=1}^{R} \left(y_i - \sum_{j=1}^{C} B_{ij} x_j \right)^2 \qquad C.3$$

Taking the derivatives of E^2 with respect to the model parameters x_k and minimising yields:

$$\begin{aligned} \frac{\partial E^2}{\partial x_k} &= 2E \frac{\partial E}{\partial x_k} \\ &= -2 \sum_{i=1}^{R} \left(y_i - \sum_{j=1}^{C} B_{ij} x_j \right) B_{ik} = 0 \end{aligned} \qquad C.4$$

Rearranging Equation C.4:

$$\sum_{i=1}^{R} y_i B_{ik} = \sum_{i=1}^{R} \left(\sum_{j=1}^{C} B_{ij} x_j \right) B_{ik} \qquad C.5$$

Equation C.5 may be written in matrix notation as:

$$\mathbf{B}^{\mathrm{T}}\mathbf{y} = \mathbf{B}^{\mathrm{T}}\mathbf{Bx} \qquad C.6$$

$\mathbf{B}^T\mathbf{B}$ is a square matrix, and provided it is non-singular, has an inverse. The elements of the solution vector $\mathbf{x}$ can then be determined from:

$$\mathbf{x} = [\mathbf{B}^T\mathbf{B}]^{-1}\mathbf{B}^T\mathbf{y} \qquad C.7$$

where $[\mathbf{B}^T\mathbf{B}]^{-1}\mathbf{B}^T = \mathbf{B}^G$ is the generalised inverse of $\mathbf{B}$ (strictly speaking, $\mathbf{B}^G$ is the least-squares inverse because $\mathbf{B}^T\mathbf{B}$ is symmetric and has real, positive eigenvalues).

Appendix D

SINGULAR VALUE DECOMPOSITION

As in Appendix C, this section is self-contained and that the symbols do not follow those used in the main body of the thesis. Consider matrix **P** having dimensions $R \times C$ where $R \geq C$. Applying the decomposition theorem of Lanczos (1961), **P** can be decomposed into:

$$\mathbf{P} = \mathbf{U}\Lambda\mathbf{V}^{\mathrm{T}} \qquad D.1$$

where **U** is a $R \times C$ matrix consisting of the orthonormalised eigenvectors of the product $\mathbf{PP}^{\mathrm{T}}$, Λ is a diagonal $C \times C$ matrix containing the eigenvalues of **P**, and the $C \times C$ **V** matrix consists of the orthonormalised eigenvectors of the product $\mathbf{P}^{\mathrm{T}}\mathbf{P}$. The factoring of matrix **P** into Λ, **U**, and **V** and is known as the singular value decomposition (SVD) technique. SVD computer subroutines are available in most numerical libraries, such as Numerical Recipes (Press *et al.*, 1990).

If matrix **P** is square, the following decomposition is possible:

$$\mathbf{P} = \mathbf{U}\Lambda\mathbf{V}^{\mathrm{T}} = \mathbf{U}\Lambda\mathbf{U}^{-1} = \mathbf{U}\Lambda\mathbf{U}^{\mathrm{T}} \qquad D.2$$

Equation B.9 can be solved by the SVD method. The non-square matrix **B** has dimensions $R \times C$, therefore $\mathbf{B}^{\mathrm{T}}\mathbf{B}$ has dimensions $C \times C$, and $\mathbf{BB}^{\mathrm{T}}$ is of dimension $R \times R$. Since these two matrices are square, Equation D.2 can be used to solve for the inverse of $\mathbf{B}^{\mathrm{T}}\mathbf{B}$ in terms of eigenvector matrices **V** and **U**.

Applying Equation D.2, the singular value decomposition of $\mathbf{B}^{\mathrm{T}}\mathbf{B}$ is as follows:

$$\mathbf{B}^{\mathrm{T}}\mathbf{B} = \mathbf{V}\Lambda_{C(2)}\mathbf{V}^{\mathrm{T}} \qquad D.3$$

where **V** is $C \times C$, and the eigenvalue matrix $\Lambda_{C(2)}$ is $C \times C$. The eigenvalues are actually just the squared values of the eigenvalues themselves, denoted with the subscript *(2)*.

In a similar way, the singular value decomposition of $\mathbf{BB}^{\mathrm{T}}$ is given by:

$$\mathbf{BB}^{\mathrm{T}} = \mathbf{U}\Lambda_{R(2)}\mathbf{U}^{\mathrm{T}} \qquad D.4$$

where **U** is a $R \times R$ matrix of eigenvectors and the eigenvalue matrix $\Lambda_{R(2)}$ is $R \times R$.

At this stage it is important to note that $\mathbf{BB}^{\mathrm{T}}$ has dimensions $R \times R$ with $R > C$, but only up to C eigenvalues are nonzero, and they are the same as those computed in

Equation D.3. The additional $(R-C)$ rows and columns of Λ_R are zeros, although the corresponding eigenvectors are not null vectors.

Computation of the generalised inverse, $\mathbf{B}^G$ (Equation D.3) requires the quantities $[\mathbf{B}^T\mathbf{B}]^{-1}$ and $\mathbf{B}^T$. The eigenvalue formulation in Equations C.3 allows the inverse, $[\mathbf{B}^T\mathbf{B}]^{-1}$, to be computed directly:

$$[\mathbf{B}^T\mathbf{B}]^{-1} = [\mathbf{V}^T]^{-1}\,[\Lambda_{C(2)}]^{-1}\,\mathbf{V}^{-1} = \mathbf{V}\,[\Lambda_{C(2)}]^{-1}\,\mathbf{V}^T \qquad D.5$$

since the inverse of $\mathbf{V}^T$ is $\mathbf{V}$, and similarly, $\mathbf{V}^{-1}$ is $\mathbf{V}^T$.

Consider $\mathbf{B}^T$. Although this is a non-square matrix of dimension $R \times C$, it can be decomposed using Equation D.2 if only up to C eigenvectors are considered in the matrix Λ_C. Therefore, the singular value decomposition of $\mathbf{B}$ yields:

$$\mathbf{B} = \mathbf{U}\Lambda_C\mathbf{V}^T \qquad D.6$$

and

$$\mathbf{B}^T = \mathbf{V}\Lambda_C\mathbf{U}^T \qquad D.7$$

Combining Equations D.5 and D.7, recognising that the eigenvector matrices are the same for $[\mathbf{B}^T\mathbf{B}]$ and $\mathbf{B}^T$, yields:

$$\begin{aligned}\mathbf{B}^G &= [\mathbf{B}^T\mathbf{B}]^{-1}\mathbf{B}^T \\ &= \{\mathbf{V}\,[\Lambda_{C(2)}]^{-1}\,\mathbf{V}^T\}\{\mathbf{V}\Lambda_C\mathbf{U}^T\} \\ &= \mathbf{V}\,[\Lambda_{C(2)}]^{-1}\,\Lambda_C\mathbf{U}^T\end{aligned} \qquad D.8$$

Since the eigenvalues in $\Lambda_{C(2)}$ are simply the square of those in Λ_C, the last line of Equation D.8 reduces to the following:

$$\mathbf{B}^G = \mathbf{V}\,[\Lambda_C]^{-1}\,\mathbf{U}^T \qquad D.9$$

where the eigenvector matrix is of the form:

$$\Lambda^{-1} = \begin{bmatrix} (1/\lambda_1)^2 & 0 & 0 & \cdots & 0 \\ 0 & (1/\lambda_2)^2 & 0 & \cdots & 0 \\ 0 & 0 & (1/\lambda_3)^2 & \cdots & 0 \\ \vdots & \vdots & \vdots & \ddots & \vdots \\ 0 & 0 & 0 & \cdots & (1/\lambda_C)^2 \end{bmatrix} \qquad D.10$$

and

$$\lambda_1 \geq \lambda_2 \geq \ldots \lambda_C \geq 0 \qquad D.11$$

Inequality D.11 is not a necessary condition since it depends on the order in which the eigenvectors appear in $\mathbf{U}$.

Appendix E

GAUSSIAN ELIMINATION WITH BACK-SUBSTITUTION

Note that the symbols do not follow those used in the main body of the thesis. Equation C.5 can be rewritten as:

$$\mathbf{y}^* = \mathbf{B}^* \mathbf{x} \qquad E.1$$

where the quantities $\mathbf{y}^*$ and $\mathbf{B}^*$ represent $\mathbf{B}^T\mathbf{y}$ and $\mathbf{B}^T\mathbf{B}$, respectively. The linear system represented by the matrix notation in Equation E.1 may be expanded as follows:

$$\begin{aligned}
E_1: &\quad y_1^* = B_{11}^* x_1 + B_{12}^* x_2 + \ldots + B_{1R}^* x_R \\
E_2: &\quad y_2^* = B_{21}^* x_1 + B_{22}^* x_2 + \ldots + B_{2R}^* x_R \\
&\quad \vdots \qquad \vdots \qquad \vdots \qquad\qquad \vdots \\
E_R: &\quad y_R^* = B_{R1}^* x_1 + B_{R2}^* x_2 + \ldots + B_{RR}^* x_R
\end{aligned} \qquad E.2$$

Gaussian elimination is a standard technique described in most texts concerning numerical analysis (e.g. Burden & Faires, 1985) and for this reason the process is not described in detail. This method is based on combining the equations linearly to eliminate the unknowns. For the system of R equations with R unknowns (Equation E.2), the first unknown is eliminated from all but the first equation, the second unknown is eliminated from all but the first and second equations, and so on, until the last equation only has one variable. The system of equations is thus reduced to upper triangular form:

$$\begin{aligned}
E_1: &\quad y_1^{**} = B_{11}^{**} x_1 + B_{12}^{**} x_2 + B_{13}^{**} x_3 + \ldots + B_{1R}^{**} x_R \\
E_2: &\quad y_2^{**} = \qquad B_{22}^{**} x_2 + B_{23}^{**} x_3 + \ldots + B_{2R}^{**} x_R \\
E_3: &\quad y_3^{**} = \qquad\qquad B_{33}^{**} x_3 + \ldots + B_{3R}^{**} x_R \\
&\quad \vdots \qquad\qquad\qquad\qquad\qquad \vdots \\
E_R: &\quad y_R^{**} = \qquad\qquad\qquad\qquad B_{RR}^{**} x_R
\end{aligned} \qquad E.3$$

where the B_{ij}^{**} represent the new coefficients.

Once the elimination process is complete, back-substitution is used to solve for the unknowns. Consider the R^{th} equation, E_R. From Equation E.3 it is evident that $x_R = \frac{y_R^*}{B_{RR}^{**}}$. Using the value computed for x_R, E_{R-1} can be solved for x_{R-1}. After the back-substitution is performed for each variable, the final solution results.

Appendix F

FILE FORMATS

F.1 Input data file format required by RMTI

RMTI reads the network parameters and seismic data from ASCII data files created by the user. The data files are divided into network and database files. The network file contains information regarding the seismic network: number of geophone sites and recording channels (*nch*), number of events (*nev*) to be used in the inversion and positions of geophone sites in (x,y,z) coordinates (Figure F.1).

```
Network parameter file
Number of sites, channels, events:  nsite, nch, nev, nphase
3     9     20     3
Geophone positions: nsite, xgeo, ygeo, zgeo
2          -36270.0          -22090.0          -2147.2
3          -36284.0          -22210.0          -2161.0
6          -36470.5          -22030.5          -2147.4
```

Figure F.1: Network file containing seismic network information.

The data file consists of an eight column text file which contains the event number, seismic event location (in local (x,y,z) coordinates), the geophone site number, and maximum phase amplitude (P, SH and SV-phases) u_{ij} of the recorded seismic events (Figure F.2). The indices i and j refer to the event number and the phase observation, respectively.

```
Seismic event data file
Event no.    x          y          z          nsite    P-amp    SH-amp    SV-amp
166232       -36374.5   -22142.6   -2162.2    2        0.126    0.323     0.464
166232       -36374.5   -22142.6   -2162.2    3        0.036    0.177     0.300
166232       -36374.5   -22142.6   -2162.2    6        0.049    0.112     0.178
166233        etc.
```

Figure F.2: Example of a database file containing information regarding the recorded seismic events.

F.2 Input data file format required by STEREO

```
: STEREO_FM2
:
: PLANES: symbol_type comment (optional)
: LINES:  symbol_type comment (optional)
:
: If symbol_type equals zero then point will be plotted as great circle
:
: RAKE: data has three components: strike, dip of the plane
: followed by the rake angle
:

TITLE: First motions calculated using moment tensor

LINES: 3  Event Number:  166240
   0.  95.      1
   0.  100.     2
   0.  105.     3
   0.  110.     4

..... etc

  360.  170.    585
  360.  175.    586
  360.  180.    587
 END-DATA:
```

Figure F.3: Example of the format required by STEREO from which a radiation pattern is plotted.

Appendix G

MANUAL FAULT-PLANE SOLUTIONS

STEREO version 2.0 (part of RockWare Inc.) is used to plot the stereonet data generated by RMTI. The stereonet data file contains the positions (azimuth and dip) on the focal sphere where a positive (compressional) P-wave motion is present. Using STEREO, the radiation pattern formed by the polarity data is projected into the lower hemisphere of an equal-area Schmidt stereonet (Figure G.1).

Note that since RMTI only writes the take-off angle and azimuth of the P-wave compressional motion to a data file (and not the dilatation), the shaded region of the diagram represents the compressional quadrant of the focal mechanism.

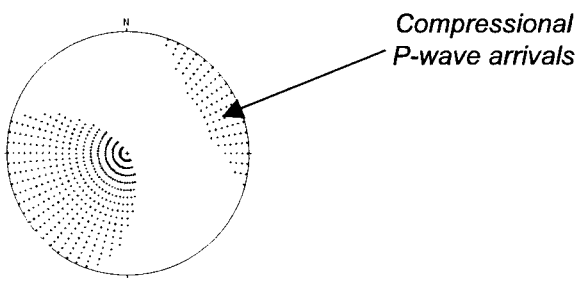

Figure G.1: Stereographic projection of double-couple radiation pattern for event 166240. Shaded area (++) represents positive (compressional) P-wave first-motions.

Two nodal planes are fitted to the projection (Figure G.2), dividing the radiation pattern into four quadrants of alternating compression and dilatation of the P-wave. Because the nodal planes are perpendicular to one another, each plane is selected so that it passes through the pole of the other plane. The orientations of the nodal planes can be determined from the projection (Figure G.3) to give a fault-plane solution. The fault-plane solution may be used to determine the type of faulting taking place, in addition to allowing fault parameters to be deduced (i.e. strike, dip and sense of displacement).

Additional geological information is necessary to distinguish the fault plane from the auxiliary plane.

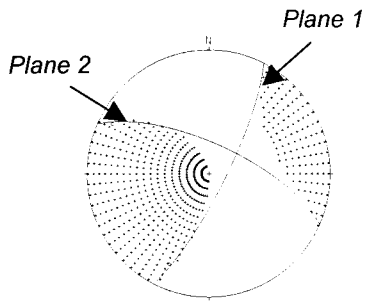

Fault plane solution:

	Strike	Dip
1.	17°	80°
2.	285°	80°

Figure G.2: Fault-plane solutions for event 166240.

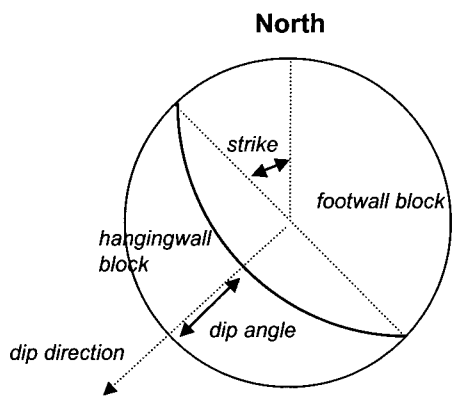

Figure G.3: The measurement of strike and dip angles from a focal mechanism diagram (lower-hemisphere, equal-area projection).

Appendix H

MEMORY REQUIREMENTS & COMPARISON OF SOLUTION PROCEDURES

H.1 Memory requirements

The total number of elements in the coefficient matrix of Equation 4.27 is given by:

$$\begin{aligned} \textit{Total number of elements} &= (\textit{Total number of rows}) \cdot (\textit{Total number of columns}) \\ &= \left(\tfrac{1}{2} nch \cdot nev(nev-1)+1\right) \cdot (6 \cdot nev) \\ &\propto (nev)^3 \end{aligned} \qquad H.1$$

For a given network (i.e. constant number of channels and observations), the number of elements increases according to a cube law with an increase in the number of events. This relationship has the potential to become computationally expensive when the amount of memory required to store the coefficient matrix is considered.

For instance, retrieving the moment tensors of ten sources, recorded by a network consisting of three triaxial sites, and using three phases (P, SH and SV-phases), will necessitate the creation of a matrix consisting of 406 columns by 60 rows, a total of 24 360 elements. If single precision arithmetic is used, and each element is stored in four bytes of memory, a total of ~ 95 kB will be needed just to store this matrix, let alone run the program. If 30 events recorded by the same network are used, a 180 column by 3916 row coefficient matrix will result, requiring ~2.7 MB of memory (Table H.1 and Figure H.1).

Table H.1: Memory required to store the coefficient matrix (three triaxial sites).

No. events	No. rows	No. columns	Total no. Elements	Memory required (bytes)
5	91	30	2730	10 920
10	406	60	24 360	97 440
20	1711	120	205 320	821 280
30	3916	180	704 880	2 819 520
40	7021	240	1 685 040	6 740 160
50	11 026	300	3 397 800	13 591 200

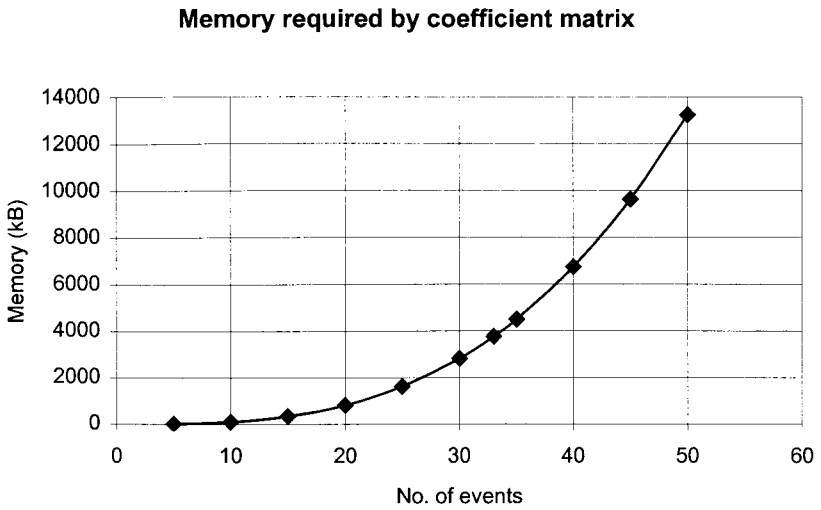

Figure H.1: Memory required to store the coefficient matrix for a variable number of events.

H.2 Comparison of solution procedures

Two different solution procedures, singular value decomposition technique and Gaussian elimination are used in the inversion of Equation 3.75. Some general comments are made regarding accuracy and solution time.

The solution procedures give rise to nearly identical results (Table H.2) having relative errors of less than 1% (Table H.3). The differences lie in their computation speed and the subsequent error analysis. Table H.4 shows the time taken to implement the singular value decomposition and the Gaussian elimination routine (for a network consisting of three triaxial geophone sites and using three phases) for different values of *nev* (number of events in source cluster).

Appendix I

DEVELOPMENT OF MTI TOOLBOX

The development of the moment tensor inversion toolbox can be divided into four main phases. The emergence of these phases was driven by the inadequacies in the programming languages used to write the toolbox.

I.1 Phase 1 - Fortran 90 using PSS input data files

The original code written to perform the relative inversion without a reference mechanism (RMTI), described in the Chapter 4, was written using Fortran 90 and ran in DOS mode as a command line program. The input data files were constructed by hand – the user had to inspect each time-integrated displacement waveform, identify the relevant wave phases and read off either the peak amplitudes or peak-to-peak amplitudes and associated polarities for each phase. It is evident from the required input data file that the moment tensor inversion was performed in the time-domain. Although this method of data file generation worked extremely well for a once-off M.Sc. project it would be prohibitively time-consuming for routine application. In addition, identification of the peak amplitude was subjective.

For these reasons, the decision was taken to automate the data file generation process. To reduce the subjectivity of identifying the peak phases in the time-domain, a frequency-domain approach was taken, where the input data consisted of the spectral plateaux below the corner frequency of the time-integrated displacement seismogram for each phase. This had the advantage of using a window of data rather than an individual pulse.

I.2 Phase 2 - Visual Basic interface and Fortran DLL using PSS input data files

At the risk of stating the obvious, the command-line driven interface approach was not user-friendly and the string parsing and error trapping capabilities in Fortran 90 were limited. The options were to either rewrite RMTI in a language that supported Windows graphics, or to write a Windows interface that communicated with the Fortran solution engine. At this stage in the project, it was decided to follow the latter option, and Microsoft Visual Basic (VB) was selected as the relevant tool.

The most elegant way to connect the Fortran solution engine to VB was by creating a Dynamic Link Library (DLL) from the Fortran source code which was then linked to the VB interface at run time. Such a process was, superficially, very simple, and was covered well in the Microsoft mixed language programming documentation.

However, it was discovered that this approach is really only applicable to simple Fortran code that processes and returns control to the VB interface almost immediately. This approach was poorly suited to more complex Fortran tasks such as iterative processing that required time. If the Fortran process took longer than a few seconds, the VB interface would appear to 'freeze' while the DLL was processing. This resulted in unacceptable Windows behaviour and destroyed the impact of creating a professional user interface in VB.

Nic Lightfoot (Manager of the CSIR Miningtek Software Development Group) researched an alternative approach to linking Fortran solution code to VB interfaces. This approach may be summarised as follows. The Fortran solution engine is run in its own thread (a thread is a path/flow of execution used by a process). This allows the Fortran code to execute in the background while leaving the VB user interface completely responsive. In order for the VB interface to keep track of what is happening to the solution engine, messages are sent back to the main process from the Fortran DLL. The VB interface periodically polls this signal to recover its current status. This process is illustrated schematically in Figure I.1.

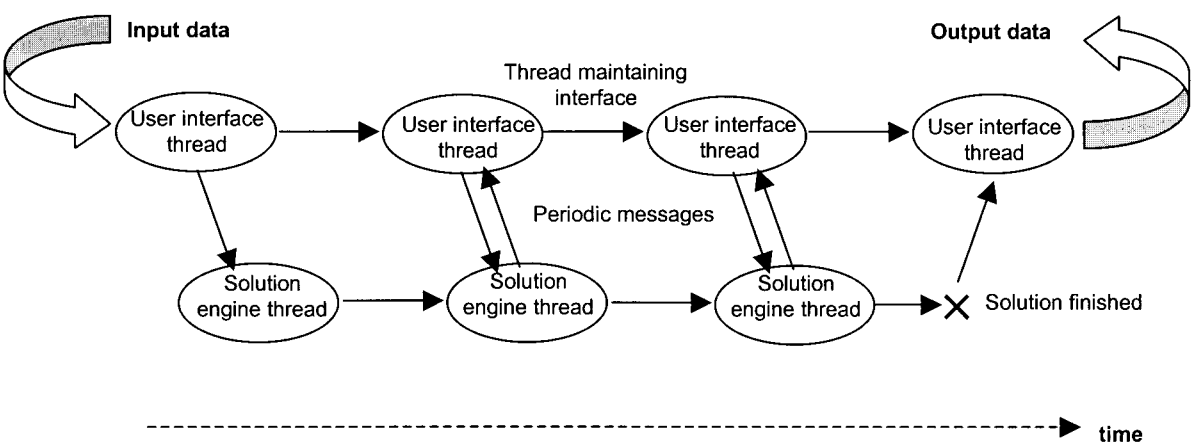

Figure I.1: Schematic representation of the relative moment tensor inversion program (without a reference mechanism)

The author applied the multi-threading approach with success, and then had to focus efforts on the data file generation aspect of the problem. The input data proved to be the most challenging of the tasks thus far, not because of the technical complexity of the task, but due to the task of generating accurate data files automatically. In phase two of the development, the user was required to generate an ASCII text file containing the event numbers of the waveforms in a cluster identified by the user (assuming that that the events had been located). The RMTI program used this master list to select the relevant information from standard output files created by SEISM and SQ32. Both SEISM and SQ32 form part of the PSS suite of software.

In phase two, four input data files were required by RMTI. A list of these files follows.

- A text file created by the user containing the list of event numbers of the waveforms in the cluster. Visualisation tools such as the AURA mine plan viewer or 4Di (ISSI visualisation software) could be used in the cluster identification. This file could also be created using most text editors (e.g.: 'notepad'). RMTI used this master list of event numbers to select the relevant information from three text files created either by AURA or SQ32 (part of the PSS suite of software).
- The second of the text files ('IOBG' file) contained network information such as geophone positions and channel numbers.
- The third file ('IO' file) contained the event information – event locations, magnitudes and scalar moments.
- The last file ('SQ32.AZ' file) contained either the peak phase amplitudes or spectral plateaux for the various phases recorded for each of the geophone channels. At this stage, both time- and frequency-domain approaches were supported because the author was still not certain which of the approaches gave the most stable results.

The challenging part of this process was generating the 'best' input file from SQ32. In this particular incarnation of the program, the author experimented with the window length to decide which gave the most representative results for a particular data set. It was also found that the frequency-domain approach was generally more stable than that applied in the time-domain.

I.3 Phase 3 - Visual Basic interface and Fortran DLL using AURA input data files

The third phase of the development focussed on interfacing RMTI with AURA. AURA is a waveform processing and analysis package written by CSIR Mining Technology. It consists of three separate programs that communicate with one another using an RPC server (remote procedure call). The three main programs are: the seismic explorer (SX); a waveform viewer and processor (PWAVES), and a mine-plan viewer (VW). SX manages the event catalogues which are stored in a Microsoft Access database. Various filters can be set up to query the database and create subsets. Subsets can also be created using the mine-plan viewer. This program displays the positions of the located events as well as the mine-plan, local geology, etc. The waveform processing is performed by PWAVES. Various filters (Low-pass, high-pass and band-pass) can be applied, the traces can be rotated, integrated or differentiated, and power spectra can be displayed and energy envelopes calculated, etc.

AURA was selected as the tool for preliminary waveform processing for several.

- AURA accommodates more channels than the PSS software. The PSS software has a limit of 14 channels, whereas AURA currently accommodates 48 channels. This limit can be extended as the need arises.
- AURA is Windows based, and 'cut and paste' and 'copy to clipboard' operations are supported. AURA interfaces with word processing tools (e.g. Word, WordPerfect) providing a more user-friendly report writing environment.

- The data structures read by AURA are more flexible than those used by the PSS, and are suitable for use with seismograms recorded by other seismic networks. For example, the PSS uses a fixed sampling rate, whereas AURA caters for variable sampling rates.
- AURA interfaces with existing software used on the mines, for example, AURA reads the MINSIM layout files.

Further refinements to the robustness of the relative inversion solution engine were made.

- In the original formulation of RMTI, the events selected in a cluster had to be of comparable magnitudes. The reason for this was that the relatively large amplitudes associated with large magnitude events would dominate the other coefficients in the system of linear equations, biasing the moment tensors of the cluster towards that of the large magnitude event. To overcome this, a normalisation procedure was introduced, where the amplitudes of each phase were normalised using the root-mean-square average amplitude for that particular event.
- A problem with RMTI was the relative nature of the resultant moment tensors. The moment tensor for each event in a cluster could only be compared with those of other events in the same cluster. Absolute quantities (such as the amount of displacement on a fault plane) could not be computed from the relative moment tensors, and comparisons were made by expressing the parameters in question as percentages. To address this issue, the output moment tensors were scaled to the appropriate size using the seismic scalar moment, which was read by RMTI as input.

I.4 Phase 4 - MTI toolbox written in Delphi 5 using AURA input data files

So far, only the developments in the code to perform the relative moment tensor inversion without a reference mechanism (RMTI) have been described. While developing this method in the frequency-domain and applying the technique extensively to a number of different data sets, it was found that the output of RMTI was strongly dependent on the events in the cluster having significantly different mechanisms. Clusters of events recorded underground cannot be guaranteed to have different mechanisms – in fact, clusters are very likely to have similar mechanisms. This criterion was found to become especially important when the input data were noisy. This is not a surprising observation since a cluster of events having very similar mechanisms leads to a near-singular least-squares matrix. When the noise level is of the same order as the differences in the mechanisms, the system of equations becomes near-singular, thereby significantly obscuring the distinction between the mechanisms and producing unreliable results.

To address the problem of having clusters comprising of similar mechanisms, the hybrid approaches were developed. This necessitated a whole new phase in

development, in which a number of different moment tensor inversion techniques were combined to form one program – the moment tensor inversion toolbox.

The reasons for writing the toolbox in Delphi are listed below.

- The system described thus far had several disadvantages: debugging the DLL created in Fortran while running VB was difficult because no error messages were provided when the program crashed. For example, a simple error in a format statement would take longer to identify than running the program from within the Fortran debugger.
- An additional problem was that VB did not compile code to a simple standalone executable file but created a setup file that installed the program on the PC. Rewriting all the code in VB was also not an option, because 'number crunching' is not one of VB's strengths.
- The installation process was found to be unreliable – successful on some PCs but not on others.
- The rapid development studio supplied by Delphi made it easy to learn the new language and write applications fairly quickly. Delphi also provides an easy 'pick-and-paste' visual component library.

Appendix J

RMTI CASE STUDY

The relative moment tensor inversion without a reference mechanism is applied to three clusters of events recorded after a number of preconditioning blasts at the Blyvooruitzicht Gold Mine experimental site. This appendix is divided into four sections. The first is descriptive and summarises the technical and geological detail pertaining to the preconditioning site. In the second section, the recorded seismic data and processing techniques are described. The results of the relative inversion constitute the third section. Lastly, an interpretation based on the inversion results is given. In addition, a discussion regarding the source mechanisms of mining-induced tremors determined using absolute inversion methods and Dahm's relative inversion is presented.

J.1 SITE DESCRIPTION

The CSIR Division of Mining Technology has been investigating proactive measures for controlling rockbursts in deep-level gold mines for several years. An example of a technique aimed at combating rockbursts that occur at stope faces (face bursts) is preconditioning[1]. An experimental preconditioning site was selected at Blyvooruitzicht Gold Mine (BGM) where a strike-stabilising pillar was being extracted. The original function of the pillar was to form part of the regional support strategy for the deeper areas of the mine when longwall mining was the primary extraction method (Kullman *et al.*, 1996). However, with depleting reserves, the mine was forced to return to areas that were originally left behind. The objectives of this study were to monitor the effectiveness of preconditioning, and to gain insight into the failure mechanisms involved.

To achieve these objectives, the site was extensively monitored and geologically mapped. An analysis of the seismicity recorded from the site was used to assess the effectiveness of preconditioning. This provided an ideal environment to test the capabilities/limitations of the new inversion technique because the outcome of the inversion (in the form of a focal mechanism projection) could be compared to the fault slip inferred from the fracture mapping. This is one of the rare cases where the inversion results can be compared with reality.

[1] Preconditioning is a method of rockburst control. The technique makes use of large diameter blast holes drilled within fractured ground 5 m ahead of and parallel to the stope face. The blast results in the dissipation of strain energy from the rock mass immediately ahead of the working face by inducing slip along existing fractures without creating new fracture sets. The resulting stress transfer away from the working face creates a zone of low stress ground capable of absorbing energy from more distant events (Kullman *et al.*, 1996).

J.1.1 Microseismic network

The BGM 17-24W stope (Figure J.1) was situated at a depth in excess of 1900m below surface. The 40m wide stabilising pillar extended for 300m in the strike direction was being mined. A microseismic network was installed to monitor the site, consisting of three triaxial and three uniaxial geophone stations, arranged to encompass the area of interest. The layout of the network is shown in Figure J.1.

The three triaxial sites (labelled *P2i, P3i* and *P6i*) form a triangle around the unmined pillar area being monitored, providing complete azimuthal coverage for events occurring ahead of the face. The microseismic network was designed to have adequate sensitivity and location accuracy to allow for the identification of meaningful trends in the recorded seismicity associated with preconditioning. The network was able to record a minimum magnitude of $M \geq -2$ with a location error of less than 5m, for events with hypocentres within the network (Kullman *et al.*, 1996).

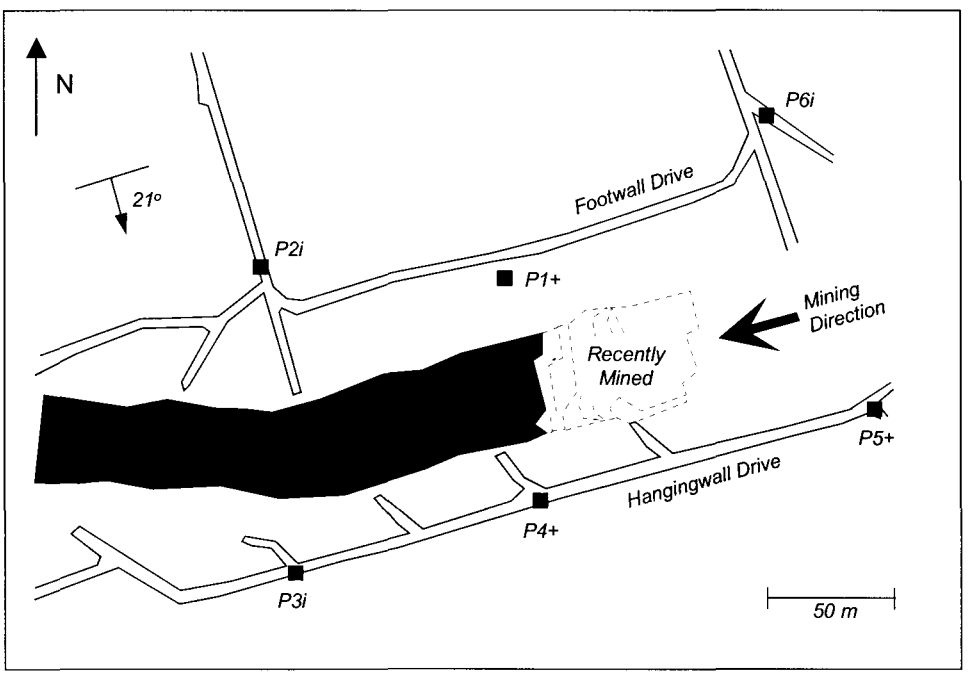

Figure J.1: Plan view of the 17-24W stope showing the layout of the microseismic system. The positions of uniaxial and triaxial geophone sites are indicated by 'P1+' and 'P2i' respectively (redrawn from Kullman et al., 1996).

J.1.2 Geological setting and fracture mapping

Kullman *et al.* (1996) identified six major fracture sets (Groups I to VI) on the basis of their dip and strike orientations (Figure J.2). The Group III faults[2] (steeply dipping shear zones) are thought to be the oldest as they are aligned with the regional strike of

[2] A note on the terminology. 'Fault' in this context refers to a fracture zone of geological origin along which there has been displacement, whereas the term 'fracture' is used to describe those induced by mining (pers. comm. Jager, 1998).

dykes and faults across the mine, suggesting that their initial development was due to large scale faulting.

Kullman *et al.* (1996) explain the fracture groups (excluding Group III) in terms of the stress history of the pillar. According to these workers, the low angle (dip ~35°) Group VI fractures associated with the Group III faults, formed during the shearing of the Group III faults. The Group I and II pillar-parallel fractures with steep (~ 85°) and intermediate (~40°) dips respectively are thought to have developed after Group III, as a result of mining the surrounding ground. The Group II fractures later dilated as the pillar slowly failed at the edges. The steeply dipping (~85°) Group IV fractures, which lie parallel to the panel faces formed in response to stress changes caused by the approaching mining. Group V fractures (dip ~ 80°) are thought to be a result of failure of the stope hangingwall in the broken rock mass immediately ahead of the stope face.

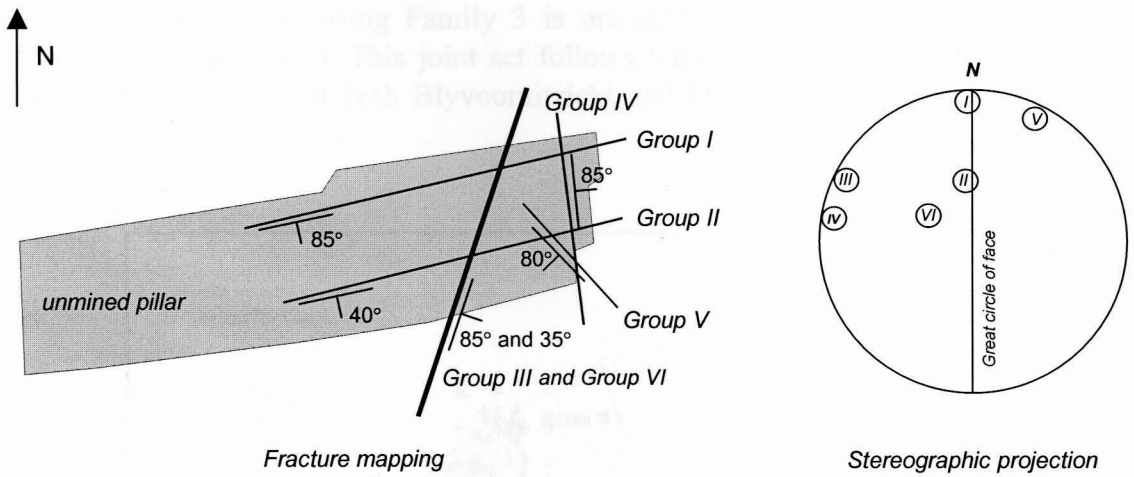

Figure J.2: Orientations of the six major fracture sets (Groups I to VI) identified at the BGM 17-24W experimental site. Fracture mapping plan view shows orientations with respect to pillar geometry. Stereographic projection (lower hemisphere) shows poles to fracture sets (redrawn from Kullman et al., 1996).

Kullman *et al.* (1996) found evidence that the Group III faults were reactivated by preconditioning. Initially, the Group III faults were extensional (indicated by the presence of void-filling minerals such as vein quartz and calcite). The presence of white crushed quartz (pers.comm. Grodner, 1998) and offset joints indicates that there is a later component of shear (parallel to the overall face shape) on the extensional fractures. The Group III faults are thought to have been reactivated as shears by the preconditioning blasts, which also sheared some of the Group IV and VI fractures.

J.2 SEISMIC DATA AND PROCESSING

During the 39 month period of mining at the BGM 17-24W site, a total of 51 preconditioning blasts were detonated. A number of seismic events occurred in response to the blasting and were recorded by the Portable Seismic System (PSS). A

total of 115 events were recorded over a time period of three and half months (3/1/95 to 17/4/95) and range in magnitude from -1.4 to 0.

J.2.1 Seismic cluster identification

The event locations determined using conventional location methods show a scattered event distribution with no obvious trends (Figure J.3). Application of the relocation procedure (HRRL) revealed three distinct families (or clusters) of events with similar waveforms. Figure J.4 shows the clusters, given the imaginative names of Family 1, Family 2, and Family 3.

The clusters of events could be correlated spatially with the fracture sets identified by the fracture mapping. Family 1 is located parallel to the long axis of the pillar (Group I fracture set), and Family 2 parallel to the active mining face (Group IV). The potentially more interesting Family 3 is oriented parallel to a pervasive joint set (Group III fracture set). This joint set follows the prominent structural direction of NNE/SSW observed at both Blyvooruitzicht and Deelkraal (pers. comm. Grodner, 1998).

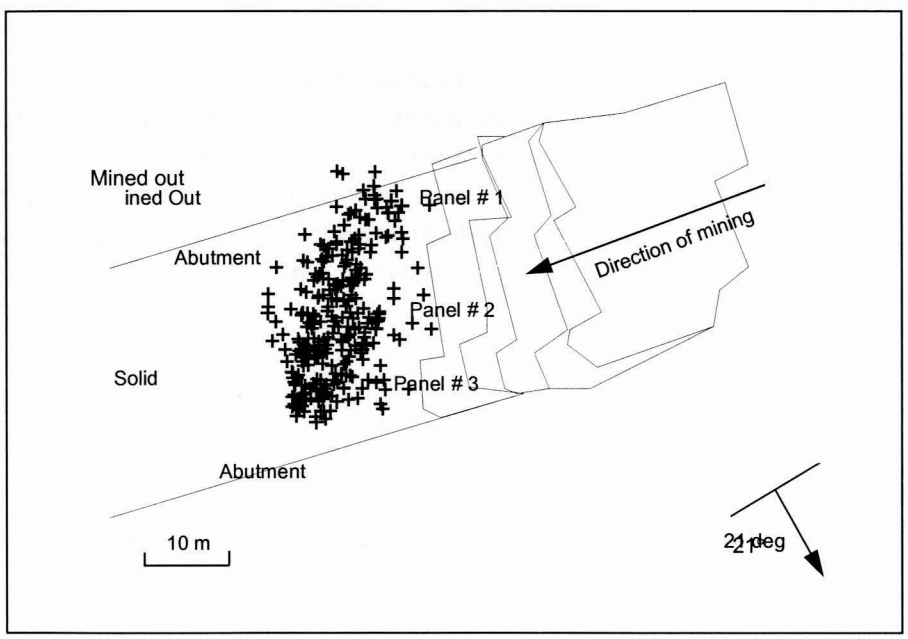

Figure J.3: Plan view of the BGM 17-24W stabilising pillar and P and S-wave seismic event locations.

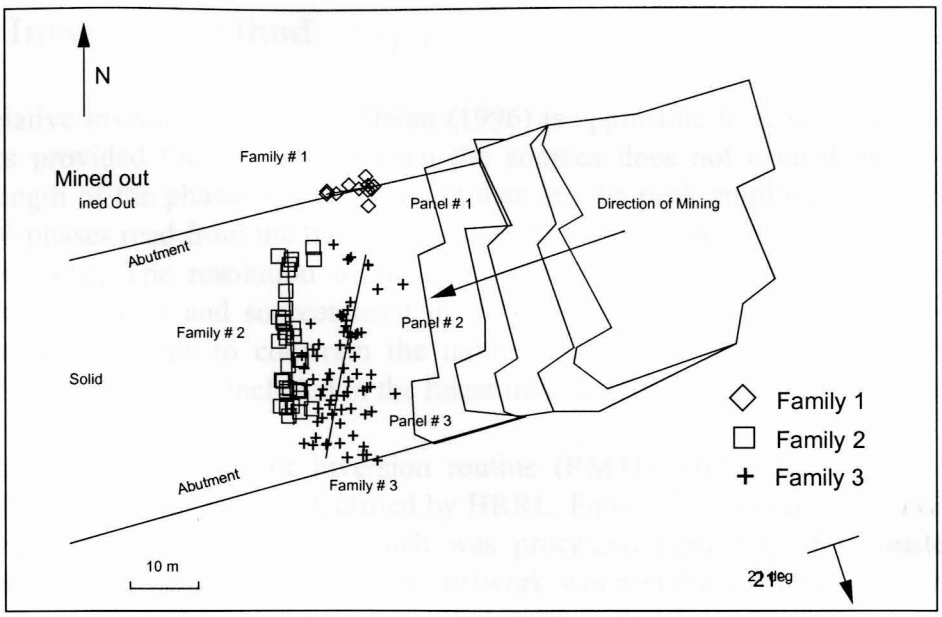

Figure J.4: Plan view of P and S-wave seismic locations after the application of the HRRL procedure.

J.2.2 Data description

For this study, 58 sources with high signal-to-noise ratios were selected from a total of 115 recorded events. Table J.1 summarises the number of events in each family used in the relative inversion. Almost 70% of the recorded events in Family 3 were rejected due to the excessive noise introduced when one of the three triaxial geophone sites ceased to function properly. Since the relative inversion requires amplitude readings of the P, SH and SV-phases, only the waveforms recorded at all of the triaxial sites are used in this study.

Table J.1: Number and time span of events used in relative inversion.

Cluster	Total no. recorded events	No. events with high signal/noise	Recording time period
Family 1	9	5	3/1/95 – 22/1/95
Family 2	34	30	29/3/95 – 17/4/95
Family 3	72	23	4/1/95 – 23/1/95

Many of the waveforms showed clear impulsive compressional and shear wave arrivals and variable P-wave polarities. The P-wave polarity measurements were used as an additional constraint in the relative moment tensor inversion. The peak P, SH and SV-phase amplitudes were measured from the time-integrated displacement traces to which a low-pass filter had been applied (Figure J.5).

J.2.3 Inversion method

The relative inversion method of Dahm (1996) is applicable to seismic sources from clusters provided the spacing between the sources does not exceed the dominant wavelength of the phases used. The input data are the peak amplitudes of the P, SH and SV-phases read from the traces of at least two sources, recorded at a minimum of three stations. The resolution of the moment tensor components depends on the number of stations and sources used in the inversion. Using both P and S-phases simultaneously helps to constrain the moment tensor components, since different condition equations are included in the linear inversion problem.

The relative moment tensor inversion routine (RMTI) written by the author was applied to each event family identified by HRRL. Family 3 was divided into two sub-clusters (Figure J.3b), each of which was processed separately. Sub-cluster 1 is located within the plane of the seismic network whereas the events comprising sub-cluster 2 are grouped approximately 30m below the network.

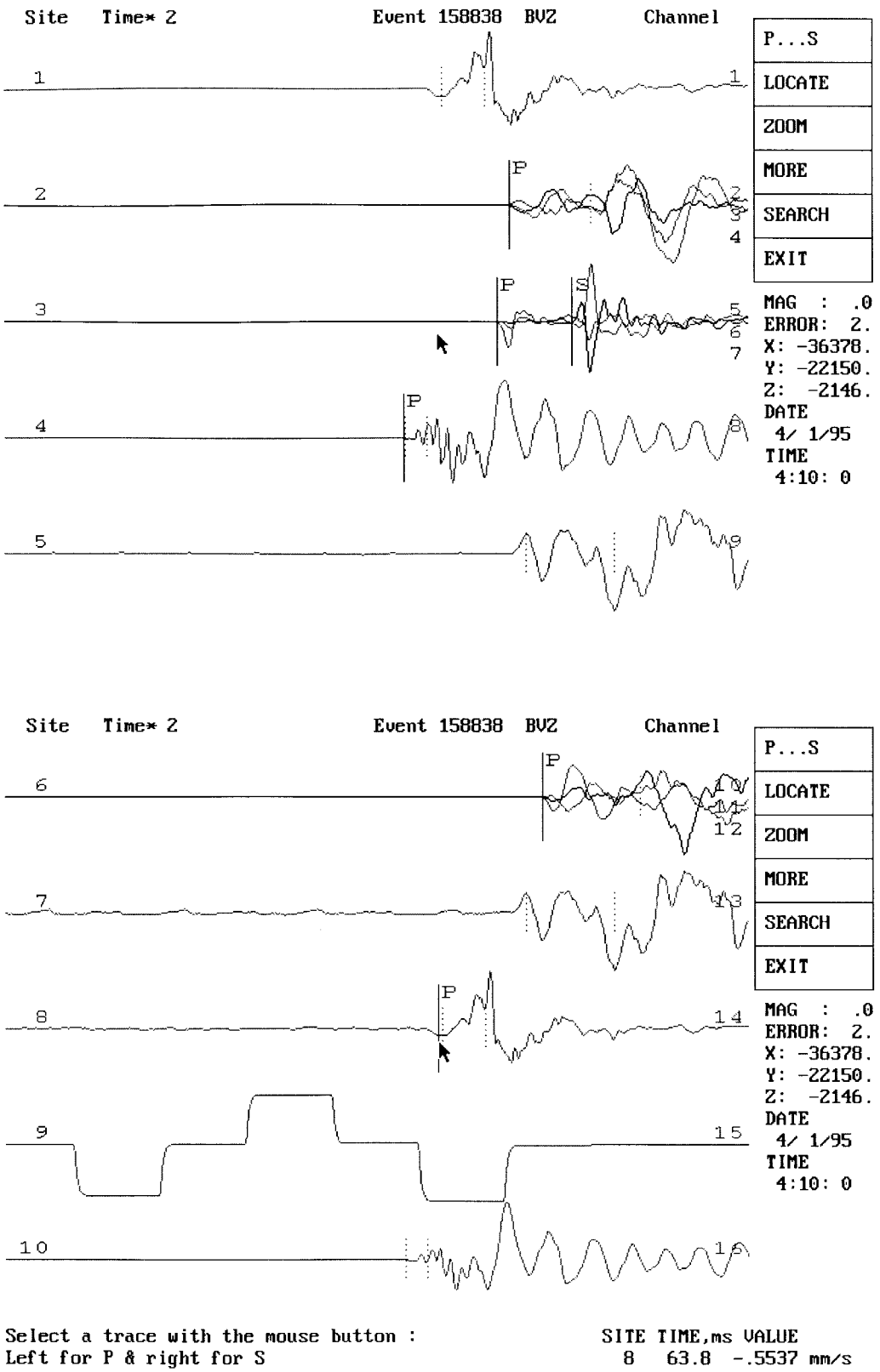

Figure J.5: An example of amplitude readings of three-component traces from source 158838 recorded at stations P3i, P3i and P6i.

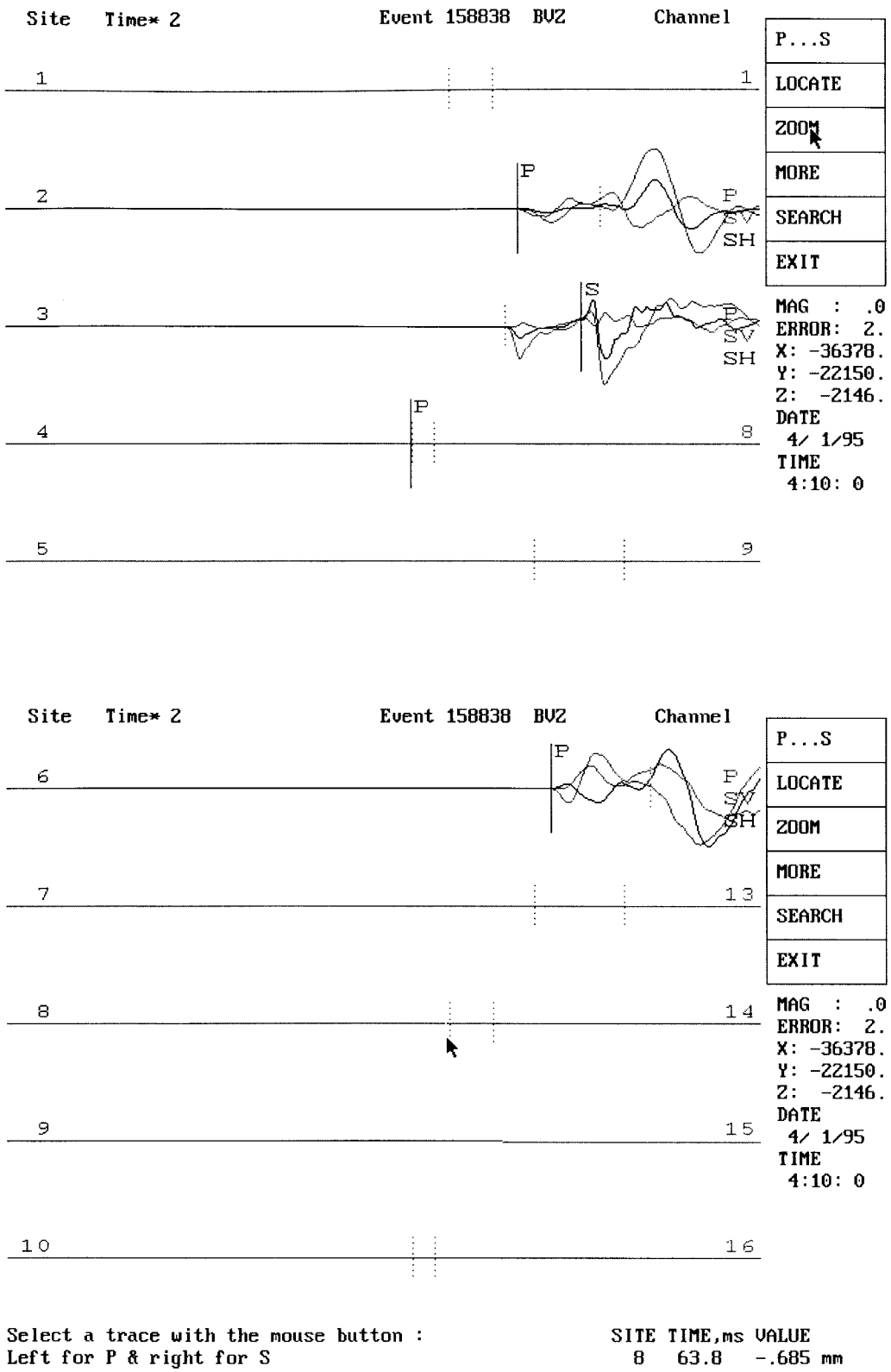

Figure J.6: Time-integrated three-component traces from source 158838 recorded at stations P3i, P3i and P6i.

J.3 RELATIVE INVERSION RESULTS

The results of the relative inversion are given as Cartesian moment tensor components (M_{11}, M_{22}, M_{33} etc., defined in Equation 4.13), where the indices refer to the geographical coordinate system (Tables J.2, J.3 and J.4). In addition, the results are given using the components defined by Dahm (m_{1i}, m_{2i}, m_{3i} etc., defined in Equation 4.12) where m_{1i} and m_{2i} represent the 2π-periodic (with azimuth) strike-slip radiation pattern of the source i; m_{3i} and m_{4i} represent the π-periodic dip-slip radiation pattern; m_{5i} represents the pattern of the vertical CLVD component, and m_{6i} represents the isotropic source component (Tables J.5, J.6 and J.7).

To facilitate interpretation of the moment tensor, radiation patterns for selected moment tensor components and a number of source parameters are calculated for each event in each family.

J.3.1 Radiation patterns and fault-plane solutions

The P-wave radiation patterns for all the components (i.e. deviatoric, double-couple, strike-slip and dip-slip components) are computed for Family 1 for illustration purposes (Figure J.7). However, only the deviatoric and double-couple patterns are given for Families 2 and 3 (Figures J.8 and J.9) because the strike-slip and dip-slip components do not give any additional insights.

A fault-plane solution was obtained by fitting two orthogonal planes to the P-wave double-couple radiation pattern. Tables J.8, J.9 and J.10 summarise the fault plane solutions for each family. The fracture mapping (Figure J.2) was used to distinguish the fault plane from the auxiliary plane.

J.3.2 Source parameters

The following source parameters are computed:

- The relative strength *MO%* between two sources (Equation 4.40) and expressed as a percentage (Dahm, 1996).

- The deviation ε of the seismic source from the model of pure double-couple (Equation 2.43) where $\varepsilon = 0$ for a pure double-couple source, and $\varepsilon = 0.5$ for a pure CLVD (Dziewonski *et al.*, 1981).

- The isotropic source component *ISO%* (Equation 2.44) expressed as a percentage (Silver & Jordan, 1982).

In addition to the source parameters, the local event magnitude M is given (Tables J.8, J.9 and J.10).

Table J.2: Cartesian moment tensor components for Family 1, BGM 24-17W site.

Event no.	M_{11}	M_{22}	M_{33}	M_{12}	M_{13}	M_{23}
158819	0.548	0.627	0.889	-0.448	1.120	1.010
158822	0.104	0.094	-0.124	-0.142	0.423	0.371
158957	0.196	0.205	0.244	-0.161	0.416	0.358
159126	0.102	0.162	0.173	-0.102	0.215	0.379
160442	0.123	0.130	-0.121	-0.058	0.166	0.237

Table J.3: Cartesian moment tensor components for Family 2, BGM 24-17W site.

Event no.	M_{11}	M_{22}	M_{33}	M_{12}	M_{13}	M_{23}
166232	0.031	0.237	0.250	0.235	0.405	0.085
166233	-0.307	0.402	0.647	0.501	0.804	-0.083
166240	-0.001	0.325	0.284	0.447	0.721	0.119
166490	0.125	0.216	0.107	0.166	0.374	0.131
166504	-0.048	0.150	0.272	0.115	0.314	0.066
166578	0.001	0.135	0.167	0.104	0.139	0.015
166596	-0.095	0.196	0.159	0.103	0.677	0.270
166646	0.127	0.185	0.106	0.133	0.338	0.124
166663	-0.010	0.146	0.227	0.115	0.292	0.065
166673	0.016	0.164	0.144	0.150	0.268	0.069
166939	-0.235	0.264	0.347	0.146	0.673	0.193
166945	0.002	0.176	0.407	0.144	0.366	-0.020
166986	0.038	0.170	0.140	0.133	0.254	0.081
167136	0.028	0.255	0.132	0.232	0.472	0.161
167211	0.035	0.173	0.200	0.159	0.279	0.066
167230	0.026	0.162	0.144	0.152	0.315	0.100
167243	0.056	0.146	0.121	0.152	0.309	0.101
167248	0.078	0.147	0.111	0.106	0.260	0.080
167268	0.057	0.229	0.168	0.213	0.435	0.130
167326	-0.024	0.170	0.133	0.169	0.291	0.077
167330	-0.087	0.183	0.239	0.142	0.407	0.125
167342	-0.021	0.218	0.159	0.167	0.455	0.167
167347	-0.023	0.418	0.187	0.405	0.474	0.168
167350	-0.223	0.786	1.450	0.708	1.313	-0.109
167380	-0.006	0.108	0.141	0.061	0.309	0.123
167429	-0.045	0.125	0.162	0.028	0.295	0.080
167430	0.109	0.198	0.122	0.146	0.394	0.137
167444	0.087	0.231	0172	0.223	0.523	0.115
167447	-0.002	0.192	0209	0.152	0.324	0.090
167509	-0.405	0.705	1.275	0.635	1.238	0.006

Table J.4: Cartesian moment tensor components for Family 3, BGM 24-17W Site.

Event no.	M_{11}	M_{22}	M_{33}	M_{12}	M_{13}	M_{23}
Sub-cluster 1						
158887	-0.117	0.147	1.576	0.066	0.440	0.107
158892	-0.088	0.107	0.468	0.045	0.114	0.030
159052	-0.086	0.094	2.228	0.142	0.532	-0.050
159079	-0.082	0.138	0.938	0.064	0.402	0.210
159255	-0.135	0.422	4.790	0.379	1.113	0.495
159348	-0.225	0.236	3.040	0.175	0.686	0.229
159349	-0.369	0.240	2.331	0.249	0.628	0.303
159364	-0.253	0.271	1.560	0.213	0.583	0.229
159406	-0.020	0.084	0.363	0.085	0.237	0.112
159491	-0.135	0.169	0.227	0.138	0.176	0.173
159795	-0.149	0.235	1.972	0.112	0.612	0.227
159956	-0.131	0.177	0.911	0.157	0.319	0.182
160450	-0.047	0.117	1.388	0.111	0.398	0.140
Sub-cluster 2						
158838	-1.349	0.896	1.239	-0.346	4.384	-0.924
158890	-0.041	0.279	0.122	0.029	0.587	0.096
158968	-0.167	0.095	0.409	0.106	0.332	-0.043
159161	-0.243	0.134	0.374	0.145	0.368	-0.059
159162	-0.195	0.122	0.633	0.156	0.704	-0.033
159299	-0.054	0.085	0.461	0.077	0.312	-0.059
159378	-0.061	0.143	-0.061	0.052	0.459	-0.004
159483	0.010	0.167	0.346	0.021	0.330	-0.003
159487	-0.077	0.090	0.564	0.098	0.367	-0.081
159492	-0.145	0.155	0.644	0.140	0.677	-0.055

Table J.5: Dahm's moment tensor components for Family 1, BGM 24-17W site.

Event no.	m_{1i}	m_{2i}	m_{3i}	m_{4i}	m_{5i}	m_{6i}
158819	0.040	-0.448	1.120	1.010	-0.101	0.688
158822	-0.005	-0.142	0.423	0.371	0.074	0.025
158957	0.004	-0.161	0.416	0.358	-0.015	0.215
159126	0.030	-0.102	0.215	0.379	-0.014	0.145
160442	0.003	-0.058	0.166	0.237	0.083	0.044

Table J.6: Dahm's moment tensor components for Family 2, BGM 24-17W site.

Event no.	m_{1i}	m_{2i}	m_{3i}	m_{4i}	m_{5i}	m_{6i}
166232	0.103	0.235	0.405	0.085	-0.039	0.173
166233	0.354	0.501	0.804	-0.083	-0.200	0.247
166240	0.163	0.447	0.721	0.119	-0.041	0.202
166490	0.045	0.166	0.374	0.131	0.021	0.149
166504	0.099	0.115	0.314	0.066	-0.074	0.125
166578	0.067	0.104	0.139	0.015	-0.033	0.101
166596	0.146	0.103	0.677	0.270	-0.036	0.087
166646	0.029	0.133	0.338	0.124	0.017	0.139
166663	0.078	0.115	0.292	0.065	-0.053	0.121
166673	0.074	0.150	0.268	0.069	-0.018	0.108
166939	0.249	0.146	0.673	0.193	-0.111	0.125
166945	0.087	0.144	0.366	-0.020	-0.106	0.195
166986	0.066	0.133	0.254	0.081	-0.012	0.116
167136	0.114	0.232	0.472	0.161	0.003	0.138
167211	0.069	0.159	0.279	0.066	-0.032	0.136
167230	0.068	0.152	0.315	0.100	-0.017	0.111
167243	0.045	0.152	0.309	0.101	-0.007	0.108
167248	0.034	0.106	0.260	0.080	0.000	0.112
167268	0.086	0.213	0.435	0.130	-0.009	0.151
167326	0.097	0.169	0.291	0.077	-0.020	0.093
167330	0.135	0.142	0.407	0.125	-0.064	0.111
167342	0.119	0.167	0.455	0.167	-0.020	0.118
167347	0.220	0.405	0.474	0.168	0.004	0.194
167350	0.505	0.708	1.313	-0.109	-0.390	2.671
167380	0.057	0.061	0.309	0.123	-0.030	0.081
167429	0.085	0.028	0.295	0.080	-0.041	0.081
167430	0.045	0.146	0.394	0.137	0.010	0.143
167444	0.072	0.223	0.523	0.115	-0.004	0.163
167447	0.097	0.152	0.324	0.090	-0.038	0.133
167509	0.555	0.635	1.238	0.006	-0.375	0.525

Table J.7: Dahm's moment tensor components for Family 3, BGM 24-17W site.

Event no.	m_{1i}	m_{2i}	m_{3i}	m_{4i}	m_{5i}	m_{6i}
Sub-cluster 1						
158887	0.132	0.066	0.440	0.107	-0.520	0.535
158892	0.097	0.045	0.114	0.030	-0.153	0.162
159052	0.090	0.142	0.532	-0.050	-0.741	0.745
159079	0.110	0.064	0.402	0.210	-0.303	0.331
159255	0.279	0.379	1.113	0.495	-1.549	1.692
159348	0.230	0.175	0.686	0.229	-1.012	1.017
159349	0.304	0.249	0.628	0.303	-0.798	0.734
159364	0.262	0.213	0.583	0.229	-0.517	0.526
159406	0.052	0.085	0.237	0.112	-0.110	0.142
159491	0.152	0.138	0.176	0.173	-0.070	0.087
159795	0.192	0.112	0.612	0.227	-0.643	0.686
159956	0.154	0.157	0.319	0.182	-0.296	0.319
160450	0.082	0.111	0.398	0.140	-0.451	0.486
Sub-cluster 2						
158838	1.122	-0.346	4.384	-0.924	-0.489	0.262
158890	0.160	0.029	0.587	0.096	-0.001	0.120
158968	0.131	0.106	0.332	-0.043	-0.148	0.112
159161	0.188	0.145	0.368	-0.059	-0.143	0.088
159162	0.158	0.156	0.704	-0.033	-0.223	0.187
159299	0.070	0.077	0.312	-0.059	-0.148	0.164
159378	0.102	0.052	0.459	-0.004	-0.034	0.007
159483	0.079	0.021	0.330	-0.003	-0.086	0.174
159487	0.084	0.098	0.367	-0.081	-0.186	0.192
159492	0.150	0.140	0.677	-0.05	-0.213	0.218

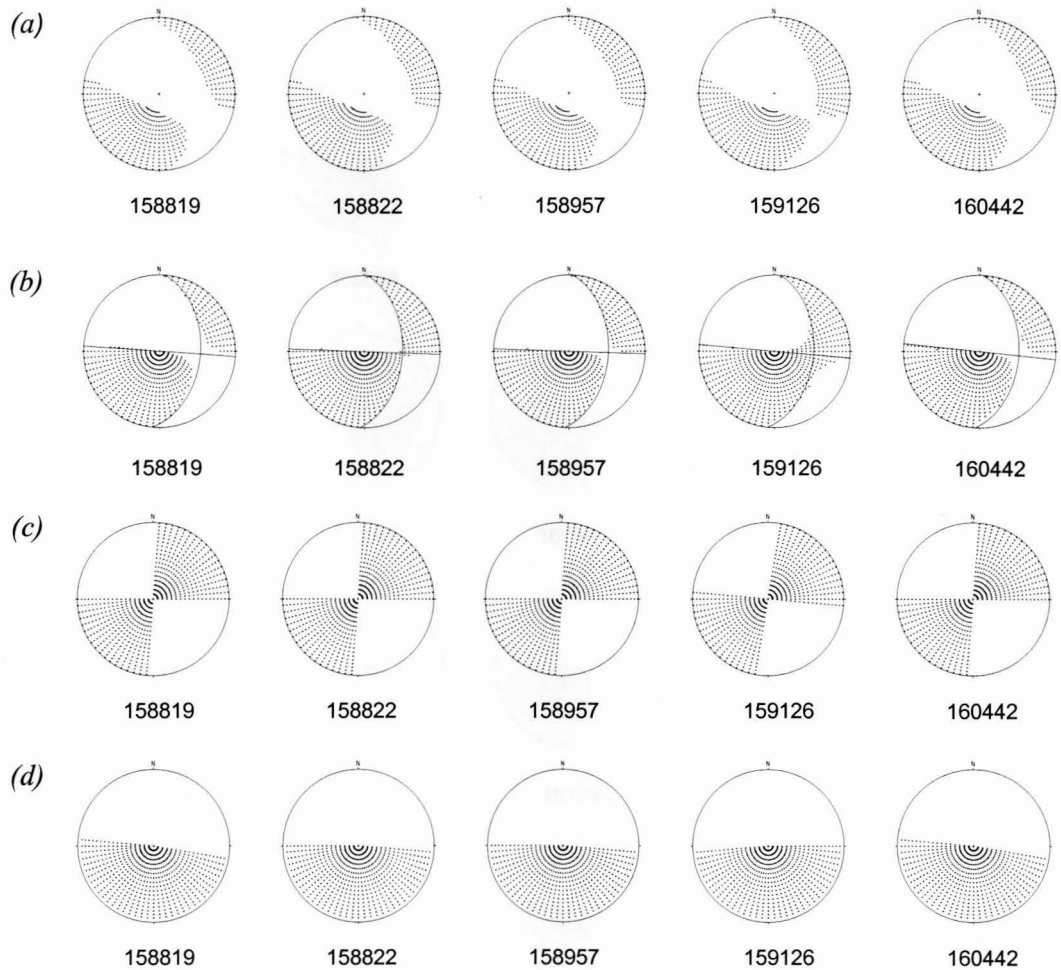

Figure J.7: P-wave radiation patterns for (a) deviatoric, (b) double-couple (strike-slip and dip-slip), (c) strike-slip, (d) dip-slip moment tensor components resulting from the relative inversion of 5 events of Family 1. Fault-plane solutions are fitted to the double-couple radiation patterns. + represents compressional P-wave arrival. Event numbers are given below each pattern.

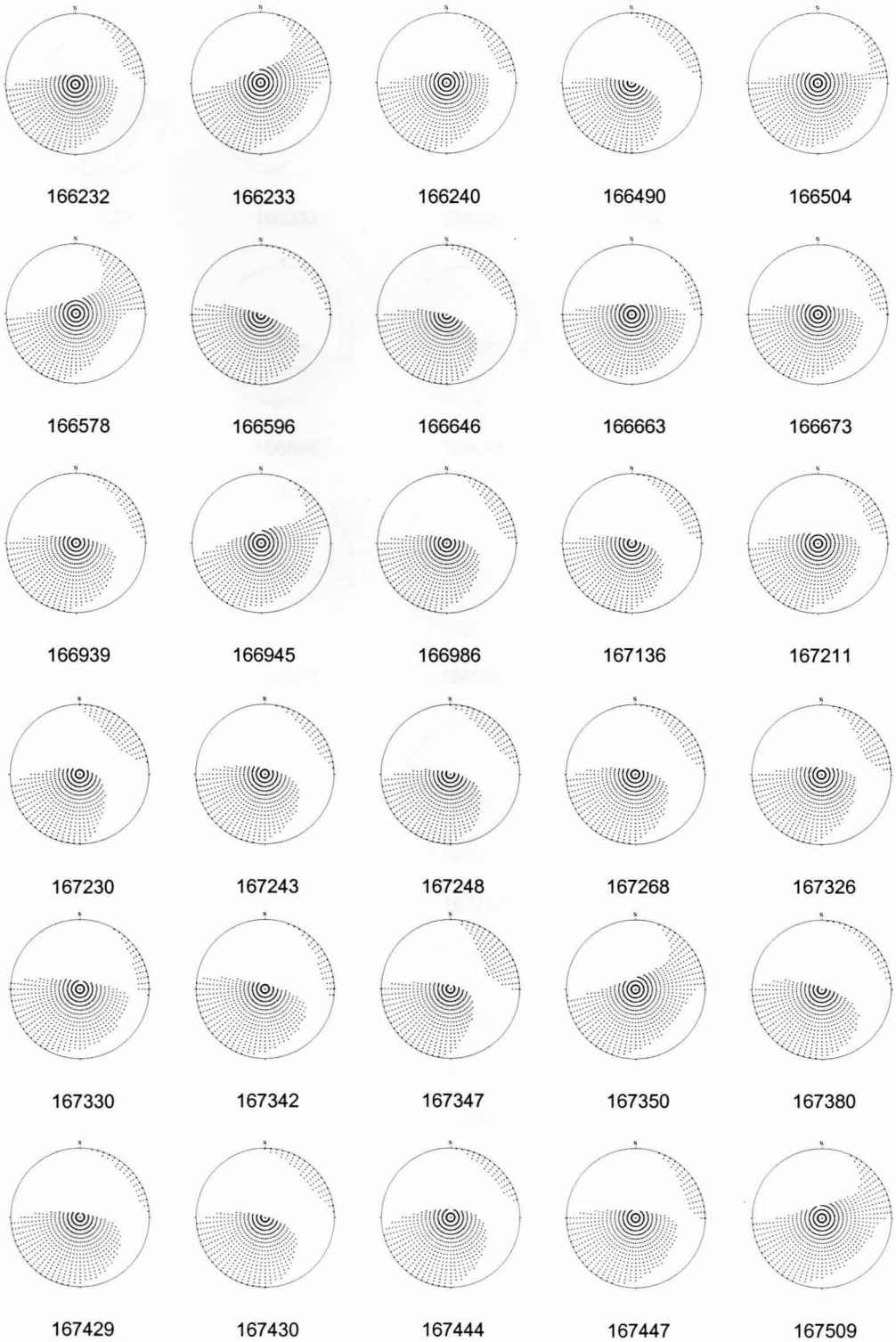

Figure J.8(a): P-wave radiation patterns for deviatoric moment tensor components resulting from the relative inversion of Family 2. + represents compressional P-wave arrival. Event numbers are given below each pattern.

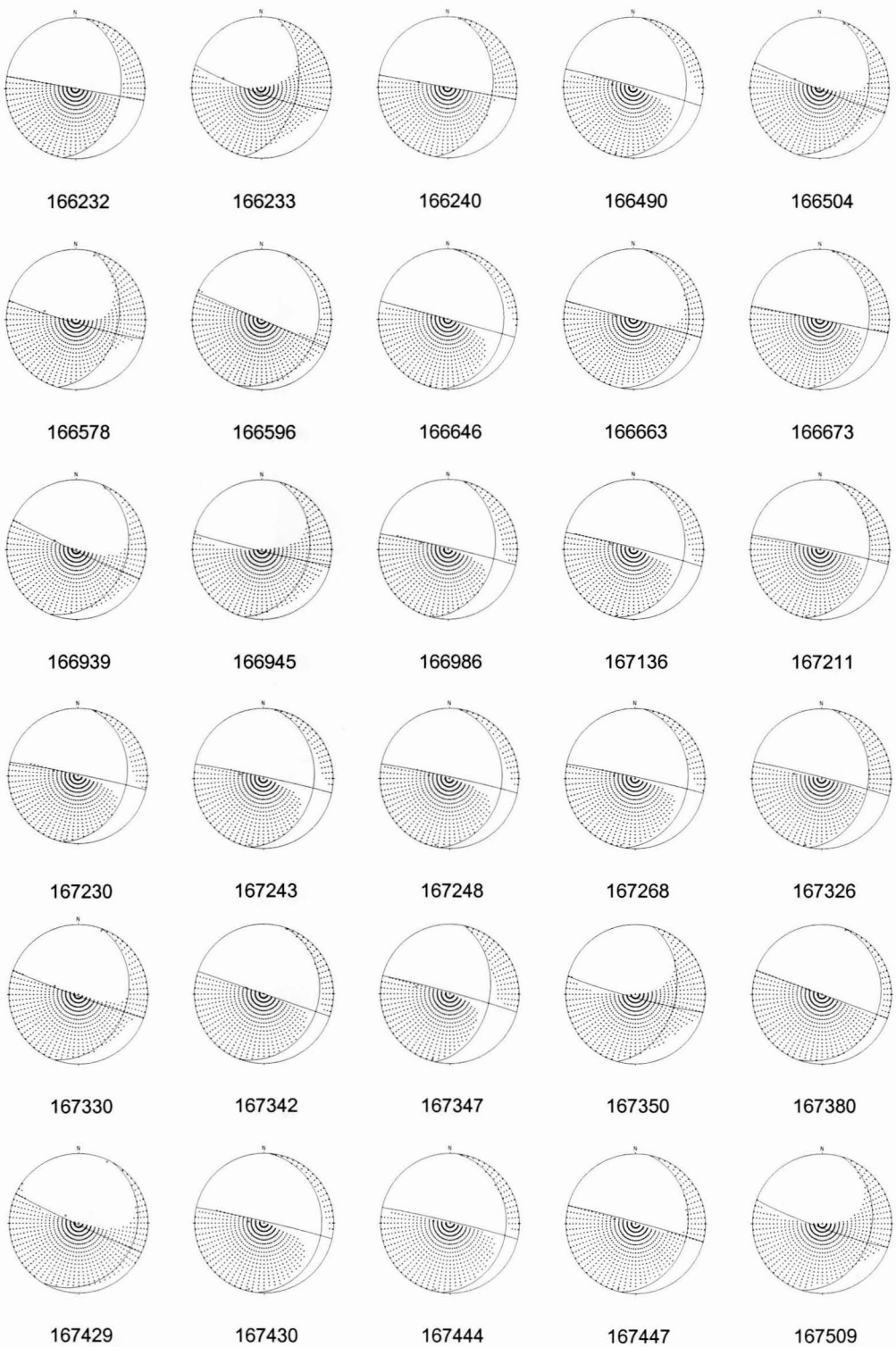

Figure J.8(b): P-wave radiation patterns and fault-plane solutions for double-couple (strike-slip and dip-slip) moment tensor components resulting from the relative inversion of Family 2. + represents compressional P-wave arrival. Event numbers are given below each pattern.

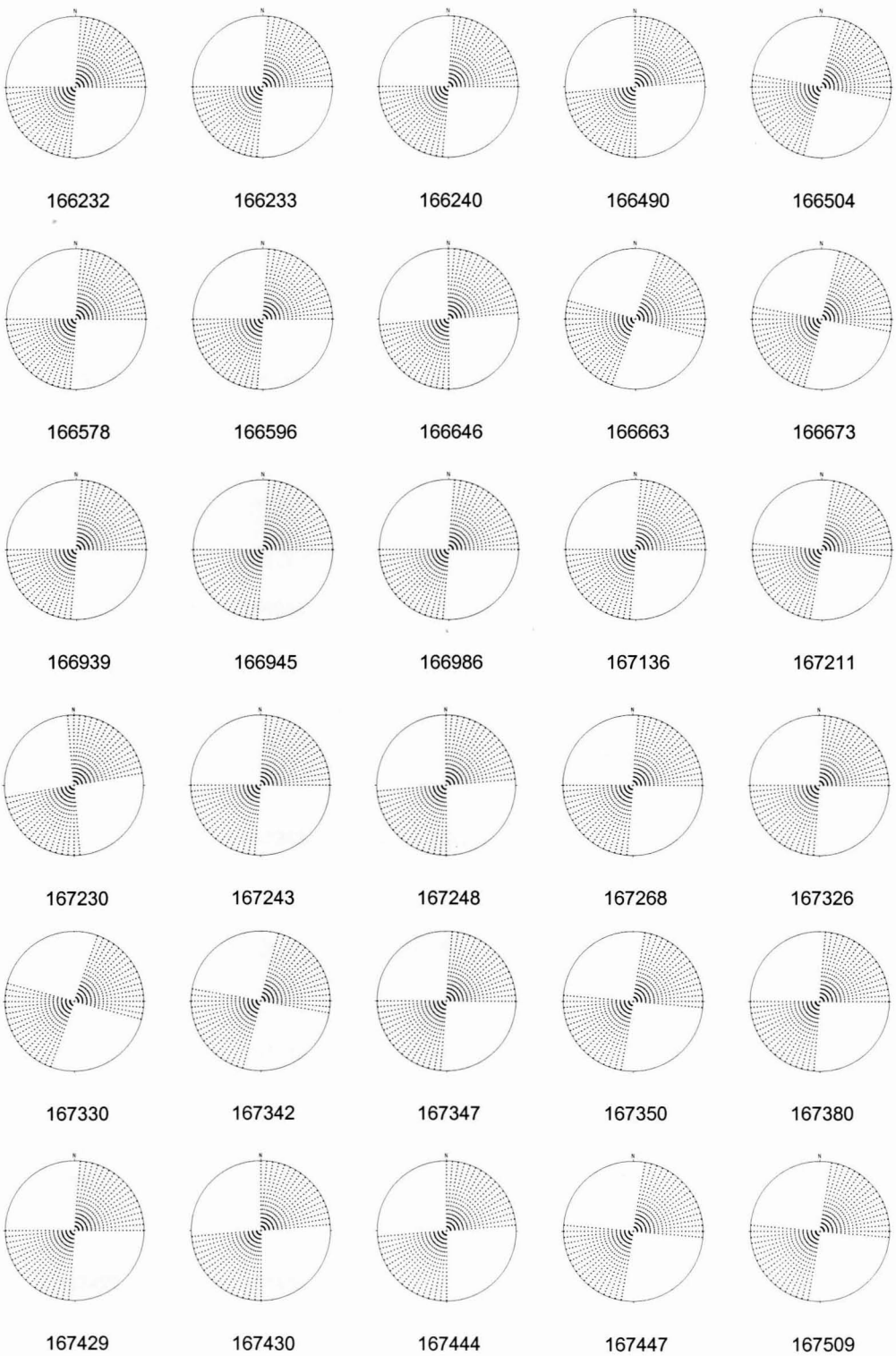

Figure J.8(c): P-wave radiation patterns for strike-slip moment tensor components resulting from the relative inversion of Family 2. + represents compressional P-wave arrival. Event numbers are given below each pattern.

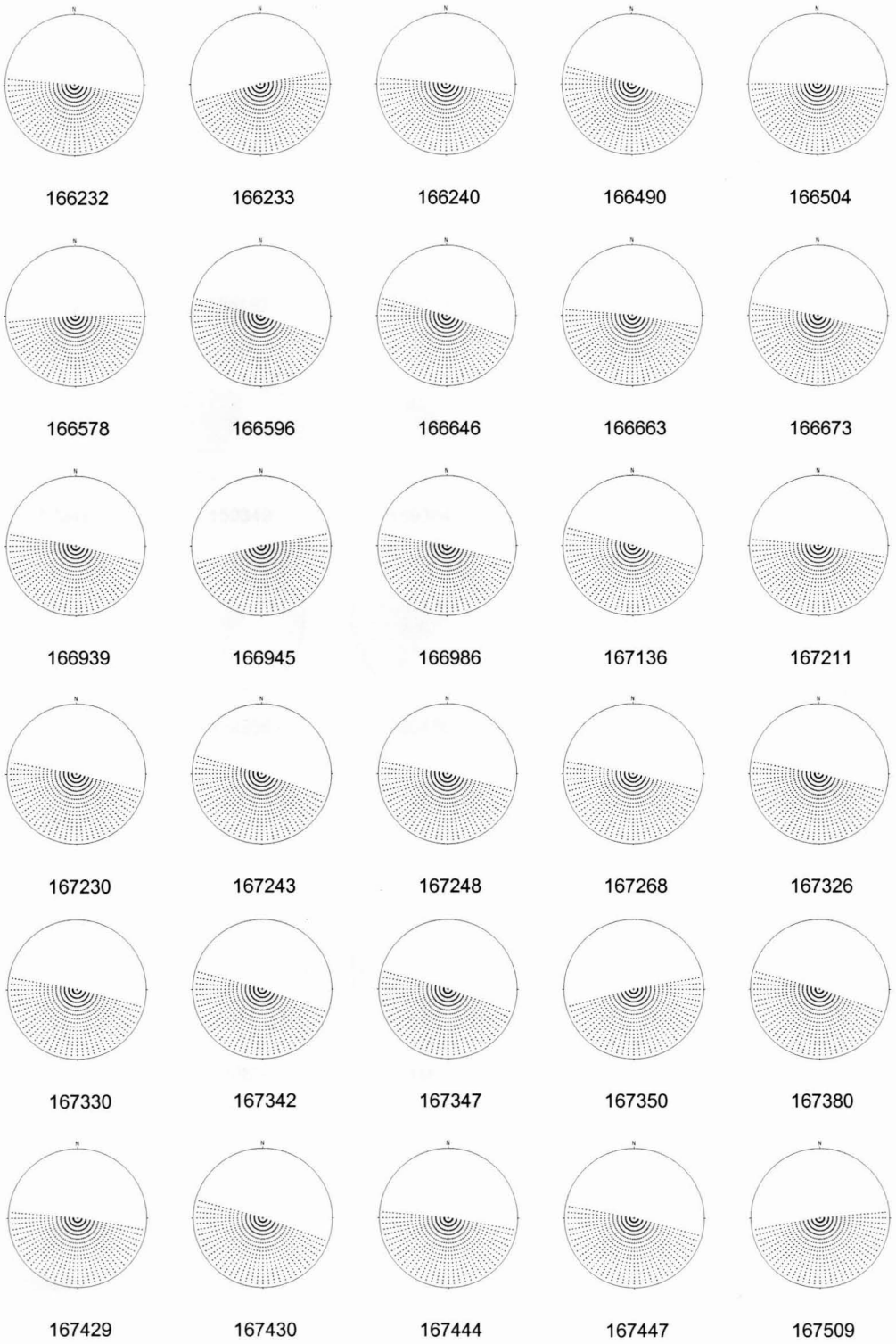

Figure J.8(d): P-wave radiation patterns for dip-slip moment tensor components resulting from the relative inversion of Family 2. + represents compressional P-wave arrival. Event numbers are given below each pattern.

Sub-cluster 1

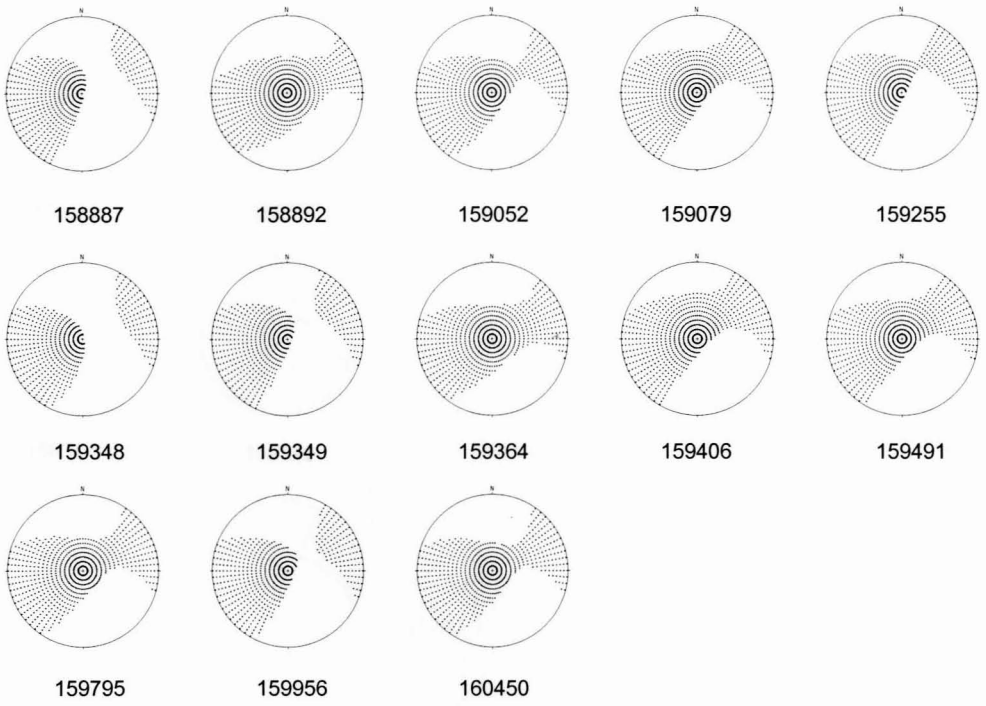

Sub-cluster 2

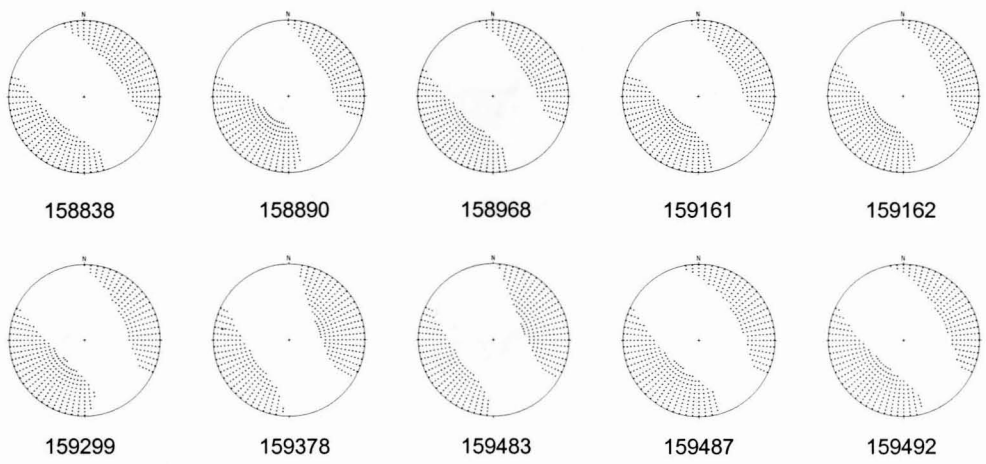

Figure J.9(a): P-wave radiation patterns for deviatoric moment tensor components resulting from the relative inversion of two sub-clusters of events within Family 3. Sub-cluster 2 is located 30 m below the plane of the seismic network. + represents compressional P-wave arrival. Event numbers are given below each pattern.

Sub-cluster 1

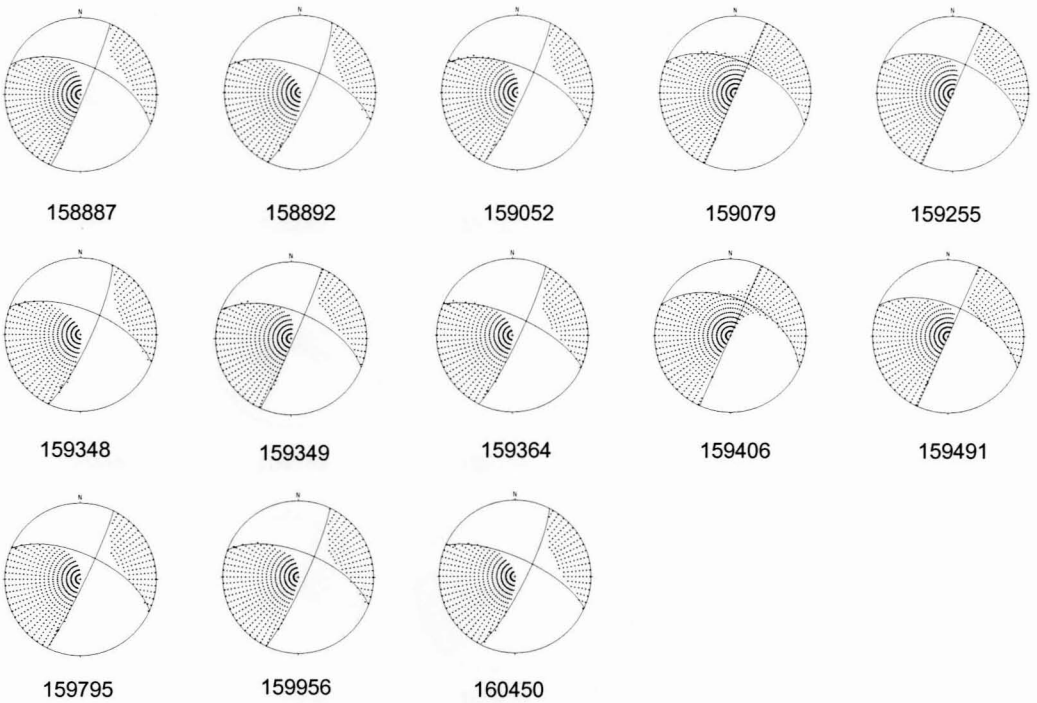

Sub-cluster 2

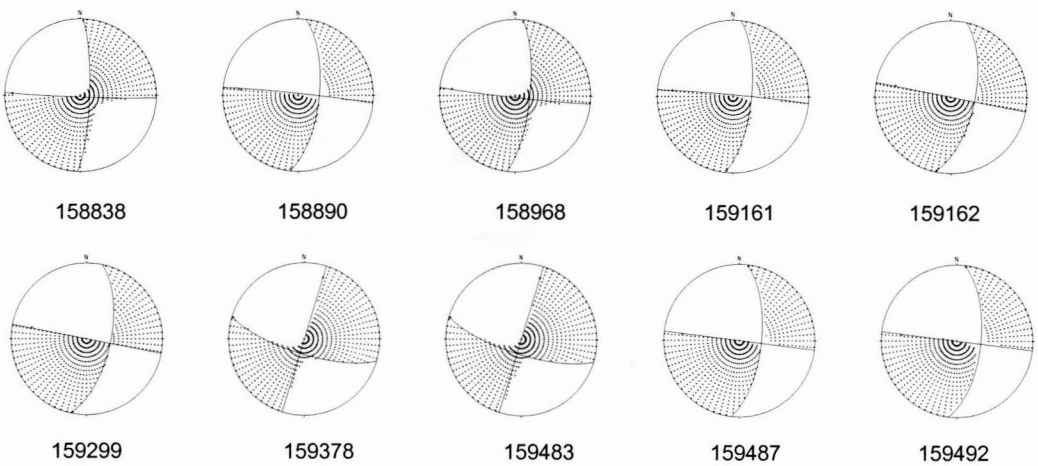

Figure J.9(b): P-wave radiation patterns and fault-plane solutions for double-couple (strike-slip and dip-slip) moment tensor components resulting from the relative inversion of two sub-clusters of events within Family 3. Sub-cluster 2 is located 30 m below the plane of the seismic network. + represents compressional P-wave arrival. Event numbers are given below each pattern.

Sub-cluster 1

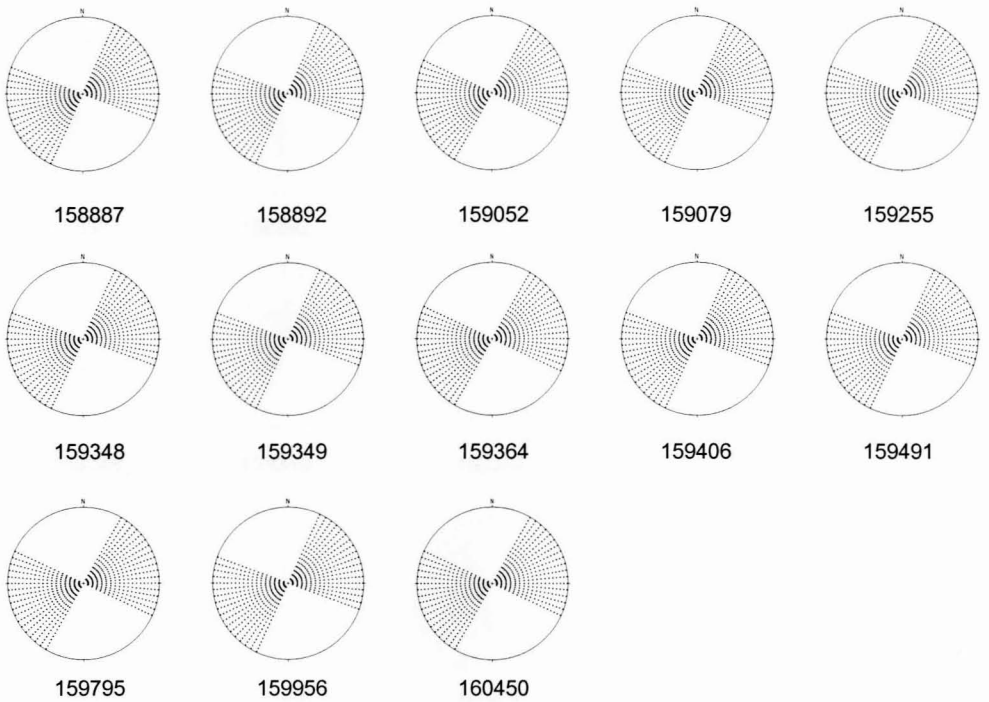

Sub-cluster 2

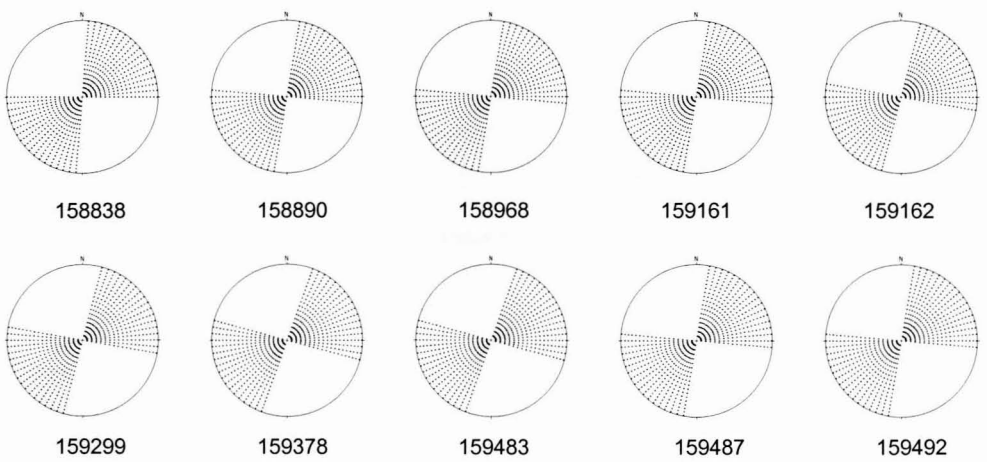

Figure J.9(c): P-wave radiation patterns for strike-slip moment tensor components resulting from the relative inversion of two sub-clusters of events within Family 3. Sub-cluster 2 is located 30 m below the plane of the seismic network. + represents compressional P-wave arrival. Event numbers are given below each pattern.

Sub-cluster 1

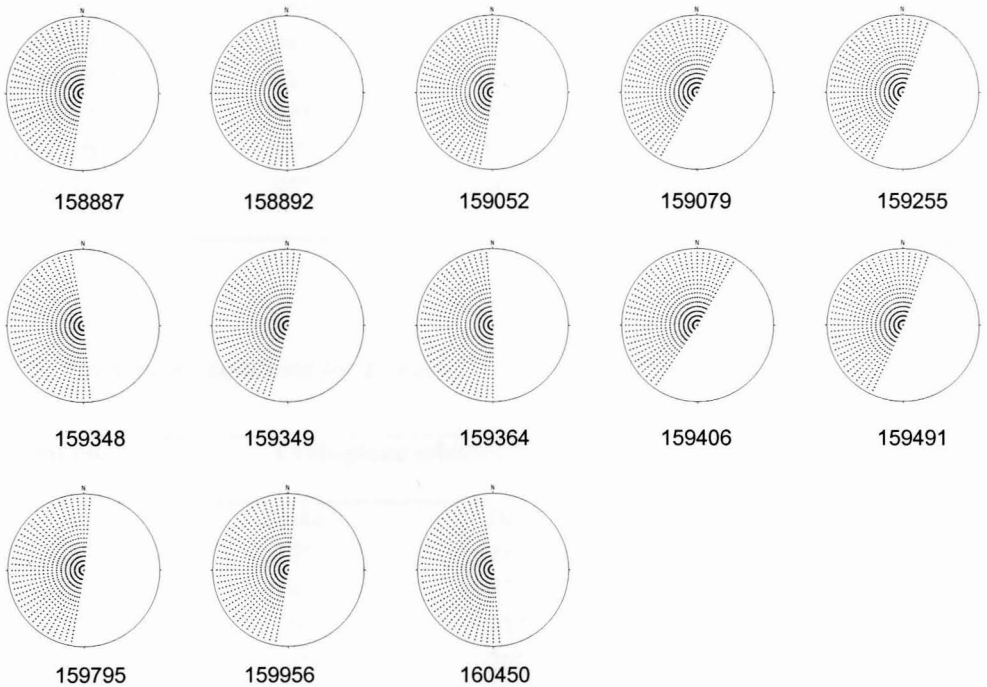

Sub-cluster 2

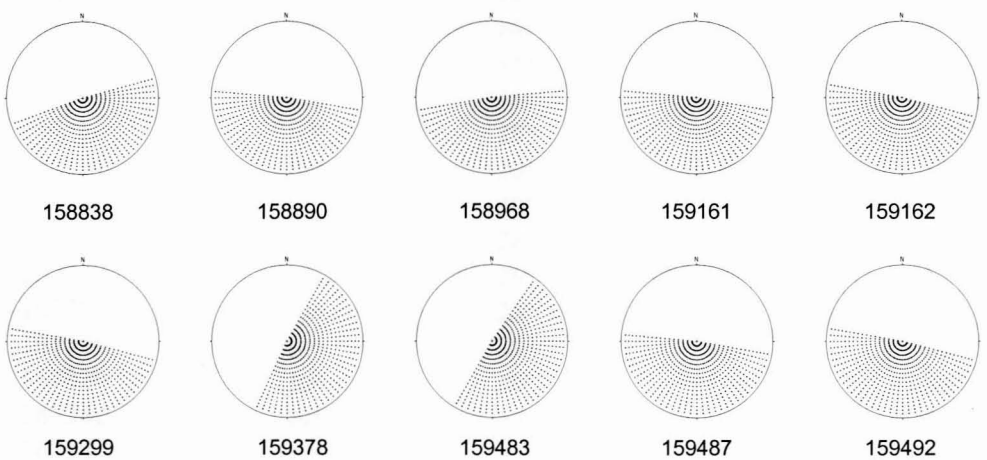

Figure J.9(d): P-wave radiation patterns for dip-slip moment tensor components resulting from the relative inversion of two sub-clusters of events within Family 3. Sub-cluster 2 is located 30 m below the plane of the seismic network. + represents compressional P-wave arrival. Event numbers are given below each pattern.

Table J.8: Fault-plane solutions for Family 1, BGM 17-24W site.

Event no.	Fault-plane solution 1		Fault-plane solution 2	
	Strike	*Dip*	*Strike*	*Dip*
158819	94°	90°	5°	45°
158822	92°	90°	3°	48°
158957	92°	90°	3°	47°
159126	95°	90°	5°	47°
160442	95°	90°	3°	47°

Table J.9: Fault-plane solutions for Family 2, BGM 17-24W site.

Event no.	Fault-plane solution 1		Fault-plane solution 2	
	Strike	*Dip*	*Strike*	*Dip*
166232	10°	35°	100°	90°
166233	14°	47°	109°	83°
166240	10°	35°	100°	90°
166490	8°	25°	285°	88°
166504	19°	31°	111°	88°
166578	15°	39°	106°	86°
166596	21°	20°	113°	89°
166646	5°	20°	285°	89°
166663	10°	22°	105°	90°
166673	10°	30°	101°	90°
166939	22°	28°	115°	88°
166945	15°	33°	103°	88°
166986	13°	33°	283°	88°
167136	13°	28°	284°	88°
167211	12°	30°	282°	88°
167230	12°	30°	282°	88°
167243	10°	28°	282°	88°
167248	8°	25°	282°	88°
167268	8°	25°	282°	88°
167326	10°	33°	284°	88°
167330	20°	30°	110°	88°
167342	19°	22°	109°	90°
167347	12°	42°	285°	88°
167350	15°	42°	105°	86°
167380	20°	17°	110°	89°
167429	30°	18°	115°	88°
167430	5°	18°	283°	88°
167444	7°	20°	283°	88°
167447	7°	30°	283°	88°
167509	17°	30°	110°	85°

Table J.10: Fault-plane solutions for Family 3, BGM 17-24W site.

Event no.	Fault-plane solution 1		Fault-plane solution 2	
Sub-cluster 1	*Strike*	*Dip*	*Strike*	*Dip*
158887	23°	86°	293°	58°
158892	25°	79°	291°	63°
159052	26°	83°	293°	63°
159079	24°	89°	294°	56°
159255	24°	89°	294°	56°
159348	25°	79°	291°	63°
159349	24°	87°	292°	61°
159364	26°	83°	294°	70°
159406	24°	89°	294°	50°
159491	24°	89°	294°	57°
159795	26°	85°	294°	63°
159956	25°	83°	291°	63°
160450	27°	79°	294°	70°
Sub-cluster 2				
158838	2°	80°	92°	88°
158890	6°	67°	276°	88°
158968	6°	74°	96°	88°
159161	6°	70°	275°	88°
159162	12°	64°	281°	89°
159299	12°	64°	281°	89°
159378	17°	89°	107°	74°
159483	17°	89°	107°	74°
159487	6°	66°	97°	89°
159492	6°	64°	97°	89°

Table J.11: Source parameters for Family 1.

Event no.	Magnitude	Relative strength	Deviation from DC	Isotropic
	M	*MO%*	ε	*ISO%*
158819	-0.6	100	0.15	12
158822	-1.2	31	0.22	12
158957	-1.1	34	0.15	12
159126	-1.0	26	0.22	14
160442	-1.3	18	0.13	12

Table J.12: Source parameters for Family 2.

Event no.	Magnitude	Relative strength	Deviation from DC	Isotropic
	M	*MO%*	ε	*ISO%*
166232	-0.9	100	0.25	14
166233	-0.4	214	0.45	16
166240	-0.6	163	0.19	15
166490	-1.1	86	0.17	13
166504	-1.2	79	0.24	13
166578	-1.2	47	0.39	13
166596	-0.8	133	0.11	15
166646	-1.2	78	0.17	13
166663	-1.1	71	0.24	13
166673	-1.1	65	0.23	14
166939	-0.6	148	0.19	15
166945	-0.9	101	0.33	13
166986	-1.1	63	0.22	13
167136	-0.9	106	0.14	14
167211	-1.1	72	0.25	13
167230	-0.8	72	0.16	14
167243	-1.0	70	0.12	13
167248	-1.1	60	0.20	13
167268	-0.9	99	0.16	14
167326	-1.0	69	0.20	15
167330	-1.0	93	0.18	14
167342	-1.0	99	0.14	15
167347	-0.2	135	0.16	14
167350	-0.2	381	0.44	14
167380	-1.1	65	0.13	14
167429	-0.7	63	0.26	15
167430	-0.7	87	0.17	14
167444	-1.1	111	0.18	15
167447	-1.1	79	0.24	14
167509	-0.3	350	0.40	14

Table J.13: Source parameters for Family 3.

Event no.	Magnitude	Relative strength	Deviation from DC	Isotropic
	M	*MO%*	ε	*ISO%*
Sub-cluster 1				
158887	-1.1	100	0.01	6
158892	-1.3	31	0.13	8
159052	-1.0	139	0.08	5
159079	-0.9	64	0.13	7
159255	-0.5	301	0.09	5
159348	-0.8	191	0.14	6
159349	-0.6	150	0.01	7
159364	-0.6	105	0.07	8
159406	-1.1	28	0.25	9
159491	-0.9	26	0.14	10
159795	-0.8	127	0.11	6
159956	-1.0	62	0.00	8
160450	-1.1	88	0.01	6
Sub-cluster 2				
158838	0.0	100	0.02	12
158890	-1.1	19	0.10	11
158968	-1.3	13	0.25	11
159161	-1.1	17	0.21	10
159162	-0.9	21	0.23	12
159299	-1.1	9	0.24	12
159378	-1.2	13	0.07	11
159483	-1.2	8	0.07	10
159487	-1.0	10	0.25	13
159492	-0.9	17	0.22	12

J.4 INTERPRETATION AND DISCUSSION

Using the radiation patterns and fault-plane solutions, focal mechanisms were determined for each event family (Figures J.10, J.11 and J.12). In each case, a representative radiation pattern (the first event in each family) is used to illustrate the sense of displacement on the fault plane. The fracture mapping was used to distinguish the fault plane from the auxiliary plane.

J.4.1 Family 1

The radiation patterns for the deviatoric, double-couple, strike-slip, and dip-slip moment tensor components computed for Family 1 (Figure J.7) are similar for all five events in the cluster. The patterns display an oblique-slip focal mechanism (refer to the triangle diagram in Figure 2.6), with a right-lateral sense of displacement (Figure J.10). The fault-plane solutions show a vertical fault plane, with an EW strike, where the fault block in the North moves downwards relative to the southerly block. The poles to the fault planes (nodal plane) are tightly clustered (Figure J.10) and correlate well with those observed for the Group I fractures.

The deviation ε of the seismic source from the pure double-couple model (the ratio of the minimum to maximum eigenvalue) for the events of Family 1 vary from 0.13 to 0.22 (Table J.11). Since $\varepsilon = 0$ for a pure double-couple source, and $\varepsilon = 0.5$ for a pure CLVD source, the values computed indicate that these events fit the double-couple model moderately well.

The events in Family 1 show a positive isotropic component (Table J.11) of ~12%. This component represents an increase in the volume of the source i.e. dilation on the fracture plane. This component is dealt with in the discussion at the end of this section.

J.4.2 Family 2

The radiation patterns of the events in Family 2 show more variation than those of Family 1, but display a similar trend (Figure J.8) for all components. The source mechanism may be described as an oblique-slip fault with a left-lateral sense of displacement and normal slip on the fault plane. The fault-plane solutions show a NS striking fault plane, dipping shallowly (~35°) towards the East. The poles to the fault planes correlate well with those observed for the Group VI fractures (Figure J.11).

The deviation ε of the seismic source for ~80% of the events of Family 2 vary show values less than or equal to 0.25 (Table J.12). It is interesting to note that the higher ε values (> 0.4) which indicate a deviation from a pure-double couple model are associated with the larger events (M > -0.4). Dziewonski *et al.* (1981) would describe the source model for these events as a CLVD.

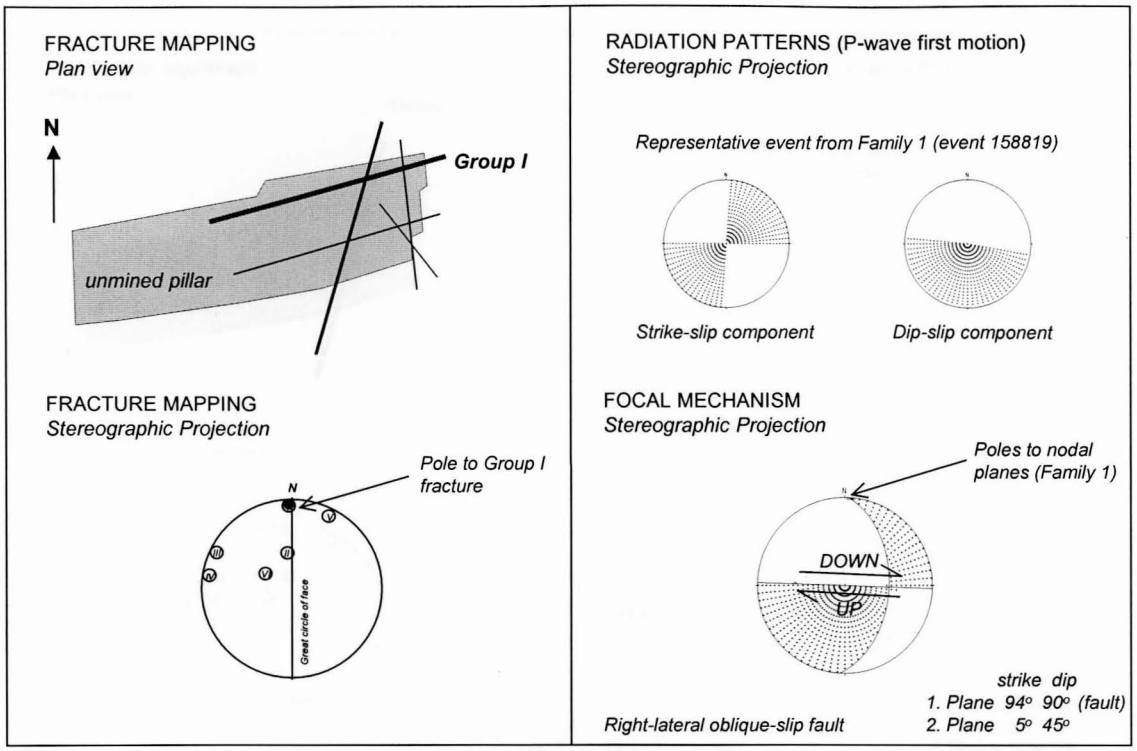

Figure J.10: Focal mechanism for Family 1 located on Group I fracture, BGM 24-17W site.

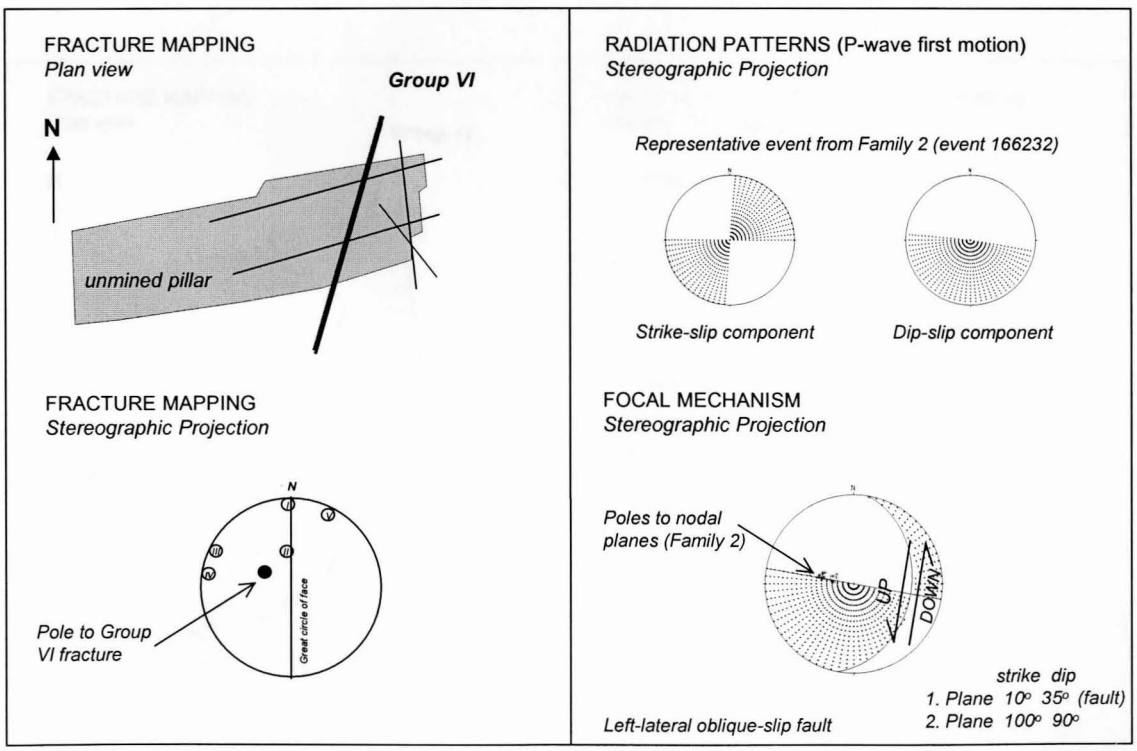

Figure J.11: Focal mechanism for Family 2, located on Group VI fracture, BGM 24-17W site.

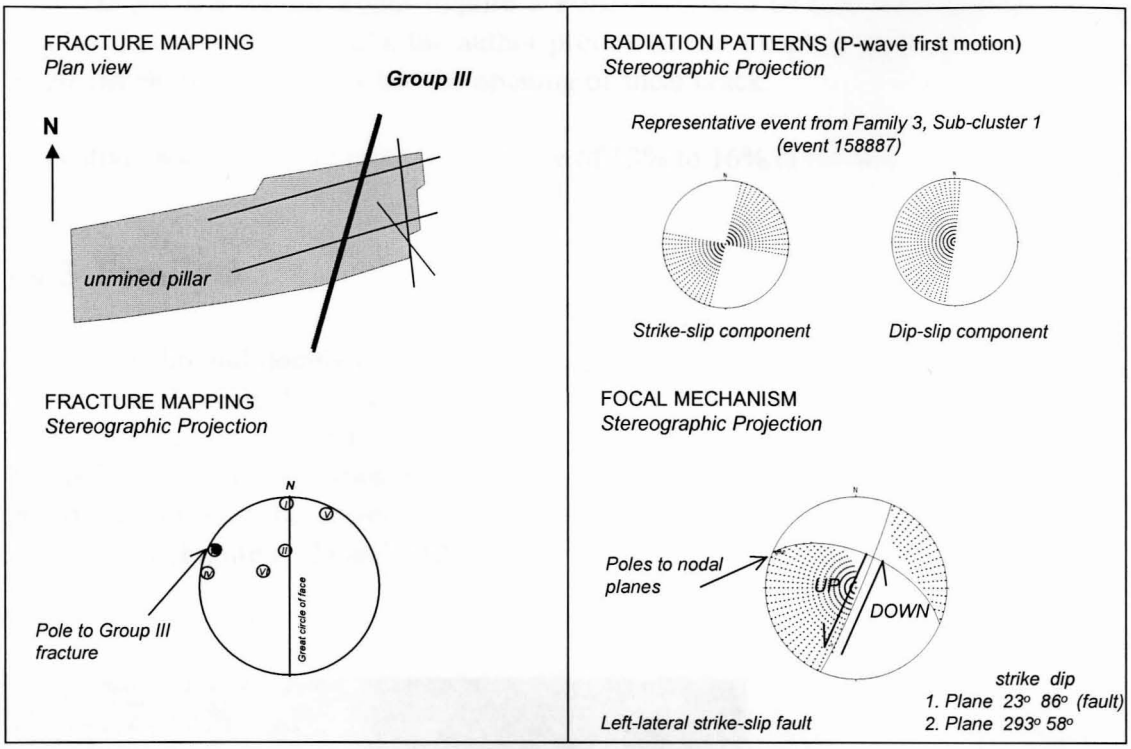

Figure J.12(a): Focal mechanism for sub-cluster 1 (Family 3) located on Group III fracture, BGM 24-17W site.

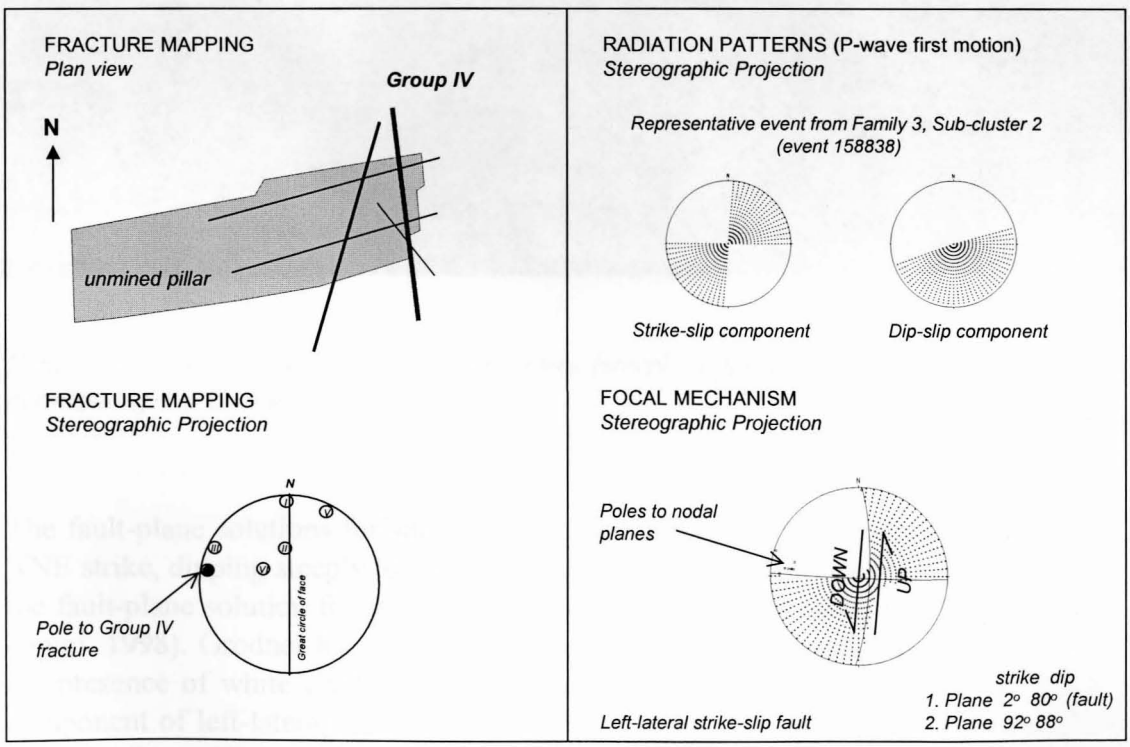

Figure J.12(b): Focal mechanism for sub-cluster 2 (Family 3) located on Group IV fracture, BGM 24-17W site.

However, since there is no physical model that matches the force system described by a CLVD (such a model would require a Poisson's[1] ratio of 0.5; rock generally has ratio of the magnitude ~0.25), the author prefers to use a triple-couple source model, where the third couple describes the opening of shear crack.

A positive isotropic component in the range of 13% to 16% is present.

J.4.3 Family 3

The strike-slip and double-couple radiation patterns for both sub-clusters of Family 3 are similar (Figures J.9b and J.9c). In contrast, there is a distinct difference in the deviatoric and dip-slip patterns between the two sub-clusters (Figures J.9a and J.9d). The poles to the nodal planes for sub-clusters 1 and 2 are concentrated in two distinct groups, which may be correlated with the poles to the Group III and IV fractures, respectively (Figure J.12a and J.12b).

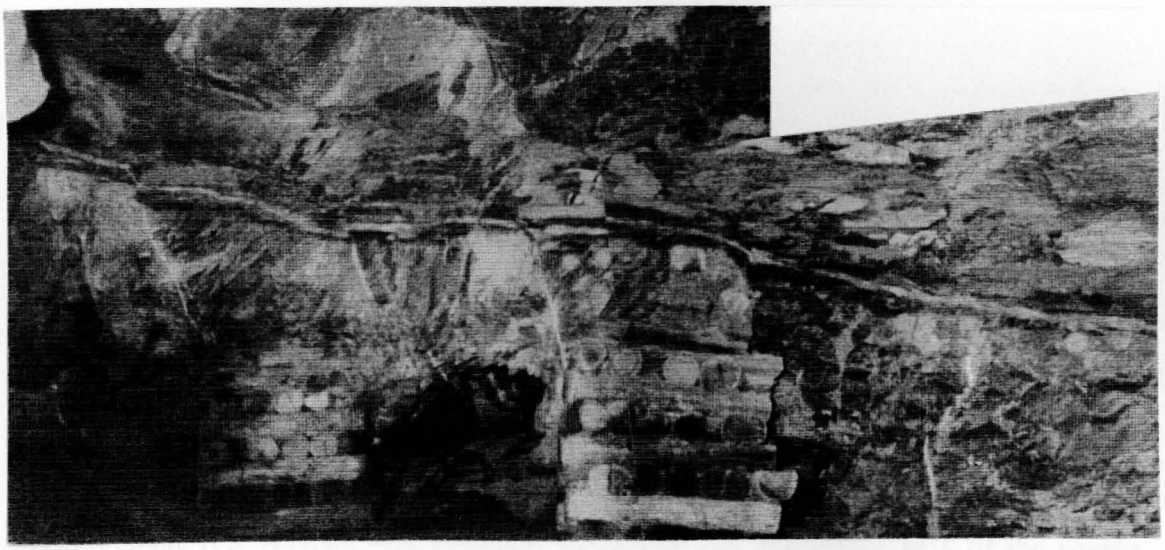

Figure J.13: Photograph of Group III fractures (steeply dipping shear zone). (Printed with permission from Grodner, 1998).

The fault-plane solutions for sub-cluster 1 show a left-lateral strike-slip fault, with a NNE strike, dipping steeply towards the East (Figure J.12a). The sense of direction of the fault-plane solution for sub-cluster 1 correlates with that noted by Grodner (pers. comm. 1998). Grodner has mapped the Group III faults in detail. He concluded that the presence of white crushed quartz and offset joints indicates that there is a later component of left-lateral shear (parallel to the overall face shape) on the extensional faults of Group III. A photograph of these shears provides final ground-truth evidence

[1] Poisson's ratio is the ratio between the lateral and axial strain.

(Figure J.13). This correlates with the fault mechanism (left-lateral strike-slip fault, with a normal dip-slip component) of the source cluster of Family 3.

The source mechanism for sub-cluster 2 may also described as a left-lateral strike-slip fault, but display a component of thrust. The fault-plane solutions show a NS striking fault plane, dipping steeply towards the East. The poles to the fault planes correlate with those with those observed for the Group IV fractures (Figure J.12b).

The ε source parameter computed for the events in sub-cluster 1 (events within the plane of the seismic network) is low, ranging from 0.0 (pure double-couple model) to 0.14 for all except one event with $\varepsilon = 0.25$, indicative of a double-couple source model. The values of this parameter are also low for sub-cluster 2 and range from 0.02 to 0.25.

The isotropic component for both sub-clusters is positive and ranges from 7% to 14%.

J.4.4 Discussion

The dips and strikes deduced from the fault plane solutions for the seismic event clusters correlate with those documented in the fracture mapping of Kullman *et al.* (1996). The focal mechanisms confirm the conclusions of Kullman *et al.* (1996), which were based on event location and detailed geological work. They concluded that the pre-existing steeply dipping shear zones (Group III) and the mining-induced fractures (Groups I, IV and VI) were reactivated by the preconditioning blasts.

The focal mechanisms determined during this study show that several mechanisms are in action at the BGM preconditioning site. The dominating mechanism in most cases is of the shear type (i.e. double-couple source model). However, source parameters computed for the larger events in Family 2 show a deviation from the double-couple mechanism. The additional component contributing to the mechanism is thought to be due to the opening of the shear crack. All of the events display small positive isotropic components (i.e. dilatant mechanisms), in general not exceeding 14% of the source mechanism.

Non-double couple sources arising from the use of conventional inversion methods (absolute methods) must be treated with caution, because they may be a result of noisy data, and/or an insufficient knowledge of the Green's functions. However, the relative inversion eliminates the potential biasing effect of poorly evaluated Green's functions, as well as being fairly stable with regard to noise. The isotropic component present in all families is therefore considered to be a genuine component, representing a volume change at the source.

The positive isotropic component is thought to be a result of over-riding of asperities on the fault plane resulting in a volume increase. An aspect contributing to the volumetric expansion could be the lack of confinement of the BGM 24-17W stabilising pillar due to mining, which allows expansion towards the stope face and exposed mining surfaces.